Université Paris Cité

École doctorale Cerveau, Cognition, Comportement (ED 158)
CNRS UMR 8003 SPPIN (Saints-Pères Paris Institute for the Neuroscience)

Anatomy, physiology and input connectivity of anterior thalamic neurons projecting to cortical head direction regions

Par Dongkyun LIM

Thèse de doctorat de Neurosciences

Dirigée par Desdemona FRICKER

Présentée et soutenue publiquement le 10/11/2025

Devant un jury composé de :

Andrea BURGALOSSI, Prof.	University of Tübingen	Rapporteur
Anita LÜTHI, Assoc. Prof.	University of Lausanne	Rapportrice
Thierry BAL, DR.	Université Paris-Saclay	Examinateur
Rebecca PISKOROWSKI, DR.	Sorbonne Université	Examinatrice
Giuseppe GANGAROSSA, Prof.	Université Paris Cité	Président du jury
Desdemona FRICKER, DR	Université Paris Cité	Directrice de Thèse

Abstract

Title: Anatomy, physiology and input connectivity of anterior thalamic neurons projecting to cortical head direction regions.

Keywords: Anterior thalamic nuclei; Head direction system; Electrophysiology; Presubiculum; Retrosplenial cortex; Mammillary body

Abstract: The anterior thalamic nucleus is a critical brain region within the head direction (HD) system. The anterodorsal (AD) and anteroventral (AV) subnuclei receive inputs from the mammillary body and relay this information to two cortical HD regions, the presubiculum (PrS) and retrosplenial cortex (RSC). However, little is known about the anatomy and input connectivity of these thalamocortical projection neurons. Also, the electrophysiological profiles of individual AD and AV neurons and how they transform input to output signals remain elusive. During my PhD, I studied 1) the anatomical organisation of AD and AV thalamic projecting neurons, 2) their intrinsic electrophysiological features, and 3) the anatomical and functional input connectivity from the mammillary body to the AD and AV.

First, I investigated the anatomical organisation of anterior thalamic neurons projecting to the PrS and to the granular retrosplenial cortex (gRSC). Thalamic projection neurons were labelled by retrograde tracers injected into the PrS and gRSC and registered onto a standardised 3D brain atlas for quantitative analysis. My results show that PrS-projecting and gRSC-projecting neurons are topographically organised within the AD and AV. The presence of double-labelled neurons demonstrates a partial overlap of the projection-defined populations in AD and AV, and indicates that individual thalamocortical projection neurons send action potentials to both PrS and gRSC.

Second, I studied the intrinsic electrophysiological properties of AD and AV neurons, using whole-cell patch clamp recordings in acute brain slices. The main finding is that AD and AV neurons possess highly distinct electrophysiological profiles in terms of excitability, firing patterns and action potential bursting. Principal component analysis based on multiple parameters extracted from the patch-clamp recording revealed that AD and AV neurons segregate in two clusters, regardless of their projection targets. Morphological properties were studied by reconstructing the biocytin filled patched neurons in 3D. I found that AD neurons possess radiating dendritic structures, while AV neurons show a bushy morphology with more complex dendritic organisation.

Third, I studied the functional input connectivity from the mammillary body (MBO) to the AD and AV. Chronos, a blue light-sensitive opsin, was expressed unilaterally in the MBO, such that photostimulation of their axons evoked excitatory postsynaptic responses in AD and AV neurons. My results show that the mammillary input to the AD and AV is monosynaptic and glutamatergic based on the short latency of their postsynaptic responses and pharmacological experiments. Axons originating from the MBO of one hemisphere innervate both ipsilateral and contralateral AD and AV neurons, with stronger input efficiency on the ipsilateral side. Monosynaptically restricted rabies tracing experiments confirmed the bilateral projection of lateral and medial mammillary bodies to the AD and AV.

Taken together, my PhD work offers new insights about anatomical and electrophysiological properties of thalamic subnuclei. My results suggest a potential integrative role for AD and AV thalamic subnuclei receiving inputs from the left and right MBOs, before sending head direction related signals to the PrS and gRSC. My thesis also lays the foundations for follow up work. I showed that AD and AV neurons are sensitive to cholinergic agonists which may be critical for attentional modulation of HD signals. Potential cholinergic input sources were identified in the mesencephalic tegmentum, based on retrograde tracing in ChAT-Cre::TOM transgenic mice. My initial calcium imaging experiments using a head mounted miniatures microscope indicates the possibility to distinguish HD signals in identified neurons in AD and AV. Eventually, it will be interesting to investigate the HD activity of AD and AV neurons in vivo and to explore how cholinergic inputs shape HD tuning.

Résumé

Titre: Anatomie, physiologie et connectivité des afférences des neurones thalamiques antérieurs projetant vers les régions corticales de la direction de la tête.

Mots clefs: Noyaux thalamiques antérieurs; Système de direction de la tête; Électrophysiologie; Presubiculum, Cortex rétrosplénial, Corps mamillaires

Résumé: Le noyau thalamique antérieur est une région cérébrale clé du système de la direction de la tête (HD). Les sous-noyaux anterodorsal (AD) et anteroventral (AV) reçoivent des afférences du corps mamillaire et transmettent ces informations à deux régions corticales HD : le présubiculum et le cortex rétrosplénial. Cependant, l'anatomie et la connectivité des afférences de ces neurones thalamocorticaux sont encore mal connues. De plus, les profils électrophysiologiques des neurones AD et AV individuels restent peu caractérisés. Au cours de ma thèse, j'ai étudié : 1) l'organisation anatomique des neurones AD et AV selon leurs cibles axonales, 2) leurs propriétés électrophysiologiques intrinsèques, et 3) la connectivité anatomique et fonctionnelle des afférences issues du corps mamillaire vers l'AD et l'AV.

Premièrement, j'ai analysé l'organisation anatomique des neurones thalamiques projetant vers le présubiculum (PrS) et vers le cortex rétrosplénial granulaire (gRSC). Les neurones projetant ont été marqués à l'aide de traceurs rétrogrades injectés dans le PrS et le gRSC, puis enregistrés dans un atlas cérébral 3D standardisé pour une analyse quantitative. Mes résultats montrent que les neurones projetant vers le PrS et ceux projetant vers le gRSC sont organisés topographiquement dans les noyaux AD et AV du thalamus. La présence de neurones doublement marqués révèle un chevauchement partiel entre les populations définies par leurs projections dans l'AD et l'AV, suggérant que certains neurones thalamocorticaux transmettent des signaux à la fois au PrS et au gRSC.

Deuxièmement, j'ai étudié les propriétés électrophysiologiques intrinsèques des neurones AD et AV à l'aide d'enregistrements en patch-clamp en configuration cellule entière sur tranche aiguë de cerveau. Le principal résultat est que les neurones AD et AV présentent des profils électrophysiologiques distincts en termes d'excitabilité, de modes de décharge et de décharge en bouffée de potentiels d'action. Une analyse en composantes principales basée sur plusieurs paramètres extraits des enregistrements patch-clamp a révélé que les neurones AD et AV se regroupent en deux clusters distincts, indépendamment de leur cible de projection. Les propriétés morphologiques ont été examinées en reconstruisant en 3D les

neurones remplis de biocytine. J'ai observé que les neurones AD présentent une morphologie radiaire, tandis que les neurones AV possèdent une morphologie plus buissonnante avec une arborisation dendritique plus complexe.

Troisièmement, j'ai étudié la connectivité fonctionnelle des afférences du corps mamillaire vers l'AD et l'AV. Chronos, une opsine activée par la lumière bleue, a été exprimée de manière unilatérale dans le corps mamillaire (MBO), permettant d'évoquer des réponses postsynaptiques excitatrices dans les neurones AD et AV par photostimulation des axones. Mes résultats montrent que les afférences mamillaires vers l'AD et l'AV sont monosynaptiques et glutamatergiques, sur la base de la latence courte des réponses postsynaptiques et d'expériences pharmacologiques. Les axones issus du MBO d'un hémisphère innervent à la fois les neurones AD et AV ipsilatéraux et controlatéraux, avec une efficacité plus forte du côté ipsilatéral. Des expériences de traçage rabique restreint à une seule synapse ont confirmé cette projection bilatérale des afférences mamillaires vers l'AD et l'AV.

Dans l'ensemble, mon travail de thèse apporte de nouvelles connaissances sur les propriétés anatomiques et électrophysiologiques des noyaux AV et AD thalamiques. Mes résultats suggèrent un rôle intégrateur potentiel pour ces noyaux, recevant des afférences des MBO gauche et droit, avant de transmettre les signaux HD au PrS et au gRSC. Ma thèse constitue également une base pour des travaux futurs. J'ai montré que les neurones AD et AV sont sensibles aux agonistes cholinergiques, ce qui pourrait jouer un rôle clé dans la modulation attentionnelle des signaux HD. Les sources potentielles des afférences cholinergiques ont été identifiées dans le tegmentum mésencéphalique, à l'aide de traçage rétrograde chez des souris transgéniques ChAT-Cre::TOM. Mes premières expériences d'imagerie calcique avec un microscope miniature monté sur la tête de la souris suggèrent qu'il est possible de distinguer les signaux HD dans des neurones identifiés dans l'AD et l'AV. À terme, il sera intéressant d'étudier l'activité HD des neurones AD et AV in vivo, ainsi que l'influence potentielle des afférences cholinergiques sur leur sélectivité HD.

Résumé substantiel

Les cellules Head direction (HD) sont souvent décrites comme la boussole du cerveau. Chaque cellule HD est réglée sur une direction particulière, déchargeant de manière maximale lorsque la tête est orientée dans cette direction, appelée direction préférée de décharge. Ensemble, la population de cellules HD code toutes les directions dans le plan horizontal, couvrant 360°. Les cellules HD ont été identifiées pour la première fois dans le Presubiculum par Ranck JB (1984). Des cellules HD ont également été retrouvées dans plusieurs régions cérébrales, incluant le dorsal tegmental nucleus (DTN), le lateral mammillary nucleus (LMN), l'anterodorsal (AD) et l'anteroventral nucleus (AV) du thalamus, le retrosplenial cortex (RSC), le presubiculum (PrS), le parasubiculum (PaS), et le medial entorhinal cortex (MEC) (Angelaki & Laurens, 2020; Taube, 2007). Bien que les cellules HD soient observées dans plusieurs régions cérébrales, la raison de leur large distribution reste incertaine (Taube, 2007).

Ces régions sont interconnectées et forment un réseau hiérarchique au sein du système HD. L'organisation hiérarchique contribue à un traitement précis du signal HD, en progressant dans le réseau grâce à l'intégration d'entrées multisensorielles et modulatrices. La source principale se situe dans le DTN du tronc cérébral, qui génère le signal à partir des entrées vestibulaires codant la vitesse angulaire de la tête (Sharp, Blair, et al., 2001; Sharp, Tinkelman, et al., 2001; Yoder & Taube, 2014). La connectivité réciproque entre le DTN et le LMN est supposée établir le signal HD initial (Bassett et al., 2007; H. T. Blair et al., 1998; J. S. Taube, 2007). En résumé, le circuit HD est organisé hiérarchiquement le long de la voie DTN → LMN → AD → PrS/RSC → MEC. Cependant, des cellules réglées directionnellement ont également été observées en dehors de cette voie hiérarchique, incluant l'AV (Lomi et al., 2023; Tsanov, Chah, Vann, et al., 2011; Yoganarasimha et al., 2006), le noyau anteromédiale du thalamus (Jankowski et al., 2015), le parataenial nucleus (Jankowski et al., 2015), le nucleus reuniens (Jankowski et al., 2015), et le lateral dorsal nucleus du thalamus (Mizumori & Williams, 1993).

Le modèle computationnel prédominant de l'activité HD est l'anneau attracteur (Angelaki & Laurens, 2020; McNaughton et al., 2006; Redish et al., 1996; Sharp, Blair et al., 2001; Skaggs et al., 1995; K. Zhang, 1996). Dans ce modèle, les cellules HD sont organisées en un anneau conceptuel, où les cellules voisines possèdent des directions préférées similaires. Chaque cellule est active uniquement lorsque la tête est orientée dans une plage angulaire restreinte, et la population couvre collectivement l'ensemble des 360°, analogue à une boussole neuronale. Les cadres théoriques proposent que la connectivité est organisée de

manière à ce que les neurones avec des directions proches soient mutuellement excitateurs, tandis que ceux avec des directions éloignées exercent une influence inhibitrice. Cet équilibre entre excitation locale et inhibition globale produit une activité localisée unique représentant l'orientation actuelle.

Dans ma thèse doctorale, nous nous concentrons sur les noyaux antérieurs du thalamus (ATN), en particulier la subdivision AD et AV. De nombreuses études ont rapporté une activité de cellules HD au sein de ces sous-noyaux (Ajabi et al., 2023; H. Blair & Sharp, 1995; H. T. Blair et al., 1999; Lomi et al., 2023; Stackman & Taube, 1997; J. Taube, 1995; Tsanov, Chah, Vann, et al., 2011; Viejo & Peyrache, 2020), soulignant leur implication centrale dans le codage directionnel. L'AD est le sous-noyau le plus étudié en relation avec le système HD. Une grande proportion de neurones de l'AD est réglée directionnellement (J. Taube, 1995), et les études de lésions ont montré son rôle crucial dans la transmission des signaux directionnels entre les régions hypothalamiques et corticales (Bubb et al., 2017; Guison et al., 1995; Lomi et al., 2021; Mathiasen et al., 2021; Shibata, 1992, 1993b, 1993a; Stackman & Taube, 1998, 1998; J. Taube, 1995; J. S. Taube, 2007; Van Groen & Michael Wyss, 1990; Van Groen & Wyss, 1990a, 1995; Vann et al., 2007; Vann & Aggleton, 2004). Il a été initialement rapporté qu'environ 60 % des neurones de l'AD sont modulé par la direction de la tête (J. Taube, 1995). Comparées aux cellules HD d'autres régions cérébrales, celles de l'AD se caractérisent par des taux de décharge relativement plus élevés (Taube, 2007). L'AD reçoit des entrées directionnelles du LMN des deux hémispheres, et envoie des sorties vers le cortex retrospleniale et le presubiculum. L'AV a reçu moins d'attention dans la recherche sur les neurones HD, étant souvent regroupé avec l'AD et décrit comme faisant partie des ATN dans les études fonctionnelles. Son rôle dans le système HD est resté longtemps incertain, la plupart des études s'étant focalisées sur l'AD comme noyau thalamique principal pour le traitement des HD. L'AV reçoit des entrées mammillaires du medial mammillary body (MMN, Dillingham et al., 2015; Jankowski et al., 2013; Umaba et al., 2021), avec une projection principalement ipsilatérale (Cruce, 1975; Dillingham et al., 2015; Seki & Zyo, 1984; H. Shibata, 1992; Veazey et al., 1982; Wiener & Taube, 2005). En raison de sa localisation anatomique dans les circuits limbiques, l'AV a été étudié pour son rôle dans le maintien de l'activité rythmique thêta. Les neurones de l'AV (jusqu'à 75 %) déchargent rythmiquement et en synchronie avec les oscillations thêta hippocampiques CA1 (Albo, 2003; Vertes et al., 2001). Des études récentes ont fourni des preuves de l'activité HD dans l'AV (Lomi et al., 2023; Tsanov, Chah, Vann, et al., 2011; Yoganarasimha et al., 2006). Trois types de cellules HD ont été rapportés dans cette région : cellules HD, cellules modulées par le rythme thêta, et cellules HD modulées par le rythme thêta. Les deux noyaux thalamiques reçoivent des entrées modulatrices de sources diverses. Des recherches anatomiques et comportementales montrent que des entrées GABAergiques modulatrices du TRN projettent vers les deux régions thalamiques et que leur inhibition altère la sélectivité directionnelle dans l'AD (Gonzalo-Ruiz et al., 1995; Vantomme et al., 2020). Une modulation cholinergique a été suggérée dans les deux noy-

aux, probablement issue du pedunculopontine nucleus et du laterodorsal tegmental nucleus (Gonzalo-Ruiz et al., 1995; Satoh & Fibiger, 1986). Des études fonctionnelles indiquent que l'acétylcholine contribue à la stabilité et à la robustesse des signaux HD, particulièrement dans des conditions nécessitant l'intégration du trajet (Yoder et al., 2017).

Alors que l'AD et l'AV ont suscité une attention croissante pour leur rôle dans le système HD (Ajabi et al., 2023; Ji, Lomi, et al., 2025; Lomi et al., 2023; Peyrache et al., 2015, 2017; Tsanov, Chah, Vann, et al., 2011; Viejo & Peyrache, 2020), leur connectivité anatomique et leurs propriétés électrophysiologiques n'ont pas encore été suffisamment étudiées. Les études antérieures de lésions et de comportement se sont concentrées sur l'organisation hiérarchique du système HD le long de la voie LMN-AD-PrS/gRSC (H. T. Blair et al., 1998, 1999; Guison et al., 1995; Lomi et al., 2023; Mathiasen et al., 2021; Seki & Zyo, 1984; H. Shibata, 1992; Van Der Goes et al., 2024). Ces études reposaient sur des approches anatomiques ou des techniques d'enregistrement extracellulaire, laissant une lacune dans notre compréhension au niveau neuronal et synaptique : les entrées mammillaires sont-elles connectées monosynaptiquement aux neurones de projection thalamocorticaux ? Si oui, comment déclenchent-elles l'activité neuronale dans l'AD et dans l'AV ? Pour répondre à cette question, j'ai combiné 1) le traçage monosynaptique rétrograde par virus rabique, afin de déterminer si les neurones de projection thalamiques reçoivent directement des entrées mammillaires, et 2) des expériences optogénétiques, utilisant la photostimulation des axones du corps mammillaire, pour examiner les transformations entrée–sortie. J'ai soigneusement examiné l'efficacité des axones mammillaires d'un hémisphère à exciter les neurones thalamiques dans l'AD et l'AV ipsilatéraux et controlatéraux. De plus, les caractéristiques électrophysiologiques des neurones individuels restent peu étudiées. Des études récentes soulignent encore davantage l'importance fonctionnelle des neurones AD et AV pour la mémoire de travail et les troubles neuropsychiatriques (Roy et al., 2021; Roy, Zhang, Aida, et al., 2022). Ici, j'ai entrepris d'identifier les propriétés électrophysiologiques et morphologiques des neurones AD et AV de manière multidimensionnelle. J'ai ensuite demandé si chaque sous-population de neurones de projection générait des signaux électrophysiologiques distincts. Pour aborder cette question, j'ai optimisé les protocoles expérimentaux pour les enregistrements patch-clamp et amélioré les outils d'analyse de notre laboratoire.

De plus, j'ai étudié si les neurones AD et AV modifient leur activité de décharge en réponse à des agonistes cholinergiques, étant donné qu'il existe des preuves anatomiques de projections cholinergiques vers les ATN (Gonzalo-Ruiz et al., 1995; Hallanger et al., 1987, 1990; M. Parent & Descarries, 2008; Sofroniew et al., 1985). L'origine de ces fibres cholinergiques étant encore incertaine, j'ai cherché à identifier les sources potentielles dans le cerveau. J'ai appris à utiliser l'imagerie calcique via un microscope miniature (« miniscope ») installé sur la tête de l'animal, afin de distinguer les signaux HD dans des neurones identifiés de l'AD et de l'AV, avec pour objectif de manipuler potentiellement les entrées

cholinergiques tout en suivant l'activité HD des neurones AD et AV pendant le comportement.

J'ai étudié les propriétés anatomiques et électrophysiologiques des neurones AD et AV dans le système HD afin d'aborder les lacunes mentionnées ci-dessus. Premièrement, je démontre l'organisation anatomique des neurones de projection thalamiques dans la connectivité mammillo-thalamo-corticale. Les expériences de traçage monosynaptique rétrograde ont révélé que ces neurones thalamo-corticales reçoivent des entrées directes depuis les corps mammillaires. Le point intéressant est que les projections mammillo-thalamiques semblent être bilatérales, puisque des neurones présynaptiques marqués par le virus rabique ont été observés dans les deux hémisphères, alors que l'injection était réalisée unilatéralement. En outre, à l'aide d'un traçage rétrograde, j'ai démontré que les neurones AD et AV projetant vers le PrS et le gRSC sont organisés topographiquement. Dans les zones de recouvrement, des neurones bifurquants ont été identifiés, révélant que certains neurones AD et AV projettent vers les deux cibles corticales.

Deuxièmement, j'ai examiné les propriétés électrophysiologiques intrinsèques des neurones AD et AV, en utilisant la technique patch-clamp en configuration whole-cell. J'ai recueilli des enregistrements électrophysiologiques dans les deux noyaux. 25 propriétés (Resting membrane potential, time constant, sag ratio, rebound spike probability, rheobase current, threshold, latency, AP peak, AP width, AP rise amplitude, afterhyperpolarisation (AHP), maximum depolarisation rate, repolarisation rate, current at 10 Hz, burst index, initial burst ISI, mean initial ISI, adaptation index, fast doublet index, fast doublet ratio, Δ peak between AP1–AP2, input-output slope, firing rate at 200 pA, rebound spike probability) ont été analysées à partir des cellules enregistrées. Un test de réduction dimensionnelle utilisant la PCA sur ces propriétés suggère que les neurones AD et AV sont électrophysiologiquement distincts, indépendamment de leur spécificité de projection. Les neurones AD présentent un potentiel de repos plus dépolarisé, une résistance d'entrée plus faible, une constante de temps plus courte, un sag plus fort suivant une impulsion hyperpolarisante, et une pente entrée–sortie plus élevée que les neurones AV. Leurs patrons de décharge à 10 Hz étaient différents entre AD et AV. Les neurones AD présentent un patron adaptatif avec un ISI augmentant progressivement, tandis que les neurones AV présentent une bouffée initiale suivie de décharges irrégulières. La reconstruction 3D des axones et dendrites de cellules remplies de biocytine a démontré que les neurones AD et AV présentent également des caractéristiques morphologiques distinctes. Les neurones AD possèdent une structure dendritique rayonnante, tandis que les neurones AV présentent une arborisation plus touffue et complexe.

Troisièmement, j'ai étudié les réponses postsynaptiques des neurones AD et AV évoquées par les entrées mammillaires. Cela a été réalisé en exprimant Chronos dans les corps mammillaires unilatéraux. La stimulation optogénétique des axones mammillo-thalamiques a révélé que les neurones AD et AV reçoivent des entrées ipsilatérales monosynaptiques et

glutamatergiques fortes, ainsi que des entrées controlatérales plus faibles. Le taux de connectivité était élevé (> 94 %) dans les noyaux AD et AV ipsilatéraux. Du côté controlatéral, le taux de connectivité restait relativement élevé dans l'AD (85 %), mais faible dans l'AV (38,9 %). Au sein de la population de neurones connectés, plus de la moitié des cellules enregistrées ont montré une activité de décharge (63 % dans l'AD et 81 % dans l'AV) du côté ipsilatéral. Du côté controlatéral, seuls 18 % des neurones AD ont montré une activité de décharge, tandis que 57 % des cellules AV en présentaient une. Ce résultat concernant la connectivité fonctionnelle corrobore nos observations avec le traçage rabique, selon lesquelles l'entrée mammillaire est monosynaptique et bilatérale.

Quatrièmement, je montre l'effet cholinergique potentiel sur les neurones AD et AV. J'ai réalisé des enregistrements patch-clamp en configuration whole-cell tout en délivrant des marches de courant dépolarisa. Le carbachol (10 μM) a été appliqué par perfusion dans le bain, dilué dans l'ACSF. Après l'application du carbachol, l'activité de décharge de chaque neurone a été abolie en réponse aux marches de courant. Cet effet a été observé dans les deux noyaux thalamiques. Partant de cette observation, j'ai cherché à identifier l'origine des entrées cholinergiques vers ces noyaux thalamiques. En utilisant des souris transgéniques ChAT::TOM et une stratégie de marquage rétrograde, j'ai étudié les sources cholinergiques potentielles projetant vers l'AD et l'AV. Les afférences vers AD/AV étaient diverses. D'après la distribution des neurones marqués, les régions candidates susceptibles de fournir une entrée cholinergique comprenaient le cuneiform nucleus, le lateral tegmental nucleus, le periaqueductal grey, le pedunculopontine nucleus, le midbrain reticular nucleus, et le lateral hypothalamic area. Ce résultat peut constituer une donnée préliminaire pour explorer plus avant l'effet cholinergique sur l'activité neuronale de l'AD et de l'AV.

Cinquièmement, j'ai réalisé de l'imagerie calcique afin d'évaluer l'activité HD des neurones thalamiques chez une souris libre de ses mouvements. L'activité des neurones projetant vers le Presubiculum dans les deux noyaux thalamiques a été enregistrée avec un miniscope pendant que la souris explorait une cage ouverte transparente dans un environnement de laboratoire conventionnel. Chez une souris, 25 cellules HD putatives ont été observées dans l'AD, et 7 dans l'AV. Un sous-ensemble de cellules modulées par la direction de la tête a montré des variations de leur direction preferentielle d'un jour à l'autre, qui étaient alignés à la fois en direction et en angle, ce qui reflète une activité cohérente de la population. Ce travail a fourni une base pour poursuivre l'étude de l'activité HD thalamique spécifiquement dans l'AD et l'AV. En combinant cette approche technique avec mes résultats sur l'effet cholinergique dans les neurones thalamiques, cette approche peut ouvrir des perspectives de recherche intéressantes. Les effets de la modulation cholinergique pourraient être étudiés en inhibant des noyaux du tronc cérébral candidats à l'aide de DREADDs dans les neurones cholinergiques, tout en enregistrant les signaux HD thalamiques. Sur la base de l'effet du carbachol, qui abolit les décharges dans l'AD et l'AV, il serait intéressant d'explorer la contribution fonctionnelle des entrées cholinergiques dans le réglage fin des

signaux HD ou dans le déplacement de leur dynamique au sein du réseau attracteur.

En parallèle de ce travail principal, j'ai contribué à des projets associés qui élargissent le champ de cette thèse vers l'intégration des circuits présubiculaires. Dans la première étude, l'intégration du signal issu des ATN et du signal issu du RSC dans le Presubiculum a été examinée. Les expériences fonctionnelles et anatomiques de ce projet ont révélé une sommation supralinéaire des deux entrées dans les neurones pyramidaux de la couche III du PrS, lesquels relaient à leur tour l'information vers la couche IV. Dans la seconde étude, les interneurones VIP du PrS ont été caractérisés de manière systématique, révélant des sous-types avec des profils électrophysiologiques et morphologiques distincts. Ces cellules reçoivent une excitation facilitatrice des ATN et participent à des motifs de désinhibition. De telles propriétés suggèrent un rôle potentiel dans la réorganisation transitoire de la dynamique des attracteurs au sein des réseaux HD. Ces études élargissent la thèse au-delà des mécanismes thalamiques pour mettre en évidence la manière dont les afférences des ATN sont intégrées dans le PrS.

Mes résultats sont ensuite interprétés en relation avec la littérature et je souligne la nouveauté de mes observations. Le premier point concerne la latéralité de la voie mammillo-thalamique. La vision prédominante est que le MMN projette vers l'AV ipsilatéral mais non controlatéral (Dillingham et al., 2015; H. Shibata, 1992; Vann & Aggleton, 2004; Wiener & Taube, 2005). Dans cette thèse, j'ai démontré que les entrées mammillaires forment des connexions excitatrices monosynaptiques sur les neurones de projection thalamiques et j'ai observé une petite population de neurones MMN marqués controlatéralement via le traçage monosynaptique rétrograde, indiquant une connectivité bilatérale MMN-AV. Certains travaux antérieurs présentaient également des résultats anatomiques suggérant une projection bilatérale potentielle de cette voie, mais cela n'avait encore jamais clairement exprimé (Mathiasen et al., 2021; Vann et al., 2007). En ce qui concerne la voie LMN-AD, nous avons confirmé la projection bilatérale. Mes résultats fournissent aussi la preuve que la voie mammillo-thalamo-corticale est monosynaptique, avec une efficacité d'entrée plus forte du côté ipsilatéral, ce qui n'avait pas encore été étudié fonctionnellement.

Deuxièmement, j'ai comparé les propriétés électrophysiologiques distinctes des neurones AD et AV avec leurs profils génétiques en expression de canaux, tels que rapportés par James W. Phillips et al. (2019). Les propriétés électrophysiologiques distinctes des neurones AD et AV peuvent être largement attribuées à l'expression différentielle des canaux HCN. Une activité HCN élevée dans les neurones AD explique leur potentiel de repos dépolarisé, leur résistance d'entrée plus faible, leur constante de temps plus rapide, leur sag marqué et leur activité de rebond, et cette interprétation est soutenue par des preuves pharmacologiques. D'autres profils génétiques, tels qu'une expression réduite des canaux Kv7 dans l'AD et une expression différentielle des canaux calciques de type T (CaV3.3 dans l'AD vs CaV3.1 dans l'AV), façonnent également leurs patrons de décharge, tandis qu'une expression plus élevée de canaux potassiques de type A dans l'AV explique un déclenchement

retardé du potentiel d'action. Ensemble, ces résultats suggèrent que, bien que plusieurs familles de canaux contribuent, la concordance entre l'expression des HCN et les propriétés intrinsèques observées indique que le niveau d'expression des HCN contribue fortement aux différences AD–AV.

Troisièmement, je discute de la manière dont les propriétés électrophysiologiques intrinsèques des neurones AD et AV peuvent soutenir leur contribution distincte à l'activité HD. Les neurones AD, avec leur potentiel de repos dépolarisé, leur sag, leur activité de rebond et leur décharge adaptative mais soutenue, semblent bien adaptés pour intégrer les entrées asymétriques du LMN et générer des signaux HD stables et prédictifs. Les neurones AV, avec leur potentiel de repos hyperpolarisé, leur profil en bouffées, et leur alignement intrinsèque au rythme thêta, sont positionnés pour délivrer des signaux HD structurés temporellement, en synchronie avec le rythme thêta hippocampique. Ils façonnent potentiellement la dynamique des cellules de grille via le Parasubiculum. En conclusion, je suggère que leurs propriétés électrophysiologiques caractéristiques correspondent bien à leur activité HD caractéristique.

Je considère ensuite l'influence cholinergique potentielle sur l'activité neuronale dans l'AD et l'AV. Mes résultats montrent des changements dans l'activité de décharge des neurones AD et AV exposés à un agoniste cholinergique. Cet effet pourrait être le mécanisme à travers lequel une antagonisation muscarinique systémique perturbe l'activité HD enregistrée dans l'AD in vivo (Yoder et al., 2017). Comme une suite possible à mon travail de thèse, je propose d'étudier les entrées cholinergiques sur l'activité HD dans le thalamus à l'aide de l'imagerie calcique. Cela permettra d'approfondir la contribution fonctionnelle des entrées cholinergiques dans le réglage fin des signaux HD et dans la dynamique HD au sein du réseau attracteur.

Enfin, je discute de la convergence anatomique des projections axonales des neurones AD et AV dans le PrS et le gRSC. En plus de mes résultats de traçage, Roy et al. (2021) ont fourni des preuves anatomiques que les entrées AD et AV convergent dans des sous-ensembles de neurones du RSC. Cependant, la signification fonctionnelle de cette convergence dans les régions corticales reste incertaine. Les données suggèrent que l'AD fournit principalement des entrées HD précises, tandis que l'AV contribue avec des signaux liés au rythme thêta, et que ceux-ci ne sont pas fortement intégrés dans les cellules HD corticales, qui manquent généralement de modulation thêta robuste. Ainsi, bien qu'une convergence anatomique existe, la convergence fonctionnelle apparaît limitée, et des études futures sont nécessaires pour clarifier comment les entrées AD et AV interagissent au niveau des circuits du PrS et du RSC.

Pour conclure, mes recherches doctorales offrent un éclairage sur les rôles fondamentaux de l'AD et de l'AV au sein du système HD. Elles approfondissent la compréhension actuelle des contributions thalamiques au réseau HD en intégrant de nouvelles données anatomiques, électrophysiologiques et fonctionnelles.

Acknowledgements

First, I would like to express my deepest appreciation to my supervisor, Desdemona Fricker. I still remember the moment when you welcome me at the airport. I arrived in Paris with two big suitcases, but I feel I am finishing this PhD journey with much more than that. These past four years have been an invaluable foundation for my academic growth. Thank you for your patience, which allowed me to step up at my own pace, and for giving me the support to explore my interests. No matter what idea I brought or which interpretation I shared, I could always enjoy the discussion thanks to your genuine interest. Your support and encouragement were among my strong motivations to pursue this PhD. I have learned a lot from you, and for that I am truly grateful.

Next, I would like to express my sincere gratitude to my thesis defence committee member Dr. Andrea Burgalossi, Dr. Anita Lüthi, Dr. Thierry Bal, Dr. Giuseppe Gangarossa, and Dr. Rebecca Piskorowski. Thank you for accepting to review my PhD thesis and for participating in my thesis defence. I am grateful for the time and attention you have given to this.

I would like to thank my former and present co-group leaders, Mathieu Beraneck and Michael Graupner. I am grateful for the discussions we had and for the guidance and support you provided along the way. Your feedback and encouragement have been valuable throughout my PhD journey.

I would like to thank my PhD committee members, Dr. Rebecca Piskowski and Charlotte Deleuze, for their constant support every year. Your encouragement and positive feedback at each evaluation meant a lot to me. Your positively supportive and hilarious reports on my progress are unforgettable, and I will certainly keep them.

I am thankful to Dr. Nathalie Sol-Foulon for your support and generosity. With your help and sharing, I was able to take a more explorative approach that enriched my experiments. I also deeply appreciate your kindness throughout the collaboration.

Within the new team, setting up the lab together and sharing this experience made the journey all more enjoyable. Thank you so much, Mario, Elja, Marin, Ivan, and Margaux. Also, I wish you all the best in the rest of your academic journey.

To my other old lab members, Louise, Jules (and Lloydie), and Corentin. Although all of you left within one or two years after I joined, we had a great time together and have

kept our friendship going ever since, as I am hesitant to write your name with Dr. The nights on the 7th floor, picnics, soirées, cooking, bubble tea walks, occasional reunions, and even buying huge packs of kimchi together from kimchi mafia are all memorable moments. Thank you for welcoming me so warmly in the beginning and for the friendship that has lasted beyond the lab.

And my field teachers, Louis and Mérie. I did not even know how to do patch clamping at the beginning. I was an awful student, constantly breaking pipettes and taking so much time to learn, with no background in electrophysiology. However, thanks to your patient and kind teaching, I was able to make it this far. I truly appreciate your guidance.

Alba and Joan, my sanctuary in Europe! Truly, without your support, I would not have been able to manage this journey. You guys have always shown up when I go through mentally tough times. Like your professions, you guys have been a great phycologist and a great doctor. Going to a concert, looking for good foods, chugging beers and being domingueros (which is not encoded in my gene!) were all good remedies. I will always be thankful for the friendship we share.

Arthur, Kasper, and Vilde, my old Master's classmate. It is always a pleasant moment when I meet you guys during the conference or other scientific events. Truly, a large part of the pleasure I took in attending conference was the chance to meet you guys. All our conversations, from scientific discussions to random gossips, have always been constructive and hilarious. I am very glad that we are/were on the same academic path.

I could never miss mentioning you, Stefan, my former supervisor. It will soon be ten years since you supervised me. Throughout these years, your encouragement has been a great support, from my national service after my Master's to the end of my PhD. Every time I write an email to you, I remember my vision was so blurry because of the exhausting days. However, it was always a great comfort to me. Your words have always meant a lot to me. Thank you, Stefan.

Also, I would like to acknowledge the experimental animals. No moral reasoning or current ethical framework can fully justify their sacrifice for science, yet I must recognise and value their contribution. As an experimenter, I have never forgotten this value and always tried to guard myself against becoming accustomed to it. There are many contradictions in this, but throughout my project I tried to keep in mind both the responsibility I carried and the preciousness of life.

마지막으로 사랑하는 가족에게. 어머니, 아버지, 유리. 4년 동안의 박사과정이 마무리 되어가네요. 긴 기간 동안 학문적인 수련도 있었지만, 개인적으로 더 가치 있게 생각하는 것은 세상을 바라보는 관점을 넓히고, 그 안에서 저만의 잘 다듬어진 생각을 할 수 있는 능력을 기른 경험이지 않을까 싶습니다. 타지에서 학위 과정을 하기로 결정하고 나서 함께 할 수 있는 시간이 적어 항상 아쉬움이 컸습니다. 그 소중한 시간에 책임감을 느끼고 제가 결정한 목표에 집중할 수 있었던 동기는 가족들의 사랑과 응원에 있었던 거라고 생각합니다. 가족들 덕분에 감사의 글을 쓰며 졸업 논문을 마무리할 수 있게 되었네요. 항상 고맙습니다.

Contents

Abstract i

Résumé iii

Résumé substantiel v

Acknowledgements xiii

List of Figures xxi

List of Tables xxiii

List of Abbreviations xxv

Introduction 1

1 Overview of spatial navigation in animals . . . 1
2 Spatially tuned neurons in the navigation system . . . 4
2.1 Head direction cells . . . 4
2.2 Grid cells . . . 7
2.3 Place cells . . . 10
2.4 Border cells . . . 12
2.5 Interaction and integration of spatially tuned cells . . . 14
3 The head direction system . . . 16
3.1 The hierarchy across the brain regions in the head direction system 16
3.2 Sensory integration in the head direction system . . . 17
3.3 Ring attractor network . . . 21
4 Thalamus . . . 24
4.1 History of the thalamus . . . 24
4.2 Anatomy and functions of the thalamus . . . 26
4.3 Anterior thalamic nuclei . . . 27
4.3.1 Structural organisation . . . 27
4.3.2 General connectivity of the ATN . . . 28
4.3.3 Functions of ATN . . . 30
5 Anterodorsal nucleus in the head direction system . . . 31
5.1 Anatomical connectivity . . . 31

5.2 HD system in the AD . . . 33
5.3 The origin of the HD signal and its progression in the network . . 35
5.4 Modulatory inputs to the AD . . . 38
6 AV and the theta modulated head direction cells . . . 42
6.1 Anatomical connectivity . . . 42
6.2 Theta rhythm in the AV . . . 49
6.3 Theta rhythms in spatial navigation: Implications for HD coding in the AV . . . 51
6.4 Modulatory inputs to the AV . . . 54
7 Ion channel expression as basis for intrinsic electrophysiological properties 56
7.1 Ion channels and transporter contributions to resting membrane potential . . . 56
7.2 Ion channels and AP kinetics . . . 57
7.2.1 Voltage-gated sodium channel . . . 58
7.2.2 Voltage-gated calcium channel . . . 58
7.2.3 Voltage-gated potassium channel . . . 59
7.2.4 Subthreshold currents . . . 59
7.2.5 Currents after the AP . . . 60
8 Aims and contribution of the thesis . . . 61

Method **63**
1 Animals . . . 63
2 Stereotaxic injections . . . 63
3 Tissue Fixation and Microscopy . . . 65
4 Registration on the 3D mouse brain diagram . . . 66
5 Thalamic acute slice preparation for electrophysiology . . . 66
6 Whole-cell patch clamp recordings . . . 67
7 Optogenetics . . . 69
8 Electrophysiological data analysis . . . 69
9 Unsupervised cluster analysis . . . 71
10 Biocytin staining and 3D reconstruction . . . 71
11 Calcium imaging using a head mounted miniatures microscope (Miniscope) 72
12 Quantification and statistical analysis . . . 74

Results **75**
1 Research manuscript from the PhD project . . . 75
2 Preliminary results to explore cholinergic modulatory effect in AD and AV 154
2.1 Cholinergic modulation on AD and AV neurons - electrophysiological aspect . . . 154
2.2 Exploring cholinergic input sources to AD and AV . . . 157
3 Calcium imaging of neuronal HD activity in the AD and AV in behaving mice 166
4 Co-authored publications . . . 172

4.1 Projection-specific integration of convergent thalamic and retrosplenial signals in the presubicular head direction cortex 172
4.2 Presubicular VIP expressing interneurons receive facilitating excitation from anterior thalamus 195

Discussion **209**
1 The mammillo-thalamo-cortical pathway revisited 210
2 The distinct electrophysiological properties of AD and AV neurons 212
3 Parallel mammillothalamic pathways in the HD system: linking functional and electrophysiological characteristics in AD and AV 217
4 Cholinergic modulation in the AD and AV and its potential effect on the HD system 220
5 Anatomical convergence of AD and AV axonal projections in the PrS and gRSC 222

General Conclusion **225**

Bibliography **227**

List of Figures

2.1 Typical tuning curves and polar plot of HD cells . . . 6
2.2 Grid cell activity in the MEC . . . 9
2.3 Place cell activity . . . 11
2.4 Border cell activity . . . 13
3.1 Anatomical network of spatially tuned cells . . . 20
3.2 Ring attractor network in the HD system . . . 23
4.1 Drawing of the human brainstem by Willis (1664) . . . 25
4.2 The anatomy of ATN . . . 28
4.3 Papez circuit diagram . . . 29
5.1 The anatomical connectivity of the AD . . . 32
5.2 HD activity in the AD . . . 35
5.3 HD signal properties across brain regions . . . 38
5.4 Modulatory inputs to the HD cells in AD . . . 41
6.1 The anatomical connectivity of the AV . . . 43
6.2 Differently reported mammillothalamic tract . . . 46
6.3 Anatomical tracing results showing mammillary afferents to the AV . . . 48
6.4 Rhythmic firing of AV neurons . . . 50
6.5 HD activity in the AV . . . 53
6.6 Modulatory inputs to the AV . . . 55
8 Schematic diagram of the network investigated in this thesis . . . 62

9 Cholinergic modulation of spiking activity in AD and AV neurons . . . 156
10 Injection site in AD and AV for retrograde tracing of brain-wide afferents . 157
11 Gallery of alternating serial brain sections from a whole mouse brain . . . 160
12 Double-labelled neurons in the LDT and CnF . . . 162
13 Double-labelled neurons in the PAG . . . 163
14 Double-labelled neurons in the PPN . . . 164
15 Double-labelled neurons in the MRN . . . 165
16 Calcium imaging of PrS-projecting AD and AV neurons using a miniscope 167
17 Calcium imaging of PrS-projecting AD neurons across three recording days 168
18 Polar plots of PrS-projecting AD neurons across two recording days . . . 169
19 Polar plots of PrS-projecting AD and AV neurons observed on a single recording day . . . 170

20 Expression profiles of AD and AV . . . 213

List of Tables

2.1 Injection volumes and anatomical coordinates for stereotaxic injections . . 64
2.2 Viruses used in this thesis project and their sources with catalogue numbers 65
2.3 Chemical composition of cutting solution and ACSF 67
2.4 Chemical composition of the internal solution for whole-cell patch clamp recordings 68
2.5 Analysed intrinsic electrophysiological properties and their detailed descriptions 70

3.1 Summary of retrogradely labelled AD/AV projecting neurons and colocalisation of GFP and Tomato fluorescence across regions. 159

List of Abbreviations

4-AP 4-aminopyridine

ACC Anterior cingulate cortex

ACSF Artificial cerebrospinal fluid

AD Anterodorsal thalamic nucleus

ADP Afterdepolarisation

AHP Afterhyperpolarisation

AHV Angular head velocity

AM Anteromedial thalamic nucleus

AP Action potential

APV 2-Amino-5-phosphonovaleric acid

ATI Anticipatory time interval

ATN Anterior thalamic nuclei

ATP Adenosine triphosphate

AV Anteroventral thalamic nucleus

AVDM Anteroventral thalamic nucleus, dorsomedial subdivision

AVVL Anteroventral thalamic nucleus, ventrolateral subdivision

Bb Bisbenzimide blue

BK Large-conductance calcium-activated potassium channel

BRh5 Bisbenzimide R h 5

BVC Boundary vector cell

CaV Voltage-gated calcium channel

ChAT Choline acetyltransferase

CnF Cuneiform nucleus

CNO Clozapine-N-oxide

CTB Choleratoxin subunit B

DAPI 4',6-diamidino-2-phenylindole

DREADDs Designer Receptors Exclusively Activated by Designer Drugs

dRSC Dysgranular retrosplenial cortex

DTN Dorsal tegmental nucleus

EB Ellipsoid body

Eb Evans blue

EC Entorhinal cortex

EEG Electroencephalography

EPSC Excitatory postsynaptic current

EPSP Excitatory postsynaptic potential

FLEX Flip-excision switch

GABA Gamma-aminobutyric acid

GCaMP Genetically encoded calcium indicator (GFP–Calmodulin–M13)

GFP Green fluorescent protein

GIRK G protein-coupled inward rectifying potassium

GRIN Gradient-index

gRSC Granular retrosplenial cortex

HCN Hyperpolarisation-activated cyclic nucleotide-gated channel

HD Head direction

hM4D Human muscarinic receptor 4 (designer receptor)

HRP Horseradish peroxidase

IAM Interanteromedial thalamic nucleus

IPSC Inhibitory postsynaptic current

ISI Interspike interval

jRGECO Genetically encoded red fluorescent calcium indicator

KCNK Two-pore domain potassium channel (K2P)

KCNQ Voltage-gated potassium channel (Kv7)

Kv Voltage-gated potassium channel

LD Lateral dorsal thalamic nucleus

LDT Laterodorsal tegmental nucleus

LED Light-Emitting Diode

LFP Local field potential

LGN Lateral geniculate nucleus

LHA Lateral hypothalamic area

LMN Lateral mammillary nucleus

LVA Low voltage activated

MBO Mammillary body

MC Motor cortex

MD Mediodorsal thalamic nucleus

Me Medial mammillary nucleus pars medianus

MEC Medial entorhinal cortex

Mmc Medial mammillary nucleus pars centralis

MML Medial mammillary nucleus pars lateralis

MMM Medial mammillary nucleus pars medialis

MMN Medial mammillary nucleus

MMP Medial mammillary nucleus pars posterior

MRN Midbrain reticular nucleus

MS Medial septum

MVN Medial vestibular nucleus

NBQX 2,3-Dihydroxy-6-nitro-7-sulfamoyl-benzo (F) quinoxaline

NMDA N-Methyl-D-aspartate

NPH Nucleus prepositus hypoglossi

NRe Nucleus reuniens

oEPSC Optogenetically evoked postsynaptic current

oEPSP Optogenetically evoked postsynaptic potential

PAG Periaqueductal grey

PaS Parasubiculum

PB Protocerebral bridge

PBS Phosphate-buffered saline

PC Postrhinal cortex

PCA Principal component analysis

PFA Paraformaldehyde

PFD Preferred firing direction

PL Prelimbic area

PMd dorsal premammillary nucleus

POm Posterior medial nucleus

PPN Pedunculopontine nucleus

PrS Presubiculum

PV Parvalbumin

REM Rapid eye movement

RMP Resting membrane potential

ROI Region of interest

RSC Retrosplenial cortex

SEM Standard error of the mean

SGN Supragenual nucleus

SK Small conductance calcium-activated potassium

SST Somatostatin

STPT Serial two-photon tomography

Sub Subiculum

SWS Slow-wave sleep

TASK TWIK-related acid-sensitive potassium channel

TRN Thalamic reticular nucleus

TTX Tetrodotoxin

TVA Avian tumor virus receptor A

TWIK Tandem of P domains in a weak inwardly rectifying K^+ channel

VGSC Voltage-gated sodium channel

VIP Vasoactive intestinal peptide

VPM Ventroposterior medial nucleus

VTN Ventral tegmental nucleus of Gudden

Introduction

1 Overview of spatial navigation in animals

The North Atlantic is known for its rough seas, where harsh waves batter ships, clouds often hide the sun, and coastlines vanish beyond the horizon. Emerging in European history around the late eighth century, the Vikings left a profound mark, sailing across these waters from neighbouring northern Europe to distant continents (McGovern, 1990; Ropars et al., 2012, 2014). They were renowned as outstanding navigators, reading the sun, moon, wind, and currents with the support of highly developed ship technologies. During their early voyages, the range was limited, allowing them to rely on local landmarks such as mountains, bays, islands, and even the local animal species for navigation (Száz et al., 2016). Later as their voyage extended, they used wooden sun compasses to guide them across open waters. Yet the compass still depended on clear skies, meaning that their journeys remained tied to favourable weather and seasons (Bernáth et al., 2014). The high latitude of their homelands around 61°N brought challenges for long-distance sailing, with unstable weather of fog, cloud, and short daylight hours, especially in winter. In such conditions, landmarks for successful navigation could no longer serve as reliable references. Then how could they manage to sail across such harsh seas and even reach the American continent? One prevailing theory is that they started to use the "Sólarsteinn" or "Solstenen", known in English as the sunstone (Bernáth et al., 2013, 2014; Byock, 2012; Ropars et al., 2012, 2014; Roslund & Beckman, 1994; Száz et al., 2016). Modern historical and physical studies suggest that this crystal was likely calcite, which allows the detection of the sun's position through clouds or fog with the naked eye. Recent experiments have demonstrated this possibility (Ropars et al., 2012). When light passes through a calcite crystal, it splits into two polarised beams, and by aligning these to an isotropy point, the direction of the sun can be inferred. A calcite crystal was even found from a sixteenth century shipwreck at Alderney, providing archaeological support to the hypothesis (Le Floch et al., 2013).

Just as the Vikings relied on tools like the sunstone to cross the seas, animals including humans have conserved internal systems that allow them to navigate their environments. Navigation is not only a practical skill but a fundamental condition of survival, influencing animal life in essential ways. Its importance becomes most evident during escape from threats, where the ability to orient, identify routes, and reach safety is accurately computed within the brain. Beyond escape, navigation is equally indispensable for locating food, shelter, and mates (Givon et al., 2022; Nyberg & Gahnstrom, 2022).

The link between navigation and survival is further illustrated by recent findings in mice. Escape behaviour has been shown to rely on the coordination of neural circuits that integrate navigation and action (W. Wang et al., 2021). In this study, Cholecystokinin-expressing neurons in the hypothalamic dorsal premammillary nucleus dorsal premammil-

lary nucleus (PMd) were identified as critical for selecting and executing adaptive escape strategies. The PMd projects both to the dorsal periaqueductal grey, which drives motor escape, and to the anteromedial ventral thalamic nucleus, which supports spatial navigation. Disruption of this integration led to panic-like, directionless movements, whereas intact circuits enabled animals to evaluate environmental layouts and reach safety. Complementary evidence comes from Campagner et al. (2023), who showed that mice rely on rapid spatial computations to guide escape towards shelter. In their experiments, animals exposed to threats did not flee randomly but instead selective direct routes. This was observed even when obstacles required detours. This behaviour depended on the rapid integration of self-location with stored spatial maps, allowing mice to calculate efficient trajectories in real time. These findings highlight that navigation is not only a tool for exploration but also an instinctive mechanism to maximise survival in the face of danger.

How is navigation implemented in the mammalian brain? Navigation relies on the brain's ability to maintain an updated representation of position and orientation, enabling animals to move effectively towards goals. Two complementary strategies support this process: path integration and landmark-based navigation (Gallistel, 1990). Path integration involves continuously updating one's location by integrating internally generated idiothetic cues such as vestibular information, proprioception, motor efference copies, and optic flow (Etienne & Jeffery, 2004; Jain et al., 2017; J. S. Taube, 2007). This strategy allows animals to estimate their current position relative to a starting point even in the absence of external references. However, errors inevitably accumulate over time and distance. Landmark navigation relies on stable external, allothetic cues including visual, auditory, and olfactory landmarks that provide fixed reference points to determine position and orientation (Jain et al., 2017; J. S. Taube, 2007) . These landmarks are used to calibrate and anchor the internal estimate from the path integration, thereby correcting accumulated drift and enhancing spatial accuracy. The brain flexibly adjusts the relative weighting of idiothetic and allocentric inputs depending on environmental demands, ensuring that navigation remains robust (Jeffery et al., 2016) Together, the integration of these two strategies provides a stable framework for spatial orientation and lays the foundation for higher order representations such as cognitive maps.

The ability to navigate depends on the brain's capacity to build and maintain an internal representation of space. This idea was first suggested by Tolman (1948), who proposed that animals construct a "cognitive map", which is a map-like internal model that encodes the spatial relationships between environmental cues. Such a representation enables flexible navigation. Rather than relying solely on a learned sequence of actions, animals can take novel routes or shortcuts to reach a goal. Classic behavioural work supports this view. In Tolman's sunburst maze experiments, rats trained to follow a fixed route to a goal were later able to choose a direct path through an unfamiliar maze layout. This indicates that they had encoded the spatial arrangement of the environment. Similarly, in the Morris water maze, rats learned the location of a hidden platform and could reliably find it even when starting from novel positions, suggesting the use of an internal representation rather than simple stimulus-response strategies (R. G. Morris, 1981).

Building on these findings, O'Keefe and Nadel (1978) proposed that the hippocampus is central to the cognitive map. This was an idea motivated by the discovery of place cells that

fire selectively when an animal occupies a specific location in space (O'Keefe & Dostrovsky, 1971). Damage to the hippocampus and subiculum was later shown to impair spatial learning, further supporting their role in storing and using cognitive maps (R. G. M. Morris et al., 1990). Since then, extensive research has established that the cognitive map is supported not only by the hippocampus but also by a distributed network of limbic circuit and cortical areas (Aggleton & Brown, 1999)

The internal cognitive map, constructed by idiothetic path integration and allothetic cues, enables animals to interpret their environment and employ flexible navigation strategies. Recent research on spatially tuned cells has advanced our understanding by linking theoretical models to concrete neuronal networks, revealing how the brain encodes and represents space. In the next chapter, different types of spatially tuned cells and their interactions in constructing the navigation system will be introduced.

2 Spatially tuned neurons in the navigation system

The neural basis of navigation has been studied extensively. Multiple types of spatially tuned neurons have been identified. These cells are named according to their functional properties. They are structurally and functionally organised to support the brain's navigation system. In this chapter, the major types of spatially tuned neurons will be introduced, and their interactions to construct the navigation system will be discussed.

2.1 Head direction cells

Head direction (HD) cells are often described as the brain's compass. Each HD cell is tuned to a particular direction, firing maximally when the head faces that direction, known as Preferred firing direction (PFD). The tuning curves of HD cells are typically Gaussian distributed and centred on the PFD (H. Blair & Sharp, 1995). The firing rate declines as the head turns away from the PFD and is mostly independent of the animal's position in the environment or behaviour (Knierim et al., 1998; Stackman & Taube, 1998; J. S. Taube & Muller, 1998; J. Taube et al., 1990b). Together, the population of HD cells encodes all directions in the horizontal plane, covering 360°. HD cells have been found in multiple brain regions, including the Dorsal tegmental nucleus (DTN), Lateral mammillary nucleus (LMN), Anterodorsal thalamic nucleus (AD) and Anteroventral thalamic nucleus (AV) within Anterior thalamic nuclei (ATN), Retrosplenial cortex (RSC), Presubiculum (PrS), Parasubiculum (PaS), and Medial entorhinal cortex (MEC). These regions form a hierarchical network for generating, updating, and resetting the HD signal. The specific connectivity of this network will be addressed in the next chapter.

HD cells were first identified in the PrS by Ranck (1984). Many HD cells are observed in layer III (Preston-Ferrer et al., 2016; Simonnet et al., 2017). Layer III pyramidal neurons show strong directional tuning and are only weakly theta-modulated, whereas layer II neurons tend to exhibit high theta rhythmicity but weak or absent HD tuning (Boccara et al., 2010; Preston-Ferrer et al., 2016; Tukker et al., 2015). Theta rhythmicity is an oscillation of 6-12 Hz in the hippocampal-entorhinal network (Buzsáki, 2002, 2005). It appears during locomotion and exploration and is linked to place cell firing (O'Keefe & Nadel, 1978). This modulation supports stable spatial processing. In addition, juxtacellular recordings have revealed that a subset of PrS neurons displays bursting patterns and spikelets, which may support temporal coding in the HD system (Coletta et al., 2018).

A typical HD cell shows a unimodal, symmetric tuning curve, with a peak at the PFD and minimal activity outside the directional firing range. Peak firing rates range from about 5 to 120 Hz, and tuning width from 60° to 150°, with subcortical regions such as LMN and AD generally showing broader tuning curves and higher peak rates than cortical areas like PrS and RSC (Cho & Sharp, 2001; P. E. Sharp, Tinkelman & Cho, 2001; Stackman & Taube, 1998). There is no clear topographical organisation of tuning curve properties in AD (Ajabi et al., 2023). HD cells in the PrS (or the dorsal portion often termed the postsubiculum in some studies) are distinguished by their precise directional tuning, generated by organised

local microcircuits. Recent work demonstrates that both excitatory and inhibitory neurons in the postsubiculum exhibit comparable HD tuning properties, independent from thalamic inputs (Duszkiewicz et al., 2024). This indicates that this region actively refines neural representations using intrinsic rules, rather than inheriting them from upstream structure. The PrS also displays a modular microcircuit organised for precise HD coding, which allows selective integration of thalamic inputs conveying HD inputs from AD and potential landmark information from Lateral dorsal thalamic nucleus (LD) (Blanco-Hernández et al., 2024). In MEC layer III, directional firing increases along the dorsal–ventral axis (Giocomo et al., 2014). Some HD cells are modulated by Angular head velocity (AHV), supporting the idea that the HD signal is constantly updated by the animal's own movements (H. Blair & Sharp, 1995; Lozano et al., 2017; Stackman & Taube, 1998; J. Taube, 1995; J. Taube et al., 1990b).

While most HD research has focused on navigation in the horizontal plane, some studies have explored HD coding in three-dimensional contexts. In rats, HD cells maintain normal tuning on vertical planes but lose directional specificity during inversion and under microgravity, indicating a reliance on gravity and orientation relative to the earth-horizontal plane (J. S. Taube & Muller, 1998; Valerio et al., 2010). In bats, many presubicular HD cells encode not only yaw angle but also pitch and roll, including conjunctive cells tuned to combinations of axes, supporting a 3D representation (Finkelstein et al., 2015; Yartsev & Ulanovsky, 2013). The rat HD system shows complex 3D sensitivity, while some studies report that cells maintain primarily horizontal tuning when rats move on vertical surface (Jeffery et al., 2013; Page et al., 2018), other work has demonstrated that many neurons conjunctively encode yaw, pitch, and roll (Laurens & Angelaki, 2019). This suggests that the rodent HD system is capable of integration across all three orientations, emerging during movement across vertical surfaces, passive rotations, or tasks requiring context.

HD cells provide a global directional metric, maintaining relative PFDs across environments and showing only weak modulation by geometry (J. S. Taube & Muller, 1998; J. Taube et al., 1990a, 1990b). When environmental manipulations alter perceived orientation, PFDs rotate equally across the population, reflecting coherent ensemble activity - a property linked to one-dimensional continuous attractor network models (Skaggs et al., 1995; K. Zhang, 1996).

Although the HD signal can be generated from self-motion (idiothetic) cues alone, as shown by stable firing in darkness or without familiar landmarks (H. T. Blair & Sharp, 1996; Goodridge & Taube, 1995; Goodridge et al., 1998; Tan et al., 2015; J. Taube et al., 1990b), these cues alone are insufficient for long-term stability, and PFDs tend to drift without vision (Goodridge et al., 1998; Mizumori & Williams, 1993; Save et al., 2000). Visual landmarks are a primary stabilising influence, with both distal and proximal cues able to anchor PFDs, though distal cues exert stronger control (Yoganarasimha et al., 2006; Zugaro et al., 2001). Landmark learning is rapid, and when landmarks are rotated, PFDs typically rotate by the same amount (Goodridge et al., 1998; Knierim et al., 1998; J. Taube et al., 1990b). The integration of visual, vestibular, and proprioceptive inputs follows a weighted scheme in which the most reliable source dominates orientation (Knierim et al., 1998; J. Taube et al., 1990b).

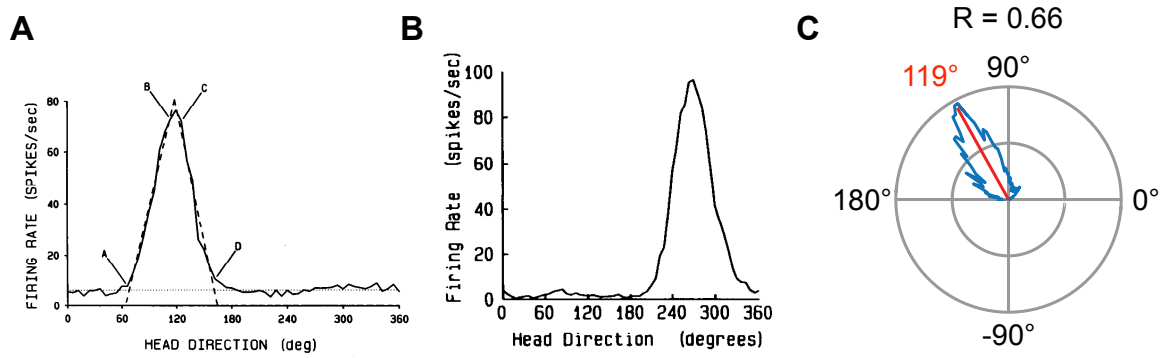

Figure 2.1 Typical tuning curves and polar plot of HD cells.

A) Triangular model of HD cell firing proposed by J. Taube et al. (1990a). Typical HD cells show a triangular firing rate profile with a peak at the PFD, which is 118.5° in this example.

B) Example tuning curve from a recorded presubicular HD cell. The experiments were carried out using extracellular recordings, with head direction analysed in 6° bins over 8-minute sessions. Adapted from J. Taube et al. (1990a).

C) Example polar plot of an HD cell in the AD. The line and the number in red indicate the PFD based on the mean vector. The blue plot shows firing rate as a function of head angle. R denotes the correlation coefficient, reflecting the strength of directional tuning. The directional polar plot was generated from *in vivo* calcium imaging data, with activity binned in 1° HD intervals while the animals freely moved on a circular platform surrounded by a Light-Emitting Diode (LED) environment displaying visual cues. Adapted from Ajabi et al. (2023).

2.2 Grid cells

Grid cells are neurons that exhibit multiple compact firing fields arranged in a regular hexagonal pattern covering the entire environment (Hafting et al., 2005). Each firing location is known as a grid field, with the position of these fields defining the grid phase. The spacing between fields is the grid scale, and the relative displacement between grids of different cells is called the offset. Neighbouring grid cells share a common orientation and scale, but differ in their phases and offsets, allowing the population to tile the environment uniformly.

First identified in the rat MEC (Hafting et al., 2005). These cells present topographical organisation in which grid scale and field size increase systematically along the dorsoventral axis, while phase and offset vary. Grid cells have also been reported in dorsal Subiculum (Sub), PrS, and PaS, where they co-localise with HD cells (Boccara et al., 2010; Gardner et al., 2022). Grids from different parahippocampal regions show distinct firing characteristics: in MEC layer II, grid cells display the highest periodicity (gridness) and strongest theta rhythmicity, whereas PrS/PaS grid cells exhibit lower theta rhythmicity and gridness but greater directional selectivity (Boccara et al., 2010). Within MEC, layers II and III differ in their hippocampal targets, intrinsic properties, and spatial tuning: layer II cells preferentially project to dentate gyrus and CA3, tend to show more phase precession, and exhibit higher gridness, whereas layers III–IV display relatively stronger directional tuning (Giocomo et al., 2014; Hafting et al., 2008; Mizuseki et al., 2009; Newman & Hasselmo, 2014; Sargolini et al., 2006).

Grid cells are active in all environments, and their firing patterns are stable across repeated visits to the same environment. The spatial offset between cells remains constant regardless of environmental manipulations (Fyhn et al., 2007; Gardner et al., 2022; Hafting et al., 2005). Changes in the geometry of an environment, such as altering the shape of a familiar enclosure, can cause grid fields to translate or rotate together, but grid scale and offset are typically preserved (Fyhn et al., 2007). Changes in enclosure size often result in more grid fields and partial adjustments of field size without altering grid scale (Barry et al., 2007; Hafting et al., 2005) Boundary manipulations, such as wall removal, cause coherent translations of grid fields without changing grid orientation or the offset between co-recorded MEC HD and grid cells (Solstad et al., 2008).

Grid cells also respond to non-metric contextual cues. For example, identical enclosures differentiated only by odour or brightness can cause the entire grid pattern to shift or rotate coherently (Marozzi et al., 2015). Such adjustments indicate that grid cells integrate both path integration signals and environmental information, with environmental features influencing grid location and orientation.

The regularity and coherence of grid cell firing patterns suggest that they are supported by an internally organised network structure. Computational models propose that grid activity resides on a two-dimensional toroidal attractor, with each cell's position on this manifold corresponding to its spatial receptive field (Burak & Fiete, 2009) In this framework, the 'torus' topology enables population activity to wrap seamlessly and periodically in both dimensions, preventing edge effects and allowing smooth updates from self-motion and environmental cues. This organisation has been confirmed experimentally by large-scale cal-

cium imaging and manifold analysis, which demonstrated that the population state of grid cells lies on a continuous 2D torus across environments and behavioural states (Gardner et al., 2022).

Recent work by Vollan et al. (2025) extends this view by showing that trajectories of grid cell population activity can sweep smoothly across the toroidal manifold during both active navigation and non-spatial tasks. This reflects internally coherent shifting of the spatial code. They also observed that many theta-modulated HD cells in PaS and MEC exhibit theta cycle skipping, firing preferentially on alternate theta cycles. This skipping coincides with left–right alternating population sweeps around the head direction axis, producing coordinated sub-second packets of directionally tuned activity. Such sweeping dynamics, embedded in the toroidal attractor framework, may enhance the temporal resolution of spatial coding and support flexible integration of directional and positional information within the entorhinal–hippocampal network (Burak & Fiete, 2009; Gardner et al., 2022; Vollan et al., 2025).

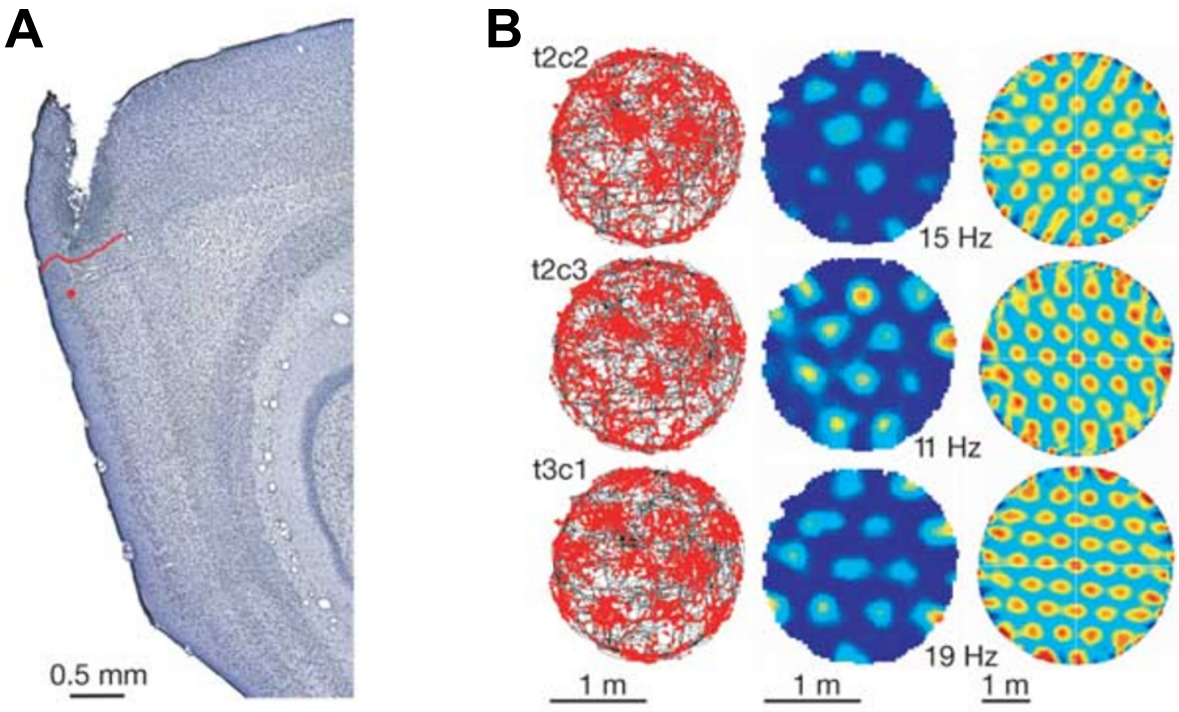

Figure 2.2 Grid cell activity in the MEC.

A) Sagittal rat brain section with Nissl-staining showing the region where grid activity was recorded. The red line indicates the border between the Postrhinal cortex (PC) and MEC. The red dot marks the recording site of grid cells.

B) Examples of three grid cells recorded during 30 minutes of exploration in a circular arena. Grid cells exhibit firing fields arranged in a hexagonal pattern. Left: Rat's trajectory shown in black with spike locations overlaid in red. Middle: Colour-coded firing rate map with peak rate indicated. Red represents the maximum firing rate and dark blue indicates zero. Right: Spatial autocorrelation of the rate map, with the colour scale: blue (r=-1), green (r=0), and red (r=1). All figures adapted from Hafting et al. (2005).

2.3 Place cells

Place cells fire in a specific location in a given environment. These cells are found in the hippocampus and Entorhinal cortex (EC). This spatially tuned area for the place cell is termed place field (O'Keefe & Dostrovsky, 1971). This discovery provided a physiological basis for the "cognitive map" hypothesis of spatial navigation (O'Keefe & Nadel, 1978). The cognitive map is described as an internal map that enables the brain to integrate the spatial information to support flexible navigation. Outside the place field, firing rates are generally low and irregular, increasing as the animal enters and peaking near the field centre before falling again upon exit (Muller & Kubie, 1987). Place cells are typically omnidirectional, meaning that within the place field, firing is independent of the animal's heading direction (Muller et al., 1994).

Most place cells have been described in the CA1 and CA3 subfields of the hippocampus (Wilson & McNaughton, 1993) Field size increases along the dorsoventral axis, with dorsal cells exhibiting small, spatially precise fields and ventral cells showing larger, less specific fields (Kjelstrup et al., 2008; E. I. Moser & Moser, 2008; Royer et al., 2010). Place-like activity has also been identified in related hippocampal regions such as the Sub, MEC, and PrS, as well as in extra-hippocampal areas including the Anteromedial thalamic nucleus (AM), Nucleus reuniens (NRe), and anterior claustrum (Boccara et al., 2010; Jankowski & O'Mara, 2015; Jankowski et al., 2015; Long & Zhang, 2021; P. E. Sharp, 1999).

In familiar environments, place fields tend to remain stable over repeated exposures (Lever et al., 2002). However, changes in environmental cues can trigger remapping, a reorganisation of spatial firing patterns. Rate remapping involves changes in firing rate without altering the field's location or shape, often due to minor contextual changes, whereas global remapping involves changes in both rate and location, typically following large modifications to environmental geometry or context (Leutgeb et al., 2005; Muller & Kubie, 1987).

Place cell activity is influenced by the integration of self-motion (idiothetic) signals and external sensory cues, especially visual landmarks and environmental boundaries (Muller & Kubie, 1987; O'Keefe & Speakman, 1987). Idiothetic cues alone can sustain position-specific firing for short periods in darkness, but positional drift accumulates over time (Save et al., 2000; S. Zhang et al., 2014). Multimodal sensory information, including visual, olfactory, tactile, and auditory cues, contributes to the stability and spatial tuning of place fields (Aronov et al., 2017; Gener et al., 2013; O'Keefe & Conway, 1978; Wood et al., 1999).

During active exploration, place cell firing is modulated by hippocampal theta oscillations. Many place cells exhibit theta phase precession, in which spikes occur at progressively earlier phases of the theta cycle as the animal moves through the place field (O'Keefe & Recce, 1993; Skaggs et al., 1996). Together with their spatial selectivity, this temporal code supports a precise representation of location and sequences of movement.

The population activity of place cells forms a distributed, large-scale map of space (Wilson & McNaughton, 1993), which can flexibly incorporate goal- or reward-related information (Dupret et al., 2010; Hok et al., 2007). Along with grid cells, boundary cells, and HD cells, place cells constitute a core element of the spatial navigation network.

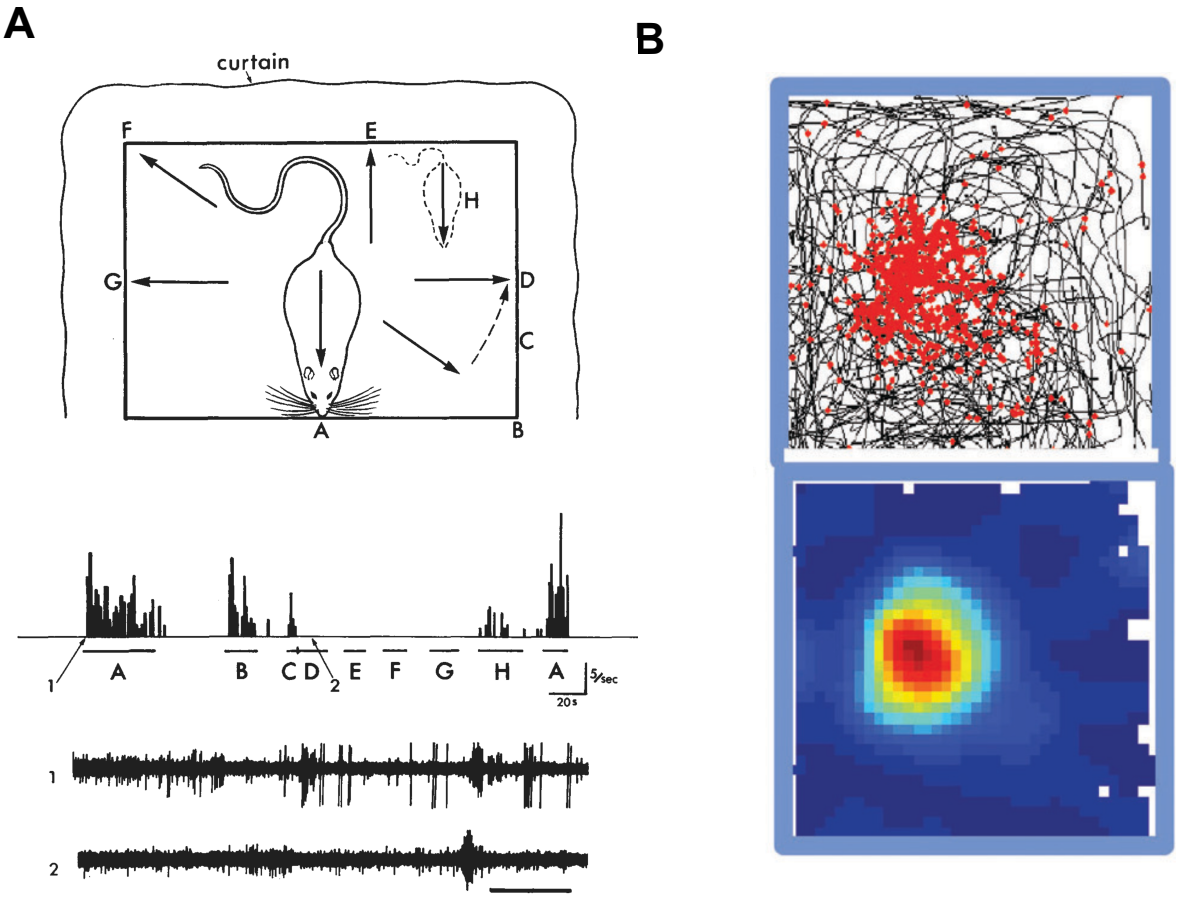

Figure 2.3 Place cell activity.

A) First experimental evidence of place fields, showing that hippocampal neurons fire selectively according to the animal's location. Arrows and letters indicate the positions where the rat was restrained while being guided counter-clockwise around the platform. The histogram shows firing rate across positions, and raw traces illustrate responsive activity at A (1) and less-responsive activity at D (2). Scale bar: 400 ms. Adapted from O'Keefe and Dostrovsky (1971).

B) Example of a place cell recorded in a foraging rat. The black trace shows the animal's trajectory, red dots indicate spike locations. The colour-coded rate map illustrates firing rate, with red denoting high activity and blue low activity. Adapted from M.-B. Moser et al. (2015).

2.4 Border cells

Border cells increase their firing when an animal is near an environmental boundary such as a wall or barrier. The activity of these cells is anchored to the location of the border itself, and does not depend on the animal's direction of movement (Bicanski & Burgess, 2020). Boundaries that elicit this response can include solid structure, gaps, or discrete objects which serve as navigational edges. Electrophysiological studies have shown that border cells are present in several brain regions. These include the MEC, Sub, PrS, and PaS, where they all contribute to robust encoding of boundaries in various environmental settings (Boccara et al., 2010; Kjelstrup et al., 2008; Savelli et al., 2008).

Two main types of border coding have been identified. Boundary vector cell (BVC)s were first described in the dorsal subiculum. These cells fire most strongly when a boundary is at a specific distance and allocentric direction from the animals (Barry et al., 2006; Lever et al., 2009). BVCs maintain their spatial tuning across environments of different shapes. Their receptive fields can attach to both nearby and distant boundaries. The size of a BVCs field increases with its preferred distance from the boundary. New firing fields may develop if a barrier is inserted into the environment. Importantly, BVCs do not respond only to solid walls. They are also sensitive to boundaries defined by gaps or objects, provided these features mark a significant spatial edge.

Allocentric boundary cells are most prevalent in the deeper layers of the MEC and also found within the PrS and PaS. Like BVCs, these boundary cells anchor their firing to boundaries in an allocentric reference frame and they maintain consistent spatial tuning, even when the geometry of the environment changes (Boccara et al., 2010; Savelli et al., 2008; Solstad et al., 2008). These cells tend to respond mainly to physical boundaries that block movement, and their reactions to new barriers are variable. Some boundary cells form a new field when a barrier appears, while others do not. This is in contrast to BVCs, which more predictably show new or split fields in response to inserted barriers (Lever et al., 2009; Solstad et al., 2008).

Allocentric boundary cells work together with representations that are egocentric, or body-centered. Egocentric boundary cells become more active when a boundary is at a specific distance and direction with respect to the animal. These cells have been observed in the RSC and PC (Alexander et al., 2023; Lian et al., 2023; Van Wijngaarden et al., 2020). The transformation between egocentric and allocentric coding is thought to involve the combination of sensory and self-motion signals. This process ensures that boundary information can be used reliably for spatial mapping and navigation.

Although the precise role of BVCs, border cells and egocentric border cells in hippocampal spatial coding remains under investigation. Anatomical and functional data suggest that parahippocampal border cells and BVCs provide important geometric input to the hippocampus. This occurs through strong projections from the MEC, PrS, and PaS (Boccara et al., 2010; Solstad et al., 2008).

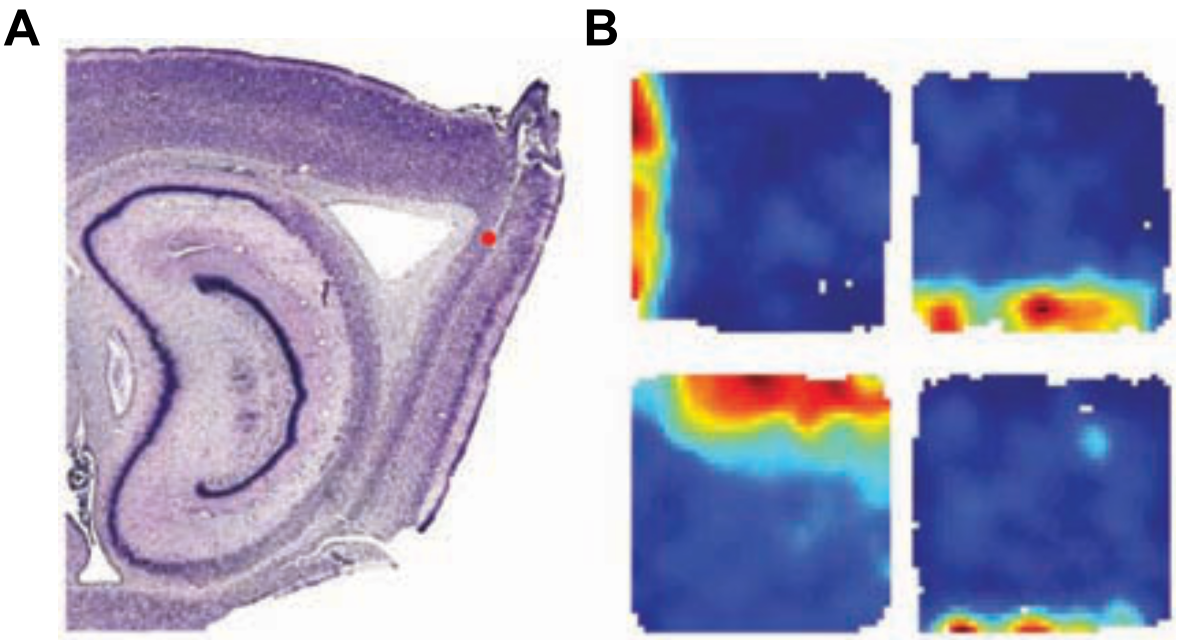

Figure 2.4 Border cell activity.

A) Sagittal rat brain section with Nissl-staining showing recording site of border cells near MEC.
B) Examples of 4 border cells. Colour-coded rate maps illustrate their activity, with higher firing rate along the boundaries of the area. Red indicates the maximum firing rate, white indicates the pixel not covered, and dark blue indicates zero. The peak firing rates: 16 Hz (top left), 8 Hz (top right), 9 Hz (bottom left), and 8 Hz (bottom right). All figures adapted from Solstad et al. (2008).

2.5 Interaction and integration of spatially tuned cells

The spatial navigation system arises from the interaction of several types of spatially tuned cells, each contributing distinct information. HD cells provide a primary directional signal that helps orient and stabilise the activity of other spatial neurons (Jankowski et al., 2013). Directional input from the subcortical HD system provides a stable directional framework that aligns the firing fields of both place and grid cells with visual landmarks (Hafting et al., 2005; Knierim et al., 1998). This influence on place cell activity is probably mediated through parahippocampal circuits, such as the PrS and MEC, rather than via direct synaptic connections. In constrained settings, such as movement along a linear track, this framework can induce strong directional modulation of place cell firing (B. McNaughton et al., 1983). In the MEC, conjunctive grid by direction neurons are found alongside HD cells, consistent with subcortical HD projections influencing grid activity (Boccara et al., 2010; Sargolini et al., 2006). Anatomical tracing confirms that HD cells in layer III of the PrS project directly to layer III of the MEC (Preston-Ferrer et al., 2016), a layer with fewer grid cells than layer II, where grid cells are most abundant. Other conjunctive cell types, including theta by place by direction cells and theta by border by HD cells, illustrate how directional, positional, and boundary information are integrated with parahippocampal circuits (Cacucci et al., 2004; Peyrache et al., 2017).

It is thought that grid cells, together with HD inputs, provide a path integration signal to the hippocampus (E. I. Moser & Moser, 2008). Their periodic firing allows self-motion to be converted into estimates of position, but these representations require anchoring to environment features for stability. Border cells convey information about the geometry of the environment (Burgess & O'Keefe, 2011). This information can anchor grid phase to environmental structure, potentially through feedback projection from the hippocampus to the MEC that corrects accumulated path integration errors (B. L. McNaughton et al., 2006; E. I. Moser & Moser, 2008). Consistent with this, inactivation of the hippocampus causes grid periodicity in MEC to degrade and firing patterns to drift (Bonnevie et al., 2013).

Place cells integrate these directional, positional, and geometric signals to produce a location-specific code. Inputs from grid cells provide self-motion based positional signals, HD cells supply directional context, and boundary cells and geometric anchoring. Although grid cells are not strictly required for the initial formation or remapping of place cells in novel settings, they help maintain spatial stability in darkness after MEC lesions (Brandon et al., 2014; Jacob et al., 2020).

Lesions and inactivation studies reveal that cortical spatial representations strongly depend on subcortical HD input. Inactivation of the AD reduces the proportion of grid cells and disrupts directional signals within the MEC (Winter et al., 2015). Lesions of the ATN abolish HD activity in the PrS (Goodridge & Taube, 1997) and spatial activity in the Sub (Frost et al., 2021). CA1 place fields retain spatial tuning but show reduced spatial information content and develop abnormal directional modulation (Calton et al., 2003). This suggests that subcortical HD signals are essential for maintaining spatial coding in many cortical and parahippocampal areas, but that the hippocampus can still sustain place codes without them, although less effectively. By contrast, lesions to cortical HD regions such as PrS mainly impair landmark control. In such cases, place fields shift unpredictably rather than

rotate with visual landmarks, indicating that PrS and RSC provide landmark-based anchoring that does not rely directly on subcortical HD signals (Calton et al., 2003).

3 The head direction system

Although HD cells are observed across multiple brain regions, the reason for their widespread distribution remains unclear (J. S. Taube, 2007). These regions are interconnected, forming a hierarchical network within the HD system. The hierarchical network contributes to precise HD signal processing ascending the network with the integration of multisensory inputs and modulatory inputs. This chapter first outlines the hierarchical organisation of the HD system. It then explores how sensory integration contributes to directional coding and informs current conceptual understandings of spatial cognition. Finally, it discusses the computational principles underlying HD signal processing, with a focus on the ring attractor model.

3.1 The hierarchy across the brain regions in the head direction system

To understand the structural organisation of the HD network, it is essential to identify where the HD signal originates. The primary source lies in the DTN of the brainstem, which generates the signal from vestibular inputs encoding AHV (P. E. Sharp, Tinkelman & Cho, 2001; P. E. Sharp, Blair & Cho, 2001; Yoder & Taube, 2014)(AHV, Sharp, Blair, et al., 2001; Sharp, Tinkelman, et al., 2001; Yoder & Taube, 2014). Reciprocal connectivity between the DTN and LMN is thought to establish the initial HD signal (Bassett et al., 2007; H. T. Blair et al., 1998; J. S. Taube, 2007). Lesion studies support this notion. Disruption of the DTN abolishes HD activity in downstream regions such as the AD, PrS, and MEC, and severely impairs overall navigation system (Bassett et al., 2007; Clark et al., 2013; Dillingham & Vann, 2019). Mammillary inputs are also critical for thalamic HD activity. Bilateral LMN lesions abolish HD activity in the AD, whereas unilateral lesions do not completely eliminate HD signals (Bassett et al., 2007; H. T. Blair et al., 1998, 1999). In animals with unilateral lesions, AD HD cells still remain active with AHV modulation, a feature normally confined to LMN HD cells. This suggests that the LMN provides essential AHV and HD input to the downstream regions. Together, the DTN and LMN support the initial signal for the HD system (H. T. Blair et al., 1999). Damage to the AD disrupts HD cell activity in downstream cortical regions such as the PrS (Goodridge & Taube, 1997) and the superficial layers of the MEC (Winter et al., 2015). In contrast, lesions of the PrS or RSC do not abolish HD signals in the AD or LMN but impair landmark control and signal stability (Goodridge & Taube, 1997; Yoder et al., 2015). These findings suggest that the PrS and RSC modulate the HD signal, particularly by integrating visual landmark information (Clark et al., 2010; Yoder, Clark, Brown et al., 2011; Yoder, Clark & Taube, 2011; Yoder et al., 2015). At the highest level of the HD network, the MEC receives a fully integrated directional signal from the ascending HD circuit. Lesions of the MEC have only minor effects on HD activity in the AD and do not affect landmark processing or angular path integration (Clark & Taube, 2011).

In summary, the HD circuit is hierarchically organised along a DTN → LMN → AD → PrS/RSC → MEC pathway. At the initial stages of this circuit, AHV inputs are crucial

for driving HD activity, particularly within the DTN and LMN. This pathway represents the primary route of head direction signal processing. However, directionally tuned cells have also been observed outside this hierarchical pathway. HD cells have been reported in the AV (Lomi et al., 2023; Tsanov, Chah, Vann et al., 2011; Yoganarasimha et al., 2006), AM (Jankowski et al., 2015), NRe (Jankowski et al., 2014), and LD (Mizumori & Williams, 1993). As a supplementary finding, lesions in the LD result in only minor effects on HD activity in the PrS (Golob et al., 1998).

3.2 Sensory integration in the head direction system

The HD system maintains a stable representation of an animal's orientation by integrating multiple sensory modalities (J. S. Taube, 2007). This integration enables accurate heading computation under a wide range of environmental conditions. Sensory inputs to the HD circuit can be broadly classified into idiothetic cues, generated by self-motion, and allothetic cues, derived from the external environment. While both are essential, they contribute in different ways. The idiothetic cues, including vestibular, proprioceptive, and motor efference signals, update heading during movement. The allothetic cues, such as visual landmarks, anchor the HD representation to the external world. The stability and precision of the HD system depend on the integration of both sources of information.

Vestibular input is indeed the principal idiothetic source for the HD system, particularly the signals from the semicircular canals, which encode AHV. These vestibular signals travel from the vestibular nuclei to the nucleus Nucleus prepositus hypoglossi (NPH), then are transmitted to the DTN, the LMN and to the rest of the HD network. This anatomical and functional flow has been detailed in multiple studies (Brown et al., 2005; Song & Wang, 2005; Yoder & Taube, 2014). While the DTN sends Gamma-aminobutyric acid (GABA)ergic projections to the LMN (Allen & Hopkins, 1989; Wirtshafter & Stratford, 1993), it is still unclear how the HD signal is processed in this pathway. Retrograde labelling of LMN indicates that it receives inputs from vestibular nuclei such as NPH, Supragenual nucleus (SGN), and Medial vestibular nucleus (MVN) (Brown et al., 2005). Some questions remain concerning the emergence of the HD signal within the DTN-LMN network (J. S. Taube et al., 2025). In DTN, approximately 75% of neurons encode the AHV of the animal (Bassett & Taube, 2001; P. E. Sharp, Tinkelman & Cho, 2001). The AHV cells were categorised based on their firing patterns; symmetric AHV cells code for both clockwise and counterclockwise directions, while asymmetric AHV cells prefer one direction. A majority of asymmetric AHV cells were located in the hemisphere opposite to the preferred AHV. Approximately 10% of these AHV cells were also directionally tuned. 50% percentage of LMN cells discharge in relation to AHV (Stackman & Taube, 1998). In the LMN, about half of the AHV cells are "fast" AHV cells, which can be either symmetric or asymmetric in their tuning. The other half are "slow" AHV cells, whose firing rates decrease with increasing head-turn speed in both clockwise and counterclockwise directions. Slow AHV cells are absent in the DTN. Overall, fast AHV cells in the LMN resemble those in the DTN, although their firing is less strongly correlated withAHV than in the DTN. Meanwhile, no HD cells were

observed upstream of DTN (P. E. Sharp et al., 2006). In LMN, 36% of cells encode both HD and AHV, while a higher percentage of conjunctive HD+AHV cells (60%) were observed in the DTN (J. S. Taube et al., 2025). Taken together, it appears that the HD signal begins in the DTN-LMN with the vestibular inputs as a primary source of idiothetic sensory information. Furthermore, motor efference copy signals can be integrated into this pathway, providing self-motion information that becomes important for updating the HD signal when vestibular inputs are diminished or absent (Stackman & Taube, 1997; Tan et al., 2015).

The RSC plays a central role in integrating visual landmark information with idiothetic self-motion cues for HD processing. Visual landmarks act as stable external references that calibrate movement-based spatial estimates, such as those generated by path integration, reducing drift and stabilising orientation by anchoring internal representations to the environment (Clark et al., 2010; Page et al., 2018; Yan et al., 2021; Yoder, Clark, Brown et al., 2011). Simultaneous recordings have revealed that HD cell activity in RSC and the AD rotates almost synchronously with visual landmark shifts, indicating strong functional coupling and rapid visual anchoring across cortical and thalamic HD networks (Van Der Goes et al., 2024). Lesion studies in humans and rodents show that damage to the Dysgranular retrosplenial cortex (dRSC) impairs the ability to use familiar landmarks for orientation, whereas lesions involving the Granular retrosplenial cortex (gRSC) or complete RSC damage disrupt spatial learning and flexible landmark use (Auger & Maguire, 2013; Auger et al., 2012; Hindley et al., 2014; Maguire, 2001; Pothuizen et al., 2010; Vann & Aggleton, 2005). Anatomical and behavioural evidence suggests that visual landmark inputs enter the HD system primarily via dRSC, which receives strong projections from visual cortex, before being routed to gRSC and then to subcortical HD structures. In contrast, gRSC predominantly receives internal or mnemonic inputs from subcortical and hippocampal networks (Fischer et al., 2020; Jacob et al., 2017; Page et al., 2018).

Electrophysiological recordings support this division. Both dRSC and gRSC contain global HD cells, but dRSC uniquely contains multidirectional cells that are strongly influenced by local visual landmarks (Jacob et al., 2017). These cells adjust their tuning according to environmental symmetry, displaying bidirectional or multidirectional firing in visually symmetric environments and unidirectional tuning in open field conditions (N. Zhang et al., 2022). The presence of multidirectional cells only in dRSC, and not in gRSC, AD or PrS, supports the idea that they receive stronger cortical visual input than subcortical HD input (Page et al., 2018). Recent connectomic and functional mapping revealed that presubicular neurons integrate converging inputs from both RSC and AD, providing an anatomical substrate for the synaptic integration of cortical landmark-based and thalamic self-motion head direction signals (Richevaux et al., 2025).

Computational modelling suggests that stable landmark anchoring emerges through Hebbian plasticity between global HD cells in gRSC, driven by AD inputs, and visually driven multidirectional cells in dRSC, driven by cortical visual inputs (Page et al., 2018; Yan et al., 2021). Such an associative mechanism may enable the HD network to link stable environmental cues to its internal directional representation. Via feedback projections to the AD and LMN (via the PrS), the RSC can potentially correct drift in path integration by integrating visual and self-motion signals (Yoder, Clark & Taube, 2011).

Landmark-modulated HD cells are also found in the MEC and PaS (Brandon et al., 2013;

Kornienko et al., 2018). When a visual cue was moved between two opposite walls of a square arena, some HD cells in both regions showed bidirectional tuning curves (Kornienko et al., 2018). 63% of these cells fired rhythmically in the theta range, while the rest lacked intrinsic spike rhythmicity. The largest landmark-driven changes in tuning occurred in the non-theta rhythmic HD cells, and these changes were often not coherent between cells recorded at the same time. This suggests that non-theta rhythmic HD cells, which are less bound by attractor dynamics, may receive stronger visual inputs either directly or via dRSC compared with inputs from subcortical HD cells in AD or theta modulated cells in AV. The theta modulation of MEC and PaS HD cells is not dependent on the septo-hippocampal system, as Medial septum (MS) inactivation disrupts grid cells without altering theta or HD activity in MEC and PaS (Brandon et al., 2013). Instead, HD and theta inputs to MEC and PaS are likely provided by separate efferents from the ATN contributing through direct projections or indirectly via gRSC (H. Shibata, 1993a; Van Groen & Michael Wyss, 1990; Van Groen & Wyss, 1990a).

In summary, the HD system functions as a multimodal integrator: allothetic cues provide stable external anchors, while idiothetic cues update heading during movement. This sensory interplay forms the basis for the stability and flexibility of the ring attractor network described in the next section.

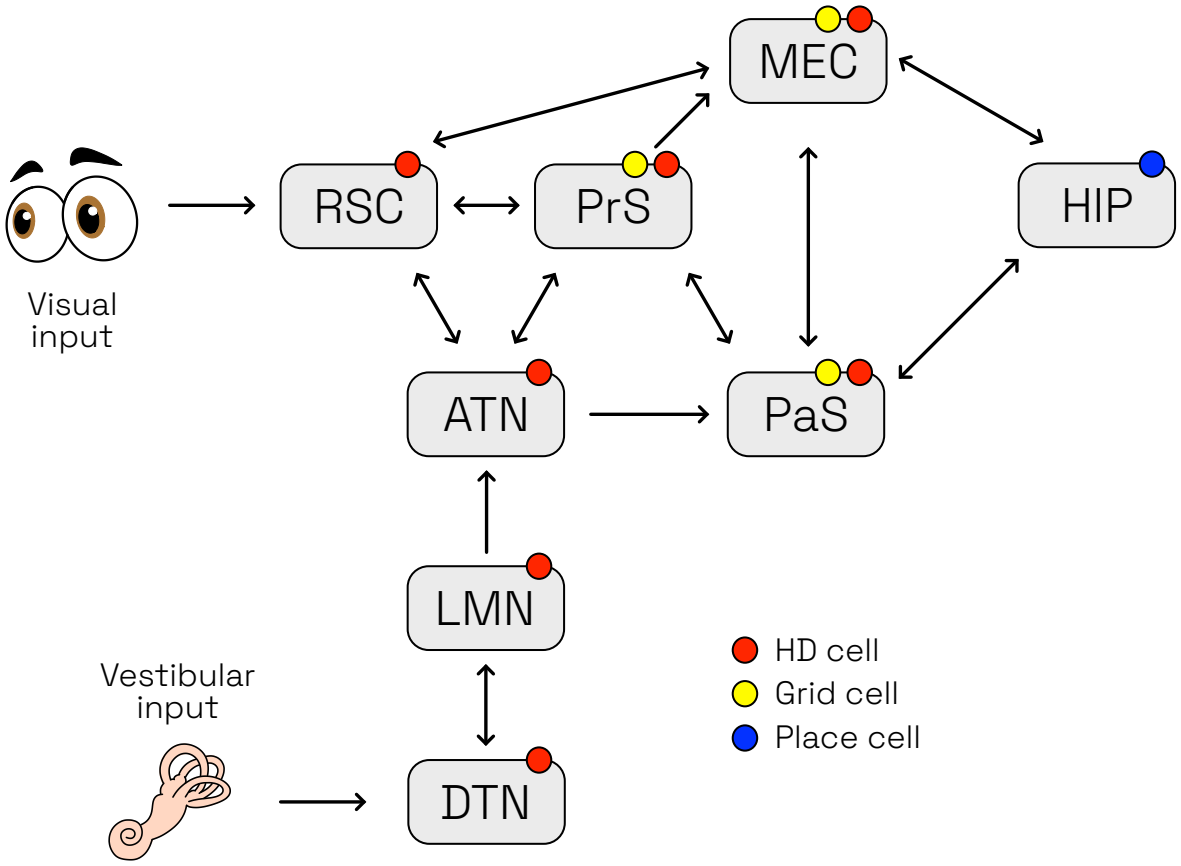

Figure 3.1 Anatomical network of spatially tuned cells.

Brain regions containing HD cells, grid cells, and place cells are shown with their connectivity. The direction of arrows indicates the anatomical connectivity between the regions in the figure, but the lesion studies demonstrate that the hierarchical HD network follows DTN → LMN → ATN → PrS/RSC pathway. Sensory integration occurs within the HD network, through visual and vestibular inputs. Grid and place cells are located downstream in this circuit. Adapted from Angelaki and Laurens (2020) and J. S. Taube (2007).

3.3 Ring attractor network

The prevailing computational model of HD activity is the ring attractor (Angelaki & Laurens, 2020; B. L. McNaughton et al., 2006; Redish et al., 1996; P. E. Sharp, Blair & Cho, 2001; Skaggs et al., 1995; K. Zhang, 1996). In this model, HD cells are arranged in a conceptual ring as neighbouring cells have similar preferred directions. Each cell is active only when the head is oriented within a narrow angular range, and the population collectively covers the full 360°, analogous to a neural compass. Theoretical frameworks propose that connectivity is organised so that neurons with nearby preferred directions are mutually excitatory, whereas those with distant preferred directions exert inhibitory influence. This balance of local excitation and global inhibition produces a single localised bump of activity that represents the current heading. As the head turns, self-motion signals from AHV cells shift this bump smoothly around the ring without altering its shape (Clark & Taube, 2012; Song & Wang, 2005). This theory has found a striking experimental correlation in Drosophila (Green et al., 2017; S. S. Kim et al., 2017; Seelig & Jayaraman, 2015; Turner-Evans et al., 2017), and zebra fish (Petrucco et al., 2023), by showing the 'bump' of internally organised HD cells when the experimental subject is exploring.

The attractor framework accounts for several key properties of HD cells. Visual landmark inputs can stabilise the bump's position, while in darkness the network can maintain and update the representation through path integration (Angelaki & Laurens, 2020). In such conditions, HD tuning can persist for extended periods but gradually drifts, with all simultaneously recorded cells shifting their preferred directions coherently. This coherence reflects a single internal HD signal maintained by the attractor as a unified activity packet moving together around the ring. Recent work by Asumbisa et al. (2022) have demonstrated that the HD ring attractor network remains stable and functional even in the absence of vision. Using recordings from blind mice with photoreceptor degeneration, they showed that HD cells in the AD maintain robust and accurate tuning comparable to sighted animals. The study revealed that, in the absence of visual landmarks, alternative sensory modalities such as olfaction can flexibly anchor the HD network, enabling a stable directional representation across diverse environments. Notably, when both visual and olfactory cues are unavailable, the attractor network persists internally but exhibits gradual drift. Also, even when visual reference frames are altered, HD cells maintain their internal organisation and instead re-anchor collectively to the new visual context (Park et al., 2019), indicating that sensory inputs dynamically anchor the attractor to different environmental frames while the internal network structure remains stable. This explains flexible anchoring to multiple sensory cues, especially allocentric cues, and its importance for precise directional coding while the internally organised attractor network remains.

Idiothetic cues, particularly vestibular-derived AHV, are essential for maintaining an accurate and stable HD representation. Rodent experiments provide strong evidence for this. The inactivation of DTN-projecting neurons in the NPH caused coordinated drift of HD cells in the ATN (Butler et al., 2017). This result underscores the critical role of AHV input in updating and preserving the bump's position within the ring attractor. Consistent with this, coordinated drift has been observed following vestibular disruption (Muir et al., 2009; Stackman & Taube, 1997), while milder decoupling effects were reported under partial vestibular lesions (Yoder & Taube, 2009). Together, these findings demonstrate that self-

motion cues are fundamental for HD system stability in the absence of visual landmarks.

Further evidence indicating that the HD system is internally organised comes from developmental studies and sleep. The HD attractor activity was observed in rat pups before eye opening (Bassett et al., 2007; Tan et al., 2015). This suggests that the internal HD attractor can form without visual experience, relying instead on early-maturing inputs like the vestibular system. Moreover, the attractor dynamics are preserved during sleep, with HD cells maintaining correlated firing patterns that reflect a drifting internal directional signal (Peyrache et al., 2015). Together, these findings support the view that the HD system operates as an internally organised network that flexibly integrates sensory inputs to anchor its representation, yet can sustain coherent directional coding in their absence.

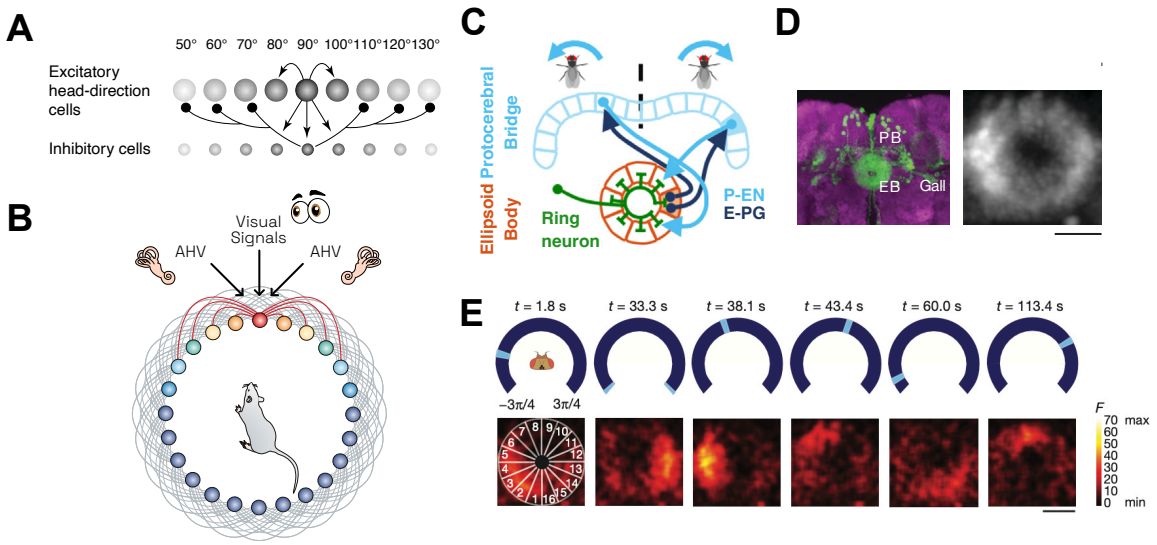

Figure 3.2 Ring attractor network in the HD system.

A) General mechanism of attractor networks. Excitatory and inhibitory neurons are interconnected to form a network that restricts activity to groups of cells coding for similar directions. Adapted from P. E. Sharp, Tinkelman and Cho (2001).

B) Schematic diagram of HD cells arranged in a virtual ring according to their PFD. Each cell (coloured dots) connects most strongly with nearby cells, with connection strength decreasing as distance increases. This organisation allows a localised bump activity to represent current HD and to shift around the ring in correspondence with head direction. Sensory inputs such as visual and vestibular signals stabilise the attractor. Adapted from B. L. McNaughton et al. (2006)

C) Schematic diagram of HD attractor in drosophila. The Ellipsoid body (EB) and Protocerebral bridge (PB) are central complex structures in drosophila. EB neurons form a ring attractor network that generates a stable bump activity representing the fly's heading, while reciprocal connections with the PB stabilise and update this direction signal. This EB-PB network is considered the insect analogue of the mammalian HD system. Adapted from Angelaki and Laurens (2020)

D) Green fluorescent protein (GFP)-expressing EB neurons in the drosophila's brain and 2 photon images of Genetically encoded calcium indicator (GFP–Calmodulin–M13) (GCaMP)6f-expressing EB neurons. Adapted from Seelig and Jayaraman (2015)

E) Top: Visual cues while the fly walks in the close-loop. Bottom: Active bump of EB neurons as fly rotates visual cue around the arena. These findings provide experimental evidence for ring attractor dynamics, in which a continuous attractor network maintains a stable bump activity that shifts with heading. Adapted from Seelig and Jayaraman (2015)

4 Thalamus

The thalamus is a complex and evolutionary conserved brain structure, centrally positioned within the diencephalon. This region is structured by several nuclei, including the ATN, which is the primary focus of this thesis. In this chapter, the thalamus will be introduced to provide an overview of its anatomical organisation and functional characteristics.

4.1 History of the thalamus

Θαλαμη. This Greek word marked the first appearance of the term thalamus in anatomical history. It was introduced by Galen of Pergamon in the 2nd century A.D. He described it in *De Usu Partium* as a chamber located at the end of the lateral ventricles and associated with the origin of the optic nerves (Galen, 1997). In ancient Greek, the word carried several meanings, including a side chamber for women or a housewife, a tomb, the hull of a ship, and a shrine (Liddell et al., 1996). Galen likely adopted the term as a metaphor for an isolated and enclosed space, in alignment with his theory of the thalamus as a hollow structure facilitating the flow of pneuma to the optic nerves. Although the anatomical concept was well preserved in the initial translations in Arabic, the term itself faded from use in Europe for several centuries as it was lost in transmission through successive and incomplete translations. The term thalamus was later reintroduced in the 17th century by Jean Riolan the Younger, who referred to it in his first anatomical work *Anatome Corporis Humani*, while describing the optic nerves (García-Cabezas et al., 2021; Riolan, 1610). Finally, Thomas Willis standardised thalamus as a neuroanatomical term in 1664, defining it as the ovoid mass from which the optic nerves emerge (García-Cabezas et al., 2021; Willis, 1664). The thalamus, the term we use today, originated from the Latin translations of Galen's anatomical text.

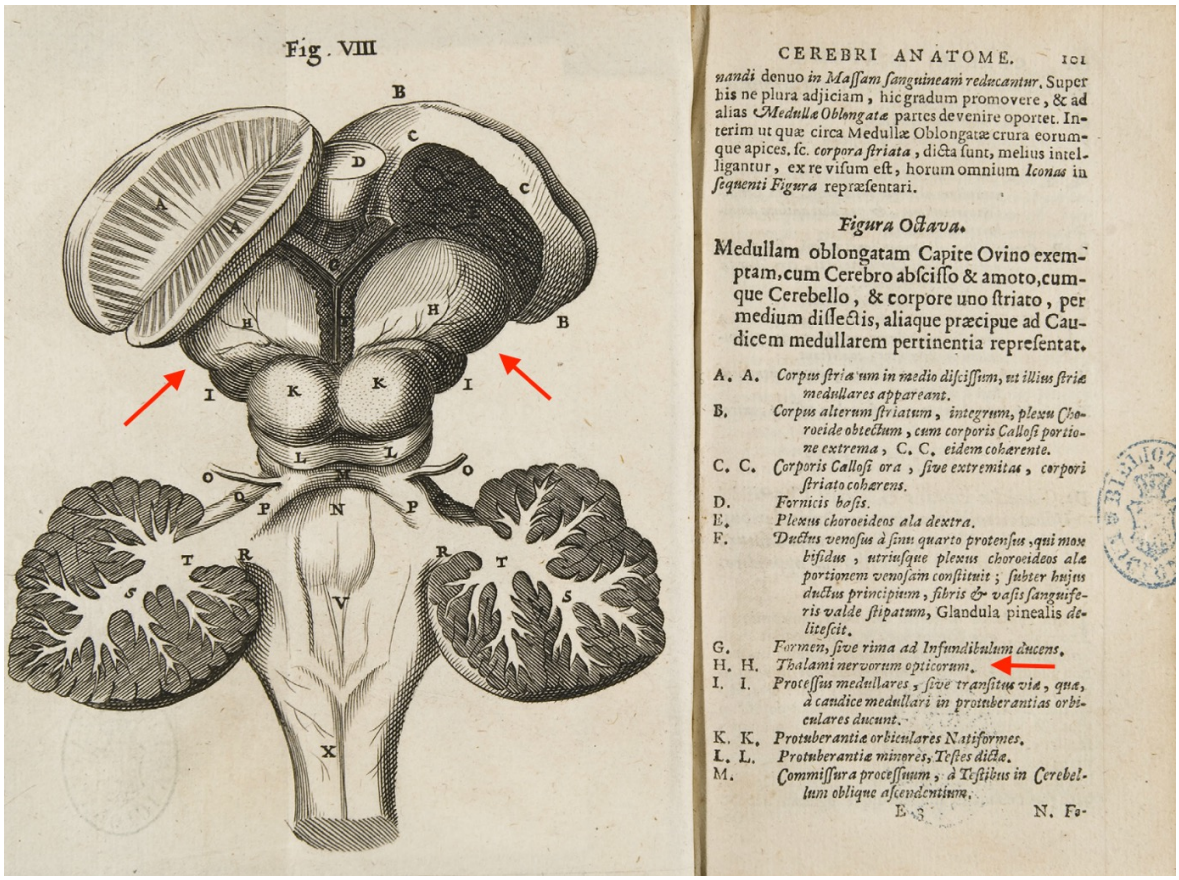

CEREBRI ANATOME. 101

nandi denuo *in Maſſam ſanguineam reducantur*. Super his ne plura adjiciam, hic gradum promovere, & ad alias *Medullæ Oblongatæ* partes devenire oportet. Interim ut quæ circa Medullæ Oblongatæ crura eorumque apices, ſc. *corpora ſtriata*, dicta ſunt, melius intelligantur, ex re viſum eſt, horum omnium *Icones* in *ſequenti Figura* repræſentari.

Figura Octava.

Medullam oblongatam Capite Ovino exemptam, cum Cerebro abſciſſo & amoto, cumque Cerebello, & corpore uno ſtriato, per medium diſſectis, aliaque præcipue ad Caudicem medullarem pertinentia repreſentat.

A. A. *Corpus ſtriatum in medio diſciſſum, ut illius ſtriæ medullares appareant.*
B. *Corpus alterum ſtriatum, integrum, plexu Choroide obtectum, cum corporis Calloſi portione extrema, C. C. eidem cohærente.*
C. C. *Corporis Calloſi ora, ſive extremitas, corpori ſtriato cohærens.*
D. *Fornicis hoſis.*
E. *Plexus choroideus ala dextra.*
F. *Ductus venoſus à ſinu quarto protenſus, qui mox bifidus, utriuſque plexus choroideos alæ portionem venoſam conſtituit; ſubter hujus ductus principium, fibris & vaſis ſanguiferis valde ſtipatum, Glandula pinealis delitescit.*
G. *Formen, ſive rima ad Infundibulum ducens.*
H. H. *Thalami nervorum opticorum.*
I. I. *Proceſſus medullares, ſive tranſitus viæ, quæ, à caudice medullari in protuberantias orbiculares ducunt.*
K. K. *Protuberantiæ orbiculares Natiformes.*
L. L. *Protuberantiæ minores, Teſtes dictæ.*
M. *Commiſſura proceſſuum, à Teſtibus in Cerebellum oblique aſcendentium.*

E 3 N. Fo-

Figure 4.1 Drawing of the human brainstem by Willis (1664).

Modified from the figure in García-Cabezas et al. (2021). Red arrows indicate his references to the thalamus.

4.2 Anatomy and functions of the thalamus

In modern neuroscience, the thalamus is defined as a grey matter complex comprising nuclei that relay information between subcortical and cortical regions in the mammalian brain (Jones, 2007). Thalamic nuclei are classically categorised into functional groups based on cytoarchitecture and connectivity profiles. The dorsal thalamus predominantly consists of excitatory and glutamatergic projecting neurons that extends outside of thalamus to target regions such as the cortex, striatum, and amygdala. This region lacks recurrent excitatory connections within the thalamus (Halassa & Sherman, 2019). The ventral thalamus includes the Thalamic reticular nucleus (TRN), which does not project to the cortex. Unlike other thalamic nuclei, it contains inhibitory GABAergic neurons that serve as a local inhibitory source within the thalamic network (Didier et al., 2018; S.-C. Lee et al., 2014).

Thalamic relay neurons receive two principal classes of inputs: drivers and modulators (Sherman & Guillery, 1998, 2011). Drivers generate strong Excitatory postsynaptic potential (EPSP)s. Retinal ganglion cells are typical drivers projecting to the Lateral geniculate nucleus (LGN) (Alitto et al., 2019; Perry et al., 1984). Drivers are often described as conveying sensory information to thalamic nuclei (Marcuse et al., 2025). Modulators, by contrast, typically originate from cortical layer VI neurons or the TRN, and release diverse neurotransmitters such as glutamate, GABA, serotonin, dopamine, and acetylcholine (C. C. Lee & Sherman, 2008). As these neurotransmitters suggest, modulators regulate thalamic output through mechanisms such as gain control, temporal precision, and inhibition (Sherman, 2016). This framework supports a functional distinction between first-order and higher-order thalamic nuclei. First-order nuclei, such as the LGN or Ventroposterior medial nucleus (VPM), receive driver inputs from peripheral sensory sources, including the retina and brainstem. In contrast, higher-order nuclei, such as the Pulvinar or Posterior medial nucleus (POm), receive their driver inputs from cortical layer V neurons and transmit this information to other cortical areas. This defines a cortico-thalamo-cortical pathway.

Recent studies indicate that the thalamus does more than relay sensory information. It plays a central role in coordinating diverse cognitive, sensory, and motor functions across brain networks. The diversity is evident in the distinct roles played by different thalamic nuclei. For instance, the ATN is crucial for spatial navigation and memory (Ajabi et al., 2023; Roy, Zhang, Aida et al., 2022; Roy et al., 2021; J. Taube, 1995; Tsanov, Chah, Vann et al., 2011), the central thalamus is involved in arousal (Schiff et al., 2013), and the Mediodorsal thalamic nucleus (MD) contributes to executive and various cognitive functions (Ouhaz et al., 2018; Saalmann, 2014). Such heterogeneity is further complicated by emerging evidence that thalamic neurons exhibit molecular diversity that does not neatly align with traditional anatomical boundaries (Roy, Zhang, Aida et al., 2022). Transcriptional profiling, for example, reveals overlapping gene expression patterns across nuclei that challenge the conventional cytoarchitectonic classification. In both rodents and primates, this molecular and functional complexity supports the idea that the thalamus is not merely a passive relay station but a dynamic hub integrating and modulating signals throughout the brain.

4.3 Anterior thalamic nuclei

The thalamus is commonly organised into groups of nuclei based on their anatomical position, including the anterior, medial, lateral, ventral, and posterior divisions. Within this organisation, the ATN form a distinct cluster located at the dorso-rostral end of the thalamus in both rodent and human brains. This region establishes complex anatomical connections with multiple brain areas, forming the basis for its involvement in diverse functional roles including spatial orientation. This section introduces the anatomical organisation of the ATN and progressively explores its functional characteristics.

4.3.1 Structural organisation

The ATN comprise the anterodorsal (AD), anteroventral (AV), and anteromedial (AM) nucleus, each named according to its anatomical position within the complex (Figure 4.1A). This subdivision is based on distinct cytoarchitectural shapes, with each region exhibiting a characteristic cellular organisation. In the human brain, these nuclei are clearly delineated and display well-defined cytoarchitecture (Morel et al., 1997). AD is the smallest of the three, containing densely packed, small-sized neurons. AV is the largest, making it easily identifiable, and consists of densely arranged cells of relatively uniform size. AM is located ventrally to AV and is composed of slightly larger, more diffusely distributed neurons. However, certain anatomical ambiguities remain. For example, the inclusion of the LD as part of the ATN has been debated (Morel et al., 1997), and some authors have noted the ambiguous boundary between AV and AM, particularly in human and non-human primates (Powell et al., 1957). In acute slices of the mouse brain, the boundary between AD and AV is clearly distinguishable (Figure 4.1B), whereas the delineation between AV and AM is not readily apparent under transmitted light microscopy without immunostaining. However, these regions can be clearly distinguished based on their anatomical connectivity and gene expression profiles in both rodents and macaques (Bubb et al., 2017; Mathiasen et al., 2021).

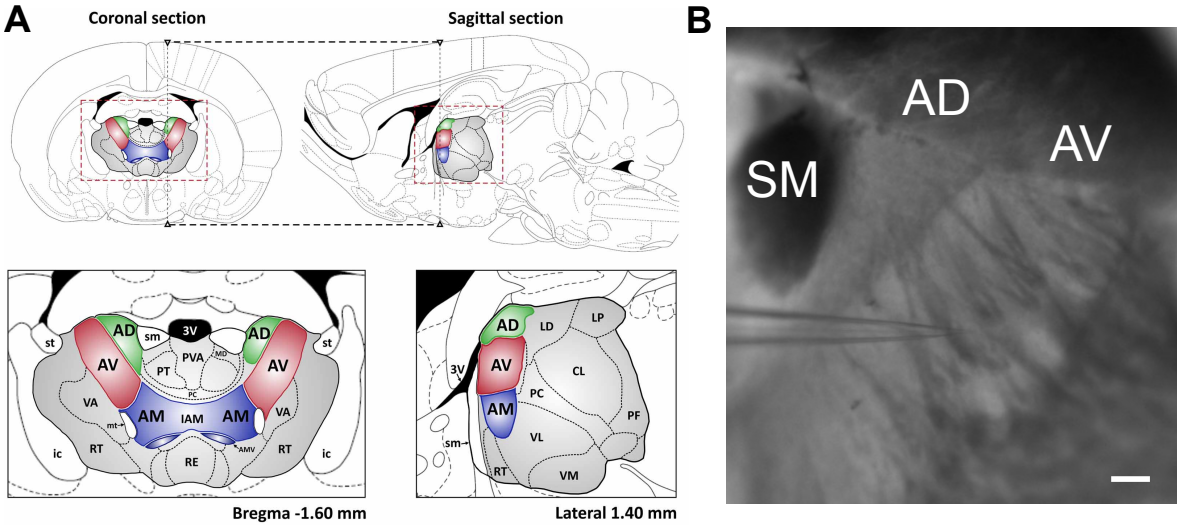

Figure 4.2 The anatomy of ATN.

A) Overall delineation of thalamic nuclei in the rat brain. The ATN are shown in colour, while other thalamic regions are displayed in grey in both coronal and sagittal views. Adapted from Jankowski et al. (2013). (Refer to the list of abbreviations for each region.)
B) Image of an acute mouse brain slice (infrared, 5x magnification, 300 µm thickness) captured after patch-clamp recording. Scale bar: 100 µm

4.3.2 General connectivity of the ATN

The circuit proposed by Papez (1937) remains anatomically significant and continues to provide a useful framework for understanding the connectivity of the anterior thalamus. This circuit describes a serial pathway linking the hippocampus with the hypothalamus, ATN, and cingulate cortex, ultimately returning to the hippocampus to form a closed loop (Figure 4.3). In the original formulation, Papez suggested that this pathway supports the neural processing of emotion.

MacLean (1952) and Maclean (1949) later expanded the concept into what became known as the limbic system, based on Papez's circuit. It incorporated additional brain regions, including the amygdala, olfactory bulb, and nucleus accumbens, alongside the structures of the original Papez circuit. MacLean proposed that these interconnected regions collectively support a wide range of functions related to emotion, memory, motivation, and physiological drives. The limbic system framework provided a broader anatomical and functional context for understanding how subcortical and cortical areas interact to mediate complex behavioural and physiological responses.

Accumulating anatomical and functional evidence has led to multiple revisions and expansions of the original Papez circuit. Among the various anatomical frameworks proposed within the broader context of the limbic system (Aggleton & Brown, 1999; J. Delay & Brion, 1969; Livingston, 1971; Nelson & Vann, 2014), the extended hippocampal–diencephalic net-

work suggested by Aggleton and Brown (1999) has gained wide acceptance. This framework places the ATN at the core of a system that integrates memory and spatial processing. It highlights both the parallel connectivity and functional specialisation of individual ATN subregions. The AD is closely associated with the HD system, as its neurons display directional tuning, functioning as a neural compass (Clark & Taube, 2012; J. Taube, 1995). The AV is part of the loop maintaining theta rhythmic activity between the thalamus and hippocampal formation. In contrast, the AM is proposed to be part of a contribution to high-order cognitive and executive functions by forming a feed-forward system between hippocampal-diencephalone and prefrontal regions. This extended network shifts the focus beyond emotional processing and situates the ATN within a broader framework supporting spatial orientation and cognition.

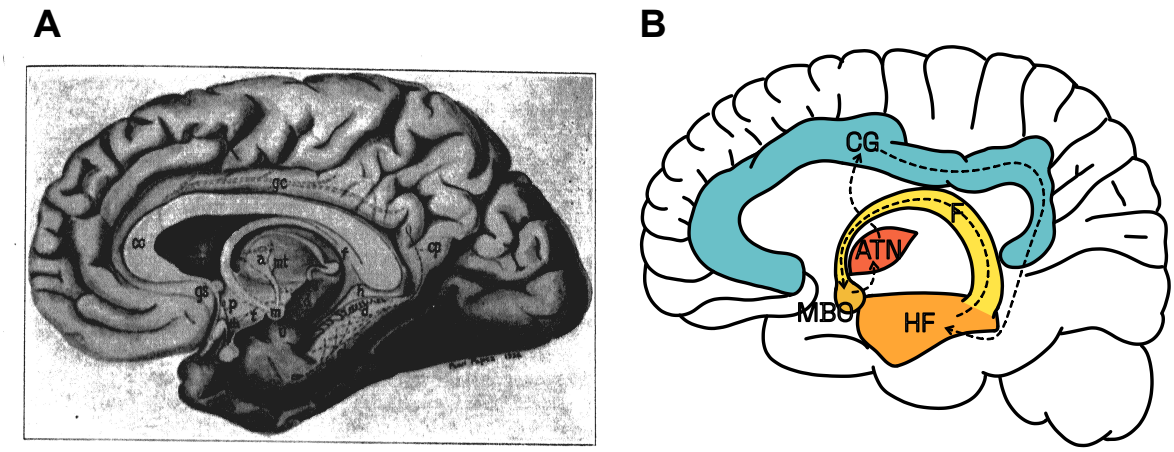

Figure 4.3 Papez circuit diagram.

A) Brain diagram from Papez (1937) illustrating the circuit processing emotions. Related abbreviations: a, anterior thalamic nucleus; m, mammillary body; mt, mammillothalamic tract; cp, cingulum posterius; gc, gyrus cinguli; f, fornix; h, hippocampus nucleus (hippocampal formation).
B) Schematic reconstruction of the Papez circuit. (Refer to the list of abbreviations for each region.)

4.3.3 Functions of ATN

Over time, the functions of the ATN have been increasingly explored. Early studies focused on the ATN and its role in emotion, acting as a critical relay that links subcortical emotional signals to cortical domains. Papez (1937) proposed that the thalamus receives sensory input and sends it along two distinct pathways: a 'thought' stream directed to the sensory cortices, where sensations are transformed into perceptions and memories, and a 'feeling' stream directed to the Mammillary body (MBO), contributing to the generation of emotional experience. Disruptions along this Papez circuit have been implicated in a wide range of disorders, including schizophrenia, autism, depression, amnesia, cognitive impairments, and Alzheimer's disease (Aggleton & Brown, 1999; Small et al., 2011). Supporting this idea, recent studies have shown that knockdown of neuropsychiatric disorder-risk genes in the AD induces neuronal hyperexcitability and results in cognitive deficits (Roy et al., 2021). Furthermore, early p-tau pathology has been observed in the AD during the preclinical stages of Alzheimer's disease in humans, when no cognitive symptoms are yet present, while the AV remains unaffected (Sárkány et al., 2024).

More recent research has increasingly emphasised the role of the ATN in spatial navigation and memory. For example, the ATN appears to be involved in both memory encoding and remote memory retrieval (Vetere et al., 2021; Yamawaki et al., 2019). Optical activation of the ATN in rats with mammillothalamic tract lesions impaired spatial memory, highlighting the critical role of the ATN in spatial memory processing (Barnett et al., 2021). The contribution of the ATN to the spatial memory system has been extensively documented (Mitchell & Dalrymple-Alford, 2006; Nelson et al., 2020; Warburton & Aggleton, 1998; Winter et al., 2015). Most importantly, the critical role of the ATN in the HD system should be discussed, which is a key focus of this thesis. Numerous studies have reported HD cell activity within ATN subnuclei (Ajabi et al., 2023; H. Blair & Sharp, 1995; H. T. Blair et al., 1999; Lomi et al., 2023; Stackman & Taube, 1997; J. Taube, 1995; Tsanov, Chah, Vann et al., 2011; Viejo & Peyrache, 2020), highlighting their central involvement in directional coding. Notably, the accumulation of p-tau in the AD has been shown to disrupt this spatial system, further emphasising the functional significance and vulnerability of this region (Jiang et al., 2024).

At this point, it is important to stress the need to approach the ATN through its individual subnuclei: AD, AV, and AM. First, as noted earlier, these subnuclei form a parallel structure within the extended hippocampal–diencephalic network. Their separate organisation suggests that they may serve distinct functional roles. In addition, recent studies have shown that thalamic nuclei possess unique genetic and electrophysiological profiles (Phillips et al., 2019; Roy, Zhang, Aida et al., 2022; Roy, Zhang, Halassa & Feng, 2022; Roy et al., 2021). These differences underline the importance of studying the ATN at the subnuclear level. In the following chapter, we will examine the specific connections and functions of each subnucleus within the HD system.

5 Anterodorsal nucleus in the head direction system

The AD is the most studied subnucleus of the ATN in relation to the HD system. A large proportion of AD neurons are directionally tuned in rodents (J. Taube, 1995), and lesion studies have shown its crucial role in bridging directional signals between the hypothalamic and cortical regions. In this chapter, the involvement of AD within the HD system will be described in detail on anatomical and functional aspects.

5.1 Anatomical connectivity

The AD possesses a complex connectivity. It receives inputs from the LMN via the mammillothalamic tract (H. T. Blair et al., 1999; Seki & Zyo, 1984; H. Shibata, 1992). This projection is bilateral, in the sense that the LMN in one hemisphere projects to the AD in both hemispheres (Guison et al., 1995). It also forms reciprocal connections with the gRSC, PrS and PaS (Van Groen & Wyss, 1990a, 1990b, 1995). The AD also receives input from the TRN (Gonzalo-Ruiz & Lieberman, 1995; H. Shibata, 1992) (no literature found about AD to TRN), which may provide inhibitory modulation. Another afferent to the AD is the Anterior cingulate cortex (ACC) (H. Shibata & Naito, 2005). Further connections include projections to the hippocampus (Amaral & Cowan, 1980; Wyss et al., 1979) and afferents from the Sub (Van Groen & Wyss, 1990a). In addition, AD receives inhibitory inputs from hippocampal CA3 (Vetere et al., 2021), and work from Satoh and Fibiger (1986) implies potential cholinergic input from the Laterodorsal tegmental nucleus (LDT).

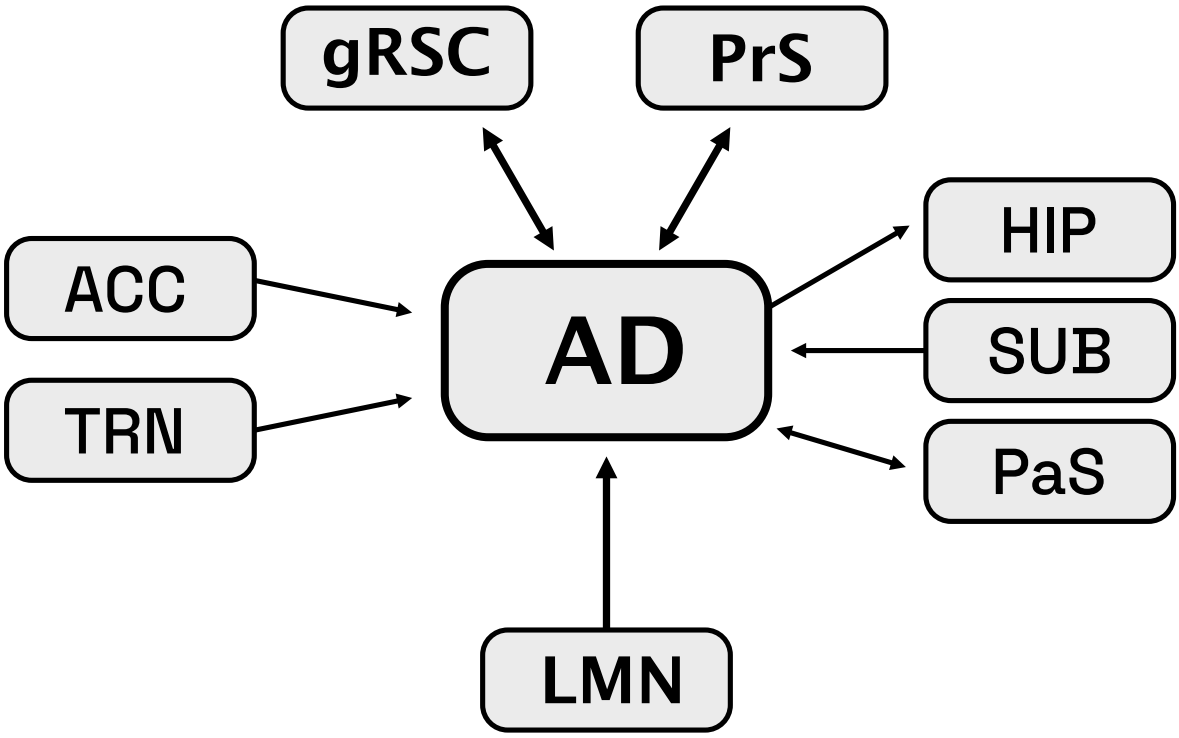

Figure 5.1 The anatomical connectivity of the AD.

Recreated based on the figure proposed by Nelson (2021).

5.2 HD system in the AD

The involvement of the AD in the HD system appears to be conserved across multiple species, including mice (Ajabi et al., 2023; Peyrache et al., 2015; Viejo & Peyrache, 2020; Yoder, Clark, Brown et al., 2011), rats (H. Blair & Sharp, 1995; J. Taube, 1995), guinea pigs (J. S. Taube, 2007), and chinchillas (Muir et al., 2009). It was initially reported that approximately 60% of neurons in the AD are directionally tuned (J. Taube, 1995). Compared to HD cells in other brain regions, those in the AD are characterised by relatively higher firing rates (J. S. Taube, 2007). HD cell activity in the AD is often modulated by AHV. AD HD cells also exhibit multimodal responsiveness to sensory inputs such as auditory cues, whisker deflection, pupil changes, and social interactions (Blanco-Hernández et al., 2024). Thalamic HD cells are known for their dependency on both external (e.g. visual) and idiothetic (e.g. vestibular and proprioceptive) cues to maintain their directional tuning (J. S. Taube, 2007; Yoder, Clark, Brown et al., 2011). Once their PFD is established within a given environment, these neurons remain active in the absence of visual input. However, in darkness, their preferred direction tends to drift over time. These cells can reorient to visual landmarks once those cues are reintroduced (Calton et al., 2008; Goodridge et al., 1998; Van Der Goes et al., 2024). Physical restraint may mildly reduce AD HD cell peak firing rates (Bassett et al., 2005; Zugaro et al., 2001), or have no significant effect (Shinder & Taube, 2011) on their directional activity.

Recent findings show that HD coding in the AD is flexible, maintaining coherent population activity during both drift and cue-driven reorientation, supporting the presence of a continuous attractor network that preserves directional stability while allowing dynamic updates (Ajabi et al., 2023). During sleep, the AD HD system remains internally organised, sustaining structured activity even without sensory input (Peyrache et al., 2015; Viejo & Peyrache, 2020). This persistent coordination further supports continuous attractor dynamics, allowing stable directional representation across brain states. AD neurons are temporally coupled to hippocampal sharp-wave ripples during non-Rapid eye movement (REM) sleep, suggesting a role in memory consolidation. These findings imply that the thalamic HD system contributes not only to spatial navigation but also to offline processing and memory integration. Taken together, the AD may serve an important role in integrating both landmark and idiothetic information, thereby delivering a more refined HD signal to the hippocampus via the PrS (J. S. Taube, 2007).

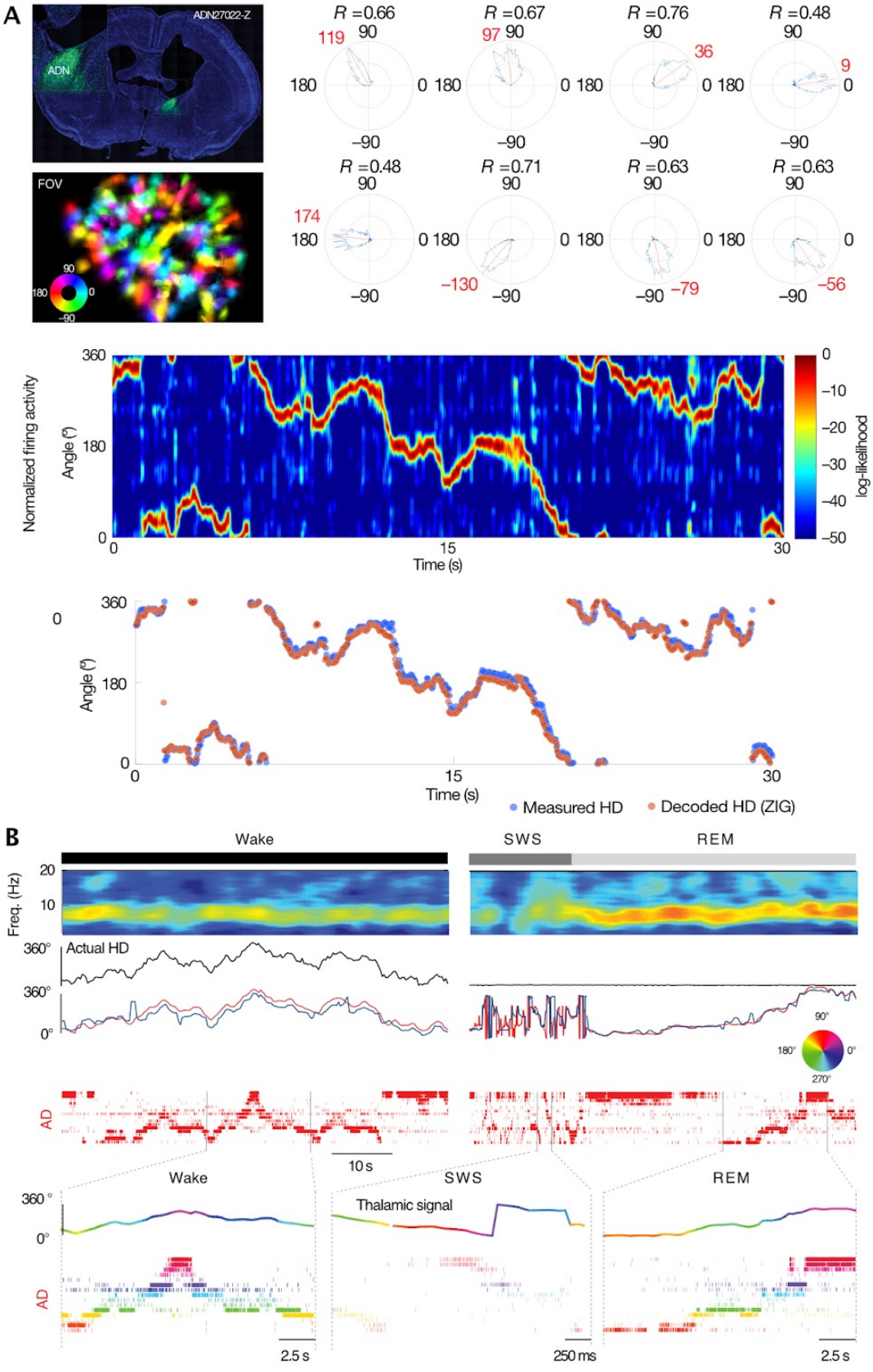
A
ADN27022-Z
ADN
FOV
R =0.66
R =0.67
R =0.76
R =0.48
R =0.48
R =0.71
R =0.63
R =0.63
Normalized firing activity
Angle (°)
Time (s)
log-likelihood
Measured HD
Decoded HD (ZIG)
B
Wake
SWS
REM
Freq. (Hz)
Actual HD
AD
10 s
Thalamic signal
2.5 s
250 ms
2.5 s

Figure 5.2 HD activity in the AD.

A) General HD cell activity in mouse AD, based on calcium imaging with GCaMP6f. Adapted from Ajabi et al. (2023). Top left: GCaMP6f expression in the AD for the calcium imaging. The field of view in AD presenting the PFD for each Region of interest (ROI). The PFDs are not topographically organised. Top right: Tuning curves of 8 example ROIs. Red numbers indicate the PFD of each ROI and vector length, R, denotes the strength of directional tuning. Bottom: HD decoding. The upper panel shows the log-likelihood distribution for decoded HD and the lower panel displays both measured HD (blue) and decoded HD (red) traces.
B) HD activity of AD neurons across brain states. Adapted from Peyrache et al. (2015). Top: Local field potential (LFP) spectrograms recorded from the PrS. The actual HD is shown as a black line. The reconstructed HD was obtained using Bayesian decoding of AD (red) and PrS (blue) activity, and is shown for awake, Slow-wave sleep (SWS), and REM sleep states. Bottom: Raster plots of AD neuron spiking activity. The order of HD cells activation is preserved across the brain states.

5.3 The origin of the HD signal and its progression in the network

Based on lesion studies described above, it is well established that HD activity in the AD originates from upstream LMN and DTN. The vestibular system plays a critical role in generating HD signals: HD activity in the AD is abolished following vestibular damage induced by neurotoxic lesions to the labyrinth in rats (Stackman & Taube, 1997) and by disruption of the semicircular canals in chinchillas (Muir et al., 2009). In these studies, AD neurons exhibited random, periodic bursting activity that was not aligned with the animal's heading direction. Similar unaligned bursting was also observed in transgenic mice with otolithic dysfunction (Yoder & Taube, 2009). Furthermore, optogenetic inhibition of neurons in the NPH that project to the DTN led to a reduction in HD activity in the AD (Butler et al., 2017). Taken together, these findings suggest that vestibular input, relayed through the NPH and MVN, is critical for HD signal generation.

Then, how is the HD signal processed across multiple brain regions throughout the network? One way to approach this question is to examine the firing properties of HD cells in each region. Two key features that help evaluate this processing are the tuning curve width and the Anticipatory time interval (ATI). The ATI reflects how far in advance HD cells fire relative to the animal's actual head orientation. Both features vary systematically along the HD circuit and reveal a functional hierarchy of directional processing.

Subcortical HD regions that are anatomically closer to vestibular inputs typically exhibit broader tuning curves and longer ATIs. For instance, HD cells in the LMN show ATIs of approximately 95 ms or 40 ms (H. T. Blair et al., 1998; Stackman & Taube, 1998), indicating that they predict HD well ahead of actual movement. In the AD, HD cells display slightly shorter ATIs, around 49 ms (Stackman et al., 2003) and 20 ms (H. Blair & Sharp, 1995; H. T. Blair et al., 1997; J. S. Taube & Muller, 1998). Further downstream, cortical regions such as the RSC and PrS show progressively shorter ATIs, consistent with their reception of more

indirect vestibular input. RSC HD cells anticipate by 25 ms (Cho & Sharp, 2001) or 48 ms (Lozano et al., 2017). In contrast, HD cells in the PrS typically reflect current head direction, with ATIs of approximately 15 ms (Lozano et al., 2017) or near zero (H. Blair & Sharp, 1995; J. S. Taube & Muller, 1998). This gradual reduction in ATI along the HD circuit suggests a temporal hierarchy, where HD cells in LMN update first, followed by AD and RSC, and finally PrS. This cascade enables the HD system to integrate incoming vestibular signals with increasing refinement across brain regions.

HD cells in several regions also exhibit AHV-dependent shifts in their preferred firing direction. This means the tuning curve of a single HD cell can differ slightly depending on whether the animal is turning clockwise or counterclockwise. Such shifts have been observed in the LMN, AD, and RSC (H. Blair & Sharp, 1995; H. T. Blair et al., 1998; P. E. Sharp, Blair & Cho, 2001; Stackman & Taube, 1998; J. S. Taube & Muller, 1998). In each case, tuning curves derived from clockwise turns are typically shifted to the left of those from counterclockwise turns. The shift is more pronounced in LMN cells than in those of AD or RSC, consistent with LMN's position closer to vestibular sources within the HD circuit (H. T. Blair et al., 1998; Stackman & Taube, 1998). This suggests that LMN neurons integrate motion cues more strongly and earlier than downstream areas, where the influence of AHV becomes attenuated. In contrast, HD cells in the PrS show no such shift, indicating they encode instantaneous HD rather than predictive or velocity-integrated signals (H. Blair & Sharp, 1995).

The explanation of HD signal development and propagation supports again the conventional hierarchical HD network described earlier. Vestibular information, primarily from the semicircular canals, ascends through brainstem vestibular structures (MVN, NPH) to the DTN, which forms a reciprocal loop with the LMN. Within this loop, AHV signals are integrated to generate the HD signal. The signal is then transmitted to the AD and subsequently to HD cortical areas such as RSC, PrS, and MEC, where it supports higher-level spatial computations.

A

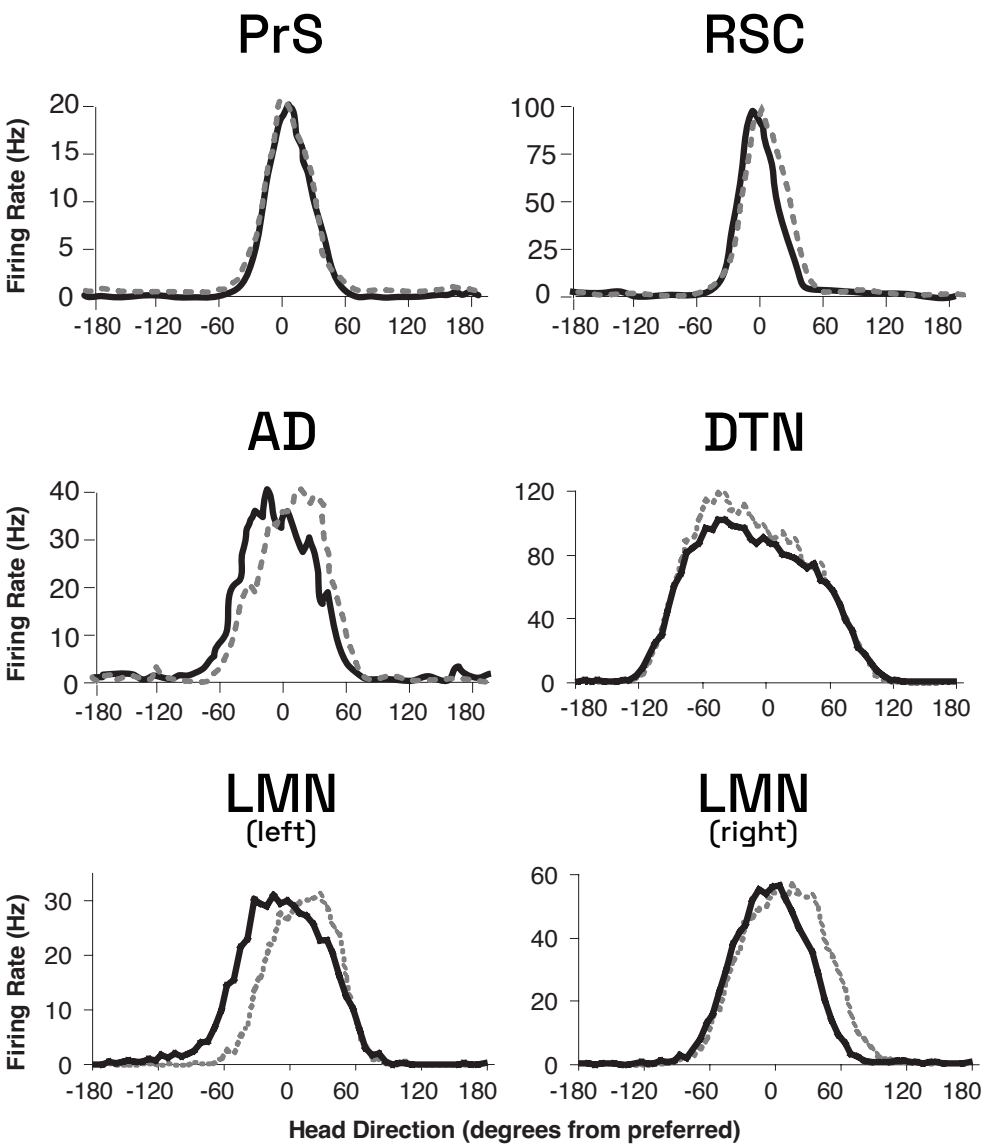

B

Regions	Tuning width (degrees)	Peak rate (Hz)	ATI (msec)
RSC	44.6 (2.7)	32.3 (10.7)	25.1 (3.3)
PrS	65.3 (3.6)	26.7 (3.2)	- 7.70 (5.6)
AD	57.4 (2.4)	50.3 (6.0)	23.2 (3.4)
LMN	79.9 (3.5)	37.2 (5.5)	38.5 (3.2)
DTN	109.4 (6.8)	47.0 (15.6)	~ 0.0

Figure 5.3 HD signal properties across brain regions.

A) Tuning curves of HD cells in different brain regions. Solid lines represent clockwise head turns and dashed lines represent counterclockwise turns.
B) Summary of directional firing properties of HD cells in each region. All recreated based on the figure proposed by Wiener and Taube (2005)

We have focused on the thalamocortical pathway in the HD system. However, the AD also receives inputs from both the RSC and the PrS. Lesion studies highlight the importance of the RSC–AD pathway. Damage to the RSC disrupts the stability of HD signals in the AD and reduces the influence of visual landmarks on directional tuning (Clark et al., 2010). This suggests that the RSC delivers top-down visual and contextual information that helps anchor the HD representation to external cues. In addition, recent work has identified a direct projection from the PrS to the ATN (The subnucleus is not specified), originating from deep-layer V–VI pyramidal neurons with high input resistance and low firing adaptation (Huang et al., 2017). These neurons are distinct from the presubicular layer IV bursting cells that project to the LMN, suggesting that the PrS contributes to the HD system through different output pathways. This organisation potentially allows visual information from the PrS to reach the AD both directly, through a slower monosynaptic route, and indirectly, through a faster disynaptic PrS–LMN–AD pathway (Huang et al., 2017; Richevaux et al., 2025).

5.4 Modulatory inputs to the AD

In addition to its main excitatory inputs, the AD receives several modulatory influences that may shape HD signal processing. GABAergic neurons in the TRN represent a critical inhibitory source to the AD (Figure 5.4A). The TRN neurons projecting to the AD are Parvalbumin (PV)-positive (Fujita et al., 2022) and/or GABAergic (Gonzalo-Ruiz & Lieberman, 1995). The inhibitory input from the TRN to the AD is mediated via feedforward inhibition originating from PrS/RSC (Figure 5.4B) (Vantomme et al., 2020). Channelrhodopsin expressed in the PrS and RSC can evoke synaptic inputs onto neurons in the TRN, AD, and AV. AD and AV neurons exhibit Excitatory postsynaptic current (EPSC)s with short latencies, indicative of monosynaptic excitatory inputs directly from cortical regions, whereas Inhibitory postsynaptic current (IPSC)s have longer latencies, suggesting they are evoked disynaptically through TRN neurons receiving glutamatergic inputs from PrS and RSC. Both Somatostatin (SST)-positive and PV-positive TRN neurons showed the same effect. Furthermore, inhibitory inputs from the TRN influence HD signals in AD HD cells. Inhibition of TRN neurons impairs HD tuning properties by increasing tuning width, suggesting that TRN-mediated inhibition is essential for precise directional tuning, even though the PFD remains intact in the AD (Figure 5.4C). Additionally, inhibition of the TRN changes the animal's navigational strategies, while it doesn't abolish it (Vantomme et al., 2020).

Another potential modulatory source is the cholinergic system. Anatomical tracing has shown that neurons from the LDT and the Pedunculopontine nucleus (PPN) project to the AD (Gonzalo-Ruiz et al., 1995; Satoh & Fibiger, 1986). However, there is rather no clear evidence whether the projections are cholinergic, while both brainstem regions are known for containing cholinergic neurons. Gonzalo-Ruiz et al. (1995) and Hallanger et al. (1987) rather mentioned that the AD is devoid of cholinergic afferents. On the contrary, a cholinergic modulation in the AD has been suggested by Yoder et al. (2017) (Figure 5.4D). The authors investigated the effects of systemic muscarinic receptor blockade using atropine. They found that atropine significantly reduced the peak firing rate of HD cells in the AD, while directional tuning width and responsiveness to visual cue rotation remained largely unaffected. However, in the absence of visual cues, atropine disrupted the stability of HD cell activity during path integration. These findings suggest that acetylcholine does not shift the core directional preference but instead fine-tunes the stability and robustness of HD signals when the brain relies on self-motion cues. Even though it is not clear where the cholinergic source region is and whether the cholinergic input directly influences the AD, the functional study supports the cholinergic effect on the directional coding in the AD.

Another inhibitory input arises from the hippocampal CA3 region (Vetere et al., 2021). This reinforces the memory consolidation through CA3–AD connectivity. However, this does not support enough evidence whether the hippocampal inhibitory input contributes to the modulation of HD activity.

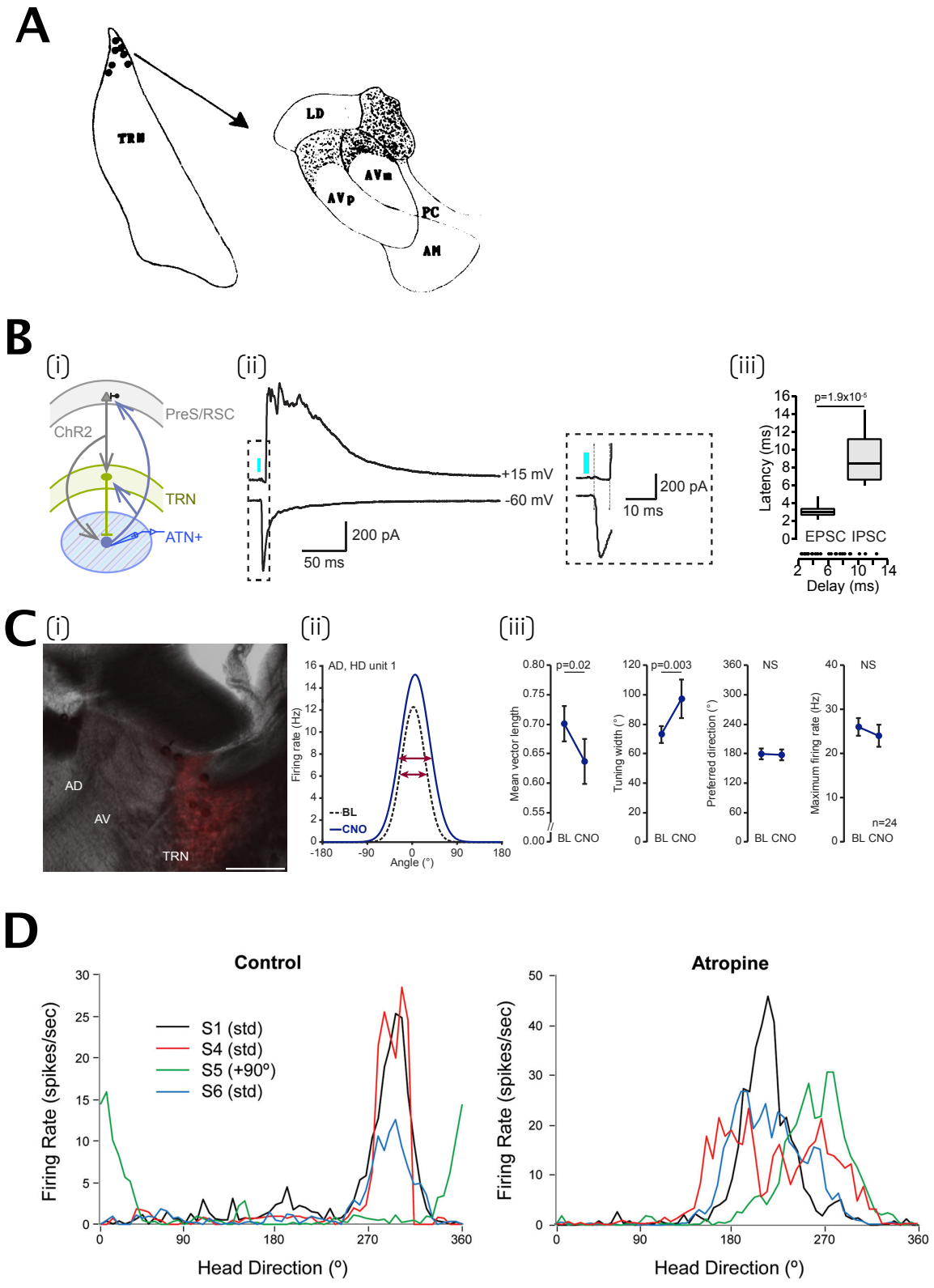
A
TRN
LD
AVm
AVp
PC
AM
B
(i)
ChR2
PreS/RSC
TRN
ATN+
(ii)
+15 mV
-60 mV
200 pA
50 ms
200 pA
10 ms
(iii)
p=1.9x10-5
Latency (ms)
EPSC IPSC
Delay (ms)
C
(i)
AD
AV
TRN
(ii)
AD, HD unit 1
Firing rate (Hz)
BL
CNO
Angle (°)
(iii)
p=0.02
Mean vector length
BL CNO
p=0.003
Tuning width (°)
BL CNO
NS
Preferred direction (°)
BL CNO
NS
Maximum firing rate (Hz)
n=24
BL CNO
D
Control
S1 (std)
S4 (std)
S5 (+90°)
S6 (std)
Firing Rate (spikes/sec)
Head Direction (°)
Atropine
Firing Rate (spikes/sec)
Head Direction (°)

Figure 5.4 Modulatory inputs to the HD cells in AD.

A) The anatomical projection of GABAergic dorsal TRN neurons to the AD and dorsal AV. Figure adapted from Gonzalo-Ruiz and Lieberman (1995).
B) Postsynaptic response in the ATN (both AD and AV) following optogenetic stimulation of projecting neurons originating in the PrS and RSC: (i) Diagram of experimental design. (ii) EPSC and IPSC traces evoked by photostimulation. EPSCs were recorded with the cells held at -60 mV, and IPSCs at +15 mV. The dashed box highlights the delayed onset of the IPSCs relative to the onset of photostimulation. (iii) Latency plot of EPSCs and IPSCs recorded in ATN neurons. Figure adapted from Vantomme et al. (2020)
C) Disruption of TRN activity with Human muscarinic receptor 4 (designer receptor) (hM4D) during HD activity in AD. (i) Expression of the inhibitory hM4D shown in red in TRN. (ii) Example AD tuning curves at baseline and Clozapine-N-oxide (CNO) condition show increased tuning width and decreased peak firing rate. (iii) Population summary comparing baseline and CNO condition: mean vector length, tuning width, preferred direction, and maximum firing rate. TRN inhibition significantly decreases vector length and increases tuning width, with a reduction in peak firing rate, while preferred direction is unchanged. Figure adapted from Vantomme et al. (2020).
D) Tuning curves of AD neurons under control condition and atropine application. The colour of each line indicates the experimental phase during cue card rotation. After atropine application, the tuning curves broaden and show a reduced firing rate, while the PFD remains approximately preserved. Figure adapted from Yoder et al. (2017)

6 AV and the theta modulated head direction cells

The AV has traditionally received less attention in HD research, often being grouped together with the AD, described as broader ATN in functional studies. Its role within the HD system has remained unclear for many years, as most studies focused on AD as the principal thalamic nucleus for HD processing. However, AV exhibits distinct anatomical connectivity that sets it apart from HD, suggesting complementary rather than identical contribution. More recently, interest in AV has grown due to its prominent rhythmic HD activity.

6.1 Anatomical connectivity

The AV possesses a more complex connectivity compared to the AD. First, AV receives mammillary input from the Medial mammillary nucleus (MMN) (Dillingham et al., 2015; Jankowski et al., 2013; Umaba et al., 2021), with current evidence supporting a primarily ipsilateral projection (Cruce, 1975; Dillingham et al., 2015; Seki & Zyo, 1984; H. Shibata, 1992; Veazey et al., 1982; Wiener & Taube, 2005). Next, the AV forms reciprocal connections with both gRSC and dRSC, as well as the PrS (H. Shibata, 1993a, 1993b; H. Shibata & Naito, 2005; Van Groen & Michael Wyss, 1990; Van Groen & Wyss, 1995, 2003; Wright et al., 2010). AV sends projections to the PaS (H. Shibata, 1993a), while there are no reports of reciprocal connectivity. It also receives inputs from the LDT and the Sub (Satoh & Fibiger, 1986; Van Groen & Wyss, 1990b; Wright et al., 2010). Additionally, AV is reciprocally connected with the TRN (Fujita et al., 2022; Gonzalo-Ruiz & Lieberman, 1995; H. Shibata, 1992), secondary Motor cortex (MC) (H. Shibata & Naito, 2005), and ACC (H. Shibata, 1993b; H. Shibata & Naito, 2005). It receives afferents from the Prelimbic area (PL) (Wright et al., 2013). AV also projects to the EC (H. Shibata, 1993a).

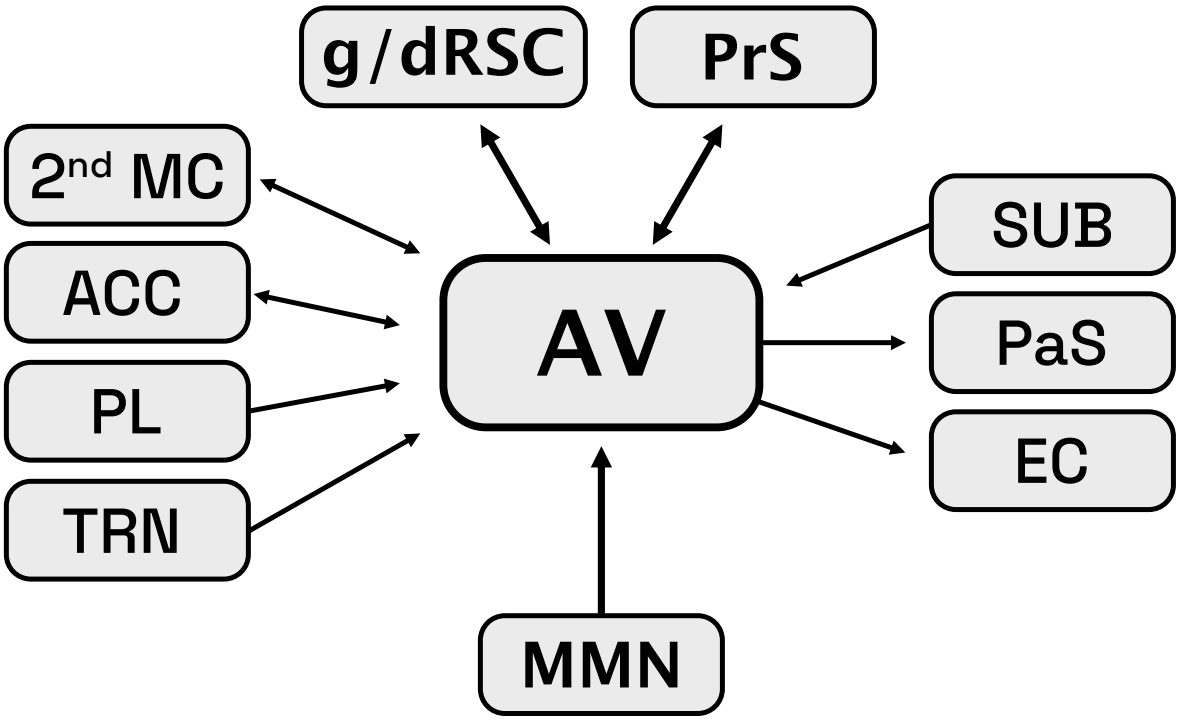

Figure 6.1 The anatomical connectivity of the AV.

Recreated based on the figure proposed by Nelson (2021).

I found contradicting descriptions on mammillothalamic pathways to the AV (Figure 6.2). The MMN is generally further subdivided into lateral (Medial mammillary nucleus pars lateralis (MML)) and medial (Medial mammillary nucleus pars medialis (MMM)) portions. According to David A. Hopkins Sidney (Wiener & Taube, 2005), the MMM projects to the Anteroventral thalamic nucleus, dorsomedial subdivision (AVDM), while the median (Medial mammillary nucleus pars medianus (Me), even more mediodorsal than the MMM) portion project to the Interanteromedial thalamic nucleus (IAM), and the MML projects to the Anteroventral thalamic nucleus, ventrolateral subdivision (AVVL) and AM (Figure 6.2A). However, in the review paper by Jankowski et al. (2013), the authors described the MMM as projecting only to the AM, while the MML projects to the AV. I followed the original citation (Watanabe & Kawana, 1980), but the full text was not available. The abstract states that the MML and Medial mammillary nucleus pars posterior (MMP) project to the AV, while the MMM projects to the AM. It also notes that the primary projection is ipsilateral, although sparse contralateral projections exist. Dillingham et al. (2015) also describe MML-AV and MMM-AV connectivity in their diagram (Figure 6.2B), although the text states that the MMN projects to both AV and AM. I followed the citations that were used in this paper (Cruce, 1975; Seki & Zyo, 1984; Vann et al., 2007). In Cruce (1975), tritiated leucine was injected into the whole bilateral MMN for anterograde labelling, showing strong projections to the AV and AM in rats (Figure 6.3A). In Seki and Zyo (1984), retrograde labelling was performed by injection Bisbenzimide blue (Bb) and Evans blue (Eb) into the AV and AM, respectively, in rats (Figure 6.3B). AM-projecting medial mammillary neurons were concentrated in the central MMM (Mmc), while AV-projecting medial mammillary neurons were observed in the dorsal MMN (Mmd). Lastly in Vann et al. (2007)'s study, the Bisbenzimide R h 5 (BRh5) was injected into the AV for retrograde tracing in macaque monkeys, and labelled cells were observed through the ipsilateral MMN, with sparse labelling in the contralateral side (Figure 6.3C). In summary, although the anatomical connectivity between the MMN and AV is not yet uniformly defined, the evidence suggests that the entire MMN including MML and MMM may project to the ipsilateral AV, with sparse projections to the contralateral side.

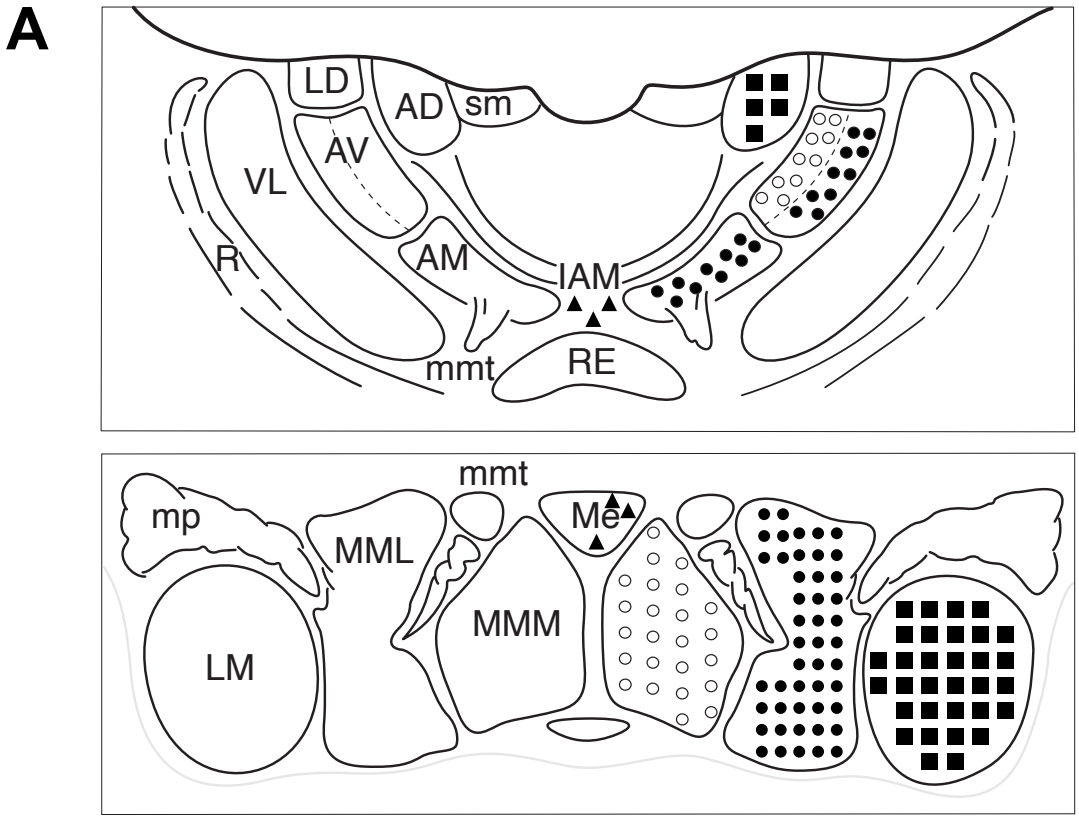
A
LD
AD
sm
AV
VL
R
AM
IAM
mmt
RE
mmt
mp
MML
Me
MMM
LM
B
Fornix
Anterior thalamus
AD
AV
LD
Postsubiculum
Prefrontal cortex
AM
Dorsal subiculum
Hippocampal formation
Medial septum
MTT
PCF
DTg
Gudden's tegmental nuclei
Mammillary bodies
LM
ML
MM
ML
LM
VTg
mtg
MP

Figure 6.2 Differently reported mammillothalamic tract.

A) Mammillothalamic tract as suggested by David A. Hopkins. This shows the projection from MMN to AVDM. Figure adapted by Wiener and Taube (2005).
B) Mammillothalamic tract as suggested by Dillingham et al. (2015). In their diagram, MMM (labelled MM in the figure) projects only to the AM, not to the AV, while MML (labelled ML in the figure) projects to the AV. These projections are described as ipsilateral only, while LMN (labelled LM) projects bilaterally to the AD.

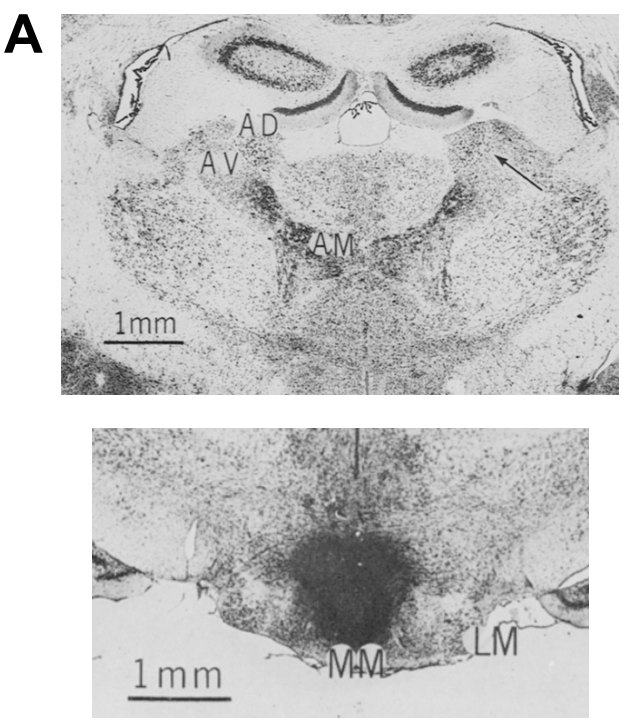
A
AD
AV
AM
1mm
MM
LM
1mm
B
Bb
st
Avm
Ad
sm
Eb
Pt
Pvt
Avp
Am
Cl
Rt
Reu
mt
f
Mmc
L
Ml
1
SUM
Cl
mt
Mmc
L
Ml
Mmd
Mb
2
rt
SUM
Cl
mp
Mmc
Mmd
L
Ml
Mb
3
rt
SUM
Cl
mp
Mmd
Ml
Mb
4
C
BRh5 (Fb-l)
11.0
BRh5 (Fb-l)
10.0

Figure 6.3 Anatomical tracing results showing mammillary afferents to the AV.

A) MMN (labelled MM in the figure) projections to the AV and AM in the rat brain. Bottom: Injection site in the MMN with tritiated leucine for anterograde labelling. Top: labelled afferents in the ventral AV and AM. Figure adapted from Cruce (1975).

B) Retrograde labelling in the rat brain by Bb injection in the AV and Eb injection in the AM. AM-projecting neurons are predominantly located in the Medial mammillary nucleus pars centralis (Mmc), while the AV-projecting neurons are distributed across the rest of the MMN. The labelling observed in the LMN is likely due to spread of the Bb injection into the AD. Figure adapted from Seki and Zyo (1984)

C) Retrogradely labelled medial mammillary neurons following BRh5 injection into the AV of the macaque monkey brain. The large central circular structures indicate MMN, while the smaller lateral circular structures indicate the LMN. Numbers denote the anterior-posterior level. Figure adapted from Vann et al. (2007).

6.2 Theta rhythm in the AV

The AV is centrally positioned within limbic circuitry. It forms part of a return-loop thought to sustain rhythmic theta activity toward the hippocampal formation. Single-unit recordings under urethane anaesthesia revealed that a large proportion of AV neurons (up to 75%) discharge rhythmically and in synchrony with both LFP and hippocampal CA1 theta oscillations (Figure 6.4) (Albo, 2003; R. Vertes et al., 2001). Such rhythmic discharge patterns were distinct in the AV because they were far less common in neighbouring thalamic nuclei such as the AD (12%) and AM (6%) (Albo, 2003; R. Vertes et al., 2001). A high proportion of AV neurons are characterised as theta-bursting neurons in slow and fast spiking activities (Tsanov, Chah, Vann et al., 2011; Tsanov, Chah, Wright et al., 2011; Welday et al., 2011). This theta-rhythmic firing (typically 4-12 Hz) was later supported by recordings from freely behaving rats, where a subset of AV neurons exhibited robust theta-bursting activity during exploration and REM sleep, consistent with earlier findings in anaesthetised animals (Tsanov, Chah, Wright et al., 2011). Interestingly, the most prominent bursting segments typically consisted of 3 to 5 spikes. Simultaneous recordings from hippocampal CA3 and AV revealed a high degree of coherence in the 7–10 Hz range, with AV theta activity preceding hippocampal theta by 7–10 ms (Tsanov, Chah, Wright et al., 2011). This phase lead suggests a potential influence of AV activity on hippocampal theta generation. Together, these electrophysiological findings demonstrate that the AV nucleus exhibits robust theta-rhythmic activity across brain states and experimental conditions. The presence of this rhythmic firing appears to be a distinguishing feature of AV compared to other ATN subnuclei, and provides a physiological marker for its identification *in vivo*.

Through its bridging position within the limbic system, the AV may coordinate theta activity by firing rhythmically in synchrony with hippocampal theta oscillations. The MMN, which provides the primary input to the AV, is composed of a high proportion of neurons firing at theta frequency (Bland et al., 1995; Kirk et al., 1996; Kocsis et al., 2001). This region integrates afferents from the Ventral tegmental nucleus of Gudden (VTN) and the MS (Dillingham et al., 2015; Gonzalo-Ruiz et al., 1992). Both regions are involved in the modulation of hippocampal theta activity (King et al., 1998; Kocsis et al., 2001; R. P. Vertes et al., 2004). First, the majority of VTN neurons exhibit theta-rhythmic firing, and notably, their rhythmic bursting often precedes the onset of hippocampal theta by 1–2 seconds (Bassant & Poindessous-Jazat, 2001; Kocsis et al., 2001). This raises the possibility that the VTN contributes to the initiation or pacing of hippocampal theta via its connections with the MMN. Supporting this, lesions targeting the supramammillary nucleus and adjacent MBO have been shown to reduce both the frequency and amplitude of theta firing in the hippocampus (P. E. Sharp & Koester, 2008; Thinschmidt et al., 1995). Second, inactivation of the MS disrupts theta-rhythmic firing in the hippocampus and MMN, but does not fully abolish such rhythmic activity in the parahippocampal region (Brandon et al., 2013). This suggests that the AV may act as a source of theta oscillations to the parahippocampal region when septal theta input is absent. Taken together, these findings suggest that the AV may receive theta inputs from two sources - the MS and brainstem - and relay them to downstream targets. Pharmacological inactivation of the MMN and AV leads to reductions in hippocampal theta power at lower (3–5 Hz) and mid (6–8 Hz) frequency bands, respectively (Żakowski, 2017). This supports the view that the AV contributes to hippocampal

theta activity in a frequency-specific manner, extending beyond a simple relay function.

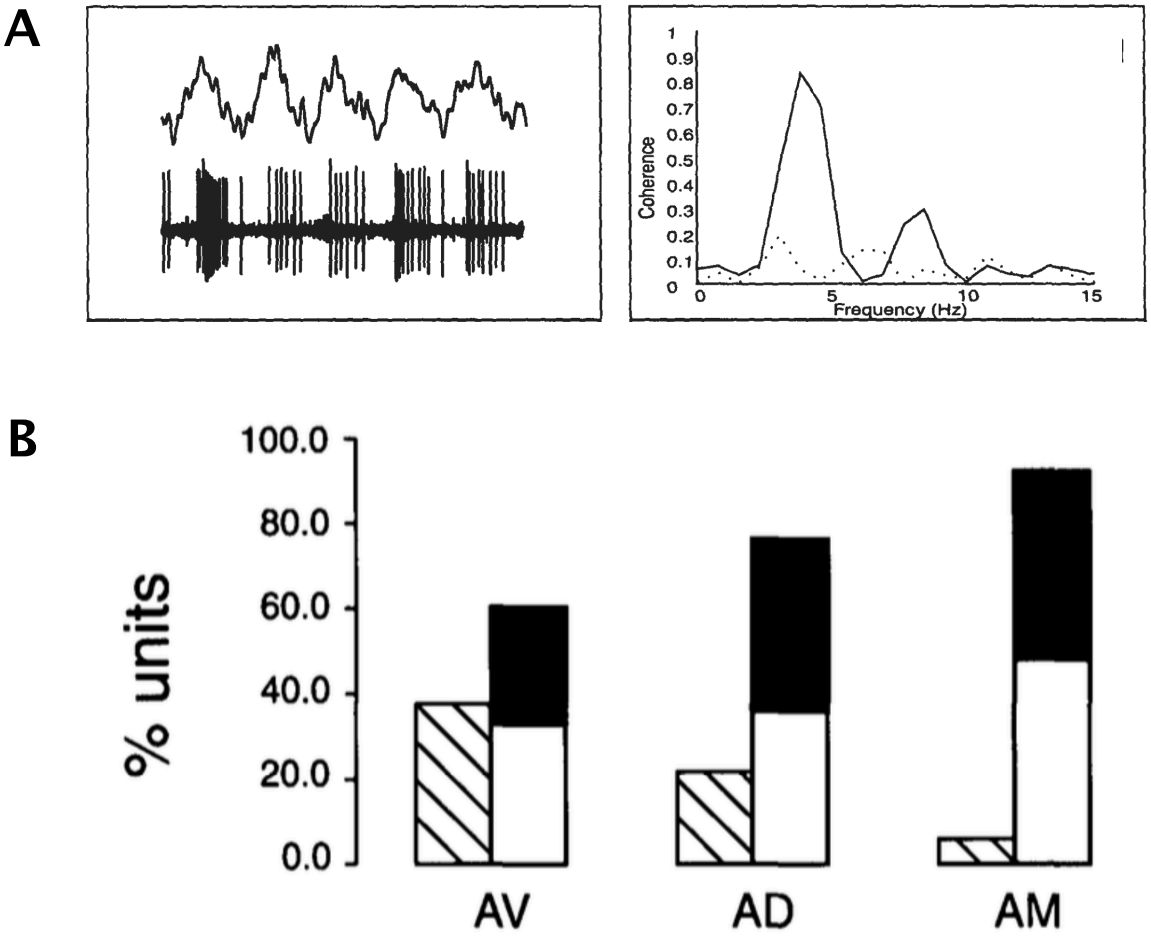

Figure 6.4 Rhythmic firing of AV neurons.

A) Left: The top trace shows hippocampal Electroencephalography (EEG) recordings and the bottom trace shows unit activity from an AV neuron. The AV neuron exhibits rhythmic firing that is synchronous with the hippocampal theta oscillation. Right: Unit spikes–EEG traces coherence of a AV neuron during theta (solid line) and control (dashed line) conditions. The firing frequency shows significant coherence with the theta phase.
B) Proportion of thalamic neurons classified by their rhythmic firing at theta frequency: strongly rhythmic (diagonal striped box), moderately rhythmic (white box), and non-rhythmic (black box). All figures adapted and reorganised from Albo (2003).

6.3 Theta rhythms in spatial navigation: Implications for HD coding in the AV

The theta rhythm plays a critical role by temporally structuring neural activity across brain regions involved in spatial navigation and memory (Buzsáki, 2005). It generally organises the activity of spatially tuned neurons such as place cells in the hippocampus (O'Keefe & Dostrovsky, 1971), grid cells in the MEC (Hafting et al., 2005), border cells in the MEC and PaS (Savelli et al., 2008; Solstad et al., 2008), and HD cells (Ji, Lomi et al., 2025; Lomi et al., 2023; Tsanov, Chah, Vann et al., 2011). These neurons are thought to enable the integration of self-motion and environmental information, allowing for both path integration and allocentric mapping (Etienne & Jeffery, 2004; McNAUGHTON et al., 1996). Throughout the spatial system, the theta rhythm provides a temporal framework that organises neural activity across several key brain regions (Buzsáki, 2005). It allows neuronal assemblies to group events together within defined temporal periods. Such a temporal mechanism provides a means to compress neuronal activity sequences within single theta cycles, facilitating synaptic plasticity and the organised progression of neuronal activity. Thus, the theta rhythm is fundamental for synchronising neuronal activity across space and time, underpinning both navigation and the formation of episodic memories.

The existence of HD cells in the AV is debatable and ambiguous (Calton et al., 2003; J. S. Taube, 2007). However, a few recent studies have reported HD activity in this region. The first report of directional activity in AV neurons came from Tsanov, Chah, Vann et al. (2011), who recorded from the medial portion of the AV (Figure 6.5A). They found that 69% of recorded units were directionally tuned, and 39% of these HD cells were modulated at theta frequency (6–12 Hz). These cells were categorised as HD-by-theta cells. Also, Yoganarasimha et al. (2006) reported directionally tuned cells in the AV. More recently, Lomi et al. (2023) provided a detailed anatomical delineation of the AVDM) and AVVL subdivisions of the AV, based on their projection targets in the granular and dysgranular RSC (AVDM–gRSC and AVVL–dRSC, respectively). They identified three types of AV neurons: HD cells, theta-modulated cells, and HD-by-theta cells (Figure 6.5B). The distribution of these cell types varied between subdivisions: HD cells and theta-modulated cells were more abundant in the AVDM, while HD-by-theta cells were more prominent in the AVVL. Additionally, they observed place cells in both subdivisions, with a higher prevalence in the AVVL.

Ji, Lomi et al. (2025) further classified theta-modulated HD cells into two categories: those exhibiting theta skipping, firing on alternate theta cycles (Figure 6.5C), and those without theta skipping. Theta-modulated HD cells with theta skipping showed significantly stronger theta phase precession relative to the turning angle compared to non-skipping cells. Statistical analysis confirmed that theta-skipping HD cells are more strongly associated with phase precession. The authors explain the relationship between theta skipping and phase precession using a ring attractor network model, intrinsic mechanism, and firing rate adaptation (Ji, Chu et al., 2025). In this model, during head turns, an internal bump representing HD sweeps forward along the direction of rotation, generating phase precession at the single-cell level. In contrast, during periods of straight movement, the internal bump performs bidirectional sweeps, resulting in theta skipping. Consequently, theta skipping is closely associated with pronounced phase precession. Theta-modulated HD cells without skipping exhibit weaker phase precession, resembling classical HD cells. Interestingly, both

categories of theta-modulated HD cells have broader directional tuning curves compared to classical HD cells.

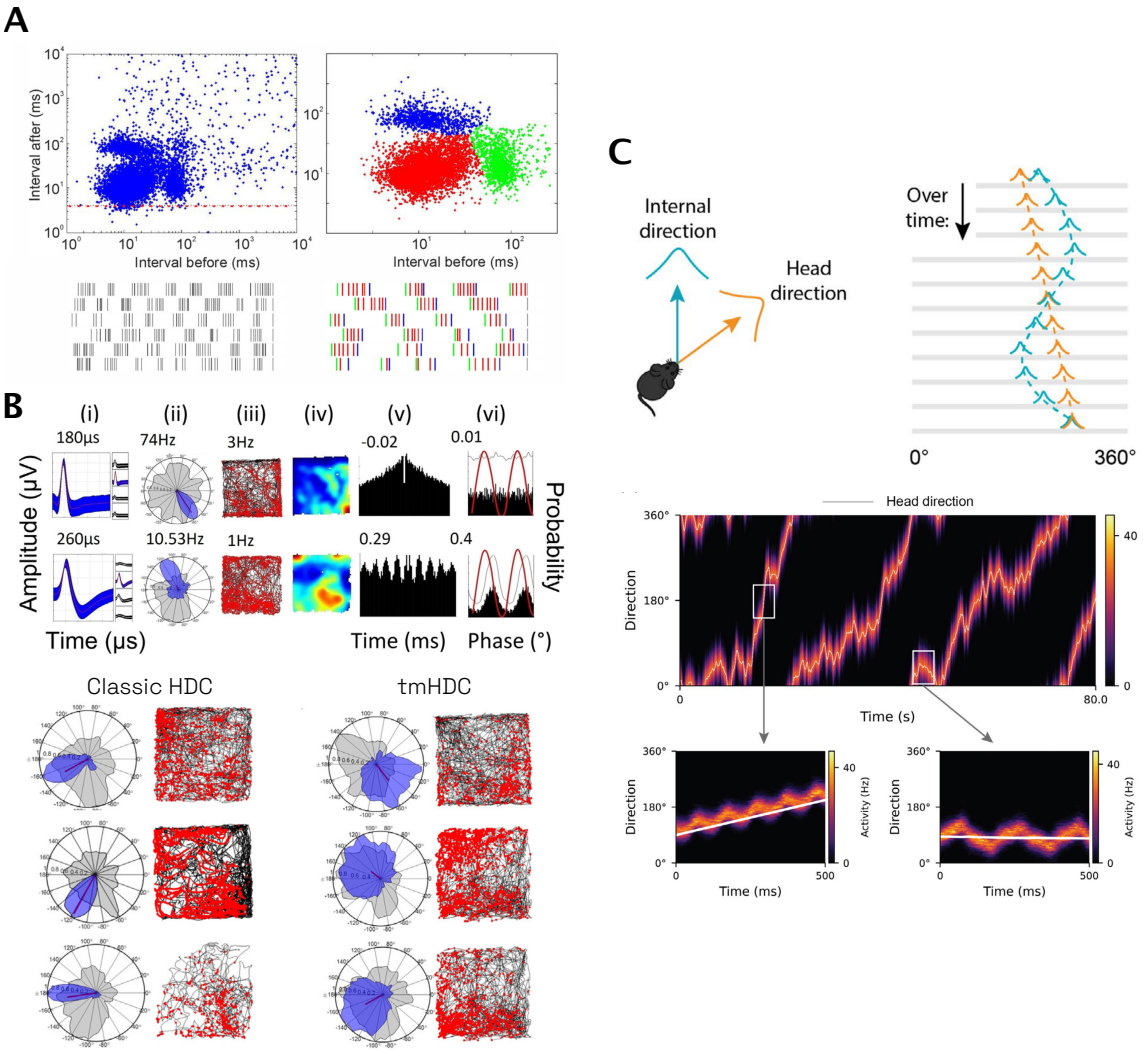

Figure 6.5 HD activity in the AV.

A) Theta-phasic activity of HD cells in the AV. Top: 2D log-scale scatter plot of inter spike intervals for each spike in a theta-by-HD cell, showing the time since the previous spike (pre-spike interval) versus the time to the next spike (post-spike interval). The data show three distinct clusters: green indicates spikes preceded by long intervals, red indicates spikes with short pre- and post-spike intervals, and blue indicates spikes followed by long intervals. Bottom: Raster plot of all spikes from the same neuron, showing that each burst of spike trains is temporally organised in theta rhythm. Figures adapted and reorganised from Tsanov, Chah, Vann et al. (2011).

B) Classical and theta modulated HD cells in the AV. Top: Analysis of a classical HD cell (top row) and a theta-modulated HD cell (bottom row) recorded in the AV. (i) Averaged tetrode waveforms. (ii) Polar plots showing firing rates across HD (blue) and dwell time across HD (grey). (iii) Spike activity overlaid on the animal's trajectory within the arena. (iv) Heatmap of mean firing rate. (v) Autocorrelogram with corresponding rhythmicity index. (vi) Histogram of spike probability relative to theta phase (red line). Bottom: Additional examples of polar plots and rate maps during light-on exploration. The left column shows three classical HD cells, and the right column shows three theta-modulated HD cells. Figures adapted and reorganised from Lomi et al. (2023).

C) Theta-phase skipping HD activity in the AV. Top: Schematic diagram illustrating theoretical theta-phase sweeping of the activity bump with attractor dynamics. The animal's internal representation of HD shifts rhythmically within each theta cycle, sweeping across adjacent directions along the physical HD. Bottom: Visualisation of theta-phase sweeping aligned to the animal's HD. The light line indicates the physical HD, while the colour-coded heatmap shows the theta–modulated internal representation. Below, the internal sweeping activities along the rotation of the animal during the high effect of angular head velocity (left) and fixed head with subtle angular head velocity (right) are shown. Figures adapted and reorganised from Ji, Lomi et al. (2025).

6.4 Modulatory inputs to the AV

The AV receives diverse modulatory inputs from multiple brain regions. As for the AD, GABAergic neurons in the dorsal TRN also project to the dorsal portion of the AV (Gonzalo-Ruiz & Lieberman, 1995) (Figure 6.6 A). There is also feedforward inhibition from the TRN via excitatory input from the PrS and RSC (Vantomme et al., 2020). These GABAergic TRN neurons are concentrated in the dorsal part of the TRN and exhibit a topographic organisation: the dorsal portion of the dorsal TRN projects to the dorsal AV, while the ventral portion of the dorsal TRN projects to the ventral AV.

Cholinergic modulation is also expected in the AV. Immunohistochemical staining shows a dense distribution of Choline acetyltransferase (ChAT)-positive fibres and terminals, particularly in the AVVL, indicating potential cholinergic input (M. Parent & Descarries, 2008; Sofroniew et al., 1985). Anatomical studies suggest that the PPN and LDT are likely cholinergic sources (Gonzalo-Ruiz et al., 1995; Hallanger et al., 1987)(Figure 6.6B-D), along with the diagonal band nucleus of Broca in the basal forebrain, in the cat (A. Parent et al., 1988). Furthermore, electron microscopy has revealed putative ChAT-positive axon terminals in the AV, with apparent synaptic contacts onto dendritic structures (Hallanger et al., 1990).

Lastly, noradrenergic modulation may also influence AV neurons. Noradrenaline has been shown to depolarise membrane potentials in thalamic neurons, suggesting a modulatory effect on AV excitability (McCormick & Prince, 1988) (Figure 6.6E).

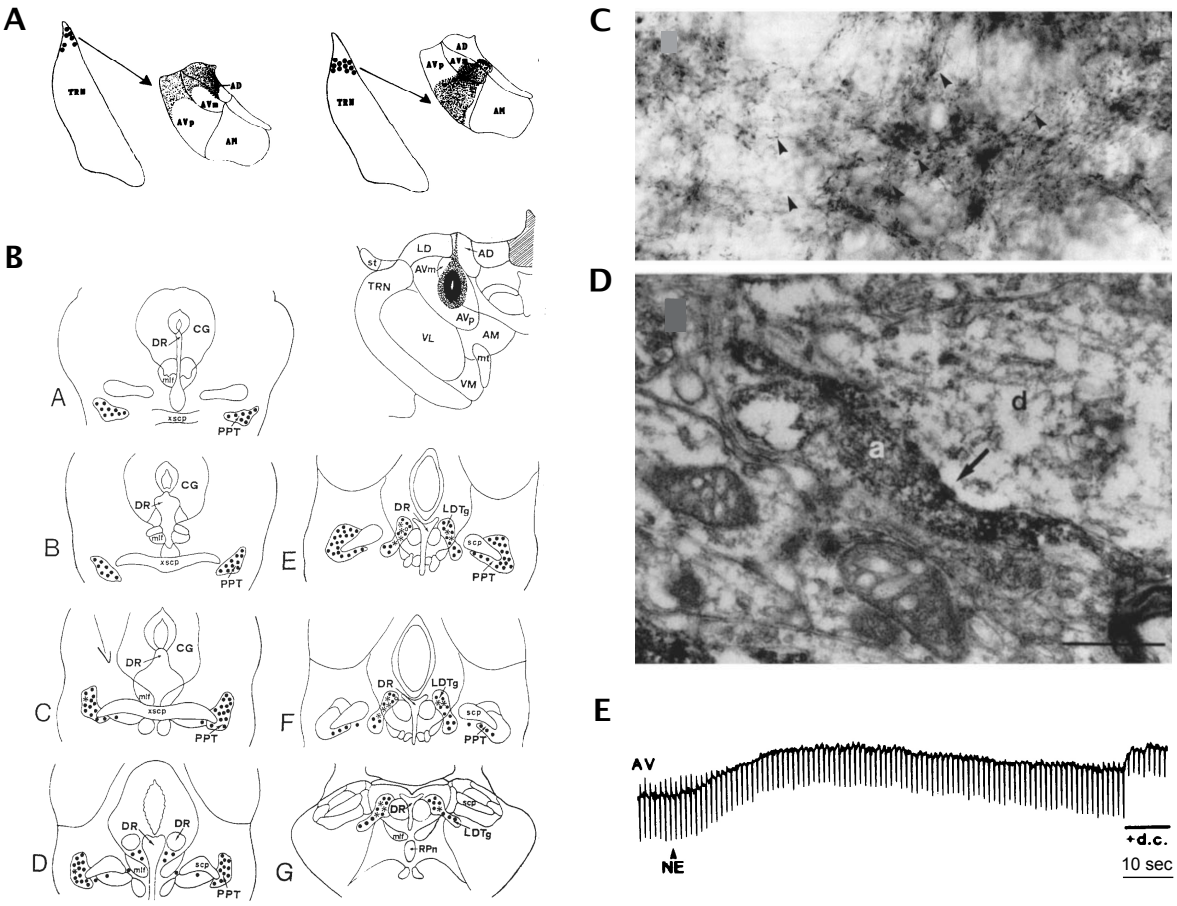

Figure 6.6 Modulatory inputs to the AV.

A) Retrogradely labelled GABAergic neurons in the TRN. Figures adapted and reorganised from Gonzalo-Ruiz and Lieberman (1995).

B) Retrogradely labelled neurons with the Horseradish peroxidase (HRP) injection in the AV. The dark circles indicate immuno-stained ChAT neurons and asterisks indicate HRP-labelled and ChAT-labelled neurons. Double labelled neurons are observed in the ipsilateral side of the PPN and in the bilateral side of LDT. Figures adapted from Gonzalo-Ruiz et al. (1995)

C) ChAT-Immunostained axon terminals (arrows) are shown in the AV. Light microscopic images. Figures adapted from Hallanger et al. (1990)

D) Electron microscope images of synapse (arrow) formed between ChAT-immunostained axon (a) and proximal dendrite (d) in the AV. Figures adapted from Hallanger et al. (1990).

E) Depolarisation of membrane potential in an AV neuron after the application of noradrenaline in guinea pig Figures adapted from McCormick and Prince (1988). +DC indicates positive direct current.

7 Ion channel expression as basis for intrinsic electrophysiological properties

Having outlined the roles of AD and AV within the HD system, this chapter turns to the molecular determinants of their electrophysiological features. Distinct profiles of ion channels and related protein expression in neurons collectively influence on the intrinsic electrophysiological properties such as the resting membrane potential, Action potential (AP) waveform, and neuronal excitability. Comparing the transcriptional profiles of different neuronal populations provides valuable insight into how specific molecular ensembles give rise to their characteristic electrophysiological features. Linking gene expression profiles with intrinsic electrophysiological properties reveals the mechanisms underlying these features and their alignment with the functional roles of each cell type within a circuit. In this chapter, key genes known to influence the electrophysiological signals of neurons are discussed. This molecular overview will provide crucial information for the subsequent discussion comparing the electrophysiological properties and channel-expression profiles of AD and AV neurons.

7.1 Ion channels and transporter contributions to resting membrane potential

The resting membrane potential is a stable electrical gradient across the neuronal membrane, essential for physiological function. In most neurons, it is around -65 mV and arises from selective ion permeability and active transport regulation. Potassium (K^+), sodium (Na^+), and chloride (Cl^-) are the main ions involved, with K^+ playing the dominant role (Nassar et al., 2025). The lipid bilayer is impermeable to ions, so their movement is mediated by ion channels. The Na^+ - K^+ Adenosine triphosphate (ATP)ase pump also regulates the membrane potential by maintaining steep ionic gradients, actively transporting three Na^+ ions out and two K^+ ions in per AV. This separation of ionic charges across the membrane generates the potential, and together these mechanisms preserve the ionic environment required for neuronal functions.

The Nernst equation describes the equilibrium potential for a single ion (Stock & Orna, 1989), while the Goldman-Hodgkin-Katz equation extends this to multiple ions, incorporating their relative permeabilities and intra-extracellular concentrations. Classic work by Hodgkin, Huxley, and Katz on the squid giant axon demonstrated that altering extracellular K^+ changes the resting potential, revealing the fundamental role of K^+conductance.

Major contributors to the high K^+ permeability during the resting status are K^+ leak channels. These channels, particularly the two-pore-domain K^+ channels (Two-pore domain potassium channel (K2P) (KCNK) family) provide a constant conductance for $K^+$to exit the cell down its concentration gradient. KCNK1, KCNK2, KCNK3, and KCNK9 are the most common subunits. Because the neuronal membrane is far more permeable to K^+

than other ions at rest, K^+ efflux leaves the intracellular environment electrically negative relative to the outside. These have been known for their involvement in resting membrane potential, input resistance, AP dynamics, and controlling the gain factor of intrinsic and synaptic currents. We can take an example in the pyramidal neurons and interneurons in CA1 (Taverna et al., 2005). Typically, pyramidal neurons exhibit -65 mV and interneurons exhibit -56 mV at the resting stage. The more hyperpolarised resting membrane potential of hippocampal pyramidal neurons compared to interneurons is linked to their higher expression of TWIK-related acid-sensitive potassium channel (TASK)-3 channel with some contributions from TASK-1. TASK (Tandem of P domains in a weak inwardly rectifying K^+ channel (TWIK)-related acid-sensitive potassium) channels are subfamilies within the KCNK family. Taverna et al. (2005) showed through electrophysiological recordings and single-cell RT-PCR that TASK-3 transcripts are abundant in pyramidal neurons, while less in interneurons. This enhanced leak K^+ conductance leads pyramidal neurons more hyperpolarised under the resting conditions. Likewise, distinct distribution and expression level of KCNK channel subtypes contribute significantly to the membrane properties in different brain areas (Talley et al., 2001).

7.2 Ion channels and AP kinetics

Various types of neurons in the mammalian brain show different shapes of APs. Glutamatergic pyramidal neurons generally exhibit wider AP than the GABAergic interneurons (McCormick et al., 1985). Also, in general, fast-spiking neurons tend to exhibit narrower AP width during prolonged stimulation (Connors & Gutnick, 1990; Nowak et al., 2003; Zhou & Hablitz, 1996). The expression of the Voltage-gated potassium channel (Kv)3 family of voltage-gated potassium channels has a strong correlation relationship with fast-spiking activity because its rapid and steeply voltage-dependent activation and deactivation kinetics helps to generate narrow spikes and short refractory periods (Du et al., 1996; Erisir et al., 1999; Martina et al., 1998; Massengill et al., 1997; Rudy & McBain, 2001). However, GABAergic neurons or interneurons are not the only ones showing fast spiking activity because GABAergic purkinje cells (projecting neurons) and subthalamic glutamatergic neurons exhibit fast spiking activities with high potassium currents mediated by Kv 3 family channels (Bevan & Wilson, 1999; Do & Bean, 2003; Martina et al., 2003; McKay & Turner, 2004; Southan & Robertson, 2000; Wigmore & Lacey, 2000). Neurons can exhibit a wide variety of firing patterns and frequencies, and these features are often not directly associated with the specific shape of their APs (McCormick et al., 1985; Nowak et al., 2003; Staff et al., 2000). The firing pattern of a neuron means multiple features. For example, firing rate changes across the stimulus levels, bursting or non-bursting, and adaptive or non-adaptive firing. Or, sometimes, the firing activity cannot be defined in this simple criteria due to its irregularity. However, the firing patterns and individual action potential shape cannot be fully separate. Changes in ionic conductances that influence firing patterns usually also influence AP shapes. Both firing pattern and AP shapes are important especially in the presynaptic terminals because even small differences in shape can shift the timing of calcium entry and cause significant changes in postsynaptic currents.

7.2.1 Voltage-gated sodium channel

Voltage-gated sodium channel (VGSC) are essential for the initiation of action potentials. Small depolarisation opens VGSCs, allowing a rapid inward Na^+ current that produces the rising phase of the spike (Catterall, 2023; Hodgkin & Huxley, 1952). Activation is voltage-dependent and driven by positively charged residues that move outward when the membrane depolarises, opening the pore (Catterall, 1986a, 1986b, 2010). Once open, VGSCs undergo two distinct forms of inactivation. Fast inactivation occurs within a few milliseconds, ensuring that the Na^+ current is brief and that each AP remains sharp (Hodgkin et al., 1952; Vassilev et al., 1989; Vassilev et al., 1988; West et al., 1992). In contrast, slow inactivation develops over tens to hundred of milliseconds during sustained or repetitive depolarisations (Adelman & Palti, 1969; Vilin & Ruben, 2001). This process involves gradual rearrangements of the pore itself, which reduce the availability of Na^+ channels and limit excitability during long spike strains (Rudy, 1978; Xiong et al., 2006). The molecular or genetic basis of these different inactivation types are not yet known (Bean, 2007). Both fast and slow inactivation mechanisms occur within the VGSCs, where fast inactivation governs the duration of individual APs, while slow inactivation modulates channel availability. Thus, this mechanism can regulate the firing patterns over longer time scales. In the ATN, AD neurons tend to show adaptive firing while AV neurons often show an initial burst, which will be presented in the result part. We return to this point later to relate the firing patterns to their expression profiles.

7.2.2 Voltage-gated calcium channel

Multiple Voltage-gated calcium channel (CaV) are expressed in the mammalian neurons. Each neuron expresses at least 4-5 types of calcium channels. These are categorised such as T-type (low-voltage activated, CaV3 family), L-type (high-voltage activated, CaV1.2, CaV1.3), P/Q-type (CaV2.1), N-type (CaV2.2), and R-type(CaV2.3). Unlike Na^+ channels, CaV channels activate more slowly and give a contribution to the depolarising phase leading up to an AP. Some open near the spike peak and during repolarisation, when the driving force for Ca^{2+} is greatest. Ca^{2+} influx during APs strongly influences spike shape. Blocking CaV channels often broadens spikes. This is a counterintuitive effect, explained by the fact that Ca^{2+} entry rapidly activates Large-conductance calcium-activated potassium channel (BK) (large conductance calcium-activated potassium, fast K^+ outflow; KCNMA1, KCNMB1-4) channels, producing a powerful outward current that accelerates repolarisation (W. Chen et al., 1996; Shao et al., 1999; Storm, 1990). Especially L-type (CaV1.2), P/Q-type (CaV2.1) and N-type (CaV2.3) are coupled with BK channels (Berkefeld et al., 2006). In contrast, Small conductance calcium-activated potassium (SK) (small conductance calcium-activated potassium, slower K+ outflow; KCNN1-3) channels are less tightly coupled, activated by Ca^{2+} diffusing from CaV2.1, CaV2.2, CaV2.3, and CaV3 family channels (Goldberg & Wilson, 2005; Hallworth et al., 2003; S. Williams et al., 1997; Wolfart & Roeper, 2002; Womack et al., 2004). Their slower activation and decay mean that they contribute less to fast repolarisation, but they generate Afterhyperpolarisation (AHP) that follows a spike,

lowering the membrane potential and stabilising interspike intervals. Blocking SK channels disrupts this process, leading to less regular firing in pacemaking neurons (Hallworth et al., 2003; Wolfart et al., 2001). In thalamic neurons, T-type Ca^{2+} channels underlie the low-threshold spike and, therefore, play a critical role in regulating the firing pattern of these cells (Jahnsen & Llinás, 1984; H. R. Kim et al., 2015).

7.2.3 Voltage-gated potassium channel

Potassium channels also play an important role in shaping APs. In glutamatergic neurons of the hippocampus and cortex, three major K^+ currents contribute to the repolarisation, which are I_A, I_D, and BK calcium-activated currents. I_A is a rapidly inactivating current, mediated primarily by Kv4 family channels (KCND1-3) and Kv1.4 (KCNA4) family (Coetzee et al., 1999; J. Kim et al., 2005; Yuan et al., 2005). I_A provides a strong repolarising drive and opposes depolarisation near threshold, but its activity-dependent inactivation contributes to frequency dependent spike broadening and synaptic facilitation (Ma & Koester, 1995; R. Shibata et al., 2000). I_D is known as a delay current that prolongs the approach to the threshold (Storm, 1988). It is mediated by Kv1 inactivation family channels (KCNA genes). Gradual inactivation of Kv1 channels during repetitive firing reduces their ability to repolarise the membrane quickly, causing action potential to last longer with broaden spikes. This broadening can alter the timing and pattern of neuronal firing (Giese et al., 1998). In contrast, BK current, mediated BK calcium-activated potassium channels (KCNMA1), is activated by both depolarisation and Ca^{2+} entry. BK current is categorised in the K^+ current but their properties have been discussed above as a rapid repolarising contribution. Kv3 channels are finely tuned to support high-frequency firing. Compared with other K^+ channels, Kv3 currents activate much more rapidly, enabling them to drive fast repolarisation of the AP. Their contribution depends not only on their speed but also on the precise timing of their gating aligning with Na^+ channel recovery and to prevent slower K^+ currents from interfering (Lien & Jonas, 2003). In addition, by shaping the AHP Kv3 currents also help preserve excitability, allowing neurons to maintain high firing rates with temporal precision.

7.2.4 Subthreshold currents

Subthreshold currents strongly influence the trajectory of the membrane potential toward the threshold. I_A and I_D K^+ current act to delay threshold crossing. I_A is activated at subthreshold voltages, where it transiently counteracts depolarisation before inactivating, thereby permitting progression to spike threshold (Connor & Stevens, 1971a, 1971b). I_D serves a comparable role but inactivates more slowly, producing a more prolonged delay in the approach to the threshold (Mitterdorfer & Bean, 2002; Storm, 1988). Low-voltage activated T-type calcium channels (CaV3 family) also operate at subthreshold voltages. Following hyperpolarisation, they recover from inactivation and contribute to rebound burst-

ing (Jahnsen & Llinás, 1984; Llinás & Yarom, 1981), while small steady T-type currents near resting membrane potential can also modulate and contribute to the firing pattern (S. R. Williams et al., 1997). Another important subthreshold current is I_h, mediated by Hyperpolarisation-activated cyclic nucleotide-gated channel (HCN) channels. This generally contributes to pacemaking by depolarising the cell from hyperpolarised potential (Pape, 1996; Robinson & Siegelbaum, 2003). HCN channels provide a mixed Na^+/K+ inward current, which steadily depolarises the membrane back toward threshold, counteracting inhibition and promoting rebound excitability. In addition to pacemaking, I_h helps set the resting membrane potential and shape how neurons integrate synaptic inputs (Kelley et al., 2021). HCN channel activity is a likely key determinant that separates the electrophysiological profiles of AD and AV. I will return to this point in the discussion. Together, the variety of threshold currents including outward (such as I_A and I_D) and inward (such as T-type calcium and I_h) establish how close the neuron comes to threshold and whether spikes are generated. The interaction of I_h and T-type calcium currents in thalamic neurons leads to phasic bursting, which might contribute to thalamic rhythmic activity (Suzuki & Rogawski, 1989).

7.2.5 Currents after the AP

After an AP, neurons can exhibit AHP that influence subsequent excitability. In mammalian neurons, AHPs are common but not universal. They can be categorised as fast, medium, and slow depending on their duration. AHPs are mediated by different K^+ channels. BK channels produce brief AHPs (Faber, 2003; Storm, 1987; Womack & Khodakhah, 2002), SK channels produce longer-lasting-AHPs due to the slow decay of intracellular calcium (Stocker, 2004), and Kv7 (M-current) channel also contributes (Gu et al., 2005; Lawrence et al., 2006; Storm, 1990). Also, many cortical and hippocampal pyramidal neurons show Afterdepolarisation (ADP), which can range from a slow repolarisation phase to a distinct depolarising trajectory following the spike (Connors et al., 1982; Raman & Bean, 1997). ADPs can reach threshold and trigger burst firing, with contributing current including persistent and resurgent Na^+ (Azouz et al., 1996; Raman & Bean, 1997), T-type and R-type Ca^{2+} (Metz, 2005; Swensen & Bean, 2003), and Ca^{2+}-activated cation channels (Haj-Dahmane & Andrade, 1997). In thalamic relay neurons, hyperpolarisation deinactivates T-type Ca^{2+} channels so that release elicits a low threshold spike that triggers a burst of action potentials (Desai & Varela, 2021; Grenier et al., 1998).

In summary, the electrophysiological dynamics of neurons emerges from the diverse contributions of specialised ion channels. Even small currents can exert powerful effects on excitability, shaping AP initiation, repolarisation, and post-spike behaviours. Appreciating the general properties of each channel provides a foundation for understanding the distinct electrophysiological traces observed across different neuronal populations.

8 Aims and contribution of the thesis

This thesis project developed from the initial observation of the topographical separation of PrS- and gRSC-projecting populations in the AD and AV (John Vyani Rajalingam and Fricker). Previous studies had only used single retrograde injections into either the PrS or RSC, (Lin et al., 2024; Lomi et al., 2021; Nassar et al., 2018; Richevaux et al., 2025; Roy, Zhang, Aida et al., 2022; Roy et al., 2021; H. Shibata, 1993b; Van Der Goes et al., 2024). Therefore, my project aimed to perform improved anatomical and functional analyses to define the input and output profiles of AD and AV neurons. AD and AV have received growing attention for their role in the HD system (Ajabi et al., 2023; Ji, Lomi et al., 2025; Lomi et al., 2023; Peyrache et al., 2015, 2017; Tsanov, Chah, Vann et al., 2011; Viejo & Peyrache, 2020), but single neuron electrophysiological features have remained understudied. Recent studies further underscore the functional importance of AD and AV neurons for working memory and neuropsychiatric disorders (Roy, Zhang, Aida et al., 2022; Roy et al., 2021). Here, I set out to identify the electrophysiological and morphological properties of AD and AV neurons in a multidimensional manner. I further asked whether each subpopulation of projecting neurons generates distinct electrophysiological signals. To address this, I optimised experimental protocols for patch-clamp recordings and improved our lab's analysis tools.

Previous lesion and behavioural studies focused on the hierarchical organisation of the HD system along the LMN-AD-PrS/gRSC pathway (H. T. Blair et al., 1998, 1999; Guison et al., 1995; Lomi et al., 2023; Mathiasen et al., 2021; Seki & Zyo, 1984; H. Shibata, 1992; Van Der Goes et al., 2024). These studies had relied on anatomical approaches or extracellular recording techniques, leaving a gap in our understanding at the neuronal and synaptic level: Are mammillary inputs monosynaptically connected to thalamocortical projection neurons? If so, how do they drive neuronal activity in AD and in AV? To address this gap, I combined 1) retrograde rabies monosynaptic tracing, to pin down whether thalamic projection neurons receive direct mammillary inputs, and 2) optogenetic experiments, using photostimulation of mammillary body axons, to examine input-output transformations. I carefully examined the efficiency of mammillary axons of one hemisphere to excite thalamic neurons in the ipsilateral and contralateral AD and AV.

In addition, I investigated whether AD and AV neurons alter their spiking activity in response to cholinergic agonists, as there is anatomical evidence for cholinergic projections to the ATN (Gonzalo-Ruiz et al., 1995; Hallanger et al., 1987, 1990; M. Parent & Descarries, 2008; Sofroniew et al., 1985). The origin of these cholinergic fibers had been unclear, so I sought to identify the potential sources in the brain. . I learned how to use calcium imaging via a head mounted miniatures microscope with the aim to distinguish HD signals in identified neurons in AD and AV. In the future, it may be possible to manipulate cholinergic inputs while monitoring HD activity of AD and AV neurons during behaviour.

Taken together, the findings obtained through this academic journey contribute to provide new insights into the functional organisation of the ATN. The detailed results will be presented in the following results section.

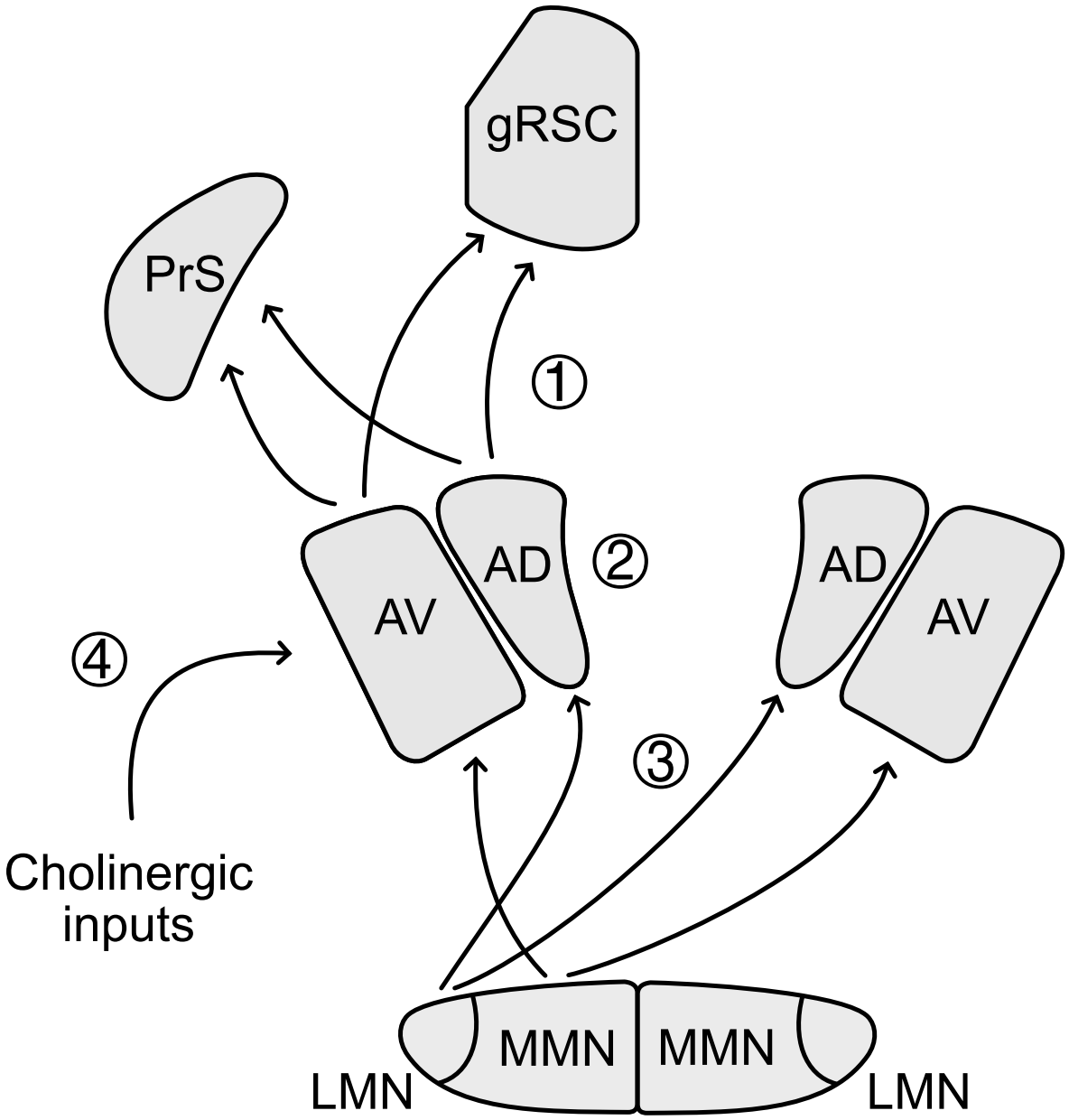

Figure 8 Schematic diagram of the network investigated in this thesis.

This diagram summarises the four main aspects addressed in this thesis: ① projection profiles of the AD and AV neurons, ② intrinsic electrophysiological properties of thalamic neurons, ③ mammillary input to the thalamic nuclei, and ④ investigation of brain areas that provide cholinergic modulation. The indicated pathway is illustrated from a unilateral perspective.

Method

This chapter describes the general methodological approaches applied throughout the experimental work conducted during this PhD project. It aims to outline the rationale behind the selection of specific techniques and to present the experimental strategies. A thorough understanding of these methods will support the interpretation of the results presented in the following chapters.

1 Animals

All experiments in this project were conducted using wild-type and transgenic mice on a C57BL/6 genetic background. For anatomical tracing experiments to identify cholinergic neurons projecting to the thalamus, ChAT::Tomato transgenic mice were used. The choice of animal age varied depending on the specific requirements of each experimental procedure. For patch-clamp recordings without prior viral injections, mice aged postnatal day 27 to 40 (P27–P40) were used. When viral expression was required prior to electrophysiological recordings, mice aged P30–P40 were selected, while older mice (P50–P79) were used for anatomical tracing or calcium imaging experiments.

Young adult mice were generally preferred for electrophysiological experiments as their brain tissue offers more favourable conditions for stable and successful patch-clamp recordings. For experiments combining viral injections and electrophysiology, the earliest possible time point for surgery was selected in accordance with developmental stages to ensure successful recordings at the time of patch-clamp recording.

Both male and female mice were used in roughly equal proportions across experiments. Animals were housed in cages containing 2 to 5 mice and maintained on a 12-hour light/dark cycle, with shelter, toys, food and water available ad libitum. For *in vivo* experiments, mice were regularly handled prior to data acquisition in order to reduce stress and improve habituation to the experimenter.

2 Stereotaxic injections

Mice were habituated in the waiting room for at least one hour prior to surgery. The waiting area was physically separated from the main surgical room. Anaesthesia induc-

tion was carried out in an induction chamber using 3% isoflurane (ISO-VET, Piramal) and maintained at 1.4 - 1.8% throughout the surgery on a digital stereotaxic apparatus (KORF®). Buprenorphine (0.05 mg/kg, Buprécare®, Axience) was administered intraperitoneally, and lidocaine (2 mg/kg, Ladocaïne®, MSD) was injected subcutaneously between the scalp and skull to provide local anaesthesia prior to the scalp incision.

Injections of viral vectors or tracers were performed using a Hamilton syringe (Nanofil syringe 10 µl, NF-SYR, WPI) connected to an automatic injector (78-8130, KD Scientific). Injection volumes and stereotaxic coordinates (AP/ML/DV, in mm) were as follows.

Region	Volume (nL)	AP (mm)	ML (mm)	DV (mm)
PrS	200	-4.06	-2.00	-2.15
gRSC	300	-2.10	-0.20	-0.85
AD & AV	200	-0.82	-0.75	-3.20
MBO	200	-2.80	-0.75	-5.35

Table 2.1 Injection volumes and anatomical coordinates for stereotaxic injections

All injections were performed unilaterally over 10 minutes. After injection, the syringe was left in place for an additional 5-10 minutes to minimise backflow and ensure complete diffusion of the injectate. Following suturing, carprofen (5 mg/kg, Rimadyl®, Zoetis) was administered subcutaneously for post-operative analgesia.

For retrograde tracing of thalamic neurons projecting to cortical regions, two types of tracers were used: Choleratoxin subunit B (CTB) conjugated to Alexa Fluor 488 or 647 (C22841 and C34778, Thermo Fisher Scientific), and red Retrobeads (Lumafluor). After CTB injection, brains were collected 5-7 days later to allow optimal visualisation of CTB-labelled neurons. For Retrobeads, patch-clamp recordings were performed at least 2 days after injection to allow sufficient labelling of neurons.

For experiments requiring viral expression, brains were collected 3-4 weeks post-injection to allow sufficient expression. The viruses used in experiments are listed in the table below.

Virus	Source	Reference
AAV5-Syn-Chronos-GFP-WPRE-bGH	Penn Vector Core	Addgene 59170P
AAV(retro)-Syn-H2B-GFP-TVA-N2c.G-WPRE3	Charité Viral Core Facility	BA-335
RABV CVS-N2c(ΔG)-tdTomato	Charité Viral Core Facility	BR-31
AAV(retro)-CAG-EGFP-WPRE-SV40p(A)	Zurich Vector Core	V-24
AAV9-syn-FLEX-jGCaMP8f-WPRE	Addgene	162379
AAV(retro)-EF1a-Cre	Addgene	55636

Table 2.2 Viruses used in this thesis project and their sources with catalogue numbers

AAV5-Syn-Chronos-GFP-WPRE-bGH was injected into the MBO for optogenetic experiments. For monosynaptic rabies tracing, AAV(retro)-Syn-H2B-GFP-TVA-N2c.G-WPRE3 was injected into the PrS or gRSC to express Avian tumor virus receptor A (TVA) protein in projecting thalamic neurons. Three weeks later, RABV CVS-N2c(ΔG)-tdTomato was injected into the AD and AV regions to label monosynaptically connected neurons in the MBO. AAV(retro)-CAG-EGFP-WPRE-SV40p(A) was injected in the ChAT::TOM mice to retrogradely label neurons projecting to the AD and AV. AAV9-syn-FLEX-jGCaMP8f-WPRE was injected into the AD and AV, and Retro-Cre was injected into the PrS to express GCaMP8f specifically in PrS-projecting thalamic neurons.

3 Tissue Fixation and Microscopy

Mice used for anatomical tracing experiments were deeply anaesthetised with a cocktail of ketamine (100 mg/kg, Kétamine™ 1000, Virbac) and xylazine (10 mg/kg, Rompun™ 2%, Elanco) before the termination. Transcardial perfusion was performed using 25 mL of Phosphate-buffered saline (PBS), followed by 25 mL of fixative (Antigent fix, P0016, DIAPATH). Brains were harvested and post-fixed overnight at 4 ℃ with constant agitation. After post-fixation, brains were washed in PBS three times for 20 minutes each at room temperature.

Fixed brains were coronally sectioned at 70-100 µm thickness using a vibratome (VT1200S, Leica). For nuclear staining and anatomical delineation, 4',6-diamidino-2-phenylindole (DAPI) (D9542, Sigma) staining was performed. Brain slices were mounted using appropriate mounting media depending on the imaging application: Vectashield Antifade Mounting Medium (H-1000, VectorLabs) for slide scanning, and ProLong Gold Antifade Mountant (P36930, Invitrogen) for confocal microscopy.

Whole-slide imaging was performed with a slide scanner (AxioScan.Z1, Zeiss) using a 10x objective to identify injection sites and expressions in the region of interests. Confocal imaging (LSM710, Zeiss) was used when higher magnification and resolution were required for detailed morphological analysis and examination of labelled cell profiles. For monosynaptic rabies tracing experiments, imaging was performed using the custom-built Serial two-

photon tomography (STPT) instrument (Ragan et al., 2012), a two-photon microscope integrated with an automated slicing system. Paraformaldehyde (PFA)-fixed brains were coronally sectioned at 40 µm, and each section was imaged through eight optical planes spanning 5 µm using BakingTray (https://github.com/SWC-Advanced-Microscopy/BakingTray) in combination with ScanImage (Vidrio Technologies, USA; RRID:SCR_014307). Image stitching was performed using StitchIt (https://github.com/SWC-Advanced-Microscopy/StitchIt). The resulting stitched images from each optical plane were subsequently z-stacked (80 - 100 µm) using the Python packages tifffile (https://github.com/cgohlke/tifffile) and NumPy (Harris et al., 2020). This work was carried out in collaboration with Dr. John J. Tukker in Dr. Dietmar Schmitz's lab at Neuroscience Research Centre, Charité-Universitätsmedizin Berlin.

4 Registration on the 3D mouse brain diagram

Whole-brain images acquired using a whole-slide scanner were used for the anatomical analysis of thalamic projecting neurons. Serial coronal sections containing the AD and AV regions were selected for analysis. Each section was aligned to the corresponding level of the standardised Allen Mouse Brain Atlas (CCFv3) (Q. Wang et al., 2020) using the ABBA registration tool (Chiaruttini et al., 2025).

Following registration, aligned images were transferred to QuPath (Bankhead et al., 2017) for cell detection and fluorescence quantification. DAPI-positive cells were automatically detected, and the cytoplasmic intensity of green and far-red fluorescence was measured to determine the projection profiles of each neuron. For this detection and quantification, built-in functions in QuPath were used. The 3D coordinates of the identified cells were then registered onto a standard 3D brain diagram using brainrender (Claudi et al., 2021) for visualisation and spatial analysis.

Additionally, when anatomical confirmation of injection sites or viral expressions was required, ABBA was used to align the microscopic images with the standard mouse brain atlas.

5 Thalamic acute slice preparation for electrophysiology

Mice used for patch-clamp experiments were deeply anaesthetised with a mixture of ketamine and xylazine, administered intraperitoneally. Depth of anaesthesia was confirmed by the absence of a toe-pinch reflex. The animal was then decapitated, and the brain was rapidly extracted in the cutting solution on an ice-cold platform. Coronal slices of 300 µm thickness were prepared using a vibratome. The slicing was performed in an ice-cold cutting

solution, continuously oxygenated with 95% O_2 / 5% CO_2. Typically, 1-2 acute coronal slices containing the AD and AV regions were obtained per mouse. Slices were then transferred to a chamber containing Artificial cerebrospinal fluid (ACSF), oxygenated with 95% O_2 / 5% CO_2 (pH 7.3, 305-315 mOsm/L). The chamber was placed in a water bath maintained at 35 ℃ for 15 minutes for recovery. Then the chamber was placed at room temperature prior to the experiments. The composition of cutting solution and ACSF is described in the table below.

Components	Cutting solution (mM)	ACSF (mM)
NaCl	125	124
Sucrose	25	0
KCl	2.5	2.5
$NaHCO_3$	25	26
NaH_2PO_4	1.25	1
D-glucose	2.5	11
$CaCl_2$	0.1	2
$MgCl_2$	7	2

Table 2.3 Chemical composition of cutting solution and ACSF

6 Whole-cell patch clamp recordings

The AD and AV were identified under a microscope (Axioskop 2 FS Plus, Zeiss) using a 5x objective and transmitted light. These nuclei were located close to the third ventricle and the anterior portion of the hippocampal formation. For the visualisation of individual neurons, a 60x liquid-immersion objective and an EMCCD camera (Luca-S, Andor) were used with infrared differential interference contrast (IR-DIC). Retrobead-labelled thalamo-cortical neurons were identified using LED fluorescence illumination (Cairn Research, via epifluorescence port).

Patch pipettes were pulled from borosilicate glass capillaries (1.5 mm outer diameter, 30-0057, Harvard Apparatus) using a horizontal puller (P-87, Sutter Instruments). When filled with internal solution, the pipettes had a resistance of 4-8 MΩ. The composition of the internal solution (pH 7.3, 290 mOsm) is described in the table below.

Components	Concentration (mM)
K-gluconate	135
KCl	1.2
HEPES	10
EGTA	0.2
$MgCl_2$	2
MgATP	4
Tris-GTP	0.4
Na_2-phosphocreatine	10
Biocytin	2.7

Table 2.4 Chemical composition of the internal solution for whole-cell patch clamp recordings

The recordings were performed using a Multiclamp 700B amplifier (Molecular Devices), and signals were digitised by a 1440A or 1550B (Molecular Devices). Patch pipettes were positioned using a Luigs and Neumann micromanipulator. The membrane potential was held at −70 mV during seal formation, and recording began after membrane breakthrough. Signals were filtered at 10 kHz and digitised at 50 kHz. Only neurons that satisfied the quality-control criteria were included in the analysis: access resistance (R_{access}) < 35 MΩ, resting membrane potential < -50 mV, action potential (AP) amplitude > 50 mV above baseline and above 0 mV in absolute terms, and stable baseline voltage throughout recordings.

Intrinsic electrophysiological properties were assessed in current-clamp mode. After achieving whole-cell access, neurons were recorded for 1-2 minutes without current injection (gap-free protocol) to measure the Resting membrane potential (RMP). To assess excitability, a rapid-step protocol was used. This began with a -20 pA prepulse for 150 ms, followed by 800 ms step currents from hyperpolarising levels sufficient to reach −100 mV of the cell membrane up to +300 - +400pA of injected current. During these steps, the membrane potential was maintained at -70 mV.

To examine the effect of I_h current blockade, ZD7288 (2 μM, N-1000, Tocris) was applied via bath perfusion. While ZD7288 was being delivered, hyperpolarising current steps were applied to monitor I_h. Typically, the effect of ZD7288 was exhibited after 5-10 minutes of perfusion. Then the rapid-step protocol was repeated under drug conditions.

To examine the effect of cholinergic input, carbachol (10 μM), a cholinergic receptor agonist, was applied via bath perfusion. During carbachol application, spiking activity was continuously monitored in response to positive current injections. Each cell was tested under three conditions: control, carbachol application, and washout. Current injections were adjusted to reliably evoke 1-5 action potentials per stimulus.

Functional connectivity between AD and AV neurons was tested using dual whole-cell current-clamp recordings. One neuron was recorded in the AD (held at -60 mV) and the other in the AV (held at -70 mV). In each pair, trains of 20 current pulses were delivered al-

ternately at 25 Hz. The pulse duration was 1 ms. This was repeated for ten sweeps. Current amplitudes were adjusted to reliably induce spiking, typically between 1.0 and 2.5 nA.

7 Optogenetics

For optogenetic experiments, acute brain slices expressing chronos in the mammillary neurons are used. The 470 nm blue light was delivered onto the soma through a 60x water-immersion objective immersed in ACSF. Light stimulation was generated using an LED system (OptoLED, Cairn Research) and controlled via pClamp software (Molecular Devices). During the experiments, screening of threshold stimulation was performed in current-clamp mode. The light intensity was gradually increased from zero to the maximum light intensity. Neurons were stimulated with a train of ten light pulses (0.5 ms duration at 20 Hz). The lowest intensity required to reliably evoke AP was recorded as the threshold. Neurons that failed to show Optogenetically evoked postsynaptic potential (oEPSP)s were classified as non-connected cells.

In connected neurons, Optogenetically evoked postsynaptic current (oEPSC)s were recorded in voltage-clamp mode at subthreshold light intensity. Amplitude was measured as the difference between the baseline and the peak of the oEPSC. Latency was calculated as the time between light onset and the point at which the oEPSC reached 10% of its maximum amplitude. These analyses were performed using AxoGraphX (AxoGraph Scientific). Both oEPSC dynamics and spike probability were averaged over 10 repetitions per stimulus. Spike probability was calculated as the proportion of light pulses that successfully evoked action potentials in current-clamp mode.

To test for direct, monosynaptic responses, neurons were recorded in voltage-clamp mode (AD neurons held at -60 mV, AV neurons at -70 mV) while Tetrodotoxin (TTX) (1 μM) and 4-aminopyridine (4-AP) (100 μM) were applied via bath perfusion. 2-Amino-5-phosphonovaleric acid (APV) (100 μM) and 2,3-Dihydroxy-6-nitro-7-sulfamoyl-benzo (F) quinoxaline (NBQX) (10 μM) were applied by bath perfusion in voltage clamp mode to confirm if the connection is glutamatergic.

8 Electrophysiological data analysis

The analysis of intrinsic electrophysiological properties was performed using a custom Python script adapted from a previously published analysis pipeline developed in our laboratory (Huang et al., 2017). The traces in current clamp mode tested in gap-free protocol and rapid-step protocol mentioned above were analysed. Electrophysiological recording files were opened and processed using the PyABF library (Harden, 2022) in Python. The

analysis script is available on Github repository (https://github.com/DLim-neuro/IPA). The analysed electrophysiological properties and their definitions are summarised in the table below.

Properties	Definitions or Descriptions
Resting membrane potential (mV)	Mean membrane potential of 20 s in gap-free
Input resistance (MΩ)	Slope of I-V curve between -80 mV and -60 mV
Time constant (ms)	Double-exponential fit applied to averaged trace at −20 pA prepulse (Golowasch, J.-2009)
Sag ratio	Minimum Vm (0-400 ms) divided by mean Vm (400-800 ms) during hyperpolarisation to approximately -100 mV
Rheobase (pA)	Amplitude of current injection that evokes the first AP
Threshold (mV)	Vm where dV/dt > 30 mV/ms on rheobase AP
Latency (ms)	Time from current onset to AP threshold
AP rise amplitude (mV)	Difference between threshold and AP peak
AP peak (mV)	Maximum Vm during the rheobase AP
AP width (ms)	Time between half-amplitude points
AHP (mV)	Difference between AP threshold and minimum Vm during repolarisation
Max depolarisation rate (V/s)	Maximum dV/dt during AP rising phase
Max repolarisation rate (V/s)	Minimum dV/dt during AP falling phase
Current at 10 Hz (pA)	Amplitude of current injection required to elicit 10 Hz firing
Burst index	Minimum ISI / Mean ISI at 10 Hz
Initial burst ISI	Number of ISIs < 6 ms within first 100 ms after current onset
Mean initial ISI (ms)	Mean of ISIs within first 100 ms after current onset
Adaptation index	Last ISI / mean ISI at 10 Hz
Fast doublet index	Mean ISI / 1st ISI at 10 Hz
Fast doublet ratio	2nd ISI / 1st ISI at 10 Hz
Δ peak between AP1-AP2 (mV)	AP peak differences between 1st and 2nd APs
Post-train AHP (mV)	Difference between lowest Vm (0–100 ms post-train) and mean Vm (500–700 ms post-train)
Input output slope (Hz/nA)	Slope of firing rate-current between 0 and 9 Hz
Firing rate at 200pA (Hz)	Spiking frequency in response to 200 pA injection
Rebound spike probability	Probability of spiking within 100 ms after hyperpolarising step

Table 2.5 Analysed intrinsic electrophysiological properties and their detailed descriptions

9 Unsupervised cluster analysis

Principal component analysis (PCA) was performed using the scikit-learn (Virtanen et al., 2020) library in Python to reduce dimensionality for comparative analysis. Properties showing pairwise Pearson correlation coefficients greater than ±0.85 were excluded from the analysis. Based on this criterion, three properties (AP rise amplitude, Max repolarisation rate, and AP width) were removed. The remaining 22 properties were standardised and included in the PCA: RMP, Input resistance, Time constant, Sag ratio, Rheobase, Threshold, Latency, AP peak, AHP, Max depolarisation rate, Current at 10 Hz, Burst index, Initial burst Interspike interval (ISI), Mean initial ISI, Adaptation index, Fast doublet index, Fast doublet ratio, Δ peak between AP1-AP2, Post-train AHP, Input output slope, Firing rate at 200 pA, and Rebound spike probability. The first three principal components were used to visualise the data in 3D space. To explore potential clusters, Ward's hierarchical clustering with Euclidean distance was applied. The cluster structure was displayed as a dendrogram.

10 Biocytin staining and 3D reconstruction

Following patch-clamp recordings, slices were fixed in fixative at 4 ℃ overnight. After fixation, slices were rinsed in PBS (3 × 20 min) and stored in 30% sucrose at 4 ℃, gently agitated. Biocytin staining was started with permeabilisation. Slices underwent three freeze-thaw cycles in the sucrose solution on dry ice. Then, the slices were rinsed by PBS (2 × 30 min and 1 × 2 hrs). A saturation step was performed by incubating slices in a blocking solution containing 2% skim milk powder and 1% Triton X-100 (T8787, Sigma-Aldrich) on PBS for 2 hours at room temperature. For staining, slices were then transferred to the solution containing streptavidin conjugated to Alexa Fluor 647 (1:500, S21374, Invitrogen) and DAPI (1:2000) and incubated overnight at 4 ℃. On the next day, slices were rinsed in PBS (2 × 30 min, 1 × 2-4 hrs). The side of the slice showing biocytin-filled neurons was identified under a fluorescence microscope (Nikon Eclipse TE-2000E). The slices were then mounted using ProLong Gold Antifade Mountant (P36930, Life Technologies).

For morphological analysis, high-resolution z-stack images were acquired using a confocal microscope (20x objective). Neuronal morphologies were reconstructed in 3D using IMARIS software. A semi-automated reconstruction function was used. 3D reconstruction of neuronal morphology was done with Mario Auvinet, a PhD student in the lab.

11 Calcium imaging using a head mounted miniatures microscope (Miniscope)

Mice used for calcium imaging required additional surgical procedures. Three weeks after viral injection, Gradient-index (GRIN) lens implantation and baseplate mounting were performed on the same day. A 1 mm diameter cylinder-like GRIN lens (1050-004595, Inscopix) was used to access both AD and AV regions. Before the lens insertion, animals were anesthetised with isoflurane and received local anaesthesia (lidocaine, 2 mg/kg, Ladocaïne®, MSD) under the scalp. The hair was removed, and a circular section of scalp tissue was excised to allow subsequent baseplate placement. Residual tissue on the skull was cleaned with H_2O_2, and the skull surface was gently scratched with a surgical blade to improve the adhesion of the dental cement. A craniotomy was then performed at the ATN coordinates using a drill, making a 1 mm window for GRIN lens implantation. Overlying cortical tissue was carefully removed using negative pressure suction until the corpus callosum was exposed. Occasional bleeding during the procedure was managed by continuously rinsing the area with ACSF until the bleeding stopped. The GRIN lens was then inserted at a rate slower than 0.01 mm/sec. The target point was; AP: -0.82 mm / ML: +1.30 mm / DV: -3.00 mm. The implanted GRIN lens was secured in place using dental cement (Super-Bond Universal Kit, SUN MEDICAL CO., LTD.). To determine the optimal focal plane for calcium imaging, a Miniscope (UCLA V4) mounted with a baseplate was temporarily positioned above the implanted GRIN lens using the stereotaxic arm. Once the appropriate recording distance was identified, the baseplate was fixed to the skull using dental cement, and the Miniscope was removed. The empty space within the baseplate was covered with a plastic cap to protect the GRIN lens surface and to help the mouse adapt to the weight of the Miniscope. The cap was custom-designed in-house to fit the baseplate and weighed 2.6 g, equivalent to the weight of the Miniscope. At least one week of recovery time was given to the mice after the surgery.

On the day of recording, the mouse was habituated in its home cage within the recording room for one hour prior to the start of the experiment. Recordings were performed in an open, transparent cage, allowing the mouse to use the surrounding laboratory environment as visual cues. Each recording session lasted four minutes, with one session conducted per day. We used Bonsai to record the behavioural video, MiniscopeDAQ (V1.11) for Miniscope recording acquisition, and ACQ4 to record digital signals such as Miniscope sync signal and camera exposure. HD information, including yaw, pitch, and roll, was obtained by the Miniscope along with calcium imaging data during the recording.

The analysis was performed using a custom-written Python script developed by Dr. Michael Graupner and Elja Belhadef. Regarding the analysis process, motion correction was performed to improve frame shifts in the recorded calcium imaging videos, and ROI identification for each calcium transient dynamics with signal extraction achieved using Suite2P software (Pachitariu et al., 2016), using parameters suitable for one-photon imaging data. The yaw data were temporally aligned with the calcium transients of each ROI to analyse HD activity. The computed HD data were smoothed using a Gaussian kernel with a standard deviation of 5 °. Directional tuning of each ROI was analysed by averaging spike probability across 5 ° bins of horizontal head angle. Deconvolved fluorescence

traces provided an estimate of neuronal spiking probability. Two factors were used to establish the criteria for determining whether cells were directionally tuned: the Rayleigh vector length (R) and the p-value. The Rayleigh vector length quantifies the concentration of neural activity around a specific HD, ranging from 0 (no tuning) to 1 (ideally tuning). It is computed as the magnitude of the mean resultant vector obtained by summing unit vectors weighted by the firing activity at each directional bin and dividing by the total activity. To assess statistical significance, 300 surrogate datasets were generated by randomly shifting the temporal alignment between yaw angle and neural activity. A ROI was considered significantly tuned if its observed Rayleigh value exceeded the 95th percentile of the shuffled distribution ($p<0.05$). ROIs that satisfied both a Rayleigh vector length greater than 0.2 and $p<0.05$ were defined as 'HD-modulated cells'. ROIs with $R > 0.4$ and $p < 0.05$ were classified as 'HD cells'. However, given the limited recording dataset, only a few ROIs met the criteria for HD-modulated cells. To expand the analysis, we introduced an additional category of 'putative HD cells', defined as ROIs with a Raylegih test significance of $p<0.05$. The identification of the same cells across recording days was achieved by manually overlaying the detected ROIs on the recording view (Figure 17A) from each session.

12 Quantification and statistical analysis

The majority of data were analysed in Python. Electrophysiological properties were extracted using the PyABF library (Harden, 2022), and dimensionality reduction and clustering were performed using scikit-learn (Pedregosa, 2011). Statistical analysis was conducted using SciPy (Virtanen et al., 2020). Properties from optogenetic experiments were analysed using AxoGraphX (AxoGraph Scientific).

Results are reported as mean ± Standard error of the mean (SEM). Group comparisons were made using the Mann–Whitney U test for unpaired data and the Wilcoxon signed-rank test for paired data. Statistical significance is indicated as follows: $p < 0.05$ (*), $p < 0.01$ (**), $p < 0.001$ (***), $p < 0.0001$ (****).

Results

This chapter presents the results of my doctoral research. In the first and main part, I present my findings on the mammillo-thalamo-cortical functional connectivity in the form of a manuscript that will be submitted to an international peer reviewed journal. Second, I include results on the cholinergic modulation of spiking activity of AD and AV neurons. The third section shows calcium imaging of neuronal HD activity in the AD and AV in a behaving mouse. Finally, I present my contributions to research projects led by former laboratory members.

1 Research manuscript from the PhD project

Research on the ATN, particularly the AD and AV, has largely focused on lesion studies and *in vivo* recordings to characterise their contribution to the HD system. These approaches have demonstrated that the ATN is essential for maintaining accurate spatial orientation and directional signalling. However, much of this work has treated the ATN as a single entity or has emphasised AD in isolation, leaving the distinct role of each of the thalamic subnuclei less clearly defined. Moreover, while functional properties of these nuclei have been explored through behavioural and electrophysiological recording *in vivo*, some aspects of their functional input connectivity, topographic organisation and intrinsic electrophysiological properties have remained unknown. This lack of fine grained anatomical and physiological resolution limits our understanding of how AD and AV contribute to HD signalling. To address this gap, this research was designed to systemically examine the anatomical organisation and intrinsic electrophysiological properties of AD and AV neurons, thereby providing a detailed and comprehensive account of their distinct roles within the HD system.

In my main manuscript, I characterised the anatomical organisation of thalamic projection neurons within AD and AV. Using retrograde tracing, I demonstrated that AD and AV neurons projecting to the PrS and gRSC are topographically organised. Within areas of overlap, bifurcating neurons were identified, revealing that some AD and AV neurons project to both cortical targets. In addition, retrograde monosynaptic tracing experiments revealed that these thalamic projection neurons are monosynaptically connected to the mammillary inputs.

I examined the intrinsic electrophysiological properties of AD and AV neurons. Using the whole-cell patch clamp technique, I collected electrophysiological recordings from both nuclei. I wrote an analysis script to quantify the specific characteristics observed in AD and

AV neurons. A range of intrinsic properties was measured, including resting membrane potential, I_h current, AP kinetics, excitability, rebound probability, and firing patterns. I used PCA to show that AD and AV neurons are electrophysiologically distinct, regardless of their projection-specificity. The 3D reconstruction of axons and dendrites of biocytin filled cells demonstrated that AD and AV neurons also exhibit distinct morphological features.

Finally, I investigated postsynaptic responses of AD and AV neurons evoked by mammillary inputs. Optogenetic stimulation of mammillo-thalamic axons revealed that AD and AV neurons receive strong ipsilateral monosynaptic and glutamatergic input and also weaker contralateral inputs. Combined with previously reported anatomical studies and my monosynaptic tracing results, this further demonstrates mammillothalamic connectivity at the subnuclear level, both anatomically and functionally.

This manuscript presents the main research of my PhD project. It provides fundamental insights into the properties of AD and AV neurons, supporting the conventional HD network while also expanding its scope.

Mammillo-thalamo-cortical functional connectivity revisited: differences in anatomy and physiology of anterodorsal and anteroventral thalamic nuclei

Authors: Dongkyun Lim[1], Mario Auvinet[1], Louis Richevaux[1], John J Tukker[3], Dietmar Schmitz[2,3,4,5,6] and Desdemona Fricker[1]*

*Corresponding author: desdemona.fricker@u-paris.fr

Affiliations:

[1] Université Paris Cité, SPPIN - Saints-Pères Paris Institute for the Neurosciences, CNRS, Paris, France.

[2] Neuroscience Research Center, Charité-Universitätsmedizin Berlin, Corporate Member of Freie Universität Berlin and Humboldt-Universität zu Berlin, 10117 Berlin, Germany

[3] German Center for Neurodegenerative Diseases (DZNE) Berlin, 10117 Berlin, Germany

[4] Einstein Center for Neuroscience, Charité-Universitätsmedizin Berlin, Corporate Member of Freie Universität Berlin and Humboldt-Universität Berlin, 10117 Berlin, Germany

[5] NeuroCure Cluster of Excellence, Charité-Universitätsmedizin Berlin, Corporate Member of Freie Universität Berlin and Humboldt-Universität Berlin, 10117 Berlin, Germany

[6] Bernstein Center for Computational Neuroscience, Humboldt-Universität zu Berlin, 10115 Berlin, Germany

Abstract

The anterior thalamic nucleus plays an important role in the head direction system. The anterodorsal (AD) and the anteroventral (AV) subnuclei are part of the Papez circuit and relay information from the mammillary bodies to the cortex. Little is known about the anatomical and electrophysiological characteristics of single AD and AV neurons. Here, we revisited the mammillo-thalamo-cortical functional connectivity, focusing on neurons in the anterior thalamus that send their axons to two main cortical head direction areas, the dorsal presubiculum (PrS) and the granular retrosplenial cortex (gRSC). Monosynaptically restricted rabies tracing showed that their hypothalamic input predominantly but not exclusively originated from the ipsilateral side of the mammillary bodies. Thalamo-cortical projecting neurons in AD and AV were topographically organised, and a large subpopulation of double labeled neurons projected to both PrS and gRSC. Accordingly, the electrophysiological properties of neurons projecting to PrS or gRSC overlapped. However, AD and AV neurons differed, as shown in unsupervised cluster analysis of parameters describing passive and action potential properties, excitability, burst firing and adapting firing patterns. AD and AV neurons also differed in their morphologies: AD neurons possessed a small number of main dendrites, while AV dendrites were characterized by a bushy, extensive dendritic domain. Photostimulation of mammillary inputs readily induced postsynaptic responses: AV neurons tended to respond with initial bursting while AD neurons produced single action potentials, and sustained adapting firing. Dynamics showed mammillothalamic driver input characteristics, with a more efficient functional connectivity on the ipsilateral side. We suggest a potential integrative role for anterior thalamic nuclei receiving inputs from the left and right mammillary bodies, before sending head direction related signals to PrS and gRSC.

Introduction

Orientation in space relies on sensory inputs that are integrated to provide spatial and directional information. Head direction (HD) cells increase their firing rate for a particular direction the animal is facing, and collectively function as the brain's compass system. (Brown et al., 2002; Butler et al., 2017; Goodridge et al., 1998; Goodridge & Taube, 1995; Knierim et al., 1998; J. S. Taube, 2007; Yoder et al., 2015). The HD signal is formed subcortically, in interactions between dorsal tegmental nucleus (DTN, Bassett & Taube, 2001; Sharp et al., 2001) and lateral mammillary nucleus (LMN, Blair & Sharp, 1995; Stackman & Taube, 1998). It is based on vestibular inputs, angular head velocity signals and rotational signals (J. S. Taube et al., 2025). Via the mamillothalamic tract, the HD signal reaches the anterodorsal thalamic nucleus (AD, J. Taube, 1995), a key area of the HD system. Similar to signals in other sensory modalities, a thalamocortical projection transmits the HD signal to cortical brain areas, the retrosplenial cortex (RSC, Chen et al., 1994; Cho & Sharp, 2001) and the presubiculum (PrS, particularly its dorsal part, which is also referred to as the postsubiculum, Ranck, 1984; J. Taube et al., 1990), where it is combined with environmental landmark information (Yoder et al., 2015). Modeling work suggests that the HD system functions like a continuous attractor such that the directional signal is maintained by the peak location of a stable, persistent activity pattern (Angelaki & Laurens, 2020; S. S. Kim et al., 2017; Redish et al., 1996; Skaggs et al., 1995; Zhang, 1996). It is coherently organised during wake and also during sleep (Peyrache et al., 2015). The HD signal is instrumental for spatial processing in the downstream medial entorhinal cortex (MEC) and hippocampus, and contributes to navigation and memory (Canto et al., 2012; Clark et al., 2024; Hulse & Jayaraman, 2020; Preston-Ferrer et al., 2016; Winter et al., 2015).

Numerous studies on the overall serial connectivity of the spatial orientation system have focused on the tractable HD signal and its transmission from the LMN, to AD, to cortex. However, the Papez circuit also comprises a parallel pathway from the medial mammillary nucleus (MMN) to AV (Aggleton et al., 2010; Cruce, 1975; Guison et al., 1995; Mathiasen et al., 2021; Seki & Zyo, 1984; Vann et al., 2007; Vann & Aggleton, 2004). In contrast to AD, most AV neurons do not signal HD (Lomi et al., 2023; Tsanov, Chah, Vann, et al., 2011). Both anterior thalamic nuclei are important

for memory (Jankowski et al., 2013; Roy et al., 2021, 2022), and AV neurons more than AD neurons possess the particularity to be modulated by theta oscillations (Lomi et al., 2023; Tsanov, Chah, Wright, et al., 2011; Viejo & Peyrache, 2020). Both AD and AV send strong projections to the cortical HD areas (Richevaux et al., 2025; Van Groen & Michael Wyss, 1990; Van Groen & Wyss, 1990b, 1990a, 1995, 2003), such that the two anterior thalamic information streams meet in the PrS and in the RSC (Aggleton et al., 2010; Bubb et al., 2017). Their convergence likely contributes to the functionally important theta modulation of HD signals in the parahippocampal area, and phase precession relative to the head turning angle (Ji et al., 2025; Vollan et al., 2025). Simultaneous recordings of AD and RSC show joint HD activity (Van Der Goes et al., 2024). Simultaneous recordings of AD and PrS indicate reliable spike transmission with head direction information flowing mainly from AD to PrS (Peyrache et al., 2015). Thus, while both PrS and RSC receive their input from AD and from AV, it is unclear to what extent these inputs are segregated, and whether one of the two subnuclei has privileged connectivities with either PrS or RSC. It is further unclear whether the thalamocortical projection neurons receive separate sets of input from the upstream mammillary bodies.

Understanding the role of the anterior thalamic nuclei has gained significance, as they serve as a crucial bridge between hypothalamic and cortical regions (Bubb et al., 2017; Guison et al., 1995; Lomi et al., 2021; Mathiasen et al., 2021; Shibata, 1992, 1993b, 1993a; Stackman & Taube, 1998, 1998; J. Taube, 1995; J. S. Taube, 2007; Van Groen & Michael Wyss, 1990; Van Groen & Wyss, 1990a, 1995; Vann et al., 2007; Vann & Aggleton, 2004). Unlike the traditional view of the thalamus as a simple relay, the anterior thalamic nuclei are involved in multiple cognitive functions. Their widespread anatomical connections with other brain regions (Nassar et al., 2018; Richevaux et al., 2025; Roy et al., 2021, 2022; Van Der Goes et al., 2024) supports not only a key role for spatial orientation, but also for memory and for interactions with hippocampal activity (Ajabi et al., 2023; Blanco-Hernández et al., 2024; Lomi et al., 2023; Peyrache et al., 2015; Roy et al., 2021, 2022; Viejo & Peyrache, 2020). However, the intrinsic and integrative properties of neurons in the AD and AV have been little investigated.

Here, we investigated the mammillo-thalamo-cortical connectivity using monosynaptic tracing and described the topographical organisation of PrS-projecting

and gRSC-projecting thalamic neurons in the AD and AV. We also analysed their intrinsic electrophysiological and morphological properties. We used slice optogenetics to examine the postsynaptic events in the ipsilateral and contralateral thalamic subnuclei driven by unilateral mamillary inputs. Our data show that AD and AV neurons are distinct, regardless of their projection targets, and that they receive inputs from lateral and medial mammillary bodies of both hemispheres.

Materials and Methods

Animals

Wild-type and transgenic mice from C57BL/6 strain were used for the experiments. The animals' age was chosen depending on the experiment: for patch clamp recording without viral injections, P27-40; for patch clamp with viral injections, P35-40; for stereotaxic injections, P50-60. Male and female mice were equally used for the experiments. Mice were housed with a 12 hours light/dark cycle with food and water available ad libitum. All experiments were conducted in accordance with the European Community Council Directive (2010/63/EU) and French law (87/848). This project was approved by the ethics committee of the Université Paris Cité and the French Ministry for Higher Education and Research (APAFIS #47881-202404291838548 v5).

Stereotaxic injections

Mice were habituated in the waiting room for at least one hour prior to the surgical process. The waiting room was separated from the main surgery room. The animals were anesthetised by isoflurane (3 % for induction and 1.4-1.8 % for maintenance, ISO-VET, Piramal). Buprenorphine (0.05 mg/kg, Buprécare®, Axience) was administered subcutaneously and lidocaine (2 mg/kg, Lidocaïne®, MSD) was locally injected into the space between the scalp and skull to provide local anesthesia. Animals were head-fixed in a digital stereotaxic apparatus (KOPF®). Injections of tracers and virus were delivered into the target brain regions by Hamilton syringe (Nanofil syringe 10 µl, NF-SYR, WPI) and automatic injector (78-8130, KD Scientific). The target injection volumes and coordinates (AP/ML/DV) for each brain region were as follows (in mm from Bregma), PrS: 200 nL at 4.06/-2.00/-2.15, gRSC: 300 nL at -2.10/-0.20/-0.85, AD & AV nuclei: 200 nL at -0.82/-0.75/-3.20, MBO: -2.80/-0.75/-5.35. All injections were performed unilaterally at each target site for 10 minutes. The Hamilton syringe was left in place for an additional 5-10 minutes before removal. Carprofen (5 mg/kg, Rimadyl®, Zoetis) was administered after suturing to provide analgesia.

For retrograde tracing of thalamic neurons projecting to cortical regions, cholera toxin subunit-B (CTB) conjugated with Alexa Fluor 488 and 647 (C22841 and C34778, Thermo Fisher Scientific), and red Retrobeads (Lumafluor) were used as retrograde tracers. Following CTB injection, we waited 5-7 days to achieve optimal visualisation of CTB fluorescence in the brain. For retrobeads, we waited a minimum of 2 day post-injection to ensure a sufficient signal.

For viral injection, we waited 3-4 weeks to achieve sufficient expression, before proceeding with slice electrophysiology or anatomical tracing. AAV5-Syn-Chronos-GFP-WPRE-bGH (Addgene 59170, Penn Vector Core) was injected into the MBO for optogenetic experiments. AAV(retro)-Syn-H2B-GFP-TVA-N2c.G-WPRE3 (BA-335, Charité Viral Core Facility) was injected into the PrS or gRSC to express TVA on the thalamic projecting neurons. After 3 weeks, RABV CVS-N2c(deltaG)-tdTomato (BR-31, Charité Viral Core Facility) was injected in the AD & AV region.

Tissue fixation and microscopy

For anatomical tracing experiments, mice were deeply anaesthetised by the cocktail of ketamine (100 mg/kg, KétamineTM 1000, Virbac) and xylazine (10 mg/kg, RompunTM 2%, Elanco). They were perfused via the heart by phosphate buffer solution (PBS) (25 mL), followed by fixative (Antigent fix, P0016, DIAPATH) (25 mL). The harvested brains were post-fixed overnight at 4°C with constant agitation. After the postfixation, the brains were washed 3 times using PBS (20 minutes each) at room temperature. The fixed brains were sliced using a vibratome (VT1200S, Leica) in 70 - 100 µm thick coronal sections. DAPI (D9542, Sigma) was used to stain nuclei for cell detection or anatomical delineation. Slices were mounted with an optimal mounting medium (for scanning: Vectashield Antifade Mounting Medium, H-1000, VectorLabs; for confocal microscopy: ProLong Gold Antifade mountant, P36930, Invitrogen). Brain sections were imaged using a whole-slide scanner (AxioScan.Z1 Slide scanner, Zeiss) with a 10x objective to confirm injection sites and expressions. A confocal microscope (LSM710, Zeiss) was used for higher resolution imaging to identify the labeled profiles and the morphology of biocytin-filled neurons.

For monosynaptic rabies tracing, PFA-fixed brains were coronally sectioned at 40 µm and imaged using a custom-made serial two-photon tomography (STPT) setup

(Timothy Ragan, 2012). For each 40 µm slice, eight images were acquired across a 5 µm optical section using BakingTray (https://github.com/SWC-Advanced-Microscopy/BakingTray) and ScanImage (Vidrio Technologies, USA; RRID:SCR_014307). Image stitching was performed with StitchIt (https://github.com/SWC-%20Advanced-Microscopy/StitchIt). The stitched images from each optical section were then z-stacked (80–100 µm) using python packages; Tifffile (https://github.com/cgohlke/tifffile) and Numpy (Harris et al., 2020).

Registration on the 3D brain diagram

Whole brain images were obtained with a whole-slide scanner (AxioScan.Z1 Slide scanner, Zeiss) and used for the anatomical analysis of thalamic projecting neurons. The serial images containing AD and AV regions were analysed. Three sets of serial whole-brain images containing thalamic nuclei were obtained. To control for potential differences in labeling efficiency between CTB-488 and CTB-647, CTB injections were alternated: in two mice, CTB-488 was injected into the PrS and CTB-647 into the gRSC, while the injections were reversed in another mouse. Each whole brain image was layered on the corresponding level in the standardised Allen Mouse Brain Atlas CCFv3 (Wang et al., 2020), using ABBA (Chiaruttini et al., 2025). The registered images were transferred to QuPath (Bankhead et al., 2017) for further analysis. First, DAPI-positive cells were detected. Within these cells, the intensity of green and far-red fluorescence in the cytoplasm was measured to identify their projection profiles. The 3D coordinates of each detected cell were registered on the 3D brain diagram by brainrender (Claudi et al., 2021).

Thalamic slice preparation for electrophysiology

For patch clamp experiments, mice were deeply anesthetised with a mixture of ketamine and xylazine, administered intraperitoneally. Brains were extracted and placed in a chilled cutting solution (4 °C) containing: 125 mM NaCl, 25 mM sucrose, 2.5 mM KCl, 25 mM NaHCO3, 1.25 mM NaH2PO4, 2.5 mM D-glucose, 0.1 mM CaCl2, and 7 mM MgCl2, equilibrated with 5% CO2 / 95% O2. Each brain was coronally cut in 300 µm thick sections using a vibratome (VT1200S, Leica). Typically, 1-2 acute

slices containing the AD and AV were obtained per mouse. The slices were then transferred to a chamber containing ACSF (124 mM NaCl, 2.5 mM KCl, 26 mM NaHCO3, 1mM NaH2PO4, 11 mM D-glucose, 2 mM CaCl2, and 2 mM MgCl2, oxygenated with 5% CO2 in O2 (pH 7.3, 305–315 mOsm/L). After a 15-minute recovery in 35 ℃, slices were stored at room temperature prior to the experiments. All salts were obtained from Sigma-Aldrich.

Whole-cell patch-clamp recordings

AD and AV were identified under a Axioskop 2 FS plus microscope (Zeiss, 5X objective, transmitted light) next to the 3rd ventricle and the anterior part of the hippocampal formation. A high magnification (60x) objective was used to visualize neurons with an EMCCD Luca-S camera (Andor) using infrared differential interference contrast. Retrobead labeled thalamocortical projecting neurons were identified with LED illumination (fed into the epifluorescence port; Cairn Research).

Glass pipettes for electrophysiological recording were prepared using a horizontal electrode puller (P-87, Sutter Instruments) from borosilicate glass (1.5 mm external diameter, 30-0057, Harvard Apparatus). The electrode resistance, when filled with an internal solution containing: 135 mM K-gluconate, 1.2 mM KCl, 10 mM HEPES, 0.2 mM ethylene glycol tetra-acetic acid, 2 mM MgCl2, 4 mM MgATP, 0.4 mM Tris-GTP, 10 mM Na2-phosphocreatine and 2.7 mM biocytin (pH 7.3 and 290 mOsm), was 4–8 MΩ. The tip of the patch pipette was placed to target the cell body of neurons in AD or AV, using a Luigs & Neumann micromanipulator. Whole-cell current-clamp recordings were made with an Multiclamp 700B amplifier (Molecular Devices), and signals were digitalised using a Digidata 1440A or 1550B (Molecular Devices).

The voltage was held at -70 mV until a gigaseal had formed, then the membrane was broken and recording began. Recordings were filtered at 10 kHz and digitized at 50 kHz. Results were not corrected for the liquid junction potential. Patched neurons needed to pass quality-control criteria that included an access resistance R_{access} <35 MΩ, relative action potential (AP) amplitude at rheobase > 50 mV and an absolute amplitude above 0 mV, a stable baseline voltage, and a resting membrane potential < -50 mV.

To analyse the intrinsic electrophysiological properties of AD and AV neurons, recordings were performed in current clamp mode. Resting membrane potential (RMP) was measured 5 to 10 minutes after gaining whole-cell access. Next, we performed further recordings by injecting incrementally increasing current steps of 800 ms duration (step protocol), while maintaining the membrane potential at -70 mV. The protocol also included a short -20 pA pulse for 150 ms to calculate the membrane time constant and to check for stability over time. The range of injected current steps started at a value sufficient to hyperpolarise the cell to -100 mV and extended up to +400 pA.

Ih current blocker ZD7288 (2 µM, N-1000, Tocris) was applied to the slices via bath perfusion. While ZD7288 was being delivered, we monitored the voltage sag by injecting hyperpolarising current steps. 5-10 minutes after its addition, the current step protocol was performed again.

We tested for functional connectivity between AD and AV neurons using dual patch-clamp recording in current clamp configuration. AD neurons were maintained at -60 mV and AV neurons at -70 mV. In each pair, current pulses were alternatively injected. A train of 20 pulses was delivered at 25 Hz, with a duration of 1 ms, repeated 10 times. Current was injected at levels sufficient to induce spiking activity in each cell, typically ranging from 1.0 nA to 2.5 nA. In the experiments of ZD7288 application and AD-AV dual recording, AD neurons were maintained at -60 mV and AV neurons at -70 mV, following their intrinsic RMP.

Optogenetics

For photostimulation experiments, a 470-nm blue light was delivered via a 60x objective immersed in ACSF, using LED illumination (OptoLED, Cairn Research) controlled by pClamp software (Molecular Devices).

We determined the threshold light intensity required to evoke oEPSPs or action potentials in each neuron. This was achieved by incrementally increasing the blue light intensity in current clamp configuration (up to a maximum of 3 mW, Figure 6A, B), using a train of 10 light pulses (0.5 ms in duration, repeated at 20 Hz), for each level of intensity. Once the postsynaptic cell fired action potentials, the light intensity was noted as threshold (red arrow, Figure 6A). For connected cells, oEPSC amplitude and

latency were measured at the subthreshold light intensity in voltage clamp mode. oEPSC amplitude was measured by the difference between the baseline and the peak. Latency was calculated by subtracting the time at which the oEPSC peak reached 10% of its maximum amplitude from the onset of the light stimulation. Quantification was performed using AxoGraphX (AxoGraph Scientific) software. The dynamics of oEPSCs and spike probability were averaged across 10 repetitions for each stimulus. oEPSCs were measured in voltage clamp mode, and spike probability was measured in current clamp mode. Spike probability was calculated as the proportion of stimulations that successfully evoked action potentials.

To test for direct, monosynaptic photostimulation evoked postsynaptic currents, neurons were recorded in voltage clamp mode (AD neurons held at -60 mV and AV neurons held at -70 mV) in presence of TTX (1 µM) and 4-AP (100 µM). The glutamatergic nature of synaptic currents was probed by bath applying APV (100 µM) and NBQX (10 µM) at -60 mV (for AD neurons) or -70 mV (for AV neurons) and +70 mV holding potential.

Electrophysiological data analysis

The analysis of intrinsic electrophysiological properties was performed using a custom written Python script (https://github.com/DLim-neuro/IPA). The resting membrane potential was measured as the mean membrane potential over 20 seconds of the recording without current injection. Neuronal input resistance was calculated as the slope of the current-voltage relationship measured between -80 mV and -60 mV. The membrane time constant (τ) was calculated by fitting a double-exponential function to the membrane response evoked by a -20 pA hyperpolarising pulse, averaged across all sweeps (Golowasch et al., 2009). Sag ratio, reflecting Ih current, was calculated as the ratio of the minimum membrane potential during the first half (0-400 ms during the current injection) of a hyperpolarising current injection to the mean membrane potential during the second half (400-800 ms during the current injection). This was measured on a trace where the membrane potential was hyperpolarised to approximately -100 mV. The minimal current injection necessary to evoke an action potential was determined (Rheobase). Action potential kinetics were quantified from the rheobase spike, defined as the first action potential evoked during the recording.

Threshold was defined as the membrane potential when dV/dt > 30 mV/ms. The latency was defined as the time between the beginning of current injection and the threshold. AP peak was measured at the maximum membrane potential of action potential. AP width was measured as the time between the two points at half-amplitude, calculated between the threshold and the AP peak. AP rise amplitude was measured between the threshold and AP peak. Afterhyperpolarisation (AHP) was defined as the difference between threshold potential and the minimum membrane potential during repolarisation. Max depolarisation and max repolarisation were the maximum and minimum points of dV/dt, respectively. Multiple aspects of the neuronal firing pattern were analysed from the voltage trace that displayed action potential firing at close to 10 Hz. A Burst index was calculated as the shortest interspike interval (ISI) divided by the mean ISI. A 100 ms initial bursting window was defined from the onset of current injection to analyse initial bursting activity. The number of initial burst ISIs (< 6 ms) and mean ISI was measured during this time window. The Adaptation index was calculated as the last ISI divided by mean ISI. The Fast doublet index was calculated as the mean ISI divided by the first ISI. The Fast doublet ratio was calculated as the second ISI divided by the first ISI. The Δ peak AP1-AP2 means the peak difference between first and second AP when the neuron is firing at nearly 10 Hz. Post-train AHP was defined as the difference between the lowest membrane potential within 100 ms after the end of the current injection and the mean membrane potential measured over a 200 ms window starting 500 ms after the current injection, at +100 pA step above rheobase. The input-output slope was calculated by plotting firing frequency as a function of injected current between 0 Hz to 9 Hz. Lastly, the firing rate in response to 200 pA current injection was measured. Lastly, Rebound spike probability indicates the presence of rebound spikes occurring within 100 ms after the offset of a hyperpolarising current injection.

Cluster analysis

We performed principal component analysis (PCA) using scikit-learn library in Python to reduce the dimensionality for comparative analysis. From the original set of 25 electrophysiological properties, three variables (AP rise amplitude, Max repolarisation rate, and AP width) were excluded, because their pairwise Pearson

correlation coefficients were greater than ±0.85. The remaining 23 properties were standardised and included in the PCA (RMP, Input resistance, Time constant, Sag ratio, Rheobase, Threshold, Latency, AP peak, AHP, Max depolarisation rate, Current at 10 Hz, Burst index, Initial burst ISI, Mean initial ISI, Adaptation index, Fast doublet index, Fast doublet ratio, Δ peak between AP1-AP2, Post-train AHP, Input output slope, Firing rate at 200 pA, and Rebound spike probability). The first three principal components were used to visualise the data in 3D space. To investigate potential categorisation, Ward's hierarchical clustering method with Euclidean distance was applied. The cluster structure was shown as a dendrogram.

Biocytin staining and 3D reconstruction

Following patch clamp recording, slices were fixed overnight at 4 ℃, then rinsed in PBS (3 times, 20 minutes each), and stored in 30% sucrose at 4 ℃, and agitated. To permeabilise the cell membrane, slices underwent three freeze-thaw cycles in the sucrose solution on dry ice, then were rinsed in PBS (2 times for 30 minutes each, then last rinse for 2 hours). A saturation step was performed by incubating slices in a solution containing 2% skim milk powder and 1% Triton X-100 (T8787, Sigma-Aldrich) in PBS for 2 hours at room temperature. After this, the solution was replaced with one additionally containing streptavidine conjugated with Alexa-647 (1:500, S21374, Invitrogen) and DAPI (1:2000), and the slices were incubated overnight at 4 ℃. After the staining, slices were rinsed with PBS (2 times for 30 minutes each, and the last rinse for 2-4 hours). The side of the slice showing biocytin-labelled neurons was identified under a microscope (Nikon Eclipse TE-2000E) before mounting using Prolong Gold Antifade mountant (Life technologies, P36930). For morphological analysis, high-resolution z-stack images (20x) were acquired using a confocal microscope. The morphologies of biocytin filled neurons were reconstructed using IMARIS software.

Quantification and statistical analysis

Data were analysed in Python, using PyABF (Harden, 2022) to extract electrophysiological properties and scikit-learn (Pedregosa, 2011) for dimensionality

reduction and clustering. Statistical analysis was performed using SciPy (Virtanen et al., 2020). AxoGraphX (AxoGraph Scientific) software was used to extract the properties from optogenetic experiments. Results are reported as mean ± SEM. Group comparisons were made using the Mann-Whitney U test for unpaired data, and the Wilcoxon signed-rank test for paired data. Significance levels are indicated using a four-star system: $p < 0.05$ (*), $p < 0.01$ (**), $p < 0.001$ (***), $p < 0.0001$ (****).

Results

Mammillo-thalamo-cortical connectivity

The mammillothalamic tract provides the main inputs to the AD and AV thalamic nuclei. We asked, what is the origin of signals that are destined to be transmitted to either PrS or to gRSC? To determine the location of input neurons that are presynaptic to identified thalamocortical projection neurons, trans-monosynaptic rabies virus tracing was used. Retrograde TVA-expressing helper virus was injected into the PrS (Figure 1A-B) and gRSC (Figure 1E,F) to selectively label thalamocortical projection neurons. Four weeks later, EnvA-pseudotyped rabies virus was injected into the anterior thalamus. Starter cells were found in AD and in AV, for PrS (Figure 1C) or gRSC (Figure 1G) projecting neurons. Presynaptic neurons were labelled in the lateral and medial mammillary bodies, in the thalamic reticular nucleus (TRN), the orbitofrontal cortex, and the claustrum. Presynaptic neurons were also present in the deep layers of RSC and in the deep layers of PrS, where cortico-thalamic backprojections originate. Here, we focus on the distribution of presynaptic cells in the lateral and medial mammillary bodies (Figure 1D, H). We found that more neurons in the ipsilateral than in the contralateral LMN were labeled, consistent with a strong ipsilateral and less strong contralateral projection to neurons in AD (Guison et al., 1995; Seki & Zyo, 1984; Shibata, 1992). In MMN, the labeling was also predominantly ipsilateral. However, some labeled neurons were present in the contralateral MMN, close to the midline, in the most anterior parts of the mammillary bodies. It is expected that neurons in the LMN target AD, and neurons in MMN target AV (Cruce, 1975; Dillingham et al., 2015; Guison et al., 1995; Jankowski et al., 2013; Seki & Zyo, 1984; Shibata, 1992; Veazey et al., 1982). Here, we report no apparent differences in mammillary inputs as a function of the cortical projection target of AD and AV neurons. To follow-up on those observations, we aimed at clarifying the topography, segregation or overlap, of neurons with different cortical projection targets in the AD and the AV. The bilateral mammillary-thalamic input connectivity was further investigated on a functional level using optogenetics.

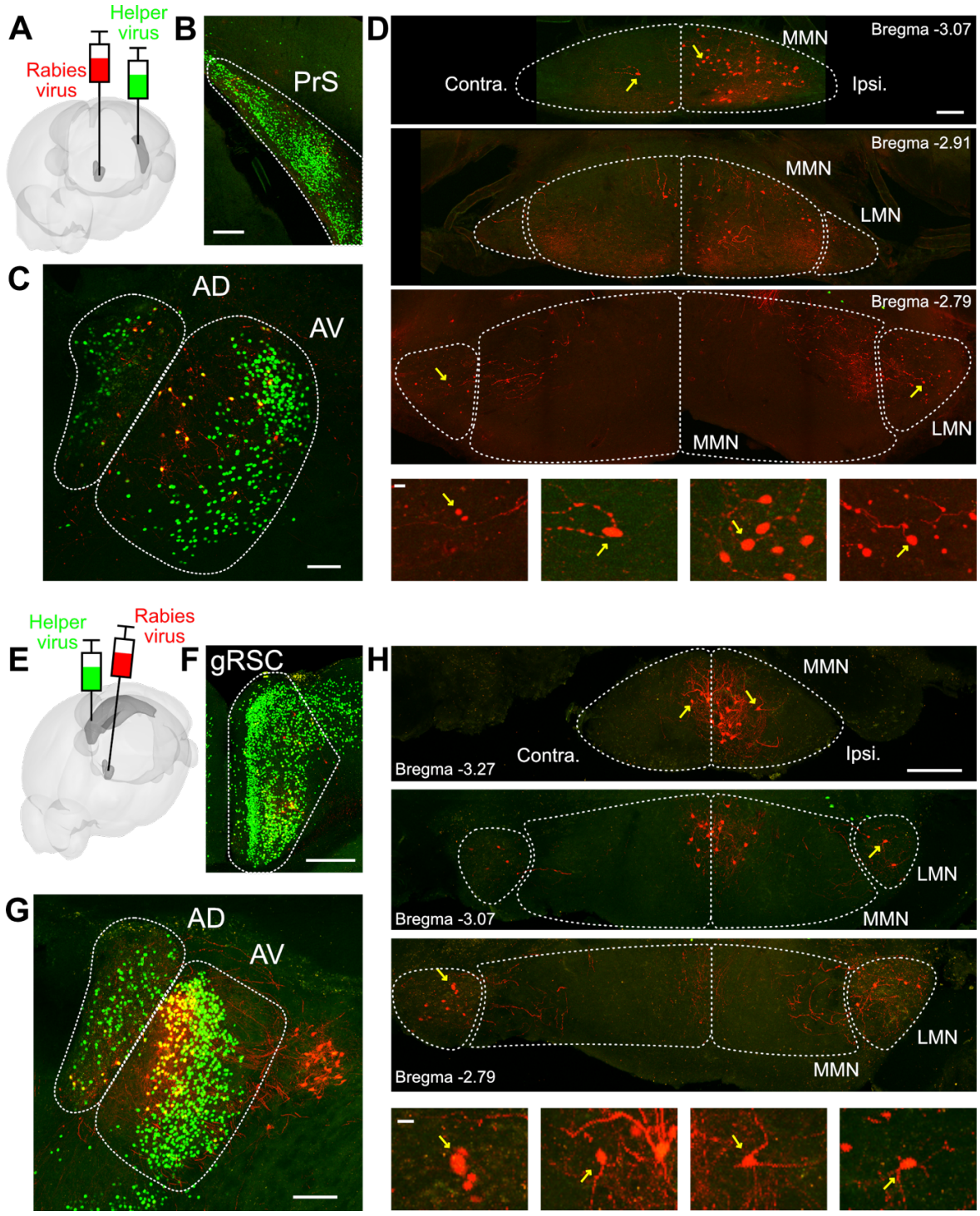
A
Helper virus
Rabies virus
B
PrS
C
AD
AV
D
Bregma -3.07
MMN
Contra.
Ipsi.
Bregma -2.91
MMN
LMN
Bregma -2.79
MMN
LMN
E
Helper virus
Rabies virus
F
gRSC
G
AD
AV
H
MMN
Bregma -3.27
Contra.
Ipsi.
LMN
Bregma -3.07
MMN
LMN
Bregma -2.79
MMN

Figure 1. Monosynaptic rabies tracing of PrS-projecting / gRSC-projecting thalamic neurons.

A) Injection strategy. The helper virus is injected in the PrS to retrogradely express TVA in thalamic neurons projecting to the PrS. The G-deleted rabies virus is injected into the anterior thalamus, labeling PrS-projecting starter cells in the thalamus. By retrogradely crossing one synapse, neurons whose axons make synaptic contacts with thalamic neurons projecting to PrS will be labelled.
B) Injection site of helper virus in the PrS. Scale bar: 200 μm.
C) Viral expression in the AD and AV. Helper virus-expressing cells (green) and starter cells (green and red) are found in both subnuclei. Scale bar: 100 μm.
D) Rabies-labeled input neurons (red) in the MMN and LMN at 3 antero-posterior levels. Relevant AP levels from bregma are indicated in order relative to the MBO images. Scale bar: 100 μm.
E) Injection strategy. The helper virus is injected in the gRSC to retrogradely express TVA in thalamic neurons projecting to the gRSC. The g-deleted rabies virus is injected into the anterior thalamus, labeling gRSC-projecting starter cells in the thalamus. By retrogradely crossing one synapse, neurons whose axons make synaptic contacts with thalamic neurons projecting to gRSC will be labelled.
F) Injection site in the gRSC. Scale bar: 200 μm.
G) Viral expression in the AD and AV. Helper virus-expressing cells (green) and starter cells (green and red) are shown in both subnuclei. Scale bar: 100 μm.
H) Rabies-labeled input neurons (red) in the MMN and LMN at 3 antero-posterior levels. Scale bar: 100 μm.

PrS, Presubiculum; gRSC, granular Retrosplenial Cortex; AD, anterodorsal thalamic nucleus; AV, anteroventral thalamic nucleus. MMN, Medial Mammillary Nucleus; LMN, Lateral Mammillary Nucleus.

Topographical organization of neurons in AD and AV projecting to PrS and gRSC

To study the anatomical distribution of anterior thalamic neurons projecting to the PrS and RSC we retrogradely labelled them using cholera toxin subunit-B (CTB) conjugated with two different fluorophores. CTBs were injected unilaterally in the PrS and in the gRSC, covering most of the PrS, and a significant portion of the antero-posterior extent of the gRSC (Figure 2A; injection sites are documented in figure supplement 1). Two subnuclei of the anterior thalamus, AD and AV, were strongly labeled, indicating that they send their axons to PrS and to gRSC (Figure 2B). In addition, some retrogradely labelled neurons from the gRSC injection were observed in the anteromedial thalamic nucleus (AM). A high proportion of cells in AD and AV were thalamo-cortical projecting neurons: out of all DAPI-labelled cells, 43 ± 3 % of cells in AD projected to PrS, while 27 ± 6 % projected to gRSC. In AV, 25 ± 8 % of cells projected to PrS, and 26 ± 8 % projected to gRSC. PrS- and gRSC-projecting neurons were partly segregated in the AD and in the AV. PrS-projecting neurons were distributed in the dorsomedial portion of AD and the dorsolateral portion of AV, while gRSC-projecting neurons were distributed in the ventrolateral portion of AD and in the ventromedial portion of AV (Figure 2B). We examined the topographic organisation of thalamocortical projection neurons in serial brain slices containing the anterior thalami from three well labeled brains. The combined 3D reconstruction of thalamic projection neurons showed their topographical distribution in coronal sections, and also in the sagittal and horizontal planes (Figure 2D, E). In AD, gRSC-projecting neurons were concentrated in the posterior region, while PrS-projecting neurons were distributed across the anterior-posterior axis. In AV, PrS-projecting neurons were located in the anterior region, while gRSC-projecting neurons were located in the posterior part of AV. While the PrS- and gRSC-projecting neurons were partly segregated within AD and AV, they were also overlapping. The presence of double labeled neurons indicates that their axons bifurcate, targeting both PrS and gRSC. These double-projecting neurons were located in the center of AD and AV respectively, wedged in the fringe areas of neurons that are solely projecting to either the PrS or RSC. Among the projecting neurons, 28 ± 5 % were double-projecting in AD, and 12 ± 3 % in AV (Figure 1F). We note that the actual proportion of double-projecting neurons may be even higher, limited here by the efficiency of the retrograde labeling approach.

Overall, our findings show that PrS-projecting and gRSC-projecting thalamic neurons are topographically arranged in the AD and AV subdivisions of the anterior thalamus. This suggests that many individual thalamocortical projection neurons transmit action potentials to both PrS and gRSC.

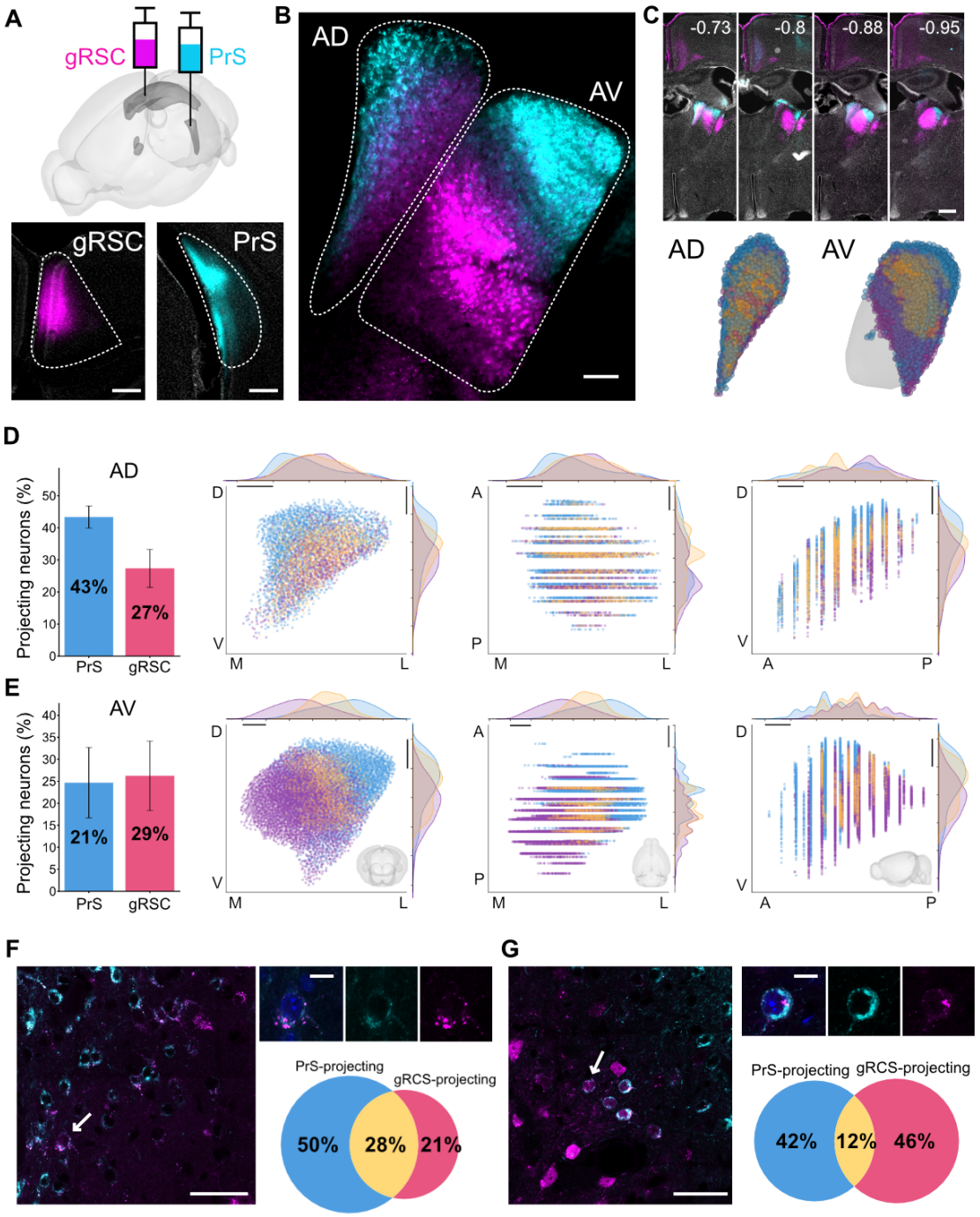

Figure 2. Segregation and overlap of thalamocortical projection neurons in AD and in AV.

A) Top: Injection of CTB-647 in gRSC and CTB-488 in PrS, to retrogradely label the thalamic projecting neurons. Bottom: Injection sites in gRSC and PrS. Scale bar: 300 μm
B) Topographical organization of retrogradely labelled neurons in AD and AV in coronal brain sections. Cyan indicates PrS-projecting neurons and magenta indicates gRSC-projecting neurons. Scale bar: 100 μm.
C) Top: Series of whole brain images with CTB-labelled neurons in the ATN at different antero-posterior levels. Scale bar: 500 μm. Bottom: 3D whole brain diagrams with CTB-labelled neurons in the AD and AV (n = 3).
D) Left: Proportion of each projecting profile in the AD. Right: Scattered plots presenting the standardised coordinates of each CTB-labelled neuron in coronal, horizontal, and sagittal orientation. Coronal slices collected from Bregma -0.30 to -0.12mm. Scale bars in each orientation (vertical/horizontal in mm): coronal (0.1/0.2), horizontal (0.1/0.1), sagittal (0.1/0.2).
E) Same for AV.
F) Single and double-positive neurons in AD. PrS-projecting neurons, cyan; gRSC-projecting neurons, magenta. Scale bar, 50 ¬μm. Arrow indicates double-labeled neurons, cell bodies shown at higher resolution. Scale bar, 10 μm. Pie charts indicate the proportions of single and double-positive neurons.
G) Same for AV.

Cluster analysis of electrophysiological parameters segregates AD and AV thalamic neurons

We measured the passive membrane properties, action potential (AP) waveforms and firing patterns of 137 thalamic neurons in AD and AV. Coronal slices containing the anterior thalamus were prepared from a total of 54 mice (1-2 slices per animal). The AD and AV nuclei are shown next to the highly myelinated stria medullaris, that delimits AD on its medial side (Figure 3A, B). The AD had a characteristic ovoid or drop-like shape, and AV appeared as an oblong structure, traversed by fiber bundles. In a subset of experiments, PrS- or gRSC-projecting neurons had been labelled with retrograde tracers for targeted patch clamp recordings. Representative recordings are shown for four retrobead labeled neurons in AD and in AV, each projecting either to PrS or to gRSC (Figure 3C).

To evaluate if AD and AV thalamocortical neurons fall into distinct physiological groups, we performed Principal Component Analysis (PCA) (Figure 3D) and Ward's unsupervised cluster analysis (Ward, 1963) based on 25 electrophysiological variables as listed in Table 1. Measurements for each variable in our data set were transformed to standard scores across all cells. To avoid artificially weighting highly correlated variables, we excluded the AP maximum repolarisation rate, AP rise amplitude and AP width, because they were highly correlated with maximum depolarization rate and AP peak, respectively ($r > 0.85$ or $R < -0.85$ in the correlation matrix, cf. Figure 3 - figure supplement 1A,B). The results of the PCA are shown in Figure 3D. The first principal component (PC1) accounted for 24.88 % of the variance (see Figure 3 - figure supplement 1C). The properties of highest loading in this component were sag ratio, Initial burst ISI, Δ peak between AP1-AP2, post-train AHP, and firing rate at 200 pA. The second principal component (PC2) captured 16.56 % of the variance. Input resistance, max depolarisation rate, time constant, AP peak, and resting membrane potential gave the highest loading on this component. Lastly, the third principal component captured 13.16 % of the variance, with rheobase, mean initial ISI, threshold, current at 10 Hz, and firing rate at 200 pA contributing most strongly. The PCA shows a clear separation between AD and AV neurons. The dendrogram was generated using hierarchical clustering on the first three principal components (PC1, PC2, and PC3; Figure 3E). It reveals two well separated clusters that correspond largely to neurons in AD or AV, indicating that they possess distinct

electrophysiological properties. As expected from the anatomical overlap between PrS- and gRSC-projecting neurons within AD and AV, projection specific neurons were not segregated in the dendrogram. They were found in both AD and AV clusters (Figure 3D,E). The properties of PrS-projecting or gRSC-projecting neurons within AD or within AV were not significantly different (Table 1 - table supplement 2), with the exception that PrS-projecting AD neurons were more hyperpolarized than gRSC-projecting AD neurons. The complete set of intrinsic properties of PrS- or gRSC-projecting neurons in AD and AV is shown in the plots in the Table 1 - figure supplement 1, along with measures from unlabeled neurons in AD and AV. In the following, we describe the electrophysiological properties of neurons in AD and in AV, and how they are different.

A total of 64 neurons were recorded in AD (16 PrS-projecting, 12 gRSC-projecting, and 36 unlabelled neurons) and 73 neurons were recorded in AV (13 PrS-projecting, 12 gRSC-projecting, and 48 unlabelled neurons). The average resting membrane potential (RMP) of AD neurons was significantly more depolarized than in AV neurons (-60.3 ± 0.5 mV vs. -71.0 ± 0.5 mV; $p < 0.0001$), but neither AD nor AV neurons were spontaneously firing action potentials. The input resistance in AD neurons was 171 ± 8 MOhm, while it was significantly higher in AV neurons (222 ± 12 MOhm; $p = 0.003$). The time constant of AD neurons was shorter than that of AV neurons (tau, 9.6 ± 0.5 ms vs 17.1 ± 0.6 ms respectively; $p < 0.0001$). AD neurons had a stronger voltage sag following hyperpolarizing pulses than AV neurons (sag ratio, 1.41 ± 0.02 vs 1.06 ± 0.00; $p < 0.0001$). AD neurons had a stronger voltage sag following hyperpolarizing pulses than AV neurons (sag ratio, 1.41 ± 0.02 vs 1.06 ± 0.00; $p < 0.0001$) suggesting differences in hyperpolarisation-activated Ih currents.

Action potential properties also differed between AD and AV neurons. To induce the first action potential, a higher rheobase current was required for AD neurons (84 ± 5 pA) than for AV neurons (76 ± 5 pA). AD neurons possess higher threshold, shorter AP width, and higher AHP than AV neurons. We could not observe statistically significant differences in latency, AP rise amplitude, AP peak, max depolarisation rate and max repolarisation rate.

AD and AV neurons are distinguishable based on their firing pattern. We compared their firing patterns for a firing frequency close to 10 Hz. To elicit spiking at

10 Hz, AV neurons require significantly greater injected current (232 ± 14 pA) compared to AD neurons (130 ± 8 pA). AD neurons present an adaptive firing pattern, while AV neurons present an initial burst of 2-5 spikes (Figure 3C and figure supplement 2). The initial burst in AV neurons was typically followed by an interval without spikes. Once sustained firing kicked in with higher current injections, the post-burst spiking was regular or irregular(Figure 3 - figure supplement 2). Some AV cells were reluctant to generate any spikes following the initial burst. In contrast, AD neurons displayed an adaptive firing pattern, characterised by a progressive increase in spike number with increasing current injection. Notably, the difference of peaks between the first and second action potential was larger in AV neurons than AD neurons. At the offset of a depolarizing current injection, a hyperpolarization of the membrane potential was observed in AD neurons, which we named “post-train AHP”, and which was not observed in AV neurons.

AD neurons had an input-output slope of 127 ± 13 Hz/nA, whereas AV neurons had a slope of 46 ± 7 Hz/nA. For a200 pA current injection, AD neurons fired at a frequency of 46 ± 3 Hz, whereas AV neurons fired at 19 ± 3 Hz. Lastly, the rebound spiking after hyperpolarisation was observed more frequently in AD neurons than in AV neurons.

In addition, we examined the electrophysiological properties of AD neurons held at -60 mV, corresponding to their RMP (Figure 3 - supplemental figure 3 and supplemental table 1). The purpose was to identify their electrophysiological responses at their physiological resting membrane potential. At this potential, AD neurons showed modestly lower thresholds and required less current to elicit action potentials, as well as steeper input-output slope compared to -70 mV.

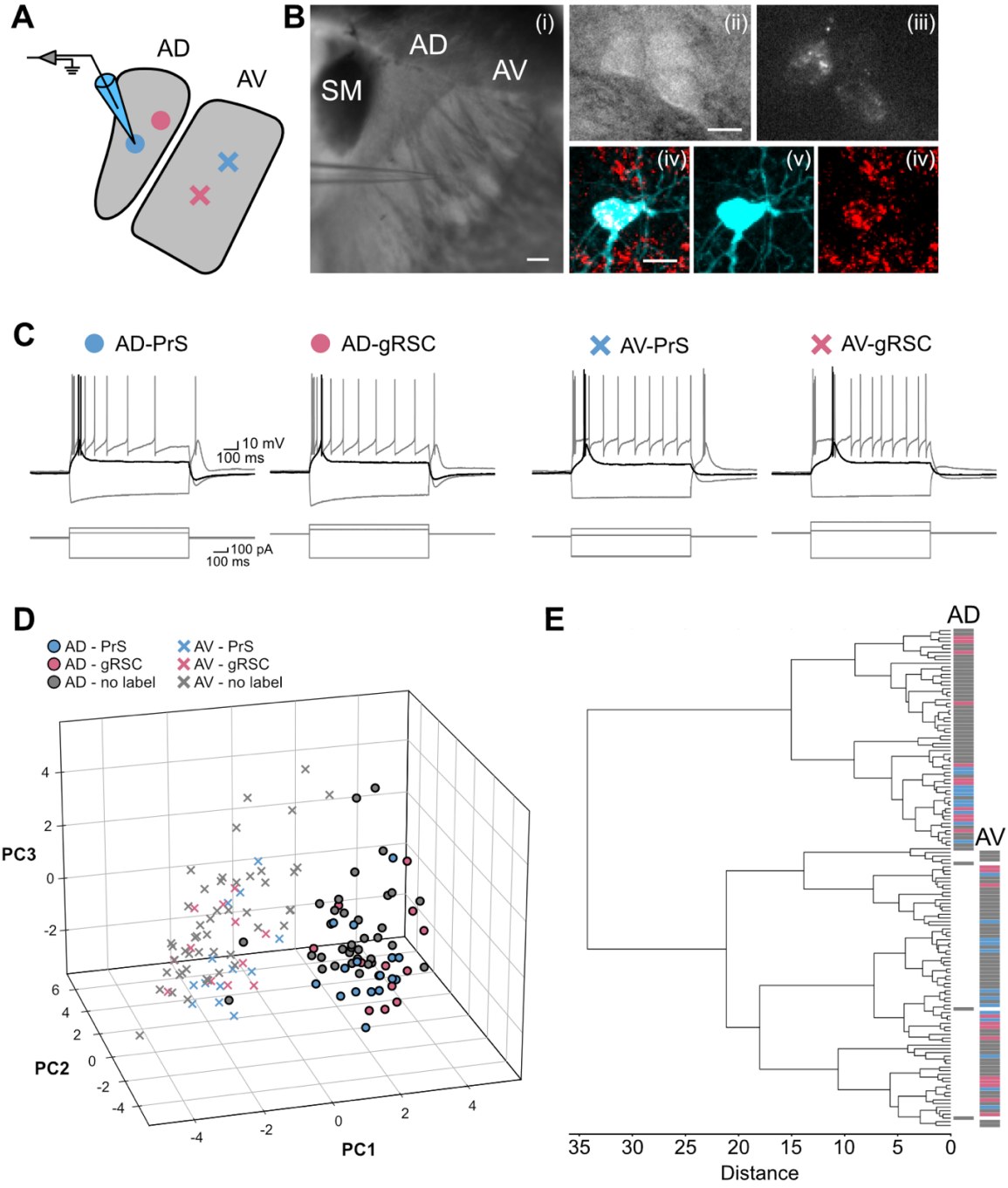
A
AD
AV
B
SM
AD
AV
(i)
(ii)
(iii)
(iv)
(v)
(iv)
C
AD-PrS
AD-gRSC
AV-PrS
AV-gRSC
10 mV
100 ms
100 pA
100 ms
D
AD - PrS
AD - gRSC
AD - no label
AV - PrS
AV - gRSC
AV - no label
PC3
PC2
PC1
E
AD
AV
35 30 25 20 15 10 5 0
Distance

Figure 3. Segregation of neurons in AD and AV, regardless of their cortical projection targets

A) Schematic diagram of patch clamp recording on labelled AD and AV neurons.
B) Images taken during the patch clamp recordings and post hoc confirmation of retrograde labelling on a patched neuron. (i) Screenshot image of acute brain slice (SM: Stria Medullaris). Scale bar: 100 μm. (ii-iii) Screenshot image of neurons under transmitted light and its fluorescent retrograde beads. Scale bar: 100 μm. (iv-vi) Confocal images showing neurons filled with biocytin in cyan and retrograde beads in red. Scale bar: 10 μm.
C) Voltage responses and firing patterns in response to hyperpolarising and depolarising current pulses in AD and AV neurons. All neurons shown in the figure were held at –70 mV using a current-clamp configuration. The relative anatomical locations where each example trace was recorded are presented on panel A.
D) Segregation of AD and AV neurons on the PC1, PC2, and PC3 planes.
E) Hierarchical dendrogram of AD and AV neurons. Anatomical and projection profiles of each leaf are indicated on the right.

	AD			Significance	AV		
	Mean	SEM	N		Mean	SEM	N
Resting membrane potential (mV)	-60.3	0.5	64	****	-71.0	0.5	73
Input resistance (MΩ)	171	8	64	**	222	12	73
Time constant (τ, ms)	9.6	0.5	64	****	17.1	0.6	73
Sag ratio	1.41	0.02	64	****	1.06	0.00	73
Rheobase (pA)	84	5	64	*	76	5	73
Threshold (mV)	-30.9	0.8	64	*	-33.3	0.6	73
Latency (ms)	56	2	64	n.s.	73	5	73
AP rise amplitude (mV)	66.6	1.7	64	n.s.	67.6	1.4	73
AP peak (mV)	35.7	1.5	64	n.s.	34.3	1.2	73
AP width (ms)	0.41	0.02	64	**	0.43	0.01	73
AHP (mV)	-21.5	0.7	64	***	-18.7	0.5	73
Max depolarisation rate (V/s)	402	19	64	n.s.	356	13	73
Max repolarisation rate (V/s)	-199	11	64	n.s.	-172	5	73
Current at 10Hz (pA)	130	8	64	****	232	14	73
Burst index	0.22	0.02	64	***	0.22	0.03	73
Initial burst ISI	0.7	0.1	64	****	2.2	0.2	73
Mean initial ISI (ms)	0.017	0.001	64	****	0.012	0.002	73
Adaptation index	2.31	0.11	64	****	1.84	0.11	73
Fast doublet index	8.00	0.89	64	***	18.16	1.65	73
Fast doublet ratio	1.89	0.10	64	****	4.37	1.75	72
Δ peak between AP1-AP2 (mV)	3.7	0.6	64	****	10.4	0.8	73
Post-train AHP (mV)	9.9	0.5	64	****	2.2	0.3	73
Input output slope (0-9Hz, Hz/nA)	127	13	64	****	46	7	73
Firing rate at 200pA (Hz)	46	3	64	****	19	3	73
Rebound spike probability	0.72	0.06	64	****	0.27	0.05	73

Table 1. Intrinsic electrophysiological properties of neurons in AD and AV.

Impact of Ih currents in AD and AV neurons

To examine the impact of HCN channel expression (Phillips et al., 2019) on the physiology of AD and AV neurons, we applied ZD7288, a selective Ih blocker (Figure 4). Exposure to ZD7288 revealed a contribution of Ih to the resting membrane potential of both AD (n = 11; -61.3 ± 0.6 mV in baseline, and -63.9 ± 2.4 mV in ZD7288) and AV neurons (n = 9; -70.6 ± 0.4 mV in baseline, and -73.5 ± 1.5 mV in ZD7288). It strongly reduced the voltage sag in AD neurons (1.47 ± 0.04 in baseline, and 1.04 ± 0.01 in ZD7288), and also in AV neurons (1.04 ± 0.01 in baseline, and 1.01 ± 0.00 in ZD7288). The AHP became significantly weaker in AD (-27.9 ± 1.2 mV in baseline, and -25.7 ± 1.3 mV in ZD7288) while no significant effect was observed in AV (-16.6 ± 0.7 mV in baseline, and -15.0 ± 0.7 mV in ZD7288). The post-train AHP was also reduced in both AD (3.3 ± 0.6 mV in baseline, and -1.0 ± 0.3 mV in ZD7288) and AV neurons (2.7 ± 0.7 mV in baseline, and -1.1 ± 0.3 mV in ZD7288). Rebound spiking, a hallmark of AD neurons, was strongly reduced (1.00 ± 0.00 in baseline, and 0.45 ± 0.16 in ZD7288) in the presence of the blocker, and abolished in two AV neurons. ZD7288 increased the time constant in AD neurons (22.3 ± 2.8 ms in baseline, and 35.4 ± 5.2 ms in ZD7288), while no significant changes were observed in AV neurons (20.6 ± 0.9 ms in baseline, and 23.0 ± 2.2 ms in ZD7288). The input resistance increased in AD neurons (186 ± 14 MΩ in baseline, and 397 ± 40 MΩ in ZD7288) following ZD7288 exposure, but not in AV neurons (232 ± 17 MΩ in baseline, and 242 ± 25 MΩ in ZD7288). HCN blockade also increased the difference between the first and second AP peaks in both AD (0.5 ± 0.2 mV in baseline, and 2.4 ± 0.9 mV in ZD7288) and AV neurons (12.2 ± 0.8 mV in baseline, and 14.7 ± 0.9 mV in ZD7288). Different levels of HCN channel expression in AD and AV neurons therefore contribute to their distinct passive properties, with stronger physiological impact in AD neurons The detailed quantitative and statistical comparisons are provided in the figure 4 - table supplement 1.

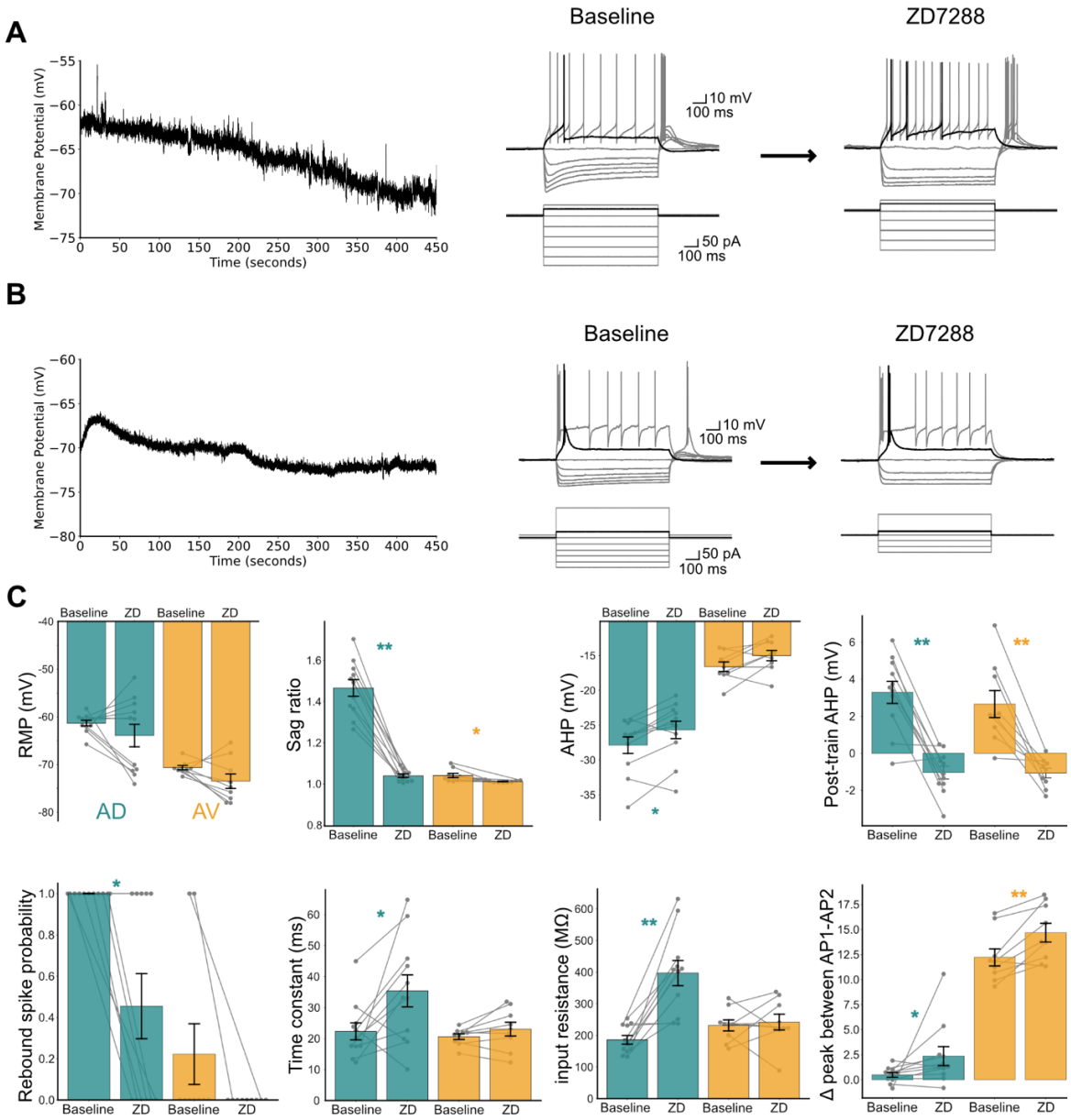
A
Baseline
ZD7288
Membrane Potential (mV)
Time (seconds)
10 mV
100 ms
50 pA
100 ms
B
Baseline
ZD7288
Membrane Potential (mV)
Time (seconds)
10 mV
100 ms
50 pA
100 ms
C
RMP (mV)
AD
AV
Sag ratio
AHP (mV)
Post-train AHP (mV)
Rebound spike probability
Time constant (ms)
input resistance (MΩ)
Δ peak between AP1-AP2
Baseline
ZD

Figure 4. Electrophysiological changes in AD and AV neurons in the presence of Ih blocker ZD7288.

A) Left: Example recordings showing changes in the membrane potential of AD neuron after bath application of ZD7288 (2 μM). The time was measured right after the ZD7288 was added in the bath. Right: Representative traces from AD in response to a series of current injections under baseline condition and during bath application of ZD7288. AD neuron was held at -60 mV. Hyperpolarising traces are shown at every 60 pA step until the holding resting membrane potential is reached. The rheobase sweep is indicated by a thick line. A typical firing pattern is also shown.
B) Example recordings showing changes in the membrane potential of AV neuron after bath application of ZD7288 (2 μM).
C) Quantified changes in electrophysiological properties of AD (teal) and AV (yellow) neurons following ZD7288 (ZD in the figures) application. Each point of the same neuron is shown connected. Statistical comparisons between AD and AV groups were performed using the Wilcoxon signed-rank test for paired comparisons. Significance levels are indicated as follows: *p< 0.05, **p < 0.01, ***p < 0.001, ****p < 0.0001.

AD and AV thalamocortical neurons have distinct morphological features

All recorded neurons were filled with biocytin to reveal their anatomy. Axonal and dendritic morphologies of 39 well filled neurons from AV (n = 20) and AD (n = 19) were completely reconstructed (Figure 5A). The morphologies of AD and AV neurons showed characteristic differences. AD neurons exhibit a radiate dendritic morphology, characterised by relatively fewer neurites that extend outward in a sparse pattern. In contrast, AV neurons show a bushy dendritic morphology, with a higher density of neurites forming a more compact and intricate structure. AD and AV dendrites were sparsely spiny (Figure 5D). They typically remained within the borders of their respective thalamic subdivisions, avoiding crossing into adjacent regions. Sholl analysis quantified structural differences by measuring neurite intersections at increasing distances from the soma (Figure 5C).

Axons were only partly preserved in the slice, exiting the anterior thalamus to the lateral side, running toward the PrS or RSC, via the cingulum (Dillingham et al., 2015) (Figure 5B). Some slices preserved long axons exhibiting recurring gaps (Figure

5D (iii) and (iv)), indicating the potential presence of partial myelination. The Sholl plot shows some intersections at distances beyond 200 µm, corresponding to axonal branching. AD neurons formed branches between 220–400 µm from the soma. Several AV neurons formed axonal ramifications at 500–600 µm. The long axons exhibited complex arborisation within the region anatomically corresponding to the TRN, while the main axonal trunk extended further (Figure 5D (iv) and Figure 5 - figure supplement 1). AD neurons also sent axon branches to TRN, as shown for one example that was reconstructed across a sufficiently long distance (Figure 5B supplementary figure 1), but no ramifications were observed In rare cases we found close appositions of axons with dendrites of nearby AD or AV neurons, but no clear evidence for synaptic interconnectivity (Figure5 - supplemental figure 2).

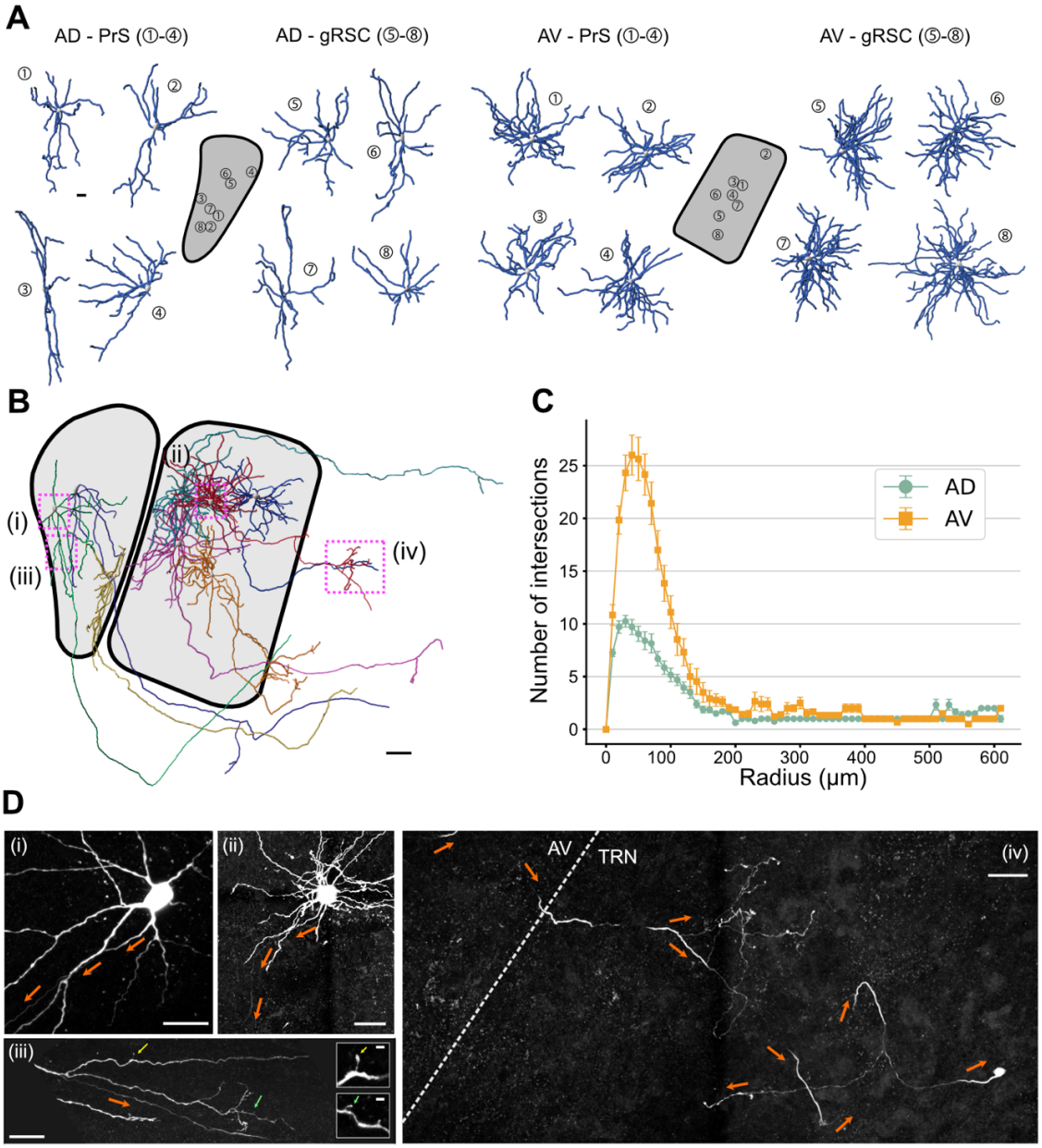
A
AD - PrS (①-④)
AD - gRSC (⑤-⑧)
AV - PrS (①-④)
AV - gRSC (⑤-⑧)
B
(i)
(ii)
(iii)
(iv)
C
Number of intersections
AD
AV
Radius (μm)
D
(i)
(ii)
(iii)
AV
TRN
(iv)

Figure 5. Morphological characteristics of AD and AV neurons.

A) 3D reconstructions of individual thalamic projecting neurons located in the AD and AV. The approximate location of each reconstructed neuron is indicated on schematic diagrams of the AD and AV. Scale bar: 20 μm.
B) 3D reconstructions of 8 thalamic neurons with their axonal projections, positioned in their approximate anatomical locations. Scale bar: 50 μm.
C) Sholl plots for 20 AD and 19 AV neurons. Error bars indicate mean ± SEM.
D) Confocal microscopy image (63x) of neurons in panel B. (i) soma of an AD neuron with a putative axon indicated by an orange arrow. Scale bar: 20 μm. (ii) soma of an AV neuron with a putative axon indicated by an orange arrow. Scale bar: 20 μm. (iii): axonal projection of AD neuron indicated by an orange arrow shown with dendrites. Scale bar: 20 μm. Spines are indicated with yellow and green arrows, and magnified in the inset. Scale bar: 2 μm. (iv) Axonal arborisation along the projection of the red-coloured AV neuron. Projection direction indicated by orange arrows. Scale bar: 20 μm.

Ipsilateral and contralateral synaptic input connectivity from the Mammillary bodies to AD and AV thalamocortical neurons

The LMN sends axons to AD (in rats, H. T. Blair et al., 1999; Guison et al., 1995; Seki & Zyo, 1984), while the MMN nucleus sends axons to AV (Vann and Aggleton, 2004). We sought to investigate the nature, laterality, strength and dynamics of these parallel synaptic connections from the mammillary bodies to thalamocortical projection neurons, by expressing channelrhodopsin (Chronos-GFP) in the mammillary bodies of one hemisphere, and recording from AD or AV neurons in ex vivo slices of both hemispheres. Patch clamp recordings were targeted to somata surrounded by channelrhodopsin expressing axons, and in a subset of experiments the thalamocortical neurons had been labeled with retrobeads (Figure 6A).

In five mice with clear unilateral Chronos-GFP expression in the lateral and medial mammillary bodies (Figure 6 - figure supplement 1), we found that mammillary body axons innervated both ipsilateral and contralateral AD and AV. Axons from the mammillary body also ramified in the anteromedial thalamus. Few, if any, axons innervated the neighboring TRN or other thalamic nuclei. The fluorescent signal of GFP labeled axonal ramifications was highest in the ipsilateral AD and ipsilateral AV,

and less strong in the contralateral AD and contralateral AV (Figure 6B,C). We quantified the fluorescence intensity, corrected for background signals, and normalized the measurements to the ipsilateral side of each region. The contralateral fluorescence intensity was 73 ± 0.06% for the AD, and 61 ± 0.11 % for AV (n = 5). This was unexpectedly high, as the medial mammillary nucleus projection to the AV is thought to be mostly unilateral (Vann and Aggleton 2004; Watanabe and Kawana 1980).

Optical stimulation of mammillary axons in slices let us investigate the functional mammillo-thalamic connectivity and compare excitatory postsynaptic responses in AD and AV neurons (Fig. 6 D,F). Light induced excitatory postsynaptic currents (oEPSCs) were recorded in all 22 neurons tested in ipsilateral AD (amplitude, -208.95 ± 54.94 pA; latencies 1.36 ± 0.04 ms) and in 16 out of 17 neurons in ipsilateral AV (amplitude, -416.63 ± 99.94 pA; latencies 1.90 ± 0.15 ms). In the contralateral AD, oEPSCs were recorded with a lower probability and amplitudes were significantly smaller (17 out of 20 neurons tested, amplitude, -72.90 ± 11.44 pA; latencies 1.34 ± 0.05 ms). oEPSCs were also recorded in 7 out of 18 tested neurons in the contralateral AV (amplitude, -371.11 ± 72.16 pA; latency, 2.17 ± 0.18 ms). All oEPSC onset latencies were < 3 ms and thus compatible with monosynaptic activation (Figure 6F). oEPSCs in ipsilateral and contralateral AD neurons had significantly shorter latencies compared to ipsilateral and contralateral AV neurons ($p = 0.00002$). Light evoked excitatory postsynaptic potentials (oEPSPs) persisted in the presence of TTX (1 µm) and 4-AP (100 µM), as expected if AD and AV neurons were contacted directly by synapses of Chronos-expressing mammillary axons (AD, n = 3; AV, n = 4; Figure 6G). oEPSCs were suppressed by bath application of AMPA and NMDA receptor antagonists (Figure 6E; AD, n = 5; AV, n = 2; Figure 5H), confirming the glutamatergic nature of mammillary body excitation. Taken together, these data show a monosynaptic mammillothalamic connection to AD and AV of both hemispheres, with a preference for the ipsilateral AD and AV.

In one case, the expression of Chronos-GFP was strictly limited to the lateral mammillary nucleus (Figure 6 - figure supplement 2) indicating a connection only to AD not to AV. Optogenetic stimulation induced action potential firing in ipsilateral AD neurons, whereas contralateral AD neurons did not exhibit action potential but oEPSPs. In contrast, AV neurons showed no detectable response to the stimulation.

This indicates a potential preferential connection between the lateral mammillary nucleus and ipsilateral AD neurons.

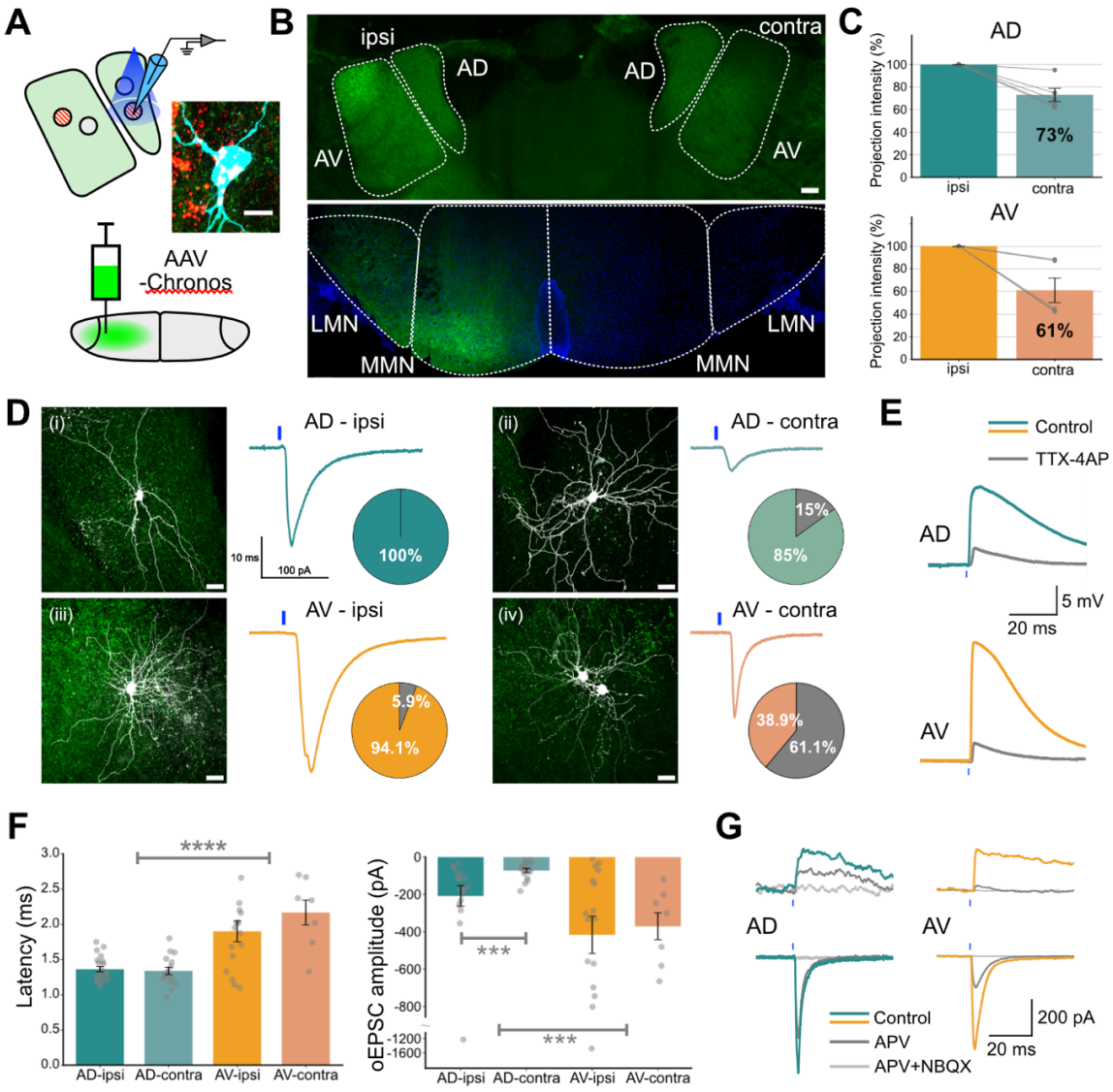

Figure 6. Functional mammillo-thalamic connectivity onto AD and AV neurons of both hemispheres.

A) Chronos-GFP was unilaterally injected in the mammillary body. Red retrobeads were injected into either the PrS or gRSC to retrogradely label thalamic projecting neurons in some experiments. Example confocal image of biocytin-filled (cyan) neuron labelled by retrobeads (red) and surrounded by mammillary projections (green) is shown. Scale bar: 10 µm. Postsynaptic responses were measured while mammillary inputs were activated with blue light (470nm). LED intensity was set to low or intermediate levels, typically 0.2 - 1 mW.
B) Mammillary axons expressing Chronos-GFP in AD and AV following strictly unilateral injection. Scale bar: 100 µm
C) Quantification of mammillary input fluorescence in the AD and AV to compare the intensity between ipsilateral and contralateral side.
D) Confocal image of a biocytin filled neuron in (i) ipsilateral and (ii) contralateral AD, and in (iii) ipsilateral AV and (iv) contralateral AV, and light evoked EPSCs in each group. The proportion of neurons showing postsynaptic responses is calculated based on the total recorded neurons. AD-ipsi: 22/22, AD-contra: 17/20, AV-ipsi: 16/17, AV-contra: 7/18. Scale bar: 10 µm.
E) oEPSPs persisted in the presence of TTX (1 µM) and 4-AP (100 µM) in the bath, but with smaller amplitudes (bottom trace, gray).
F) Average oEPSC latencies and amplitudes of AD and AV neurons. Each 1 neuron in the AD and AV generated action current in the subthreshold stimulation. Mean ± SEM are indicated by bars and vertical lines. Statistical significance is measured by Mann-Whitney U test. *$p < 0.05$, **$p < 0.01$, ***$p < 0.001$, ****$p < 0.0001$.
G) Light evoked currents at holding potentials of +70 mV and at -70 mV revealed glutamatergic EPSCs with a NMDA and AMPA receptor mediated component.

We asked, what is the efficiency of mammillary inputs to induce action potentials in AD and AV neurons? To quantify firing responses for each neuron as a function of stimulation strength, the LED intensity was increased in a stepwise fashion, while recording the postsynaptic responses to a train of ten optical stimuli delivered at 20 Hz (Figure 7A). Ipsi- and contralateral AV neurons were highly sensitive and responded readily with action potentials even to low light intensities. Ipsi- and contralateral AD neurons, on the other hand, required higher intensities to initiate an action potential (Figure 7B). Out of 19 connected neurons in ipsilateral AD, 12 responded with action potentials, but only 3 out of 17 neurons in the contralateral AD.

In ipsilateral AV, 13 out of 16 connected neurons fired action potentials, and 4 out of 7 connected neurons in the contralateral AV (Figure 7C). As soon as firing threshold was reached, most AV neurons tended to respond with bursts of action potentials to the first stimulation (12/17 neurons), while AD neurons sometimes skipped firing for the first stimulation in a train (5/15 neurons). A typical firing response is shown in Figure 7D for a pair of simultaneously recorded neurons in AD and AV. In sum, our data show that connections from the mammillary bodies are more likely in ipsilateral AD and in ipsilateral AV (Figure 6D), and that the firing threshold is reached more easily for mammillary input from the same hemisphere (Figure 7C).

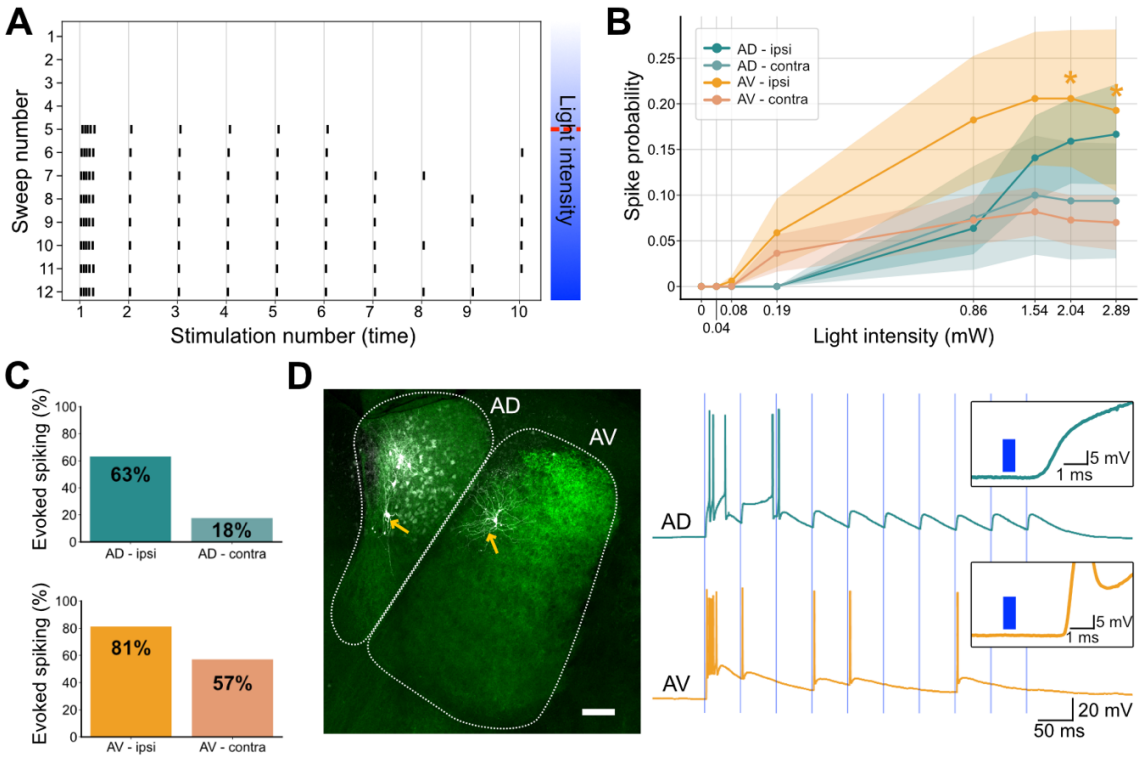

Figure 7. Photostimulation of mammillary axons induces action potential firing more readily in AV than in AD neurons

A) Raster plots of AV neuron action potential firing following a 20 Hz train of mammillary fiber stimulation. The red dash line indicates the threshold level of light stimulation to evoke firing. The gray vertical line indicates the time point of each light stimulation.

B) Spiking probability across increasing light intensities. Spike probability between ipsilateral and contralateral AV shows significant difference from 2.04 mW stimulation, marked with stars. Mann-Whitney U test. Significance is indicated by asterisks (*) between ipsilateral AV and contralateral AV. *$p < 0.05$.

C) Percentage of functionally connected neurons exhibiting light-evoked spiking. Top: AD (ipsi: 12/19, contra: 3/17). Bottom: AV (ipsi: 13/16, contra: 4/7).

D) Postsynaptic responses of ipsilateral AD and AV neurons recorded simultaneously. Note the shorter onset of AD (2.25 ms) oEPSP compared to the AV (3.16 ms) oEPSP, and the initial high frequency burst of action potentials in AV. Scale bar: 100 μm

We next investigated excitatory postsynaptic current responses to repetitive, low intensity (0.1 - 0.5 mW) stimulation of mamillary fibers (Figure 8A). In the AD, ipsilateral neurons exhibited a small progressive reduction in oEPSC amplitudes during 20 Hz photostimulations. This synaptic depression became statistically significant from the 8th stimulus onward, compared to the first oEPSC. Neurons in the contralateral AD did not exhibit significant depression across repeated stimulations. oEPSC amplitudes were significantly higher in the ipsilateral than in the contralateral AD. In contrast, in the AV, oEPSC amplitudes were similar for neurons in the ipsi- and contralateral hemisphere. The oEPSC amplitudes followed strongly depressing dynamics, both ipsilaterally (from the 6th stimulus onward) and contralaterally (from the 8th stimulus onward). These data indicate distinct synapse behaviour for mammillary-to-AV synapses, with higher initial amplitudes and more depressing dynamics, compared to the mammillary-to-AD synapses, that are less depressing. Depressing oEPSC dynamics are compatible with a driver input to the thalamic neurons. We then quantified the dynamics of firing during mammillary fiber stimuli of suprathreshold light intensities (following calibration, Figure 7B; 0.2 to 1 mW). Ipsilateral AD neurons sometimes skipped firing for the first pulse in a train (5/15 neurons), while all contralateral spiking AD neurons skipped the first stimulation but initiated APs for the 2nd or 3rd stimulation. Action potential dynamics were significantly depressing from the 4th stimulus onward for ipsilateral neurons, whereas the contralateral AD neurons maintained a low level of spiking probability across the stimulation train. AV neurons had overall higher spiking probabilities than AD neurons (Figure 7C and 8B). Most AV neurons responded with bursts of action potentials to the first out of ten successive light stimuli (8 out of 13 spiking ipsilateral AV neurons, 3 out of 4 spiking contralateral AV neurons). Following the initial high likelihood of bursting discharge, AV firing dynamics were significantly depressing, in both ipsi- and in contralateral recordings. Ipsilateral cells exhibit significantly reduced spike probability from the 3rd stimulation and from the 4th stimulation in the contralateral cells. The spiking probability between ipsilateral and contralateral AV cells were similar.

Taken together, these results demonstrate bilateral mammillothalamic projections to AD and AV with distinct dynamics, and more efficient functional connectivity to the ipsilateral side of thalamocortical neurons.

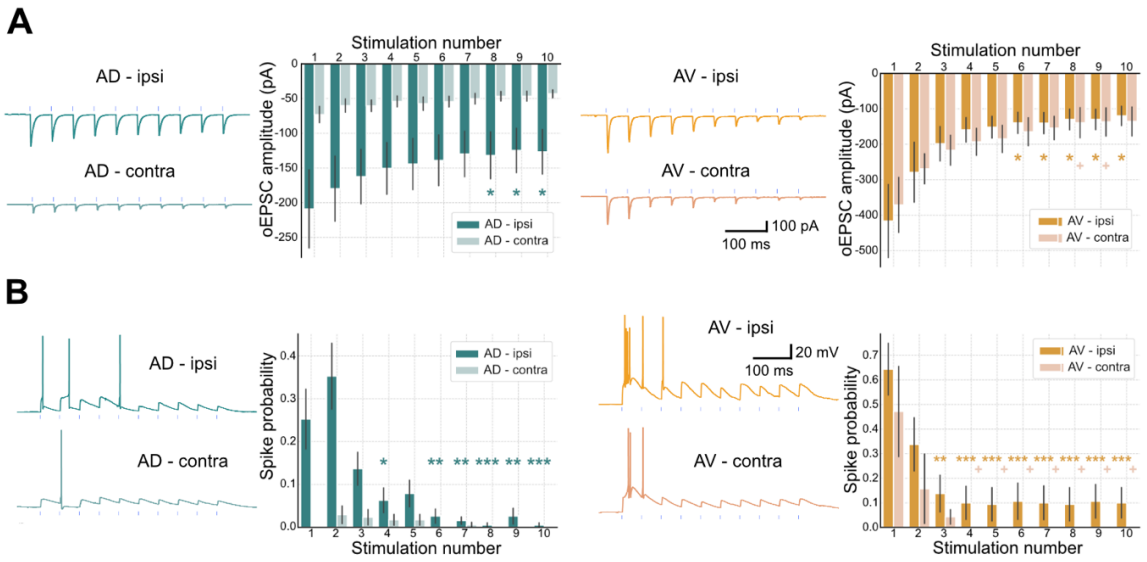

Figure 8. AD and AV specific synaptic dynamics and spiking probabilities following optical stimulation of mammillary axons.

A) oEPSCs evoked by ten successive light stimuli repeated at 20 Hz. Bar graphs indicate mean ± SEM. Differences in oEPSC amplitudes between the first and subsequent stimulations were evaluated for statistical significance using Mann-Whitney U test. Significance is indicated by asterisks (*) for the ipsilateral group and plus signs (+) for the contralateral group. *p < 0.05, **p < 0.01, ***p < 0.001, ****p < 0.0001.

B) Example traces of spiking activity across ten light stimuli and bar graphs showing spike probability across stimulations. For each stimulation, the occurrence of action potentials within the repetitions was measured as probability. This reflects the presence of at least one spike, while sometimes one stimulation initiated several spikes. Variation in spike probability between the first and subsequent stimulations were evaluated for statistical significance using Mann-Whitney U test. Significance is indicated by asterisks (*) for the ipsilateral group and plus signs (+) for the contralateral group. *p < 0.05, **p < 0.01, ***p < 0.001, ****p < 0.0001.

Discussion

Here we describe the mammillo-thalamo-cortical circuits with new anatomical and functional detail. We show that mammillary input to the AD and AV thalamic nuclei is monosynaptic and bilateral, with a functionally stronger connection on the ipsilateral side. We also reveal that subpopulations of projecting neurons, targeting cortical head direction areas gRSC and PrS, are spatially organized and overlapping in the central portion of AD and AV. . The intrinsic electrophysiological and morphological properties of AD and AV neurons are distinct and not defined by their projection specificity. These results improve our understanding of thalamic processing of Mammillary signals that are transmitted to the cortical HD areas.

Mammillary inputs to the anterior thalamic nuclei are monosynaptic and bilateral

The mammillothalamic connectivities are organised in parallel pathways, with the LMN projecting to the AD and the MMN projecting to the AV (Guison et al., 1995; Mathiasen et al., 2021; Seki & Zyo, 1984; Shibata, 1992; Vann et al., 2007; Vann & Aggleton, 2004). From there, thalamocortical axons send HD related signals to the RSC and PrS (Lomi et al., 2021; Nassar et al., 2018; Peyrache et al., 2015; Richevaux et al., 2025; Roy et al., 2021, 2022; Seki & Zyo, 1984; Van Der Goes et al., 2024; Van Groen & Wyss, 1990a, 1995). Whether mammillothalamic input connections are arranged according to the cortical targets of thalamocortical AD and AV neurons hashad not been studied.

Our retrograde monosynaptic tracing experiments showed that mammillary input neurons are directly connected to PrS- and gRSC-projecting thalamic neurons in AD and AV. While the stereotaxic precision of our thalamic injections did not allow us to target AD and AV separately, we can compare our results to previous anatomical studies. The bilateral projection of LMN to the AD is well documented (H. T. Blair et al., 1999; Cruce, 1975; Guison et al., 1995; Seki & Zyo, 1984), whereas the MMN projection to the AV has been thought to be strictly ipsilateral (Cruce, 1975; Dillingham et al., 2015; Seki & Zyo, 1984; Shibata, 1992; Vann & Aggleton, 2004; Veazey et al., 1982; Wiener & Taube, 2005). In our hands, labelled mammillary neurons were

consistently observed in the ipsilateral and also in the contralateral hemisphere. The presynaptic neurons in the contralateral MMN were sparse and mostly located in the posterior portion. One possible explanation for the slight differences between our findings and previous reports is that many studies focused on the prominent anterior part of the mammillary body. Two previous studies showed anatomical tracing results indicating bilaterality, but this was not explicitly stated or clearly highlighted by the authors (Mathiasen et al., 2021; Vann et al., 2007).

We further examined the functional connectivity of the mammillothalamic pathway using optogenetics. Photostimulation of mammillary fibers originating from one hemisphere produced excitatory postsynaptic responses in AD and AV thalamic neurons ipsilaterally and, to a lesser degree, also contralaterally. The short latency of oEPSCs and their persistence in the presence of TTX-4AP demonstrated the monosynaptic nature of the mammillothalamic pathways. The connection probability, oEPSC amplitudes and the efficiency to drive action potential firing was weighted towards the ipsilateral mammillary input, for AD and AV (Figure 6D and F, and Figure 7B and C). As in other sensory systems, receiving input from both sides can be useful for bilateral integration and specialized laterality. In the HD system, there is a hemispheric bias in angular velocity signals. The properties of HD tuning curves in both AD and LMN shift depending on the animal's angular turning motion (H. Blair & Sharp, 1995; H. T. Blair et al., 1999). The magnitude of this anticipatory shift is velocity-dependent, and larger in LMN than in the AD and dorsal presubiculum (H. Blair & Sharp, 1995; Peyrache et al., 2015; J. S. Taube & Muller, 1998). It is also notable that directionally tuned thalamic cells disrupted by unilateral vestibular loss gradually regain their tuning over time (El Mahmoudi et al., 2025). This may suggest a potential integrative and compensating role of the AD in processing asymmetrical AHV-modulated HD signals from LMN across both hemispheres.

Our data also revealed bilateral postsynaptic responses in the MMN-AV pathway. The connection rate was high in the ipsilateral AV (94.1 %), and also far from negligible in the contralateral side (38.9 %). The oEPSC amplitudes were similar in the ipsilateral and contralateral AV, and more than half of connected neurons in both sides could be driven to action potential threshold. We cannot entirely exclude that the contralateral postsynaptic events could arise from visually undetected spread of chronos expression to the contralateral MMN. However, the contralaterally labeled

mammillary presynaptic neurons observed in the rabies tracing experiments support the existence of a contralateral projection.

Spatially organised thalamic projecting neurons

Retrograde tracing enabled us to identify the spatial distribution of thalamic neurons projecting to the gRSC and PrS. The anatomical thalamocortical connectivity has been studied separately either to the PrS or RSC (Lin et al., 2024; Lomi et al., 2021; Nassar et al., 2018; Richevaux et al., 2025; Roy et al., 2021, 2022; Shibata, 1993b, 1993a; Van Der Goes et al., 2024). Also, AD and AV have often been described together as ATN, which obscures the projection profiles of the individual subnuclei. Here, we targeted the dorsal portion of PrS and granular RSC (area 29) for dual retrograde tracing. We selected the gRSC region within the broader RSC because it contains classical HDCs (Aggleton et al., 2021; Jacob et al., 2017; Lomi et al., 2021; Sripanidkulchai & Wyss, 1986; Van Groen & Michael Wyss, 1990). The two projecting subpopulations were overlapping in both AD and AV. Interestingly, the topographical pattern in the AV differed from the conventional delineation into AVVL and AVDM subregions which were originally divided based on the soma size and acetylcholinesterase histochemistry (Paxinos & Franklin, 2013; Sripanidkulchai & Wyss, 1986; Van Groen & Wyss, 1995). Recent studies also highlight this separation based on the preferred calbindin-positive mammillary projections in the AVDM and predominant dRSC-projecting neurons in the AVVL (Liu et al., 2025; Lomi et al., 2021). While our targeting in the gRSC spanned the anterior–posterior axis, the topographic patterns in the AD and AV were consistent across animals (Figure 2 - figure supplement 1).

Distinct electrophysiological and anatomical properties between thalamic subnuclei

Our electrophysiological analysis revealed clear differences between the AD and AV neurons, indicating that these nuclei possess distinct electrophysiological intrinsic properties that likely reflect their functionality. To better understand the

mechanism underlying the differences, we compared our electrophysiological findings with the genetic profiles of the AD and AV neurons (Phillips et al., 2019).

In AD neurons, several key intrinsic features-such as their depolarised resting membrane potential, low input resistance, fast membrane time constant, and prominent voltage sag-can be largely attributed to the strong expression of HCN channels (Maccaferri & McBain, 1996). Pharmacological blockade of Ih with ZD7288 confirmed its functional role, resulting in hyperpolarised RMP, increased input resistance, reduced sag, increased AHP amplitude, and partial suppression of rebound spikes (Figure 4). These effects highlight the role of Ih in setting both the resting membrane conductance and the membrane's dynamic responsiveness to current inputs in AD cells. The expression of Kcnk family leak potassium channels may also control the resting membrane potential and excitability. However, the overall expression profiles of these channels between the two thalamic regions are variable across isoforms, which made it difficult to establish a clear relationship. For example, Kcnk1, Kcnk4, and Kcnk10 are expressed at relatively higher levels in AD neurons, despite their more depolarised RMP. The adaptive firing pattern seen in AD may fit with high expression of Kcnt1, a Na^+-activated K^+ channel whose deletion is known to impair spike-frequency adaptation (Martinez-Espinosa et al., 2015). Furthermore, low expression of T-type Ca^{2+} channels (Cacna1g and Cacna1d) likely limits low-threshold calcium spiking and burst initiation (cf. Figure 3A,B and Figure 4).

AV neurons displayed a more hyperpolarised resting membrane potential, slower membrane time constant, higher input resistance, and characteristically irregular burst firing patterns. At rheobase, these cells often generated an initial high-frequency burst followed by prolonged spike suppression, and their firing during sustained depolarisation was typically sparse and irregular. M-type potassium channel subunits (KCNQ gene family) which are expressed at moderate levels in AV, while very low expression in AD potentially contributes to spike suppression following initial activation (Yoshida & Alonso, 2007; Yue & Yaari, 2004). Note, KCNQ channels have been shown to regulate spike timing locked to the theta phase how do (KCNQ3) (Gao et al., 2021). Also, AV neurons have higher expression of KCNB1 and KCNF1 encoding the alpha subunit of the Kv2.1 channel (delayed rectifier, Bishop et al., 2015), compared to AD neurons. The periodic and irregular firing patterns observed in AV neurons may be partly attributed to ion channels that affect the repolarisation

dynamics and prolong the refractory period (Thiffault et al., 2015). Indeed, some AV neurons exhibited theta-phase-like firing when sustained firing was induced by higher current injection, suggesting that theta-frequency firing may be an intrinsic property (Figure 3 - figure supplement 2). Mechanism underlying initial burst firing in AV neurons could depend on low-voltage-activated T-type calcium channels (Cav3.1, Cacna1g; and Cav3.3, Cacna1i). Yet, their expression levels are low, while genes coding for high-voltage-activated calcium channels (Cacna1a, Cacna1c, Cacna1d) are more strongly expressed (Perez-Reyes, 2003). One possible explanation is that relatively higher expression of Cacna1g and CaCna1a in AV together drives the burst activity, similar to Cacna1g dependent bursting in ventrobasal thalamic relay neurons (D. Kim et al., 2001).

Photostimulation experiments induced high amplitude oEPSCs at the beginning of a 20 Hz stimulation, that depressed over time, a response profile consistent with the driver characteristics of mammillothalamic input (Petrof & Sherman, 2009). In AD, this led to higher spike probabilities for the initial 1 - 2 stimulations. Later stimulations evoked sustained oEPSPs with a low failure rate. In AV neurons, oEPSC amplitude and spike probability was also strongest in the beginning of a 20 Hz stimulation. The initial burst firing was found to be characteristic for, AV neurons.

Relating AD and AV neuronal properties to Head Direction circuit function

The LMN serves as a key HD input to the AD (Bassett et al., 2007; H. T. Blair et al., 1998, 1999; Stackman & Taube, 1998), as it receives vestibular-driven HD signals from the dorsal tegmental nucleus of Gudden (Bassett et al., 2007). The AD contains a large population of classical HD cells, which are characterised by their persistent and sharply tuned activity (J. Taube, 1995). How might the intrinsic properties of AD neurons contribute to their ability to support HD signals? Our data showed that, at RMP, AD neurons were excitable, and little current was required to generate action potentials (Figure 3 - figure supplement 3 and table supplement 1). At subthreshold levels, input resistance was lower suggesting weaker responsiveness. AD neurons may therefore play the role of ‘selective integrative amplifiers’ within the HD system: summation of coherent inputs would be required to reach threshold,

allowing noise to be filtered out, but once firing is initiated by coherent input, excitability increases. Photostimulation of mammillary inputs elicited relatively small oEPSC amplitudes and low spiking probability, which gradually increased with stronger inputs. Such dynamics could feed into an attractor network, where AD neurons respond promptly and reliably to ongoing sensory updates (Blanco-Hernández et al., 2024), a mechanism that may provide a functional advantage during spatial navigation. AD also receives unbalanced but still functionally valid bilateral input from the LMN. The summation of EPSPs from both hemispheres suggests that AD neurons may serve an integrative role, combining vestibular-driven directional signals across hemispheres. Together, this supports its function as a dynamic and responsive hub for HD signalling.

The MMN may fire rhythmically in synchrony with hippocampal theta oscillations and relay this activity to the AV, where theta-modulated firing is also observed (Albo, 2003; Bland et al., 1995; Kocsis et al., 2001; Komisaruk, 1970; Tsanov, Chah, Wright, et al., 2011; Vertes et al., 2001; Welday et al., 2011). Recent studies have reported the presence of HD cells in the AV, indicating its potential role in the directional coding (Ji et al., 2025; Lomi et al., 2023; Tsanov, Chah, Vann, et al., 2011). The HD cells in the AV tend to exhibit theta-phase locked activity and sweeping phase precession. These functional features may be particularly important even if such temporal activity can appear to have a broader and less sharply tuned directional preference. The temporally controlled characteristics are consistent with their electrophysiological intrinsic properties; minimal influence of Ih current and reluctance to generate persistent spiking activity after the initial burst. Then, this raises a question of where the HD input to AV originates, given that HD cells have not been identified in the MMN. Potentially, HD activity in the AV could arise through its reciprocal connectivity with RSC (Lomi et al., 2021; Shibata, 1993a; Van Groen & Michael Wyss, 1990; Van Groen & Wyss, 1995). The AV itself may act as an integrative hub where theta phased-locked activity converges with directional input. A functionally analogous population of theta-modulated sweeping head direction cells has been identified in the parasubiculum, where they appear to coordinate with grid cells to drive the alternating directional sweeps characteristic of entorhinal spatial coding (Vollan et al., 2025). Given that AV projects to the parasubiculum, it could serve as a potential upstream source of the theta-modulated sweeping HD signals. (Jankowski et al., 2013; Perry & Mitchell, 2019; Roy et al., 2022; Van Groen & Wyss, 1990a) Theta modulation seems

to be a key organising principle for HD activity in the RSC, supporting temporally structured and precise directional tuning (Brandon et al., 2013; Lomi et al., 2021). However, HD cells in the PrS appear to be less likely modulated by theta rhythm (Boccara et al., 2010; Sharp, 1996; J. Taube et al., 1990; Tukker et al., 2015), and the functional role of AV-PrS connectivity remains unclear (Roy et al., 2022). Nevertheless, Cacucci et al. (2004) reported a distinct class of theta-modulated place-by-direction cells in the presubiculum and parasubiculum, which integrate both positional and directional information, while being strongly entrained to the theta rhythm. This suggests that AV inputs may still contribute to spatial coding in the presubiculum and parasubiculum, even though HD cells in these regions show weak theta modulation. The theta rhythmic influence of AV on these parahippocampal circuits remains to be clarified in the future studies.

In conclusion, our study provides a fundamental understanding of anatomical and electrophysiological properties in AD and AV supporting the conventional HD system. The inter-regional connectivities bridging the hypothalamic region to the cortices through the thalamus are considered to be organised in parallel pathways; LMN-AD-PrS/gRSC and MMN-AV-PrS/RSC. Our electrophysiological analysis of each thalamic subnucleus highlights the distinct contributions of AD and AV to the network. Understanding how their anatomical convergence in cortical regions reflects physiological convergence-and how this interaction shapes their systemic contribution will provide new insight into the dynamic coordination of spatial orientation signals. Additionally, traditional anatomical delineation reveals strong acetylcholinesterase expression in specific thalamic subnuclei, reflecting dense cholinergic innervation (Bolton et al., 1993; Sofroniew et al., 1985) as well as corresponding gene expression profiles (Phillips et al., 2019). This raises the further question of whether cholinergic modulation in these regions fine-tunes their activity within the system, underscoring a more nuanced architecture of the HD network.

Data availability

Processed data and the functions used to generate the figure panels in this study are available at https://github.com/DongkyunLIM/ADAV and backed up on local servers.

Acknowledgements

This work is supported by the Centre National de la Recherche Scientifique and the Université Paris Cité. DL was funded by the Université Paris Cité international PhD program. DF received funding from the Agence Nationale de la Recherche from the ERA-NET NEURON Program (ANR-20-NEUR-0005 VELOSO), and the FLAG-ERA HBP Program (ANR-21-HBPR-0002 VIPattract). This work has benefited from support by the BioMedTech Facilities at Université Paris Cité (Institut National de la Santé et de la Recherche Médicale Unité S36/Unité Mixte de Service 2009), and the Charité Vector Core Facility. We acknowledge help with initial experiments from Jothini John Vyani Rajalingam and Mérie Nassar. We thank Rosanna Sammons from the Schmitz lab for technical training. We thank Fabrice Licata and Dr. Abdelali Jalil from the UPC Microscopy platform and Dr. Michael Graupner for comments on the manuscript.

Supplemental materials

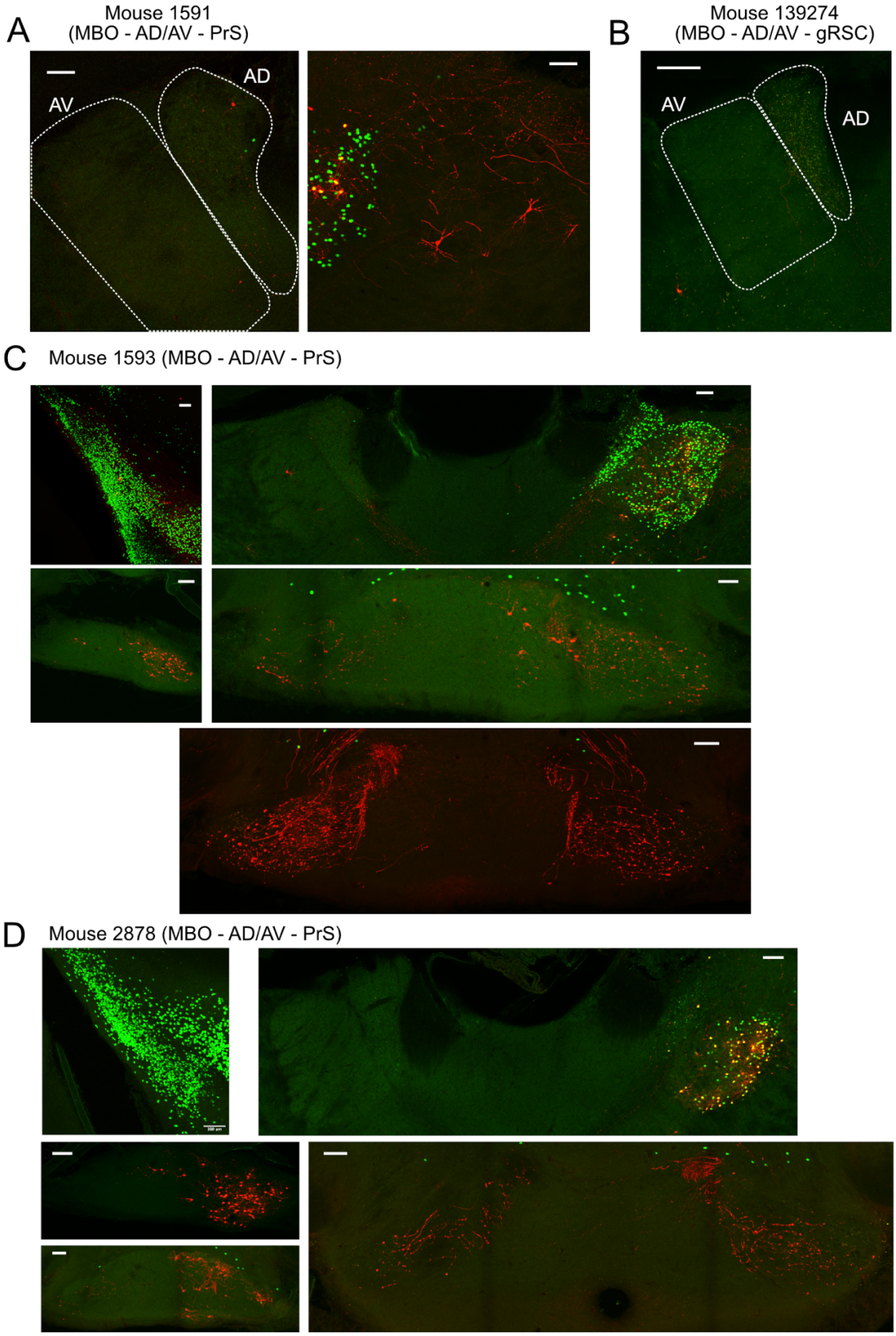

Figure 1 - figure supplement 1. Additional images of monosynaptic rabies tracing.

A) Left: Contralateral side of Figure 1C. Right: rabies-labelled neurons in the TRN. Scale bars: 100 μm.
B) Contralateral side of Figure 1G. Scale bar: 100 μm
C) Images of Mouse #1593 from monosynaptic rabies tracing experiment to label PrS-projecting thalamic neurons (green) and monosynaptic inputs in the mammillary body. Unilateral injections were performed on the right side of the images. Scale bars: 100 μm
D) Images of Mouse #2878 from monosynaptic rabies tracing experiment to label PrS-projecting thalamic neurons (green) and monosynaptic inputs in the mammillary body. Unilateral injections were performed on the right side of the images. Scale bars: 100 μm

Mouse #1 (M55)

Thalamic projecting neurons

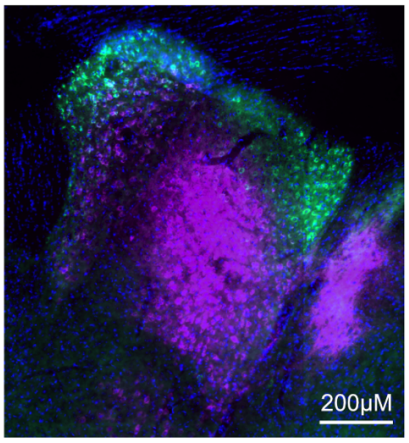

Injection sites

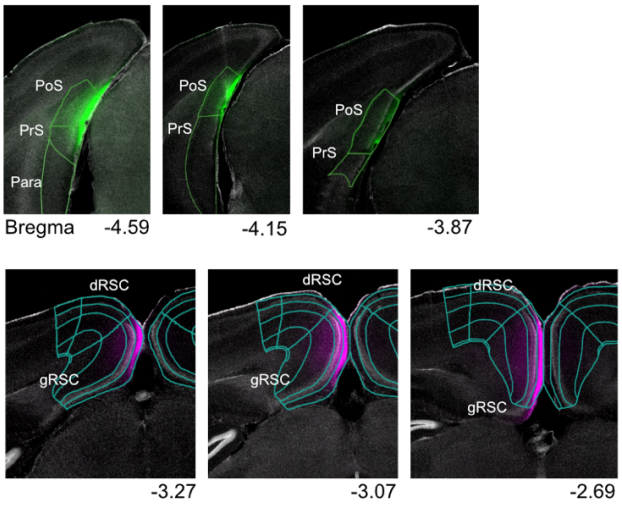

Mouse #2 (4106)

Thalamic projecting neurons

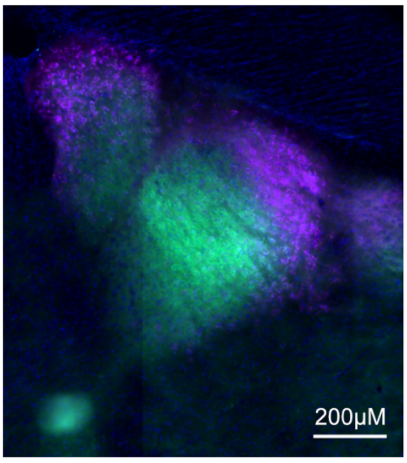

Injection sites

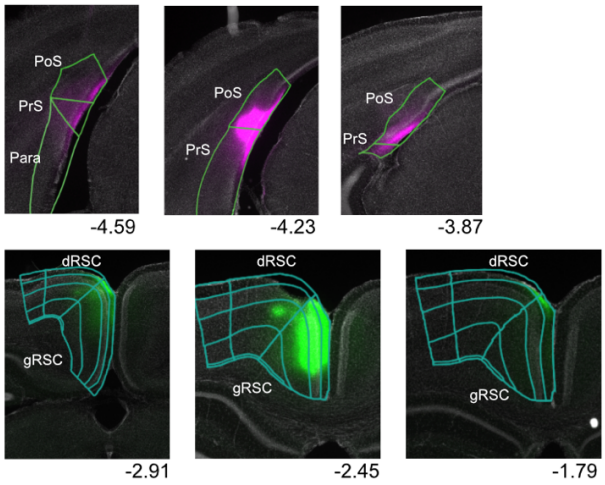

Mouse #3 (5177)

Thalamic projecting neurons

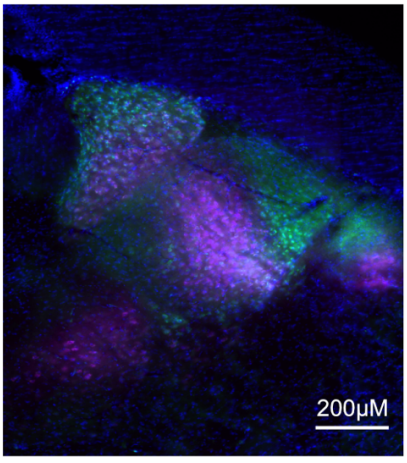

Injection sites

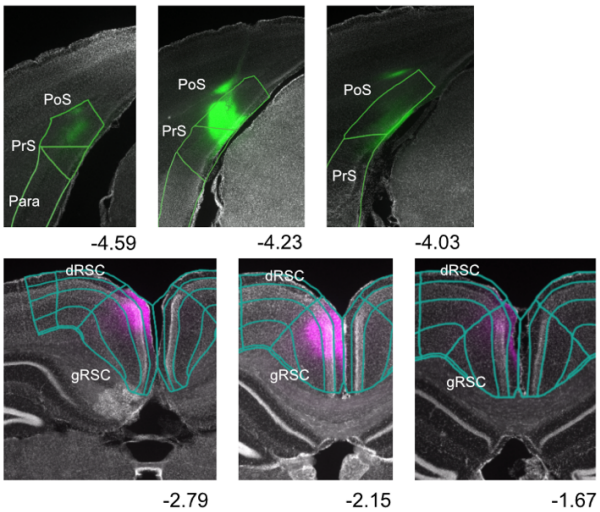

Figure 2 - figure supplement 1. Injection sites and labelled thalamic neurons.

The injection sites of 3 mice which are included in the pooled analysis. The anterior thalamic nucleus of Mouse #1 is shown in Figure 1. CTB-488 was injected in the PrS and CTB-647 was injected in the gRSC in Mouse #1, and #2. To avoid biases due to labeling efficiency of the two CTBs, in Mouse #3 the CTBs were switched between the PrS and gRSC.

	Projecting neurons in AD			Significance	Projecting neurons in AV		
	Mean	SEM	N		Mean	SEM	N
Resting membrane potential (mV)	-59.9	0.7	28	****	-70.9	0.6	25
Input resistance (MΩ)	139	9	28	***	221	19	25
Time constant (τ, ms)	7.1	0.3	28	****	15.8	0.8	25
Sag ratio	1.42	0.02	28	****	1.06	0.00	25
Rheobase (pA)	95	8	28	***	61	5	25
Threshold (mV)	-31.8	0.9	28	*	-34.6	0.7	25
Latency (ms)	55	4	28	n.s.	71	7	25
AP rise amplitude (mV)	74.2	1.6	28	n.s.	74.4	1.3	25
AP peak (mV)	42.5	0.9	28	*	39.8	0.9	25
AP width (ms)	0.34	0.02	28	***	0.38	0.01	25
AHP (mV)	-22.6	0.9	28	***	-18.8	0.6	25
Max depolarisation rate (V/s)	517	24	28	**	429	15	25
Max repolarisation rate (V/s)	-255	17	28	**	-203	7	25
Current at 10Hz (pA)	147	13	28	*	191	17	25
Burst index	0.18	0.02	28	*	0.26	0.07	25
Initial burst ISI	0.8	0.2	28	****	2.4	0.2	25
Mean initial ISI (ms)	0.016	0.001	28	****	0.009	0.002	25
Adaptation index	2.50	0.13	28	**	1.84	0.15	25
Fast doublet index	8.64	1.55	28	*	17.88	2.95	25
Fast doublet ratio	1.88	0.15	28	****	1.53	0.43	24
Δ peak between AP1-AP2 (mV)	3.7	0.5	28	****	12.4	1.0	25
Post-train AHP (mV)	11.2	0.8	28	****	2.3	0.5	25
Input output slope (0-9Hz, Hz/nA)	110	9	28	****	41	9	25
Firing rate at 200pA (Hz)	42	5	28	**	19	4	25
Rebound spike probability	0.82	0.07	28	***	0.36	0.10	25

Table 1 - table supplement 1. Electrophysiological property comparison of labelled projection neurons in the AD and AV.

	AD-PrS			Significance	AD-gRSC			AV-PrS			Significance	AV-gRSC		
	Mean	SEM	N		Mean	SEM	N	Mean	SEM	N		Mean	SEM	N
Resting membrane potential (mV)	-61.5	1.0	16	*	-57.9	0.8	12	-71.0	0.7	13	n.s.	-70.7	1.2	12
Input resistance (MΩ)	134	11	16	n.s.	147	14	12	213	25	13	n.s.	230	29	12
Time constant (τ, ms)	6.8	0.4	16	n.s.	7.5	0.4	12	16.2	1.2	13	n.s.	15.4	1.0	12
Sag ratio	1.44	0.03	16	n.s.	1.41	0.04	12	1.06	0.01	13	n.s.	1.06	0.00	12
Rheobase (pA)	98	12	16	n.s.	92	9	12	58	6	13	n.s.	63	7	12
Threshold (mV)	-32.9	1.0	16	n.s.	-30.2	1.7	12	-35.2	1.0	13	n.s.	-33.9	1.0	12
Latency (ms)	55	5	16	n.s.	54	5	12	67	8	13	n.s.	76	11	12
AP rise amplitude (mV)	75.3	2.1	16	n.s.	72.8	2.7	12	74.3	2.0	13	n.s.	74.6	1.6	12
AP peak (mV)	42.4	1.4	16	n.s.	42.6	1.3	12	39.1	1.4	13	n.s.	40.7	1.1	12
AP width (ms)	0.33	0.02	16	n.s.	0.35	0.02	12	0.37	0.02	13	n.s.	0.39	0.01	12
AHP (mV)	-22.0	0.7	16	n.s.	-23.5	1.8	12	-19.3	1.0	13	n.s.	-18.3	0.7	12
Max depolarisation rate (V/s)	534	35	16	n.s.	494	31	12	430	26	13	n.s.	428	16	12
Max repolarisation rate (V/s)	-266	24	16	n.s.	-239	25	12	-209	11	13	n.s.	-196	6	12
Current at 10Hz (pA)	154	21	16	n.s.	138	14	12	198	17	13	n.s.	183	31	12
Burst index	0.18	0.03	16	n.s.	0.18	0.04	12	0.12	0.06	13	n.s.	0.41	0.12	12
Initial burst ISI	0.9	0.2	16	n.s.	0.7	0.2	12	2.2	0.4	13	n.s.	2.5	0.2	12
Mean initial ISI (ms)	0.015	0.002	16	n.s.	0.017	0.001	12	0.011	0.003	13	n.s.	0.006	0.002	12
Adaptation index	2.64	0.13	16	n.s.	2.31	0.23	12	2.02	0.25	13	n.s.	1.64	0.16	12
Fast doublet index	9.58	2.63	16	n.s.	7.39	0.96	12	20.19	3.95	13	n.s.	15.39	4.48	12
Fast doublet ratio	2.01	0.23	16	n.s.	1.70	0.17	12	1.89	0.79	13	n.s.	1.11	0.05	11
Δ peak between AP1-AP2 (mV)	4.0	0.6	16	n.s.	3.3	1.0	12	11.3	1.4	13	n.s.	13.6	1.3	12
Post-train AHP (mV)	10.3	0.9	16	n.s.	12.3	1.2	12	2.9	0.7	13	n.s.	1.7	0.6	12
Input output slope (0-9Hz, Hz/nA)	105	13	16	n.s.	115	14	12	32	4	13	n.s.	51	17	12
Firing rate at 200pA (Hz)	42	7	16	n.s.	43	7	12	16	4	13	n.s.	21	7	12
Rebound spike probability	0.81	0.10	16	n.s.	0.83	0.11	12	0.54	0.14	13	n.s.	0.17	0.11	12

Table 1 - table supplement 2. Electrophysiological property comparison between PrS-projecting group and gRSC-projecting group in the AD and AV

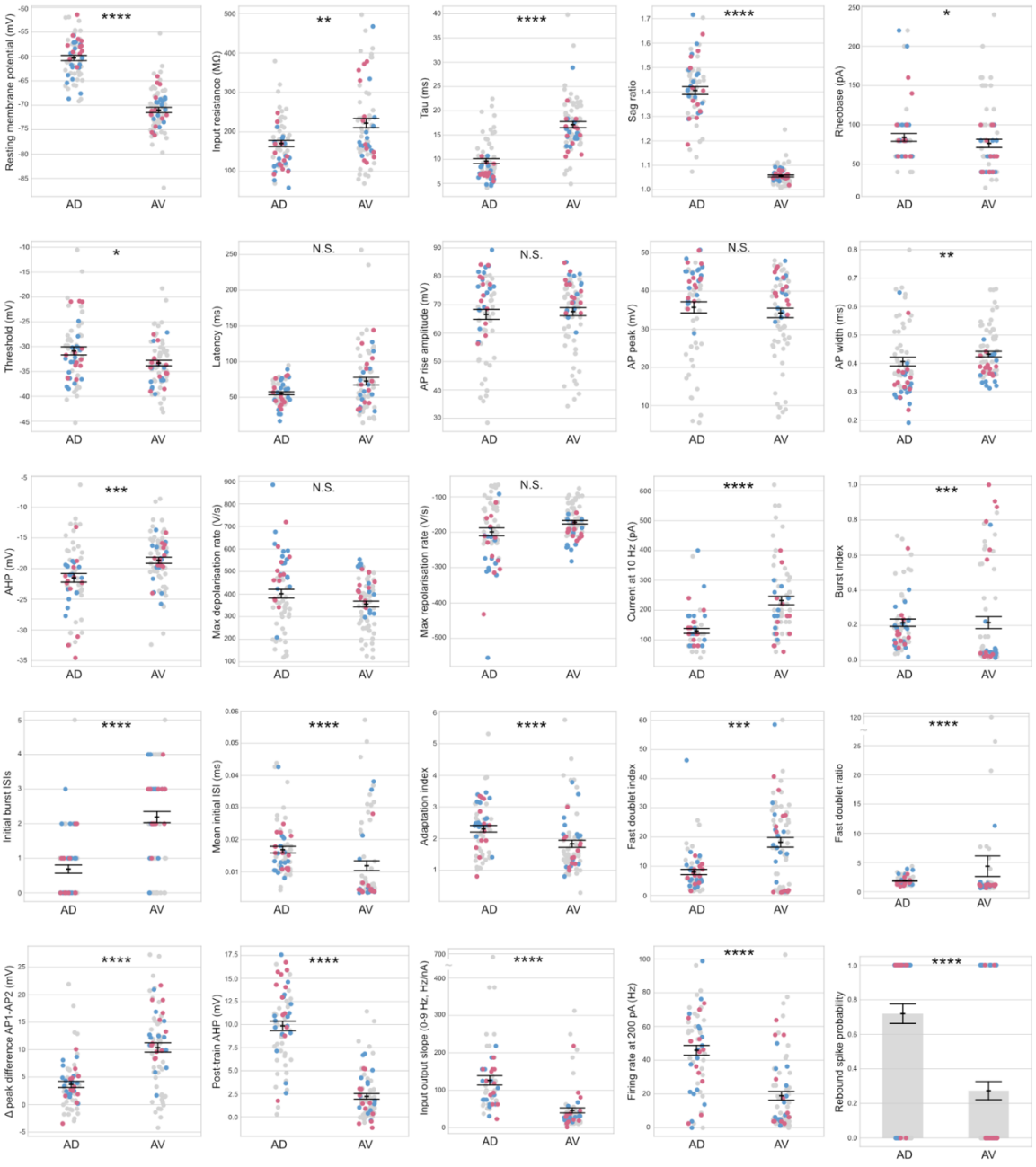

Table 1 - figure supplement 1. Comparison of 25 intrinsic electrophysiological properties between AD and AV neurons.

Cyan points represent neurons projecting to the PrS, and magenta points represent neurons projecting to the gRSC. Neurons without retrograde labeling are shown in gray.Mean values ± SEM for each group (AD vs. AV) are indicated. Statistical comparisons between AD and AV groups were performed using the Mann–Whitney U test. Significance levels are denoted as follows: * $p < 0.05$, **$p < 0.01$, ***$p < 0.001$, ****$p < 0.0001$.

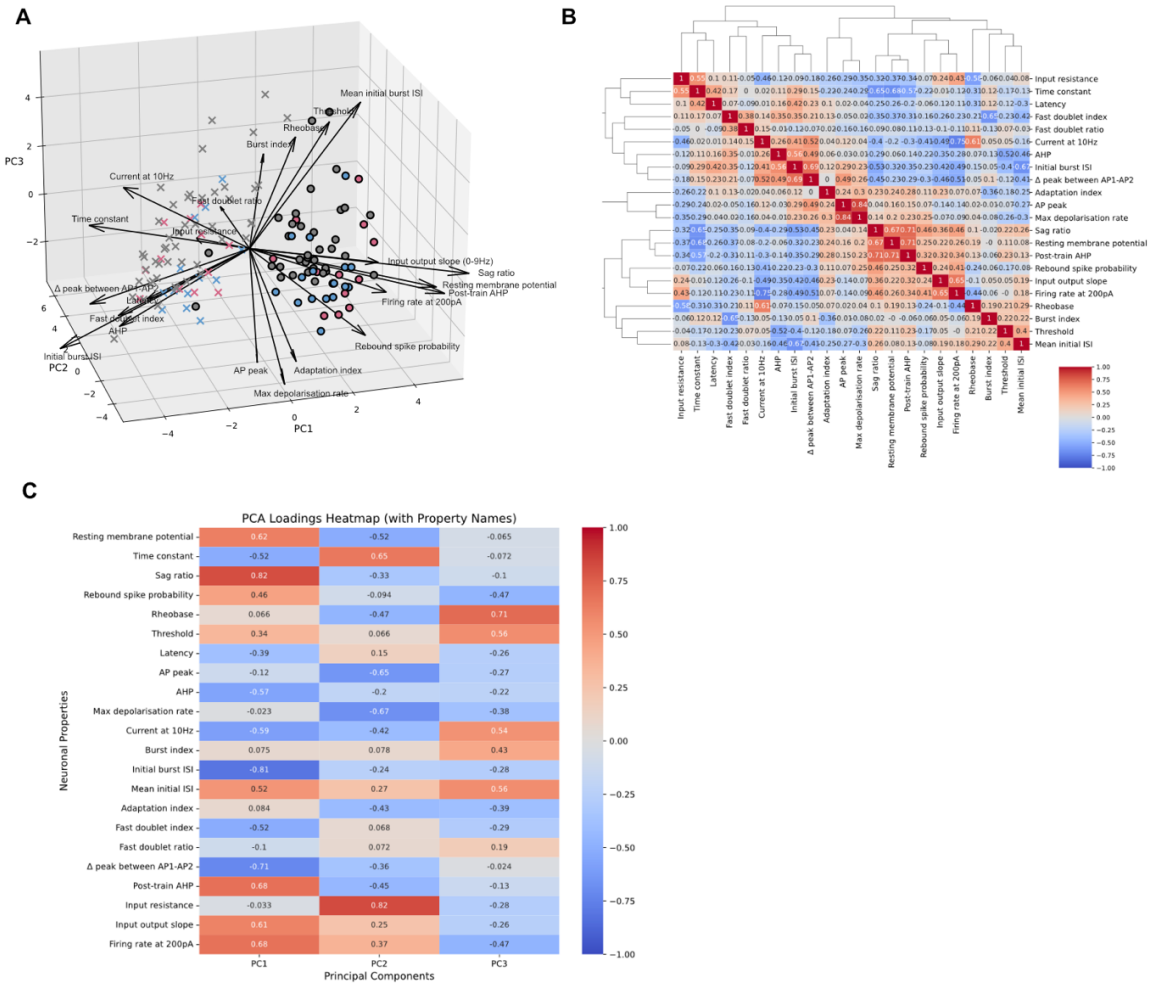

Figure 3 - figure supplement 1. Correlation of the intrinsic electrophysiological properties for PCA

A) PCA biplots showing the correlations of each electrophysiological property on the PC1, PC2, and PC3 planes.
B) Correlation heat-map among electrophysiological properties.
C) PCA loading heat-map illustrating the contribution of each property to the principal components.

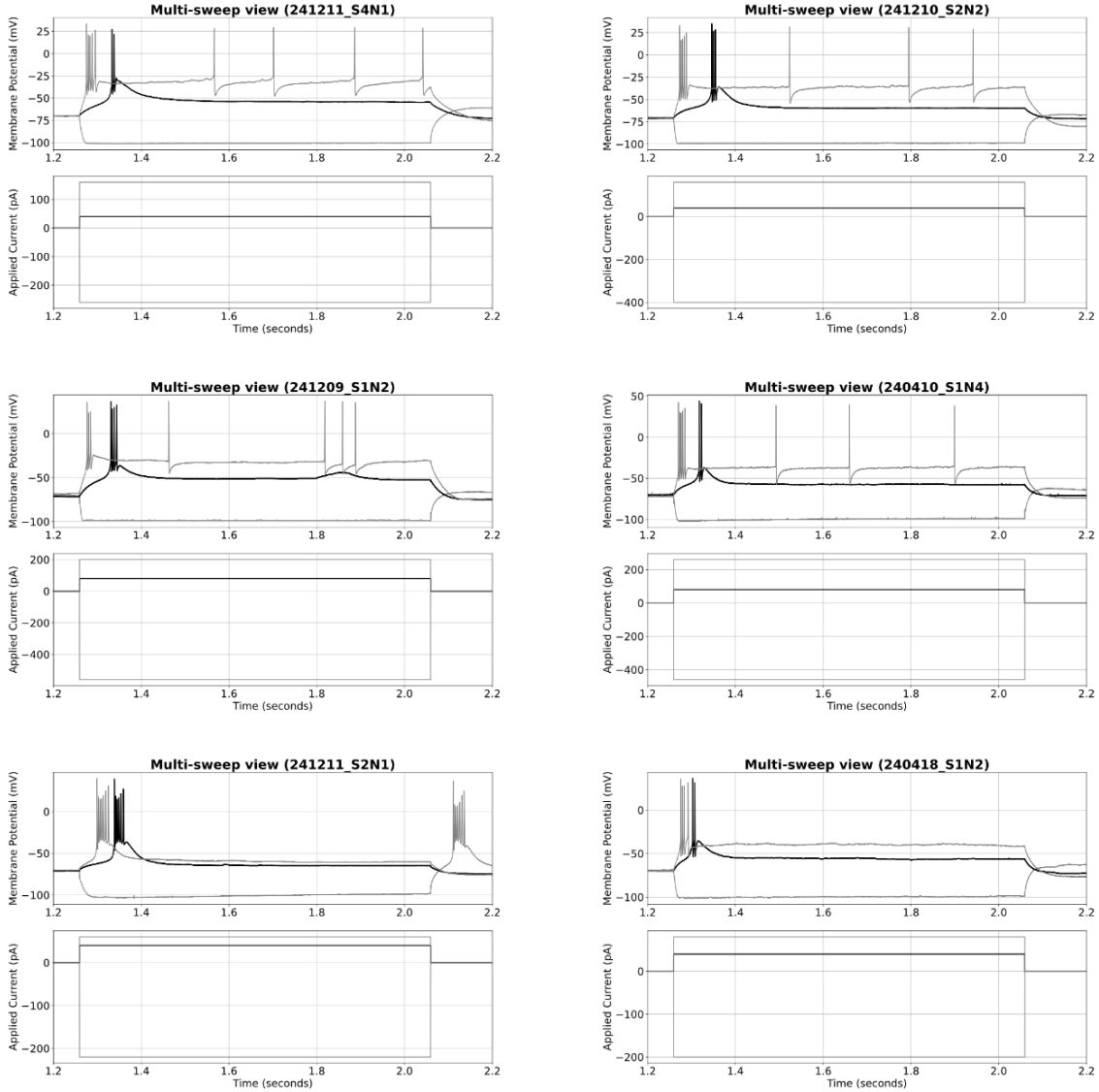

Figure 3 - figure supplement 2. Typical firing patterns of AV neurons

Example traces from six AV neurons (N=4). The rheobase sweep is shown in black, while hyperpolarised and 10 Hz sweeps are shown in grey. The first four cells exhibit irregular firing following an initial burst at 10 Hz sweep. Some AV neurons did not fire beyond the initial burst like the last two examples.

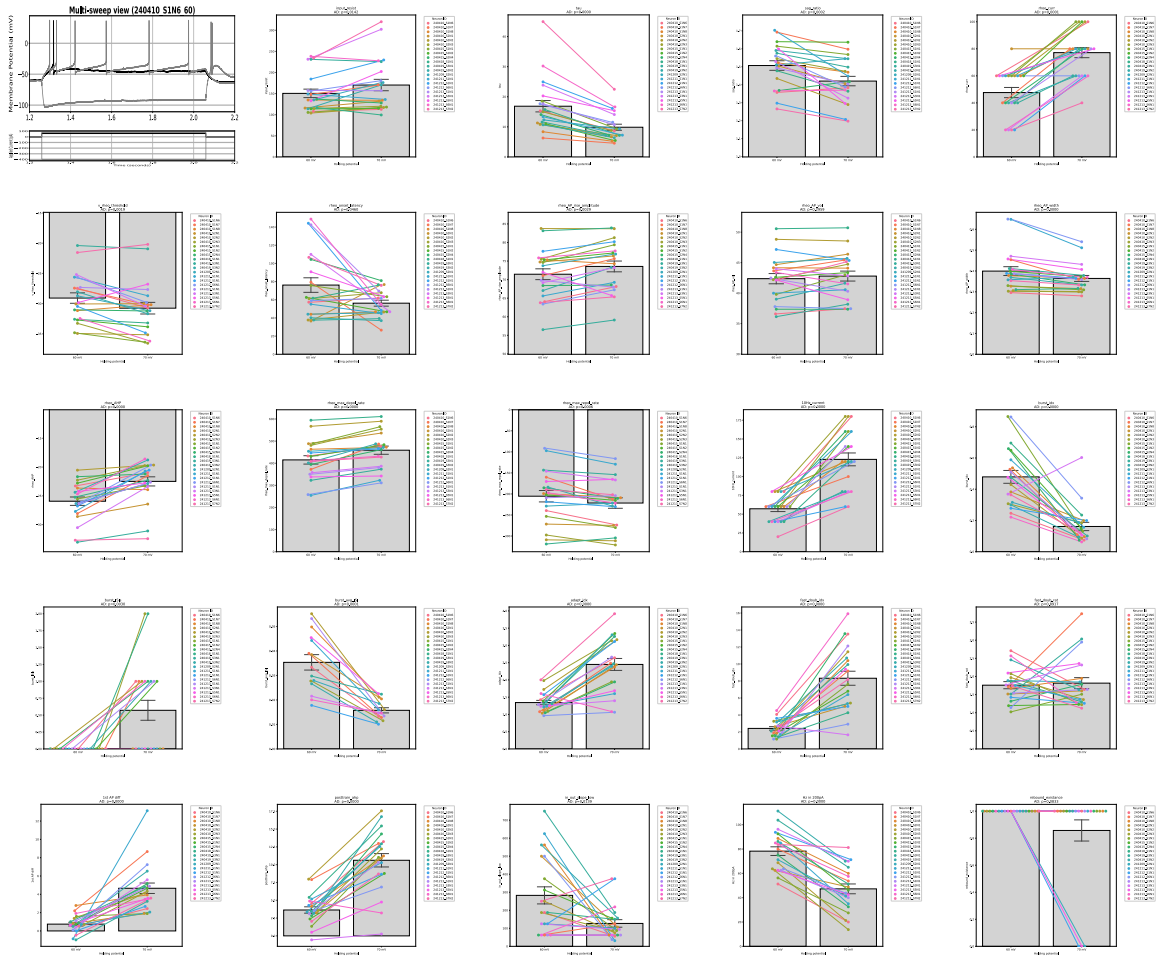

Figure 3 - figure supplement 3. Electrophysiological properties of AD neurons at -60 mV and -70 mV.

Electrophysiological properties of AD neurons were measured in the same cells at -60 mV and -70 mV. The paired differences were calculated for each property. Top left: example trace from an AD neuron held at -60 mV. At -60 mV, lower rheobase current elicits action potentials in AD neurons (48 ± 3 pA at -60 mV and 77 ± 4 pA at -70 mV), and voltage threshold slightly increased (-29.1 ± 0.9 mV at -60 mV and -30.8 ± 1.0 mV at -70 mV). All neurons exhibited rebound spiking activity followed by hyperpolarisation, when held at -60 mV. The input resistance was lower at -60 mV (151 ± 10 MΩ at -60 mV and 170 ± 13 MΩ at -70 mV). The membrane time constant (16.9 ± 0.9 ms at -60 mV and 9.9 ± 1.0 ms at -70 mV) and latency (76 ± 8 ms at -60 mV and 56 ± 3 ms at -70 mV) were increased at -60 mV. The AP waveform was largely preserved, with only subtle changes: reduced AP rise amplitudes, increased AP widths, and decreased max depolarisation rate and max repolarisation rate. However, the AHP amplitude was significantly larger (-26.0 ± 0.7 mV at -60 mV and -22.5 ± 0.8 mV at -70 mV). Also, less current was required to generate 10 Hz firing (57 ± 4 pA at -60 mV and 123 ± 9 pA at -70 mV), and the input-output slope was steeper (283 ± 47 Hz/nA at -60 mV and 127 ± 21 Hz/nA at -70 mV). The firing pattern became more distinctly adaptive, without

showing initial burst. Interestingly, the difference between the peaks of the first and second APs was reduced (0.7 ± 0.2 mV at -60 mV and 4.7 ± 0.6 mV at -70 mV). Statistical comparisons were performed with the Wilcoxon signed-rank test and the p-value is shown in each plot. Detailed mean ± SEM values and the number of cells are shown in the Figure 3 - table supplement 1.

	AD at -60mV			Significance	AD at -70mV		
	Mean	SEM	N		Mean	SEM	N
Input resistance (MΩ)	151	10	21	0.01417	170	13	21
Time constant (τ, ms)	16.9	1.9	21	0.00000	9.9	1.0	21
Sag ratio	1.51	0.03	21	0.00016	1.42	0.03	21
Rheobase (pA)	48	4	21	0.00007	77	4	21
Threshold (mV)	-29.1	0.9	21	0.00186	-30.8	1.0	21
Latency (ms)	76	8	21	0.04599	56	3	21
AP rise amplitude (mV)	71.5	1.5	21	0.00286	73.5	1.5	21
AP peak (mV)	42.4	0.8	21	0.29588	42.8	0.8	21
AP width (ms)	0.40	0.02	21	0.00002	0.36	0.01	21
AHP (mV)	-25.9	0.7	21	0.00000	-22.5	0.8	21
Max depolarisation rate (V/s)	415	19	21	0.00000	459	19	21
Max repolarisation rate (V/s)	-205	14	21	0.00061	-222	12	21
Current at 10Hz (pA)	57	4	21	0.00000	123	9	21
Burst index	0.48	0.04	21	0.00002	0.16	0.03	21
Initial burst ISI	0.0	0.0	21	0.00296	0.6	0.1	21
Mean initial ISI (ms)	0.035	0.003	15	0.00006	0.016	0.001	15
Adaptation index	1.34	0.06	21	0.00001	2.45	0.17	21
Fast doublet index	2.42	0.21	21	0.82643	5.91	0.00	21
Fast doublet ratio	1.76	0.10	21	0.15184	0.06	0.89	21
Δ peak between AP1-AP2 (mV)	0.7	0.2	21	0.00000	4.7	0.6	21
Post-train AHP (mV)	3.6	0.4	21	0.00000	10.6	0.9	21
Input output slope (0-9Hz, Hz/nA)	283	47	21	0.01387	127	21	21
Firing rate at 200pA (Hz)	78	4	21	0.00000	47	4	21
Rebound spike probability	1.00	0.00	21	0.08326	0.86	0.08	21

Figure 3 - table supplement 1. Electrophysiological properties of AD neurons at -60 mV and -70 mV.

	AD-Baseline			Significance	AD-ZD7288		
	Mean	SEM	N		Mean	SEM	N
Resting membrane potential (mV)	-61.3	0.6	11	n.s.	-63.9	2.4	11
Sag ratio	1.47	0.04	11	***	1.04	0.01	11
AHP (mV)	-27.9	1.2	11	*	-25.7	1.3	11
Post-train AHP (mV)	3.3	0.6	11	**	-1.0	0.3	11
Rebound spike probability	1.00	0.00	11	*	0.45	0.16	11
Time constant (τ, ms)	22.3	2.8	11	*	35.4	5.2	11
Input resistance (MΩ)	186	14	11	**	397	40	11
Δ peak between AP1-AP2 (mV)	0.5	0.2	11	*	2.4	0.9	11

	AV-Baseline			Significance	AV-ZD7288		
	Mean	SEM	N		Mean	SEM	N
Resting membrane potential (mV)	-70.6	0.4	9	n.s.	-73.5	1.5	9
Sag ratio	1.04	0.01	9	*	1.01	0.00	9
AHP (mV)	-16.6	0.7	9	n.s.	-15.0	0.7	9
Post-train AHP (mV)	2.7	0.7	9	**	-1.1	0.3	9
Rebound spike probability	0.22	0.15	9	n.s.	0.00	0.00	9
Time constant (τ, ms)	20.6	0.9	9	n.s.	23.0	2.2	9
Input resistance (MΩ)	232	17	9	n.s.	242	25	9
Δ peak between AP1-AP2 (mV)	12.2	0.8	9	**	14.7	0.9	9

Figure 4 - table supplement 1. Quantitative and statistical comparison of electrophysiological properties between baseline and ZD7288 application in AD and AV neurons.

241212_S2 (same cell as panel D-iv)

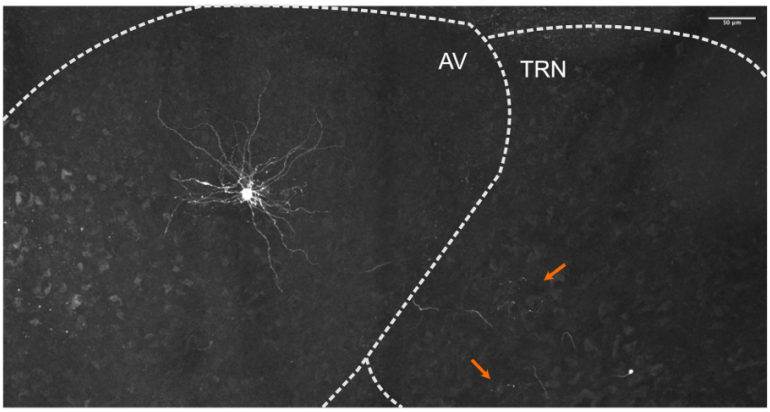

241230_S1 (same cell as panel B yellow AD cell)

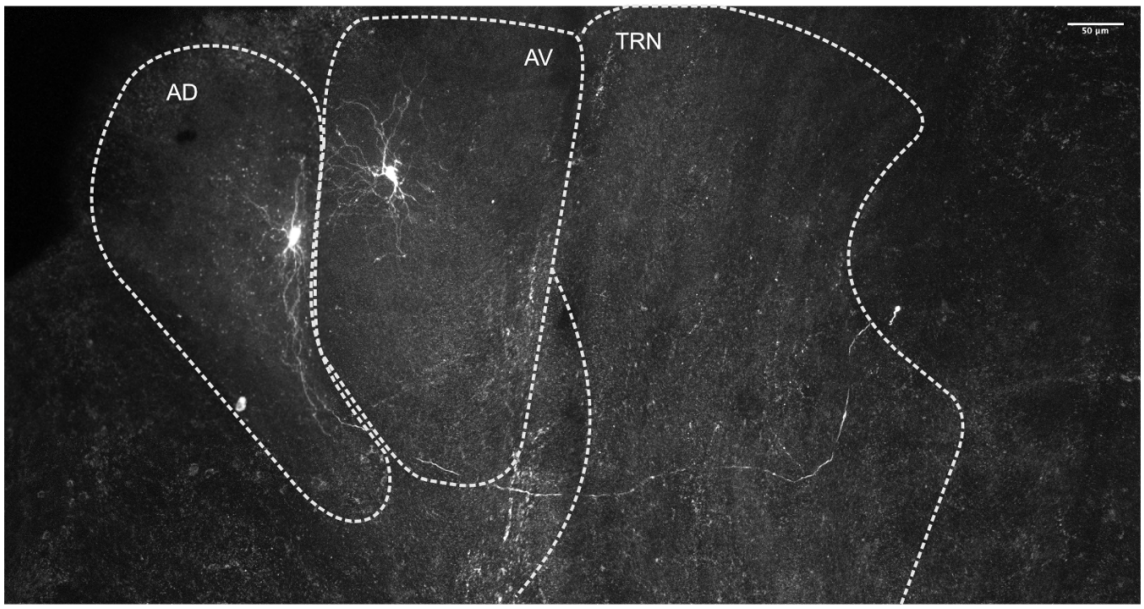

Figure 5 - figure supplement 1. Original confocal images of biocytin-filled AD and AV neurons with long axonal projection.

2 example images of 3D reconstructed neurons shown in figure 4B. The anatomical delineation was referred to by Paxinos (2013) and stephen thankachan (2019). Top : Z-stacked confocal image of red AV neuron. Orange arrows indicate the axonal arborisation in the TRN. Bottom: Z-stacked confocal image of yellow AD neuron. The

axonal projection passes through the TRN but does not ramify. Yellow arrows follow the axonal projection. Scale bar: 50 um

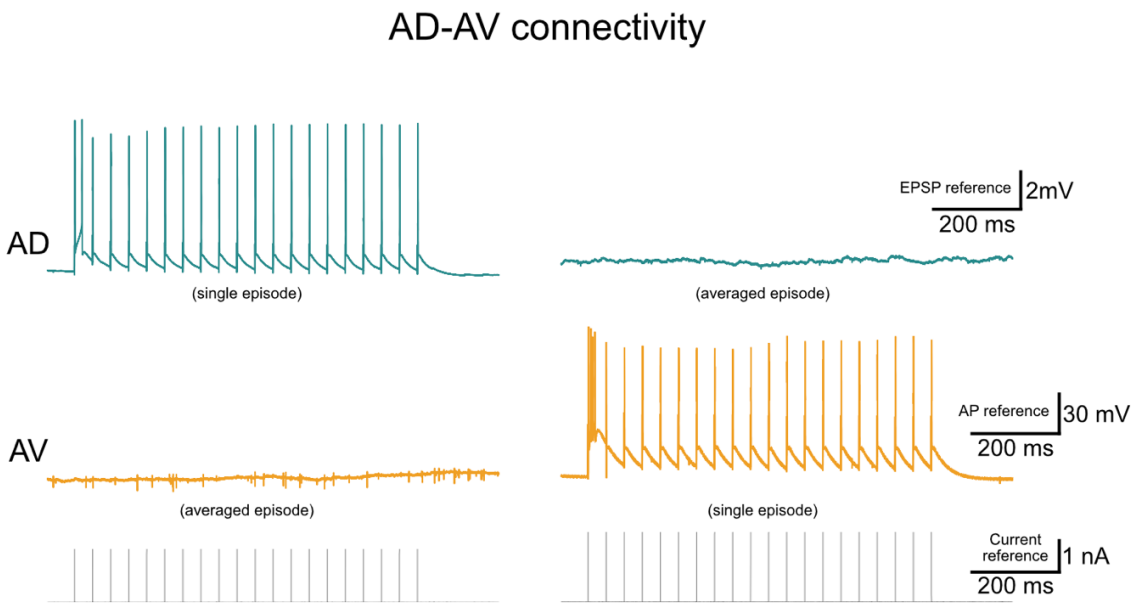

Figure 5 - figure supplement 2. Examination of functional connectivity between AD and AV neurons.

Pair recording of AD and AV neurons performed with current injection into each neuron individually to assess their functional connectivity. Left: Current injection into AD neuron and the responses (silent) of the AV neuron. Right: Current injection into AV neuron and the responses of the AD neuron (silent). (n=8)

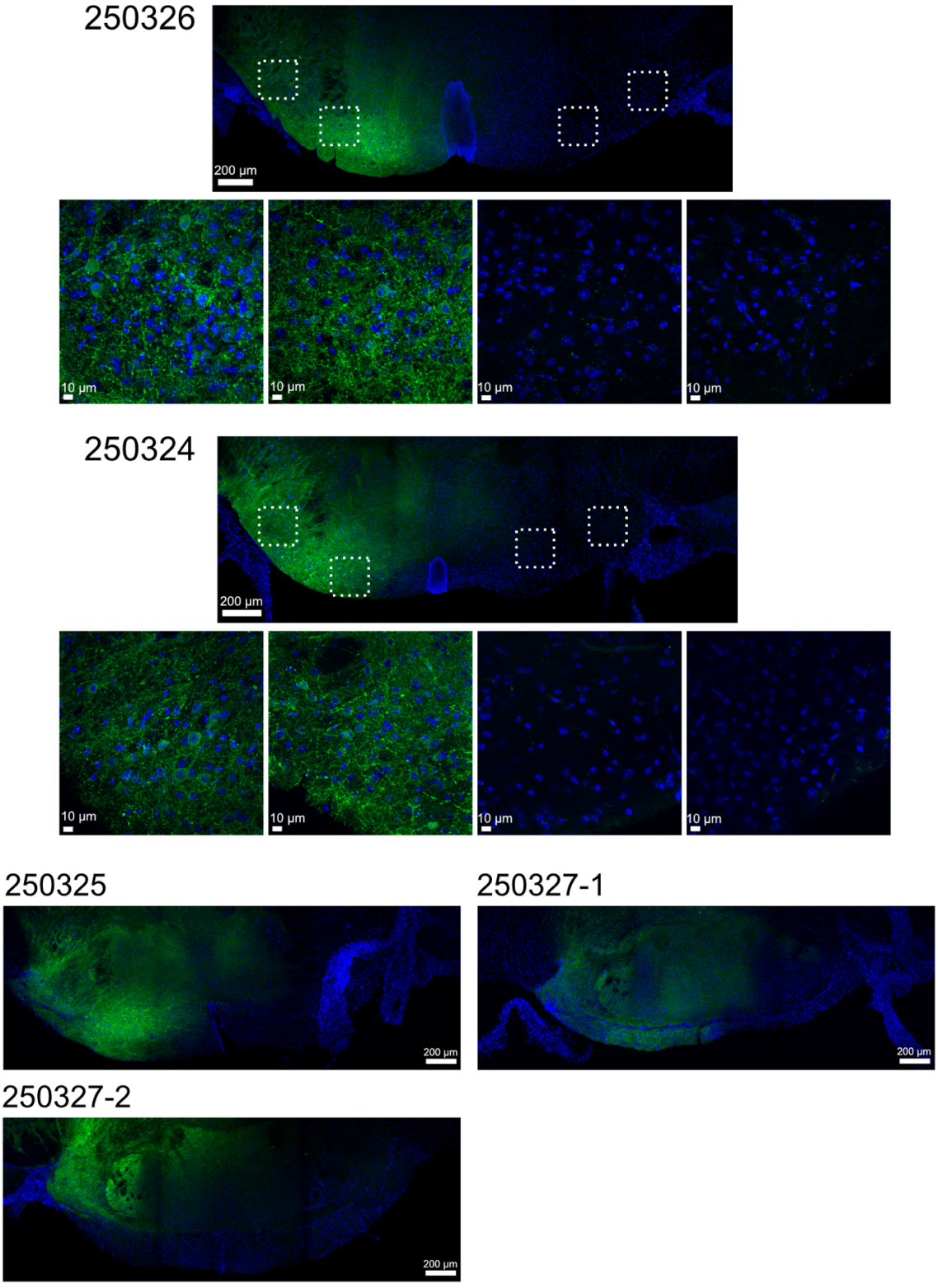

Figure 6 - figure supplement 1. Chronos expression in the unilateral MBO.

Confocal images (10x magnification, tiled images, scale bar: 200 um) of the mammillary body expressing chronos from 5 mice. Each number indicates mouse

identification numbers. 40x magnified images in the ipsilateral and contralateral side of LMN and MMN from 2 mice (250326 and 250324) are shown.

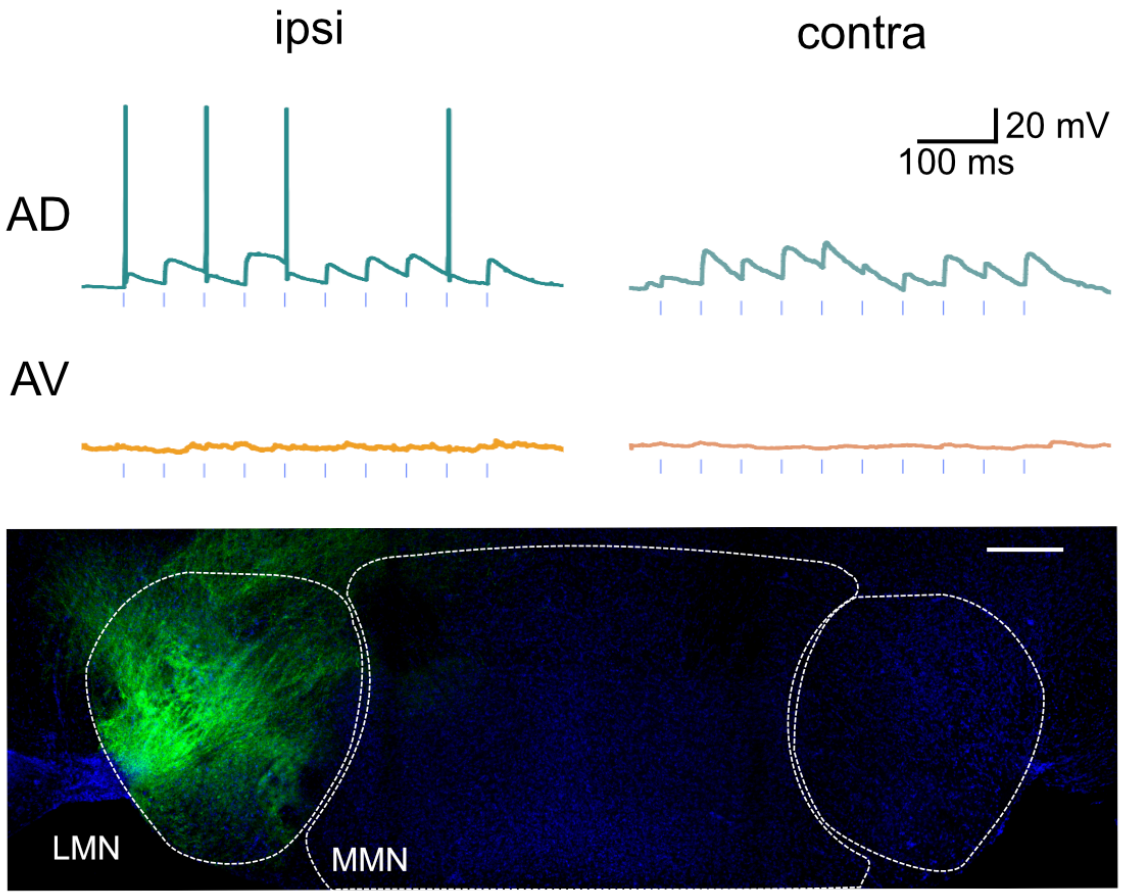

Figure 6 - figure supplement 2. Post-synaptic events in the AD and AV evoked by unilateral LMN input.

Unilaterally targeted injection in the LMN leads to action potential firing in the ipsilateral AD, and subthreshold EPSPs in the contralateral AD. No response in neurons recorded in the ipsi-and contralateral AV. Scale bar in the image: 200 μm

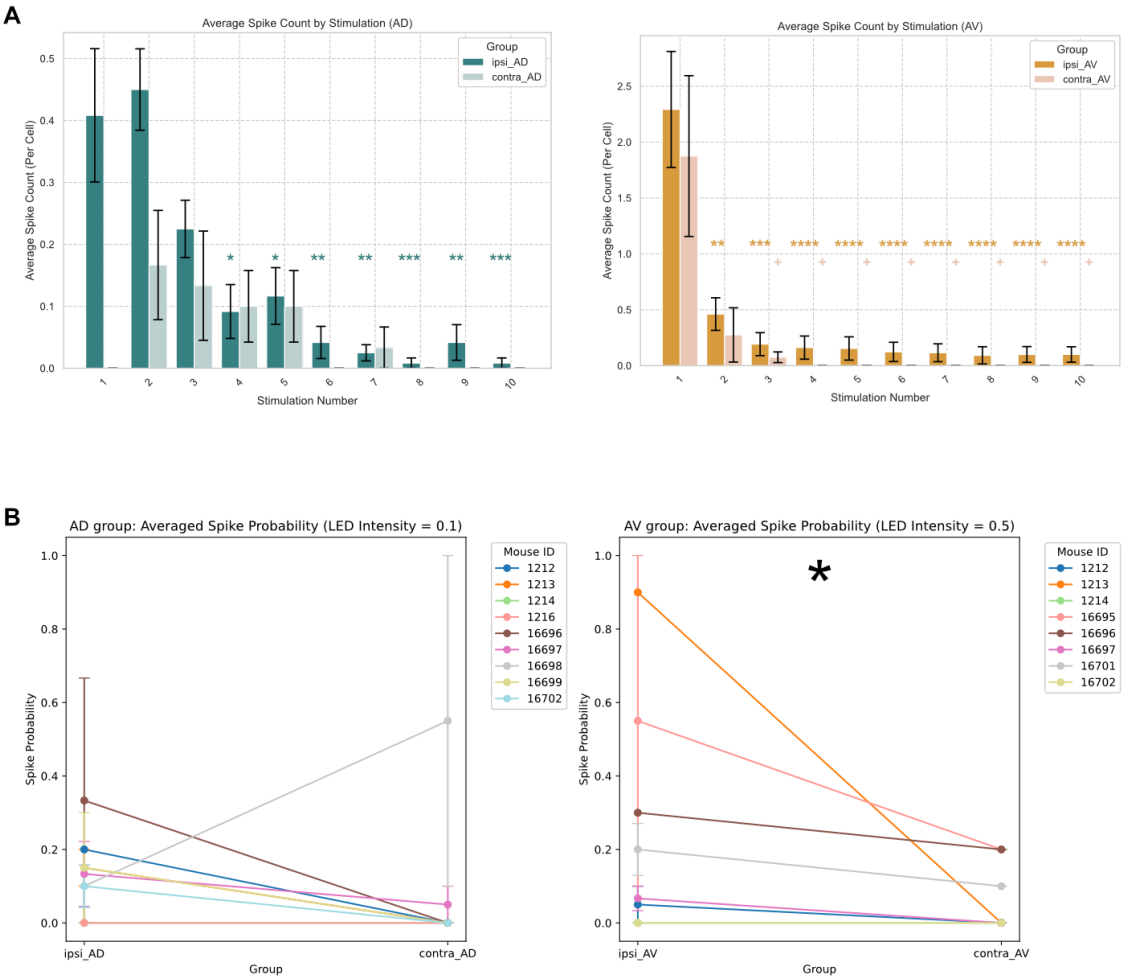

Figure 7 - figure supplement 1. Quantification of spiking activities of AD and AV neurons by mammillary inputs.

A) Averaged number of spikes across 10 light stimulations in AD and AV neurons functionally connected to LMN projections. The bar graph indicates the averaged number of spikes in each stimulation and vertical lines indicate ± SEM. Differences in averaged spike numbers between the first and subsequent stimulations were evaluated for statistical significance using Mann-Whitney U test. Significance is indicated by asterisks (*) for the ipsilateral group and plus signs (+) for the contralateral group. *p < 0.05, **p < 0.01, ***p < 0.001, ****p < 0.0001.

B) Comparison of spike probability between ipsilateral and contralateral side of AD and AV within the same mouse. Each data point represents the averaged spike probability of recorded neurons. The spike probability from the same mouse is indicated in the same colour code and connected by line. Statistical comparisons were performed using the Wilcoxon signed-rank test. *p < 0.05, **p < 0.01, ***p < 0.001, ****p < 0.0001

References

Aggleton, J. P., O'Mara, S. M., Vann, S. D., Wright, N. F., Tsanov, M., & Erichsen, J. T. (2010). Hippocampal–anterior thalamic pathways for memory: Uncovering a network of direct and indirect actions. *European Journal of Neuroscience*, *31*(12), 2292–2307. https://doi.org/10.1111/j.1460-9568.2010.07251.x

Aggleton, J. P., Yanakieva, S., Sengpiel, F., & Nelson, A. J. (2021). The separate and combined properties of the granular (area 29) and dysgranular (area 30) retrosplenial cortex. *Neurobiology of Learning and Memory*, *185*, 107516. https://doi.org/10.1016/j.nlm.2021.107516

Ajabi, Z., Keinath, A. T., Wei, X.-X., & Brandon, M. P. (2023). Population dynamics of head-direction neurons during drift and reorientation. *Nature*, *615*(7954), 892–899. https://doi.org/10.1038/s41586-023-05813-2

Albo, Z. (2003). Anterior thalamic unit discharge profiles and coherence with hippocampal theta rhythm. *Thalamus & Related Systems*, *2*(2), 133–144. https://doi.org/10.1016/S1472-9288(03)00006-2

Angelaki, D. E., & Laurens, J. (2020). The head direction cell network: Attractor dynamics, integration within the navigation system, and three-dimensional properties. *Current Opinion in Neurobiology*, *60*, 136–144. https://doi.org/10.1016/j.conb.2019.12.002

Bankhead, P., Loughrey, M. B., Fernández, J. A., Dombrowski, Y., McArt, D. G., Dunne, P. D., McQuaid, S., Gray, R. T., Murray, L. J., Coleman, H. G., James, J. A., Salto-Tellez, M., & Hamilton, P. W. (2017). QuPath: Open source software for digital pathology image analysis. *Scientific Reports*, *7*(1), 16878. https://doi.org/10.1038/s41598-017-17204-5

Bassett, J. P., & Taube, J. S. (2001). Neural Correlates for Angular Head Velocity in the Rat Dorsal Tegmental Nucleus. *The Journal of Neuroscience*, *21*(15), 5740–5751. https://doi.org/10.1523/JNEUROSCI.21-15-05740.2001

Bassett, J. P., Tullman, M. L., & Taube, J. S. (2007). Lesions of the Tegmentomammillary Circuit in the Head Direction System Disrupt the Head Direction Signal in the Anterior Thalamus. *The Journal of Neuroscience*, *27*(28), 7564–7577. https://doi.org/10.1523/JNEUROSCI.0268-07.2007

Bishop, H. I., Guan, D., Bocksteins, E., Parajuli, L. K., Murray, K. D., Cobb, M. M., Misonou, H., Zito, K., Foehring, R. C., & Trimmer, J. S. (2015). Distinct Cell- and Layer-Specific Expression Patterns and Independent Regulation of Kv2 Channel Subtypes in Cortical Pyramidal Neurons. *The Journal of Neuroscience*, *35*(44), 14922–14942. https://doi.org/10.1523/JNEUROSCI.1897-15.2015

Blair, H., & Sharp, P. (1995). Anticipatory head direction signals in anterior thalamus: Evidence for a thalamocortical circuit that integrates angular head motion to compute head direction. *The Journal of Neuroscience*, *15*(9), 6260–6270. https://doi.org/10.1523/JNEUROSCI.15-09-06260.1995

Blair, H. T., Cho, J., & Sharp, P. E. (1998). Role of the Lateral Mammillary Nucleus in the Rat Head Direction Circuit. *Neuron*, *21*(6), 1387–1397. https://doi.org/10.1016/S0896-6273(00)80657-1

Blair, H. T., Cho, J., & Sharp, P. E. (1999). The Anterior Thalamic Head-Direction Signal Is Abolished by Bilateral But Not Unilateral Lesions of the Lateral Mammillary Nucleus. *The Journal of Neuroscience*, *19*(15), 6673–6683. https://doi.org/10.1523/JNEUROSCI.19-15-06673.1999

Blanco-Hernández, E., Balsamo, G., Preston-Ferrer, P., & Burgalossi, A. (2024). Sensory and behavioral modulation of thalamic head-direction cells. *Nature Neuroscience*, *27*(1), 28–33. https://doi.org/10.1038/s41593-023-01506-1

Bland, B. H., Konopacki, J., Kirk, I. J., Oddie, S. D., & Dickson, C. T. (1995). Discharge patterns of hippocampal theta-related cells in the caudal diencephalon of the urethan-anesthetized rat. *Journal of Neurophysiology*, *74*(1), 322–333. https://doi.org/10.1152/jn.1995.74.1.322

Boccara, C. N., Sargolini, F., Thoresen, V. H., Solstad, T., Witter, M. P., Moser, E. I., & Moser, M.-B. (2010). Grid cells in pre- and parasubiculum. *Nature Neuroscience*, *13*(8), 987–994. https://doi.org/10.1038/nn.2602

Bolton, R. F., Cornwall, J., & Phillipson, O. T. (1993). Collateral axons of cholinergic pontine neurones projecting to midline, mediodorsal and parafascicular thalamic nuclei in the rat. *Journal of Chemical Neuroanatomy*, *6*(2), 101–114. https://doi.org/10.1016/0891-0618(93)90031-X

Brandon, M. P., Bogaard, A. R., Schultheiss, N. W., & Hasselmo, M. E. (2013). Segregation of cortical head direction cell assemblies on alternating theta cycles. *Nature Neuroscience*, *16*(6), 739–748. https://doi.org/10.1038/nn.3383

Brown, J. E., Yates, B. J., & Taube, J. S. (2002). Does the vestibular system contribute to head direction cell activity in the rat? *Physiology & Behavior*, *77*(4–5), 743–748. https://doi.org/10.1016/S0031-9384(02)00928-9

Bubb, E. J., Kinnavane, L., & Aggleton, J. P. (2017). Hippocampal–diencephalic–cingulate networks for memory and emotion: An anatomical guide. *Brain and Neuroscience Advances*, *1*, 2398212817723443. https://doi.org/10.1177/2398212817723443

Butler, W. N., Smith, K. S., Van Der Meer, M. A. A., & Taube, J. S. (2017). The Head-Direction Signal Plays a Functional Role as a Neural Compass during Navigation. *Current Biology*, *27*(9), 1259–1267. https://doi.org/10.1016/j.cub.2017.03.033

Cacucci, F., Lever, C., Wills, T. J., Burgess, N., & O'Keefe, J. (2004). Theta-Modulated Place-by-Direction Cells in the Hippocampal Formation in the Rat. *The Journal of Neuroscience*, *24*(38), 8265–8277. https://doi.org/10.1523/JNEUROSCI.2635-04.2004

Canto, C. B., Koganezawa, N., Beed, P., Moser, E. I., & Witter, M. P. (2012). All Layers of Medial Entorhinal Cortex Receive Presubicular and Parasubicular Inputs. *The Journal of Neuroscience*, *32*(49), 17620–17631. https://doi.org/10.1523/JNEUROSCI.3526-12.2012

Chen, L. L., Lin, L.-H., Green, E. J., Barnes, C. A., & McNaughton, B. L. (1994). Head-direction cells in the rat posterior cortex: I. anatomical distribution and behavioral modulation. *Experimental Brain Research*, *101*(1), 8–23. https://doi.org/10.1007/BF00243212

Chiaruttini, N., Castoldi, C., Requie, L. M., Camarena-Delgado, C., Dal Bianco, B., Gräff, J., Seitz, A., & Silva, B. A. (2025). ABBA+BraiAn, an integrated suite for whole-brain mapping, reveals brain-wide differences in immediate-early genes induction upon learning. *Cell Reports*, *44*(7), 115876. https://doi.org/10.1016/j.celrep.2025.115876

Cho, J., & Sharp, P. E. (2001). Head direction, place, and movement correlates for cells in the rat retrosplenial cortex. *Behavioral Neuroscience*, *115*(1), 3–25. https://doi.org/10.1037/0735-7044.115.1.3

Clark, B. J., LaChance, P. A., Winter, S. S., Mehlman, M. L., Butler, W., LaCour, A., & Taube, J. S. (2024). Comparison of head direction cell firing characteristics across thalamo-parahippocampal circuitry. *Hippocampus*, *34*(4), 168–196. https://doi.org/10.1002/hipo.23596

Claudi, F., Tyson, A. L., Petrucco, L., Margrie, T. W., Portugues, R., & Branco, T. (2021). Visualizing anatomically registered data with brainrender. *eLife*, *10*, e65751. https://doi.org/10.7554/eLife.65751

Cruce, J. A. F. (1975). An autoradiographic study of the projections of the mammillothalamic tract in the rat. *Brain Research*, *85*(2), 211–219. https://doi.org/10.1016/0006-8993(75)90072-4

Dillingham, C. M., Frizzati, A., Nelson, A. J. D., & Vann, S. D. (2015). How do mammillary body inputs contribute to anterior thalamic function? *Neuroscience & Biobehavioral Reviews*, *54*, 108–119. https://doi.org/10.1016/j.neubiorev.2014.07.025

El Mahmoudi, N., Huret, A., Laurent, C., Laurens, J., Jacob, P.-Y., & Sargolini, F. (2025). *Dynamics of thalamic directional coding under vestibular imbalance*. Neuroscience. https://doi.org/10.1101/2025.03.31.646416

Gao, X., Bender, F., Soh, H., Chen, C., Altafi, M., Schütze, S., Heidenreich, M., Gorbati, M., Corbu, M.-A., Carus-Cadavieco, M., Korotkova, T., Tzingounis, A. V., Jentsch, T. J., & Ponomarenko, A. (2021). Place fields of single spikes in hippocampus involve Kcnq3 channel-dependent entrainment of complex spike bursts. *Nature Communications*, *12*(1), 4801. https://doi.org/10.1038/s41467-021-24805-2

Golowasch, J., Thomas, G., Taylor, A. L., Patel, A., Pineda, A., Khalil, C., & Nadim, F. (2009). Membrane Capacitance Measurements Revisited: Dependence of

Capacitance Value on Measurement Method in Nonisopotential Neurons. *Journal of Neurophysiology*, *102*(4), 2161–2175. https://doi.org/10.1152/jn.00160.2009

Goodridge, J. P., Dudchenko, P. A., Worboys, K. A., Golob, E. J., & Taube, J. S. (1998). Cue control and head direction cells. *Behavioral Neuroscience*, *112*(4), 749–761. https://doi.org/10.1037/0735-7044.112.4.749

Goodridge, J. P., & Taube, J. S. (1995). Preferential use of the landmark navigational system by head direction cells in rats. *Behavioral Neuroscience*, *109*(1), 49–61. https://doi.org/10.1037/0735-7044.109.1.49

Guison, N. G., Ahmed, A. K., Dong, K., & Yamadori, T. (1995). Projections from the lateral mammillary nucleus to the anterodorsal thalamic nucleus in the rat. *The Kobe Journal of Medical Sciences*, *41*(6), 213–220.

Harden, S. (2022). *Analysis of electrophysiological recordings was performed with custom software written for this project using Python 3.10 and the pyABF package*. https://pypi.org/project/pyabf

Harris, C. R., Millman, K. J., Van Der Walt, S. J., Gommers, R., Virtanen, P., Cournapeau, D., Wieser, E., Taylor, J., Berg, S., Smith, N. J., Kern, R., Picus, M., Hoyer, S., Van Kerkwijk, M. H., Brett, M., Haldane, A., Del Río, J. F., Wiebe, M., Peterson, P., … Oliphant, T. E. (2020). Array programming with NumPy. *Nature*, *585*(7825), 357–362. https://doi.org/10.1038/s41586-020-2649-2

Hulse, B. K., & Jayaraman, V. (2020). Mechanisms Underlying the Neural Computation of Head Direction. *Annual Review of Neuroscience*, *43*(1), 31–54. https://doi.org/10.1146/annurev-neuro-072116-031516

Jacob, P.-Y., Casali, G., Spieser, L., Page, H., Overington, D., & Jeffery, K. (2017). An independent, landmark-dominated head-direction signal in dysgranular

retrosplenial cortex. *Nature Neuroscience*, *20*(2), 173–175. https://doi.org/10.1038/nn.4465

Jankowski, M. M., Ronnqvist, K. C., Tsanov, M., Vann, S. D., Wright, N. F., Erichsen, J. T., Aggleton, J. P., & O'Mara, S. M. (2013). The anterior thalamus provides a subcortical circuit supporting memory and spatial navigation. *Frontiers in Systems Neuroscience*, *7*. https://doi.org/10.3389/fnsys.2013.00045

Ji, Z., Lomi, E., Jeffery, K., Mitchell, A. S., & Burgess, N. (2025). Phase Precession Relative to Turning Angle in Theta-Modulated Head Direction Cells. *Hippocampus*, *35*(2), e70008. https://doi.org/10.1002/hipo.70008

Kim, D., Song, I., Keum, S., Lee, T., Jeong, M.-J., Kim, S.-S., McEnery, M. W., & Shin, H.-S. (2001). Lack of the Burst Firing of Thalamocortical Relay Neurons and Resistance to Absence Seizures in Mice Lacking α1G T-Type Ca2+ Channels. *Neuron*, *31*(1), 35–45. https://doi.org/10.1016/S0896-6273(01)00343-9

Kim, S. S., Rouault, H., Druckmann, S., & Jayaraman, V. (2017). Ring attractor dynamics in the *Drosophila* central brain. *Science*, *356*(6340), 849–853. https://doi.org/10.1126/science.aal4835

Knierim, J. J., Kudrimoti, H. S., & McNaughton, B. L. (1998). Interactions Between Idiothetic Cues and External Landmarks in the Control of Place Cells and Head Direction Cells. *Journal of Neurophysiology*, *80*(1), 425–446. https://doi.org/10.1152/jn.1998.80.1.425

Kocsis, B., Viana Di Prisco, G., & Vertes, R. (2001). Theta synchronization in the limbic system: The role of Gudden's tegmental nuclei. *European Journal of Neuroscience*, *13*(2), 381–388. https://doi.org/10.1111/j.1460-9568.2001.01392.x

Komisaruk, B. R. (1970). Synchrony between limbic system theta activity and rhythmical behavior in rats. *Journal of Comparative and Physiological Psychology*, *70*(3, Pt.1), 482–492. https://doi.org/10.1037/h0028709

Lin, X., Ghafuri, A., Chen, X., Kazmi, M., Nitz, D. A., & Xu, X. (2024). Projection-specific circuits of retrosplenial cortex with differential contributions to spatial cognition. *Molecular Psychiatry*. https://doi.org/10.1038/s41380-024-02819-8

Liu, H., Shi, Y., Zhang, Q., Yue, M., Qi, Y., Xu, B., Jing, J., Zhang, L., Yang, K., Zheng, M., Zhou, J., Lu, J., Gong, L., & He, M. (2025). Two distinct cell types of the medial mammillary body forming segregated subcircuits. *Molecular Psychiatry*, *30*(10), 4845–4858. https://doi.org/10.1038/s41380-025-03079-w

Lomi, E., Jeffery, K. J., & Mitchell, A. S. (2023). Convergence of location, direction, and theta in the rat anteroventral thalamic nucleus. *iScience*, *26*(7), 106993. https://doi.org/10.1016/j.isci.2023.106993

Lomi, E., Mathiasen, M. L., Cheng, H. Y., Zhang, N., Aggleton, J. P., Mitchell, A. S., & Jeffery, K. J. (2021). Evidence for two distinct thalamocortical circuits in retrosplenial cortex. *Neurobiology of Learning and Memory*, *185*, 107525. https://doi.org/10.1016/j.nlm.2021.107525

Maccaferri, G., & McBain, C. J. (1996). The hyperpolarization-activated current (Ih) and its contribution to pacemaker activity in rat CA1 hippocampal stratum oriens-alveus interneurones. *The Journal of Physiology*, *497*(1), 119–130. https://doi.org/10.1113/jphysiol.1996.sp021754

Martinez-Espinosa, P. L., Wu, J., Yang, C., Gonzalez-Perez, V., Zhou, H., Liang, H., Xia, X.-M., & Lingle, C. J. (2015). Knockout of Slo2.2 enhances itch, abolishes KNa current, and increases action potential firing frequency in DRG neurons. *eLife*, *4*, e10013. https://doi.org/10.7554/eLife.10013

Mathiasen, M. L., Nelson, A. J. D., Amin, E., O'Mara, S. M., & Aggleton, J. P. (2021). A Direct Comparison of Afferents to the Rat Anterior Thalamic Nuclei and Nucleus Reuniens: Overlapping But Different. *Eneuro*, *8*(5), ENEURO.0103-20.2021. https://doi.org/10.1523/ENEURO.0103-20.2021

Nassar, M., Simonnet, J., Huang, L.-W., Mathon, B., Cohen, I., Bendels, M. H. K., Beraneck, M., Miles, R., & Fricker, D. (2018). Anterior Thalamic Excitation and Feedforward Inhibition of Presubicular Neurons Projecting to Medial Entorhinal Cortex. *The Journal of Neuroscience*, *38*(28), 6411–6425. https://doi.org/10.1523/JNEUROSCI.0014-18.2018

Paxinos, G., & Franklin, K. B. J. (2013). *Paxinos and Franklin's the mouse brain in stereotaxic coordinates* (Fourth edition). Elsevier, Academic Press.

Pedregosa, F. (2011). Scikit-learn: Machine Learning in Python. *Journal of Machine Learning Research*.

Perez-Reyes, E. (2003). Molecular Physiology of Low-Voltage-Activated T-type Calcium Channels. *Physiological Reviews*, *83*(1), 117–161. https://doi.org/10.1152/physrev.00018.2002

Perry, B. A. L., & Mitchell, A. S. (2019). Considering the Evidence for Anterior and Laterodorsal Thalamic Nuclei as Higher Order Relays to Cortex. *Frontiers in Molecular Neuroscience*, *12*, 167. https://doi.org/10.3389/fnmol.2019.00167

Petrof, I., & Sherman, S. M. (2009). Synaptic Properties of the Mammillary and Cortical Afferents to the Anterodorsal Thalamic Nucleus in the Mouse. *Journal of Neuroscience*, *29*(24), 7815–7819. https://doi.org/10.1523/JNEUROSCI.1564-09.2009

Peyrache, A., Lacroix, M. M., Petersen, P. C., & Buzsáki, G. (2015). Internally organized mechanisms of the head direction sense. *Nature Neuroscience*, *18*(4), 569–575. https://doi.org/10.1038/nn.3968

Phillips, J. W., Schulmann, A., Hara, E., Winnubst, J., Liu, C., Valakh, V., Wang, L., Shields, B. C., Korff, W., Chandrashekar, J., Lemire, A. L., Mensh, B., Dudman, J. T., Nelson, S. B., & Hantman, A. W. (2019). A repeated molecular architecture across thalamic pathways. *Nature Neuroscience*, *22*(11), 1925–1935. https://doi.org/10.1038/s41593-019-0483-3

Preston-Ferrer, P., Coletta, S., Frey, M., & Burgalossi, A. (2016). Anatomical organization of presubicular head-direction circuits. *eLife*, *5*, e14592. https://doi.org/10.7554/eLife.14592

Ranck, J. (1984). Head direction cells in the deep cell layer of dorsolateral pre-subiculum in freely moving rats. *Soc Neurosci Abstr*.

Redish, A. D., Elga, A. N., & Touretzky, D. S. (1996). A coupled attractor model of the rodent head direction system. *Network: Computation in Neural Systems*, *7*(4), 671–685. https://doi.org/10.1088/0954-898X_7_4_004

Richevaux, L., Lim, D., Nassar, M., Rodrigues, L. D., Mauthe, C., Cohen, I., Sol-Foulon, N., & Fricker, D. (2025). *Projection-specific integration of convergent thalamic and retrosplenial signals in the presubicular head direction cortex*. https://doi.org/10.7554/eLife.92443.2

Roy, D. S., Zhang, Y., Aida, T., Choi, S., Chen, Q., Hou, Y., Lea, N. E., Skaggs, K. M., Quay, J. C., Liew, M., Maisano, H., Le, V., Jones, C., Xu, J., Kong, D., Sullivan, H. A., Saunders, A., McCarroll, S. A., Wickersham, I. R., & Feng, G. (2021). Anterior thalamic dysfunction underlies cognitive deficits in a subset of

neuropsychiatric disease models. *Neuron*, *109*(16), 2590-2603.e13. https://doi.org/10.1016/j.neuron.2021.06.005

Roy, D. S., Zhang, Y., Aida, T., Shen, C., Skaggs, K. M., Hou, Y., Fleishman, M., Mosto, O., Weninger, A., & Feng, G. (2022). Anterior thalamic circuits crucial for working memory. *Proceedings of the National Academy of Sciences*, *119*(20), e2118712119. https://doi.org/10.1073/pnas.2118712119

Seki, M., & Zyo, K. (1984). Anterior thalamic afferents from the mamillary body and the limbic cortex in the rat. *Journal of Comparative Neurology*, *229*(2), 242–256. https://doi.org/10.1002/cne.902290209

Sharp, P. E. (1996). Multiple Spatial/Behavioral Correlates for Cells in the Rat Postsubiculum: Multiple Regression Analysis and Comparison to Other Hippocampal Areas. *Cerebral Cortex*, *6*(2), 238–259. https://doi.org/10.1093/cercor/6.2.238

Sharp, P. E., Tinkelman, A., & Cho, J. (2001). Angular velocity and head direction signals recorded from the dorsal tegmental nucleus of gudden in the rat: Implications for path integration in the head direction cell circuit. *Behavioral Neuroscience*, *115*(3), 571–588.

Shibata, H. (1992). Topographic organization of subcortical projections to the anterior thalamic nuclei in the rat. *Journal of Comparative Neurology*, *323*(1), 117–127. https://doi.org/10.1002/cne.903230110

Shibata, H. (1993a). Direct projections from the anterior thalamic nuclei to the retrohippocampal region in the rat. *Journal of Comparative Neurology*, *337*(3), 431–445. https://doi.org/10.1002/cne.903370307

Shibata, H. (1993b). Efferent projections from the anterior thalamic nuclei to the cingulate cortex in the rat. *Journal of Comparative Neurology*, *330*(4), 533–542. https://doi.org/10.1002/cne.903300409

Skaggs, W. E., Knierim, J. J., Kudrimoti, H. S., & McNaughton, B. L. (1995). A model of the neural basis of the rat's sense of direction. *Advances in Neural Information Processing Systems*, *7*, 173–180.

Sofroniew, M. V., Priestley, J. V., Consolazione, A., Eckenstein, F., & Cuello, A. C. (1985). Cholinergic projections from the midbrain and pons to the thalamus in the rat, identified by combined retrograde tracing and choline acetyltransferase immunohistochemistry. *Brain Research*, *329*(1–2), 213–223. https://doi.org/10.1016/0006-8993(85)90527-X

Sripanidkulchai, K., & Wyss, J. M. (1986). Thalamic projections to retrosplenial cortex in the rat. *Journal of Comparative Neurology*, *254*(2), 143–165. https://doi.org/10.1002/cne.902540202

Stackman, R. W., & Taube, J. S. (1998). Firing Properties of Rat Lateral Mammillary Single Units: Head Direction, Head Pitch, and Angular Head Velocity. *The Journal of Neuroscience*, *18*(21), 9020–9037. https://doi.org/10.1523/JNEUROSCI.18-21-09020.1998

Taube, J. (1995). Head direction cells recorded in the anterior thalamic nuclei of freely moving rats. *The Journal of Neuroscience*, *15*(1), 70–86. https://doi.org/10.1523/JNEUROSCI.15-01-00070.1995

Taube, J., Muller, R., & Ranck, J. (1990). Head-direction cells recorded from the postsubiculum in freely moving rats. I. Description and quantitative analysis. *The Journal of Neuroscience*, *10*(2), 420–435. https://doi.org/10.1523/JNEUROSCI.10-02-00420.1990

Taube, J. S. (2007). The Head Direction Signal: Origins and Sensory-Motor Integration. *Annual Review of Neuroscience*, *30*(1), 181–207. https://doi.org/10.1146/annurev.neuro.29.051605.112854

Taube, J. S., Butler, W. N., Dumont, J. R., Graham, J. A., Marcroft, J. L., Shinder, M. E., Stackman, R. W., & Yoder, R. M. (2025). *Generating the head direction signal: Two types of head direction cells in the lateral mammillary nuclei and dorsal tegmental nuclei*. Neuroscience. https://doi.org/10.1101/2025.04.11.648409

Taube, J. S., & Muller, R. U. (1998). Comparisons of head direction cell activity in the postsubiculum and anterior thalamus of freely moving rats. *Hippocampus*, *8*(2), 87–108. https://doi.org/10.1002/(SICI)1098-1063(1998)8:2%253C87::AID-HIPO1%253E3.0.CO;2-4

Thiffault, I., Speca, D. J., Austin, D. C., Cobb, M. M., Eum, K. S., Safina, N. P., Grote, L., Farrow, E. G., Miller, N., Soden, S., Kingsmore, S. F., Trimmer, J. S., Saunders, C. J., & Sack, J. T. (2015). A novel epileptic encephalopathy mutation in KCNB1 disrupts Kv2.1 ion selectivity, expression, and localization. *Journal of General Physiology*, *146*(5), 399–410. https://doi.org/10.1085/jgp.201511444

Tsanov, M., Chah, E., Vann, S. D., Reilly, R. B., Erichsen, J. T., Aggleton, J. P., & O'Mara, S. M. (2011). Theta-Modulated Head Direction Cells in the Rat Anterior Thalamus. *Journal of Neuroscience*, *31*(26), 9489–9502. https://doi.org/10.1523/JNEUROSCI.0353-11.2011

Tsanov, M., Chah, E., Wright, N., Vann, S. D., Reilly, R., Erichsen, J. T., Aggleton, J. P., & O'Mara, S. M. (2011). Oscillatory Entrainment of Thalamic Neurons by Theta Rhythm in Freely Moving Rats. *Journal of Neurophysiology*, *105*(1), 4–17. https://doi.org/10.1152/jn.00771.2010

Tukker, J. J., Tang, Q., Burgalossi, A., & Brecht, M. (2015). Head-Directional Tuning and Theta Modulation of Anatomically Identified Neurons in the Presubiculum. *The Journal of Neuroscience*, *35*(46), 15391–15395. https://doi.org/10.1523/JNEUROSCI.0685-15.2015

Van Der Goes, M.-S. H., Voigts, J., Newman, J. P., Toloza, E. H., Brown, N. J., Murugan, P., & Harnett, M. T. (2024). Coordinated head direction representations in mouse anterodorsal thalamic nucleus and retrosplenial cortex. *eLife*, *13*, e82952. https://doi.org/10.7554/eLife.82952

Van Groen, T., & Michael Wyss, J. (1990). Connections of the retrosplenial granular a cortex in the rat. *Journal of Comparative Neurology*, *300*(4), 593–606. https://doi.org/10.1002/cne.903000412

Van Groen, T., & Wyss, J. M. (1990a). The connections of presubiculum and parasubiculum in the rat. *Brain Research*, *518*(1–2), 227–243. https://doi.org/10.1016/0006-8993(90)90976-I

Van Groen, T., & Wyss, J. M. (1990b). The postsubicular cortex in the rat: Characterization of the fourth region of the subicular cortex and its connections. *Brain Research*, *529*(1–2), 165–177. https://doi.org/10.1016/0006-8993(90)90824-U

Van Groen, T., & Wyss, J. M. (1995). Projections from the anterodorsal and anteroveniral nucleus of the thalamus to the limbic cortex in the rat. *Journal of Comparative Neurology*, *358*(4), 584–604. https://doi.org/10.1002/cne.903580411

Van Groen, T., & Wyss, J. M. (2003). Connections of the retrosplenial granular b cortex in the rat. *Journal of Comparative Neurology*, *463*(3), 249–263. https://doi.org/10.1002/cne.10757

Vann, S. D., & Aggleton, J. P. (2004). The mammillary bodies: Two memory systems in one? *Nature Reviews Neuroscience*, *5*(1), 35–44. https://doi.org/10.1038/nrn1299

Vann, S. D., Saunders, R. C., & Aggleton, J. P. (2007). Distinct, parallel pathways link the medial mammillary bodies to the anterior thalamus in macaque monkeys. *European Journal of Neuroscience*, *26*(6), 1575–1586. https://doi.org/10.1111/j.1460-9568.2007.05773.x

Veazey, R. B., Amaral, D. G., & Cowan, W. M. (1982). The morphology and connections of the posterior hypothalamus in the cynomolgus monkey (*Macaca fascicularis*). II. Efferent connections. *Journal of Comparative Neurology*, *207*(2), 135–156. https://doi.org/10.1002/cne.902070204

Vertes, R. P., Albo, Z., & Viana Di Prisco, G. (2001). Theta-rhythmically firing neurons in the anterior thalamus: Implications for mnemonic functions of Papez's circuit. *Neuroscience*, *104*(3), 619–625. https://doi.org/10.1016/S0306-4522(01)00131-2

Viejo, G., & Peyrache, A. (2020). Precise coupling of the thalamic head-direction system to hippocampal ripples. *Nature Communications*, *11*(1), 2524. https://doi.org/10.1038/s41467-020-15842-4

Virtanen, P., Gommers, R., Oliphant, T. E., Haberland, M., Reddy, T., Cournapeau, D., Burovski, E., Peterson, P., Weckesser, W., Bright, J., Van Der Walt, S. J., Brett, M., Wilson, J., Millman, K. J., Mayorov, N., Nelson, A. R. J., Jones, E., Kern, R., Larson, E., … Vázquez-Baeza, Y. (2020). SciPy 1.0: Fundamental algorithms for scientific computing in Python. *Nature Methods*, *17*(3), 261–272. https://doi.org/10.1038/s41592-019-0686-2

Vollan, A. Z., Gardner, R. J., Moser, M.-B., & Moser, E. I. (2025). Left–right-alternating theta sweeps in entorhinal–hippocampal maps of space. *Nature*, *639*(8056), 995–1005. https://doi.org/10.1038/s41586-024-08527-1

Wang, Q., Ding, S.-L., Li, Y., Royall, J., Feng, D., Lesnar, P., Graddis, N., Naeemi, M., Facer, B., Ho, A., Dolbeare, T., Blanchard, B., Dee, N., Wakeman, W., Hirokawa, K. E., Szafer, A., Sunkin, S. M., Oh, S. W., Bernard, A., … Ng, L. (2020). The Allen Mouse Brain Common Coordinate Framework: A 3D Reference Atlas. *Cell*, *181*(4), 936-953.e20. https://doi.org/10.1016/j.cell.2020.04.007

Ward, J. H. (1963). Hierarchical Grouping to Optimize an Objective Function. *Journal of the American Statistical Association*, *58*(301), 236–244. https://doi.org/10.1080/01621459.1963.10500845

Welday, A. C., Shlifer, I. G., Bloom, M. L., Zhang, K., & Blair, H. T. (2011). Cosine Directional Tuning of Theta Cell Burst Frequencies: Evidence for Spatial Coding by Oscillatory Interference. *The Journal of Neuroscience*, *31*(45), 16157–16176. https://doi.org/10.1523/JNEUROSCI.0712-11.2011

Wiener, S. I., & Taube, J. S. (2005). *Head direction cells and the neural mechanisms of spatial orientation*. MIT Press.

Winter, S. S., Clark, B. J., & Taube, J. S. (2015). Disruption of the head direction cell network impairs the parahippocampal grid cell signal. *Science*, *347*(6224), 870–874. https://doi.org/10.1126/science.1259591

Yoder, R. M., Peck, J. R., & Taube, J. S. (2015). Visual Landmark Information Gains Control of the Head Direction Signal at the Lateral Mammillary Nuclei. *The Journal of Neuroscience*, *35*(4), 1354–1367. https://doi.org/10.1523/JNEUROSCI.1418-14.2015

Yoshida, M., & Alonso, A. (2007). Cell-Type–Specific Modulation of Intrinsic Firing Properties and Subthreshold Membrane Oscillations by the M(Kv7)-Current in Neurons of the Entorhinal Cortex. *Journal of Neurophysiology*, *98*(5), 2779–2794. https://doi.org/10.1152/jn.00033.2007

Yue, C., & Yaari, Y. (2004). KCNQ/M Channels Control Spike Afterdepolarization and Burst Generation in Hippocampal Neurons. *The Journal of Neuroscience*, *24*(19), 4614–4624. https://doi.org/10.1523/JNEUROSCI.0765-04.2004

Zhang, K. (1996). Representation of spatial orientation by the intrinsic dynamics of the head-direction cell ensemble: A theory. *The Journal of Neuroscience*, *16*(6), 2112–2126. https://doi.org/10.1523/JNEUROSCI.16-06-02112.1996

2 Preliminary results to explore cholinergic modulatory effect in AD and AV

In this section, I present preliminary data examining potential cholinergic modulation of AD and AV neurons. The initial experiments revealed that both AD and AV neurons exhibited altered spiking activity when exposed to the cholinergic agonist carbachol. Building on this finding, we sought to identify the origin of cholinergic inputs to these thalamic nuclei. Using ChAT::TOM transgenic mice and retrograde labelling strategy, I studied potential cholinergic sources projecting to the AD and AV. In parallel, I attempted to develop and validate a technical approach to analyse the HD activity in AD and AV. I chose to use calcium imaging in combination with our lab's analysis pipeline to assess HD activity in freely moving mice using a Miniscope. I expected to analyse thalamic HD activity in AD and in AV neurons in behaving mice. In the future, this approach may also be used to examine cholinergic influences on AD and AV activity by inhibiting an identified cholinergic source region, for example, using Designer Receptors Exclusively Activated by Designer Drugs (DREADDs). Among multiple trials, one mouse successfully expressed the calcium indicator GCaMP8f in PrS-projecting neurons of the AD and AV. This was achieved by expressing Cre-dependent GCaMP8f in the thalamic nuclei, combined with retro-Cre virus injection into the PrS. The HD activities of these cells were then analysed.

Here, I present my current achievement. First, I show the altered spiking activity of AD and AV neurons in response to carbachol, in slices. Second, I present the potential cholinergic input sources to the AD and AV. Finally, I show the HD activity of PrS-projecting thalamic neurons *in vivo*, demonstrating the technical feasibility for future experiments.

2.1 Cholinergic modulation on AD and AV neurons - electrophysiological aspect

To test cholinergic effect in AD and AV neurons, I performed whole cell patch clamp recording while delivering periodic depolarising current steps. For each cell, a current amplitude was chosen that evoked stable spiking activity just above threshold. Typically the current evoking 1-5 spikes was chosen and applied. Carbachol (10 μM) was applied by the bath perfusion diluted in the ACSF. The bath was replaced by fresh ACSF after 2-3 minutes from the wash-in. The effect of carbachol was observed within this time frame. After the carbachol application, the spiking activity of each neuron was abolished in response to the current steps (Figure 9A and B). Meanwhile, the depolarising voltage response was maintained. Spiking activity recovered on wash-out of carbachol. This effect was observed in both nuclei (AD, n=3; AV, n=5). Carbachol activates both muscarinic and nicotinic receptors. Therefore, I next asked about the relationship between muscarinic receptors and the suppression of spiking activity. Within the same experimental set up, muscarine (10 μM) was applied through the perfusion bath. Like the results from carbachol, spiking activity was abolished during the wash-in period (Figure 9C and D). The spiking activity was

recovered after the wash-out in the AD neuron but not in the AV neuron, in this preliminary trial (AD, n=1; AV, n=1). Taken together, these observations indicate that muscarinic cholinergic input modulates the spiking activity in both AD and AV neurons, while potential nicotinic contributions require further investigation.

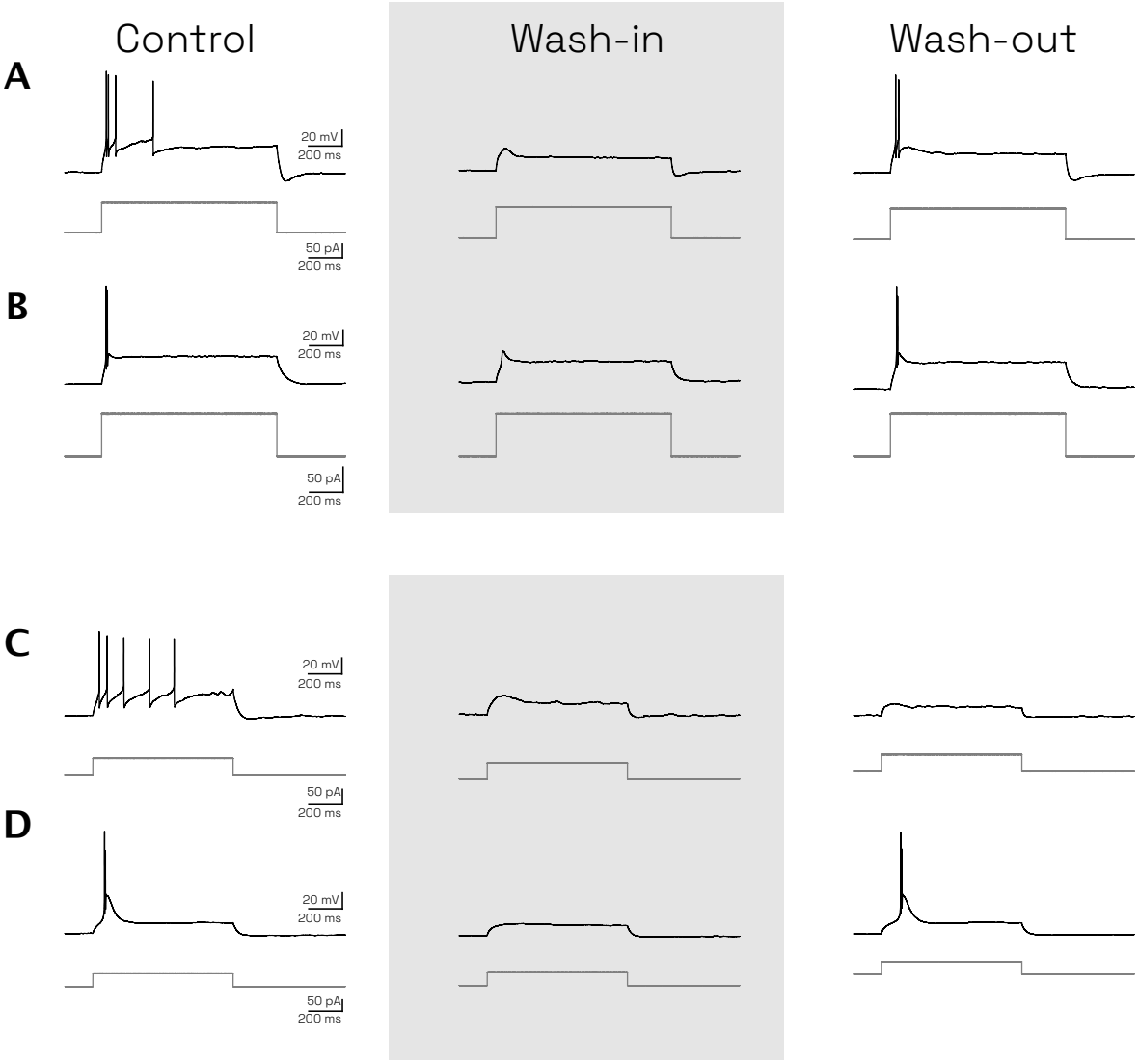

Figure 9 Cholinergic modulation of spiking activity in AD and AV neurons.

A) Example traces (a single sweep per condition) from an AD neuron in control, during carbachol (10 µM) wash-in, and wash-out. AP was absent throughout the wash-in condition.
B) Example traces from an AV neuron in control, during carbachol (10 µM) wash-in, and wash-out. AP was absent throughout the wash-in condition.
C) Example traces from an AD neuron in control, during muscarine (10 µM) wash-in, and wash-out. AP was absent throughout the wash-in condition. In addition, the AP was not shown after the wash-out.
D) Example traces from an AV neuron in control, during muscarine (10 µM) wash-in, and wash-out. AP was absent throughout the wash-in condition.

2.2 Exploring cholinergic input sources to AD and AV

Then, where do cholinergic inputs to AD and AV originate? Previous studies suggested that the LDT and the PPN are the potential cholinergic source to the ATN (Gonzalo-Ruiz & Lieberman, 1995; Gonzalo-Ruiz et al., 1995; Hallanger et al., 1987; Satoh & Fibiger, 1986). To re-examine this question, I carried out anatomical labelling experiments. The first step was to screen the whole brain in order to identify the general origin of afferents to AD and AV. The second step was to confirm potential cholinergic source regions, in line with previous reports.

To achieve these aims, I injected retro-AAV-EF1a-GFP into AD and AV of ChAT::TOM mice (N=1). The injection site was accurately confined to AD and AV, with minimal spread into adjacent lateral habenula and MD (Figure 10). Representative whole-brain serial sections were aligned to the Allen Mouse Brain Atlas CCFv3 (Q. Wang et al., 2020). The whole brain sections were alternatively selected and the expression levels of labelled regions are summarised in Table 3.1. The whole brain image dataset is shown in Figure 11. This dataset provided an initial overview of potential cholinergic source regions. For candidate regions, I performed confocal imaging to confirm double labelling of GFP and Tomato fluorescent, thereby identifying cholinergic neurons projecting to AD or/and AV.

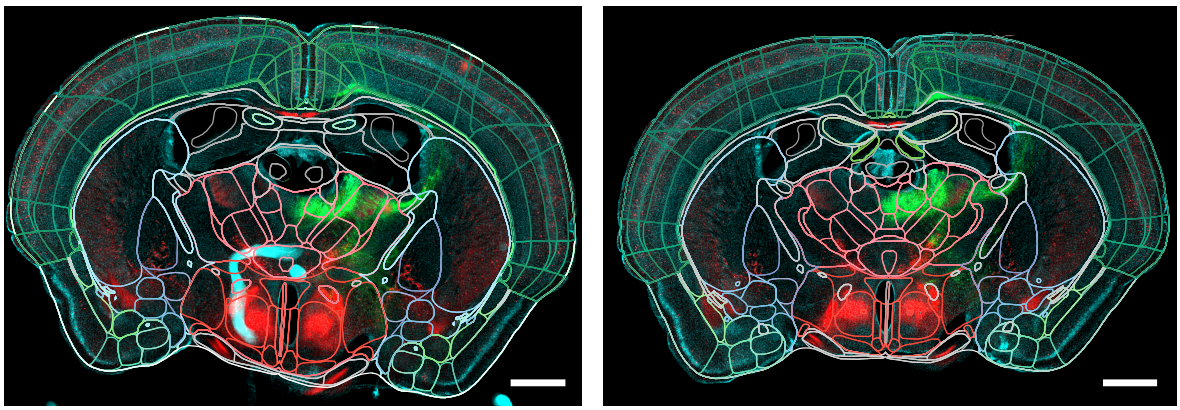

Figure 10 Injection site in AD and AV for retrograde tracing of brain-wide afferents.

Two adjacent coronal sections at the injection site of retro-AAV-EF1a-GFP. The site was inferred from the cortical surface damage along the injection track and the location of the AD and AV. The Allen Mouse Brain Atlas (CCFv3) was overlaid to annotate expected brain regions. DAPI staining is presented in cyan and ChAT-positive neurons are shown in red. Section thickness: 100 µm, Scale bar: 200 µm.

Two adjacent coronal sections at the injection site of retro-AAV-EF1a-GFP. The site was inferred from the cortical surface damage along the injection track and the location of the AD and AV. The Allen Mouse Brain Atlas (CCFv3) was overlaid to annotate expected brain regions. The expression encompasses the AD and AV with spread to the MD. DAPI staining is presented in cyan and ChAT-positive neurons are shown in red. Section thickness: 100 µm, Scale bar: 200 µm.

Regions	Ipsilateral	Contralateral	Colocalisation
Agranular insular area	++	+	no
Amygdala	++	none	no
Anterior cingulate area, dorsal part, layer V	+++	+ (anterior portion)	no
Anterolateral visual area	++	+	no
Claustrum	++	none	no
Cuneiform nucleus (CnF)	+++	++	yes
Dentate gyrus	++	+	no
Ectorhinal area layer V	++	+	no
Fastigial nucleus	+++	++	no
Lateral hypothalamic area	++	none	yes
Lateral mammillary nucleus	++	+	no
Laterodorsal tegmental nucleus (LDT)	+++	++	yes
Lateral visual area	++	none	no
Magnocellular nucleus	+	none	no
Medial vestibular nucleus	++	+	no
Medial mammillary nucleus	++	+	no
Midbrain raphe nuclei	++	+	no
Midbrain reticular nucleus (MRN)	++	+	yes
Nucleus accumbens	+	none	no
Nucleus of the posterior commissure	++	+	no
Orbital area	+++	++	no
Pallidum	++	none	no
Parabrachial nucleus	++	+	no
Pedunculopontine nucleus (PPN)	++	+	yes
Periaqueductal grey (PAG)	++	+	yes
Perirhinal area layer V	++	no	no
Pontine reticular nucleus	++	+	no
Posterior auditory area	++	+	no
Posterior hypothalamic nucleus	+	+	no
Postpiriform transition area	+	none	no
Postrhinal area layer V	+++	none	no
Prelimbic area	+++	++	no
Presubiculum	++	none	no
Primary motor area layer V	+++	none	no
Primary visual area layer V	+++	none	no
RSC layer V	+++	none	no
Secondary motor area layer 5	+++	none	no
Subiculum	+	none	no
Superior colliculus	++	+	no
Supramammillary nucleus	+	+	no
Temporal association area	++	none	no
Thalamic reticular nucleus	++	none	no
Ventral tegmental area	++	+	no
Zona incerta	++	+	no

Table 3.1 Summary of retrogradely labelled AD/AV projecting neurons and colocalisation of GFP and Tomato fluorescence across regions.

Expression levels are indicated semi-quantitatively as +++, ++, +, or none. The colocalisation column notes whether the two populations were locally overlapping. Regions containing double-labelled neurons are shown in bold.

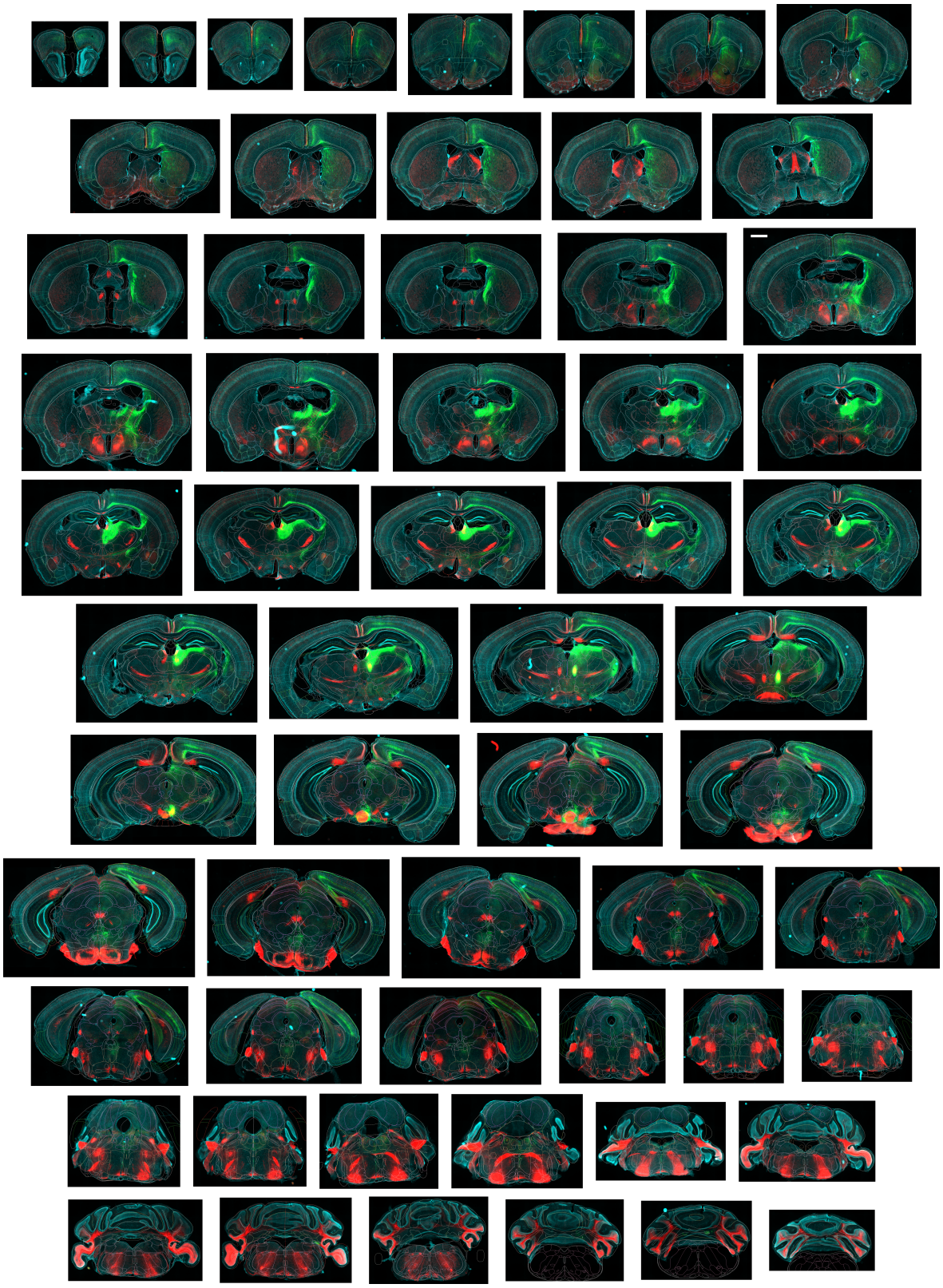

Figure 11 Gallery of alternating serial brain sections from a whole mouse brain.

Green indicates retrogradely labelled neurons, red indicates cholinergic neurons, and cyan indicates DAPI staining. All sections were processed with identical imaging enhancement. Scale bar: 100 µm.

The afferents to the AD and AV were diverse. Based on the distribution of labelled neurons, candidate regions that could provide cholinergic input included the Cuneiform nucleus (CnF), LDT, Periaqueductal grey (PAG), PPN, Midbrain reticular nucleus (MRN), and Lateral hypothalamic area (LHA). These regions showed the colocalisation of ChAT cells and retrogradely labelled AD/AV-projecting cells. To confirm if these cells were doubly labelled, I performed confocal imaging in these regions. In the CnF, LDT, PAG, PPN, and MRN double labelled neurons were observed (Figure 12-15). Among these, CnF, LDT, and PAG presented a high proportion of double-labelled neurons. However, I did not observe double labelled neurons in the LHA.

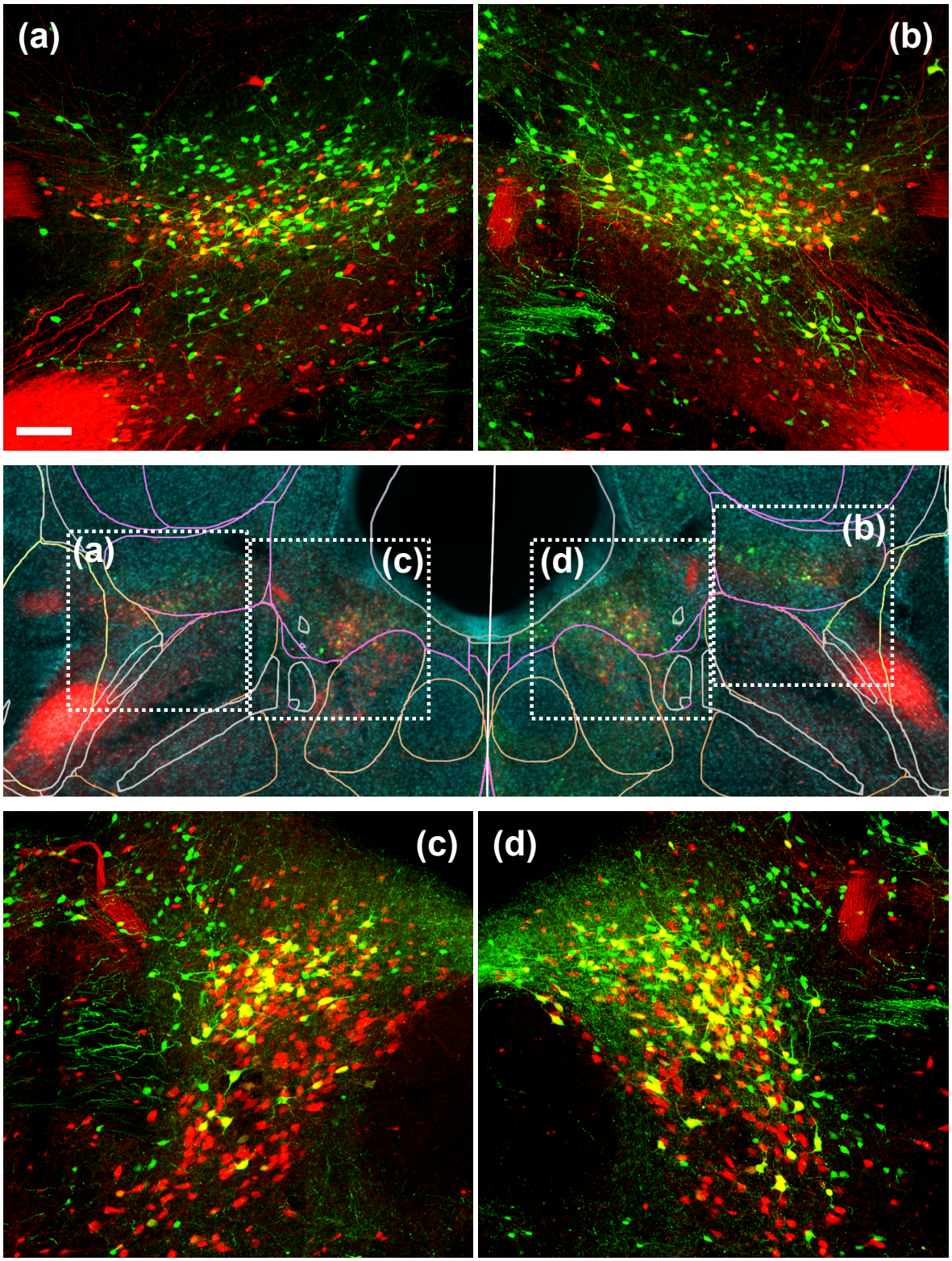

Figure 12 Double-labelled neurons in the LDT and CnF.
Confocal images (10x) of each region are shown. In the middle panel, dashed boxes indicate the magnified regions. Red: ChAT-positive cells. Green: retrogradely labelled AD/AV afferent cells. (a, b) Magnified images of the LDT. (c, d) Magnified images of the CnF. Anatomical delineations were manually adapted with reference to both the Allen Brain Atlas and Paxinos & Franklin's atlas. The left side of the figure corresponds to the contralateral side, and the right side to the ipsilateral side relative to the injection site. Scale bar: 100 µm.

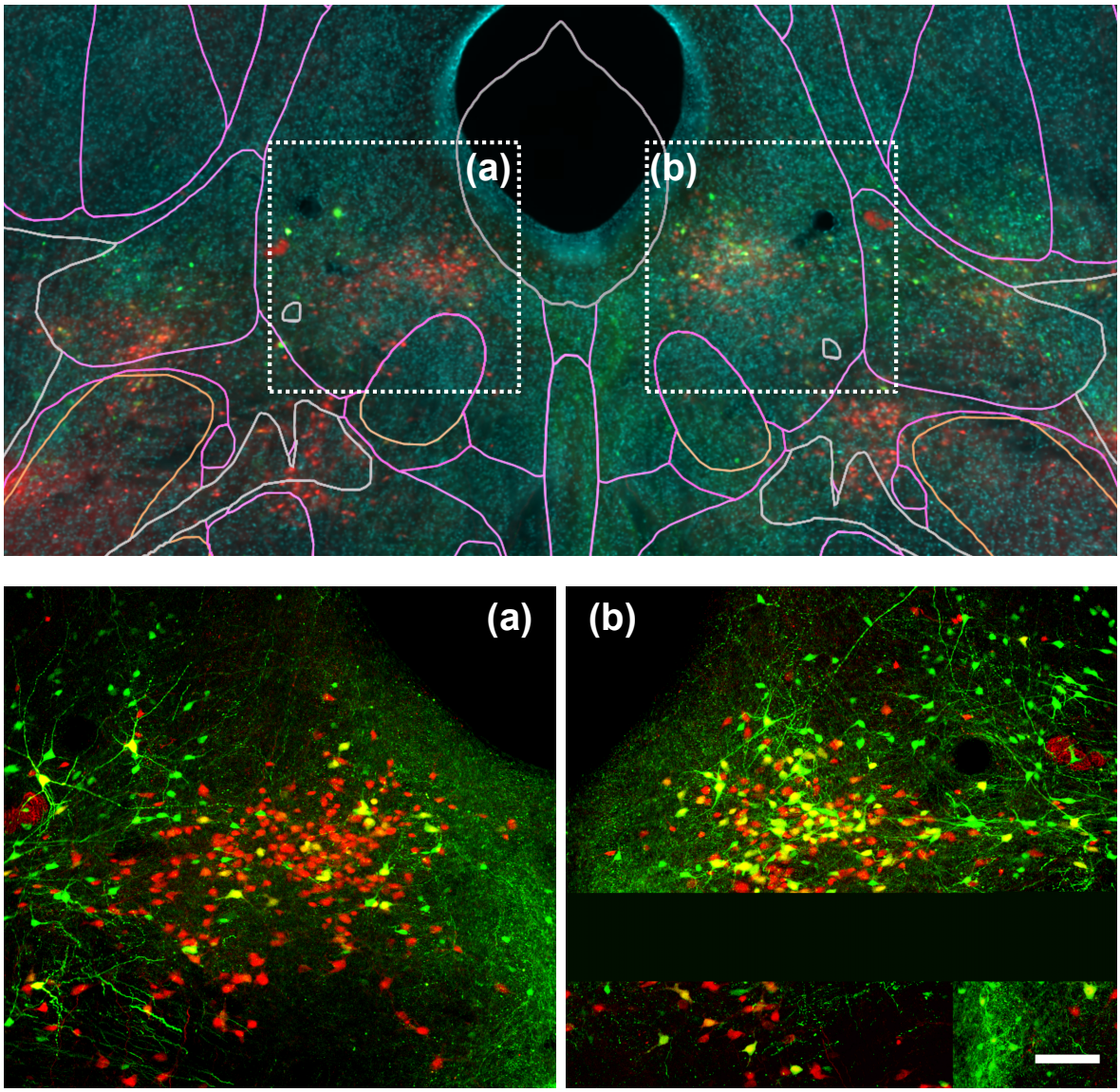

Figure 13 Double-labelled neurons in the PAG.

Confocal images (10x) of each region are shown. Dashed boxes indicate the magnified regions. (a) Magnified images of the contralateral side. (b) Magnified images of the ipsilateral side. Scale bar: 100 µm.

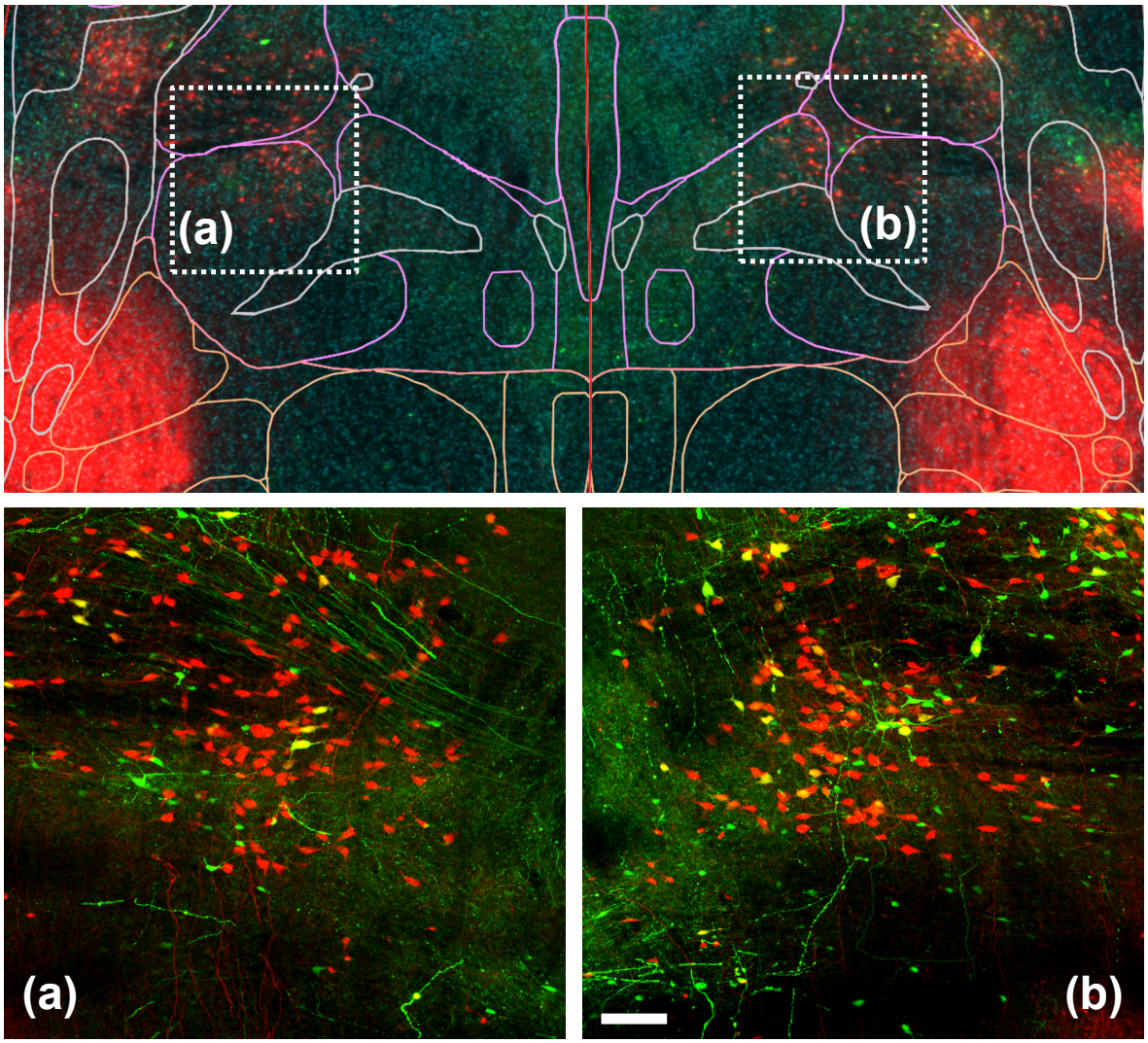

Figure 14 Double-labelled neurons in the PPN.

Confocal images (10x) of each region are shown. Dashed boxes indicate the magnified regions. (a) Magnified images of the contralateral side. (b) Magnified images of the ipsilateral side. Scale bar: 100 μm.

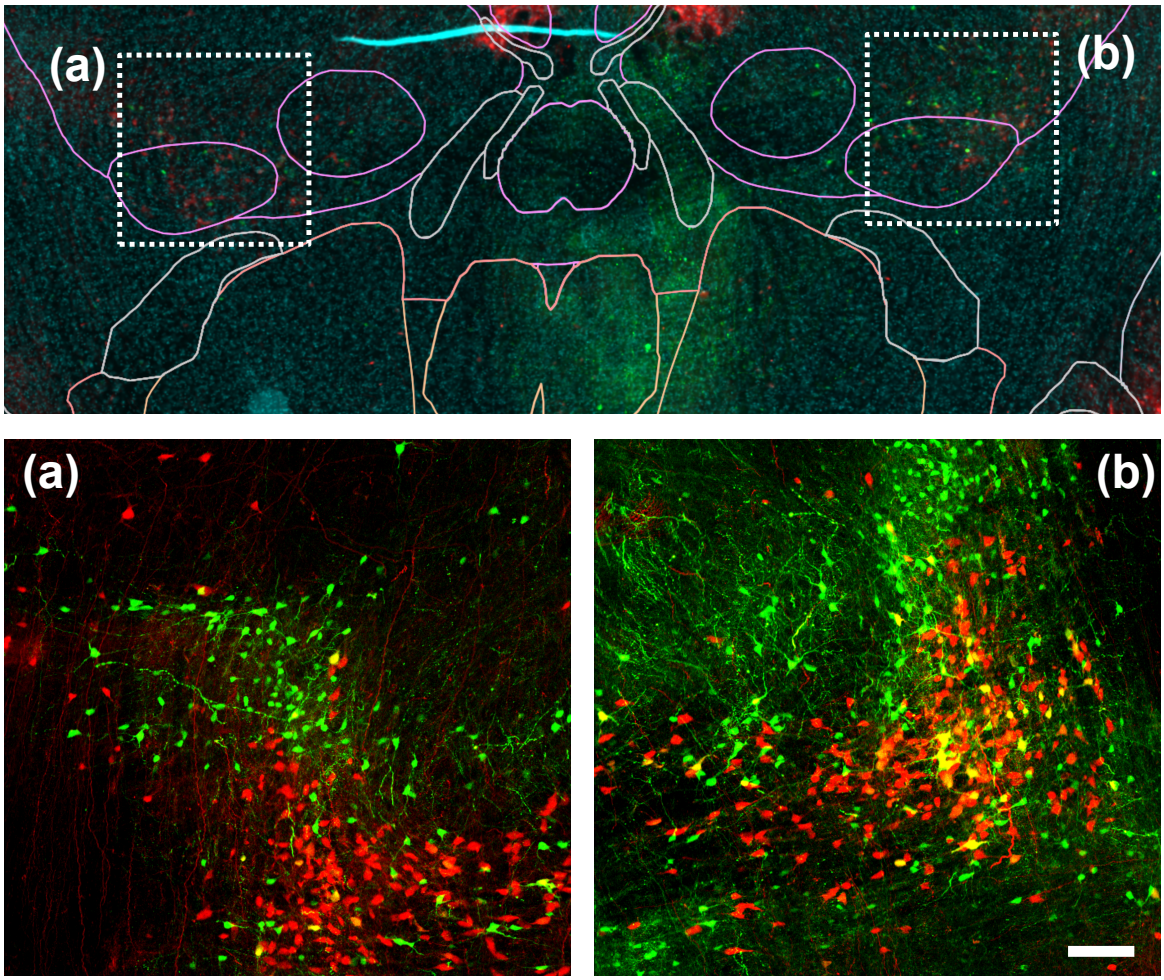

Figure 15 Double-labelled neurons in the MRN.

Confocal images (10x) of each region are shown. Dashed boxes indicate the magnified regions. (a) Magnified images of the contralateral side. (b) Magnified images of the ipsilateral side. Scale bar: 100 μm.

3 Calcium imaging of neuronal HD activity in the AD and AV in behaving mice

I performed calcium imaging to assess HD activity of thalamic neurons in a freely behaving mouse, using an analysis tool developed by Dr. Michael Graupner and Elja Belhadef in our lab. Activity of PrS-projecting neurons in both thalamic nuclei was recorded with a miniscope while the mouse explored a transparent open-field cage within a conventional lab environment (Figure 16B). Conditional expression of GCaMP8f in PrS-projecting thalamic neurons was confirmed post hoc, showing overlap with the GRIN lens implantation site (Figure 16C). Recordings were conducted across three separate days. During each session, the mouse displayed continuous locomotor and exploratory behaviour that enabled reliable assessment of HD-related activity (Figure 16D).

An in-house analysis pipeline established by Dr. Michael Graupner and Elja Belhadef identified 25 putative HD cells ($p<0.05$) in the AD and 7 in the AV. Regional boundaries for AD and AV were estimated based on post hoc microscopy (Figure 16C) and the orientation of Miniscope recording angle. To determine the diagonal delineation of AD and AV, I focused on the tuning curves of the ROIs observed in the central recording view. Along the diagonal line, I could observe several ROIs exhibiting relatively sharp tuning curves, which are likely to be classical HD activity in the AD. In contrast, on the other side of the line, one cell (cell #51) presented a broader tuning curve, possibly reflecting theta precession HD activity in AV. The diagonal boundary was therefore placed between these two populations. Among the AV population, 2 cells, Cell #1 and #2, were imaged across three recording days, and both met the criteria for HD-modulated cells ($R>0.2$ and $p<0.05$) on the first and third recording days (Figure 17B). Between these two days, analysis of PFD revealed that Cell #1 and #2 shifted by +29 ° and +33.2 ° respectively. Both cells did not satisfy the criteria of the HD-modulated cell on the second recording day. 7 other AD cells were detected across two recording days (Figure 18). Cell #8 was considered an HD-modulated cell and showed shifts of +67.8° between the second and third recording day. Cell #6 and #9 showed intermediate R values ($R>0.11$) across the same recording days and showed shifts in the same positive direction (+77.3 ° and +116 °, respectively). Additional putative HD cells were detected on each recording day, although these were only observed on a single day each (Figure 19). In the AV, 1 cell (Cell #51) fulfilled the criteria for an HD-modulated cell (Figure 19, orange plots), and another cell was also close to the criteria (Cell #53). Although this approach presented minor limitations, including slightly off-target GRIN lens placement, short recording durations, and a limited number of detected ROIs, the results demonstrate the accessibility of *in vivo* calcium imaging for HD analysis in thalamic projecting neurons. Future work using stable calcium imaging recording, combined with post hoc anatomical identification of the thalamic delineation and individual recorded neurons, will enable more precise analysis. This approach will provide a clearer characterisation of HD tuning properties and allow further investigations such as to examine coherent shifts in PFD across HD cell populations over days or assessing changes in HD activity under modulatory influences.

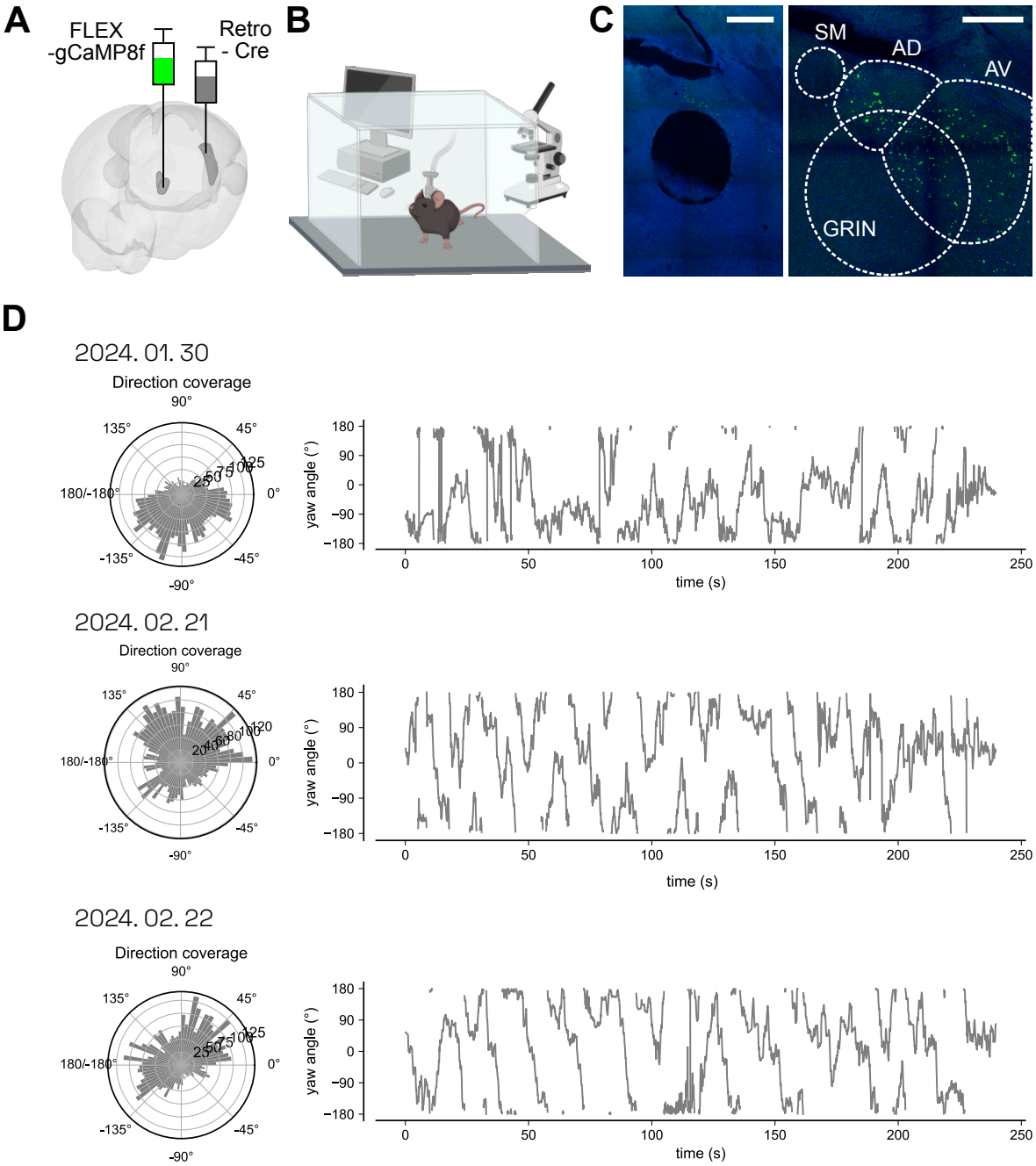

Figure 16 Calcium imaging of PrS-projecting AD and AV neurons using a miniscope.

A) Schematic of viral injection strategy to express GCaMP8f in PrS-projecting neurons in the AD and AV.

B) Neuronal activity was recorded during free exploration in an open cage with visual landmarks provided by the laboratory environment.

C) Confocal images from the recorded mouse (horizontal sections). Left: site of GRIN lens insertion indicated by the circular empty space in the brain slice. Scale bar: 500 µm. Right: first section immediately below the GRIN lens track. The expected coverage of the GRIN lens includes partial overlap with AD and AV regions. Scale bar: 200 µm.

D) Directional coverage during free exploration across three recording days on the left and the yaw angle shown over time on the right.

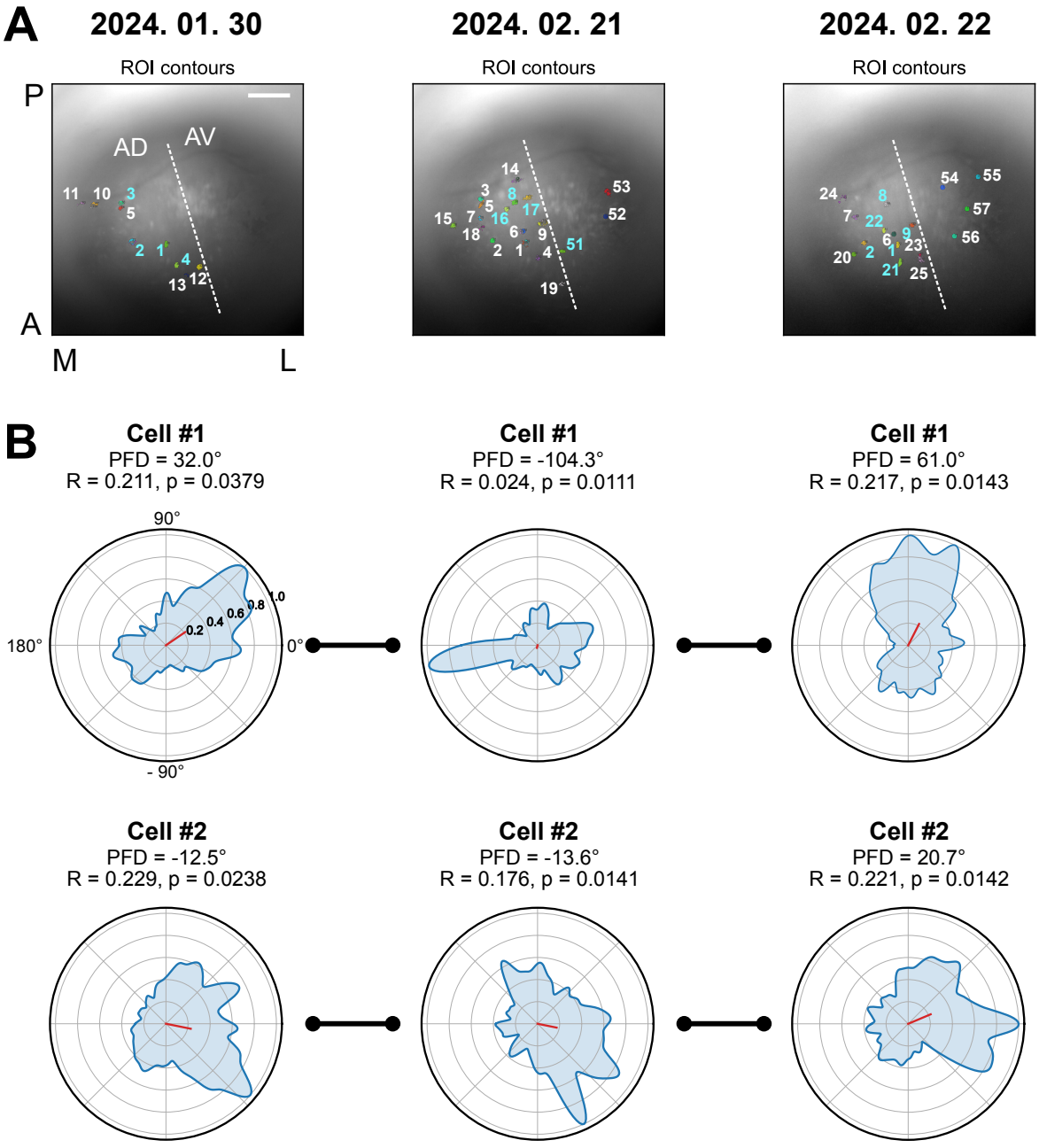

Figure 17 Calcium imaging of PrS-projecting AD neurons across three recording days.

A) GRIN lens field of view with ROI contours. Cell numbers are indicated. Cells labelled in cyan are considered as HD-modulated cells. The expected delineation between AD and AV is shown as a dashed line. Orientation: P: posterior, A: anterior, M: medial, L: lateral. Scale bar: 100 µm.
B) Polar plots of two AD neurons that were consistently observed across all three recording days. PFD: preferred direction. R: Rayleigh vector length. p = p-value of statistically significant tuning.

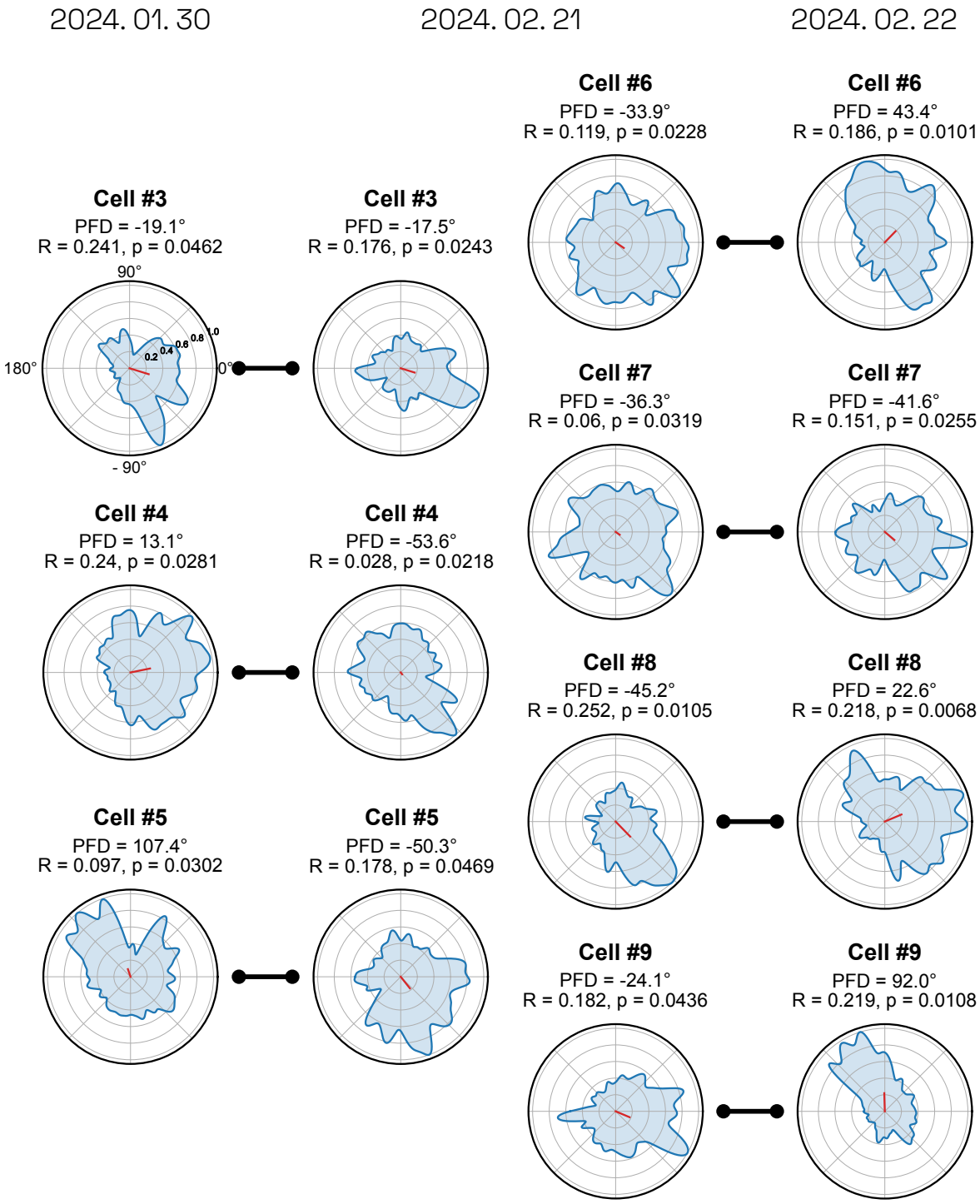

Figure 18 Polar plots of PrS-projecting AD neurons across two recording days.

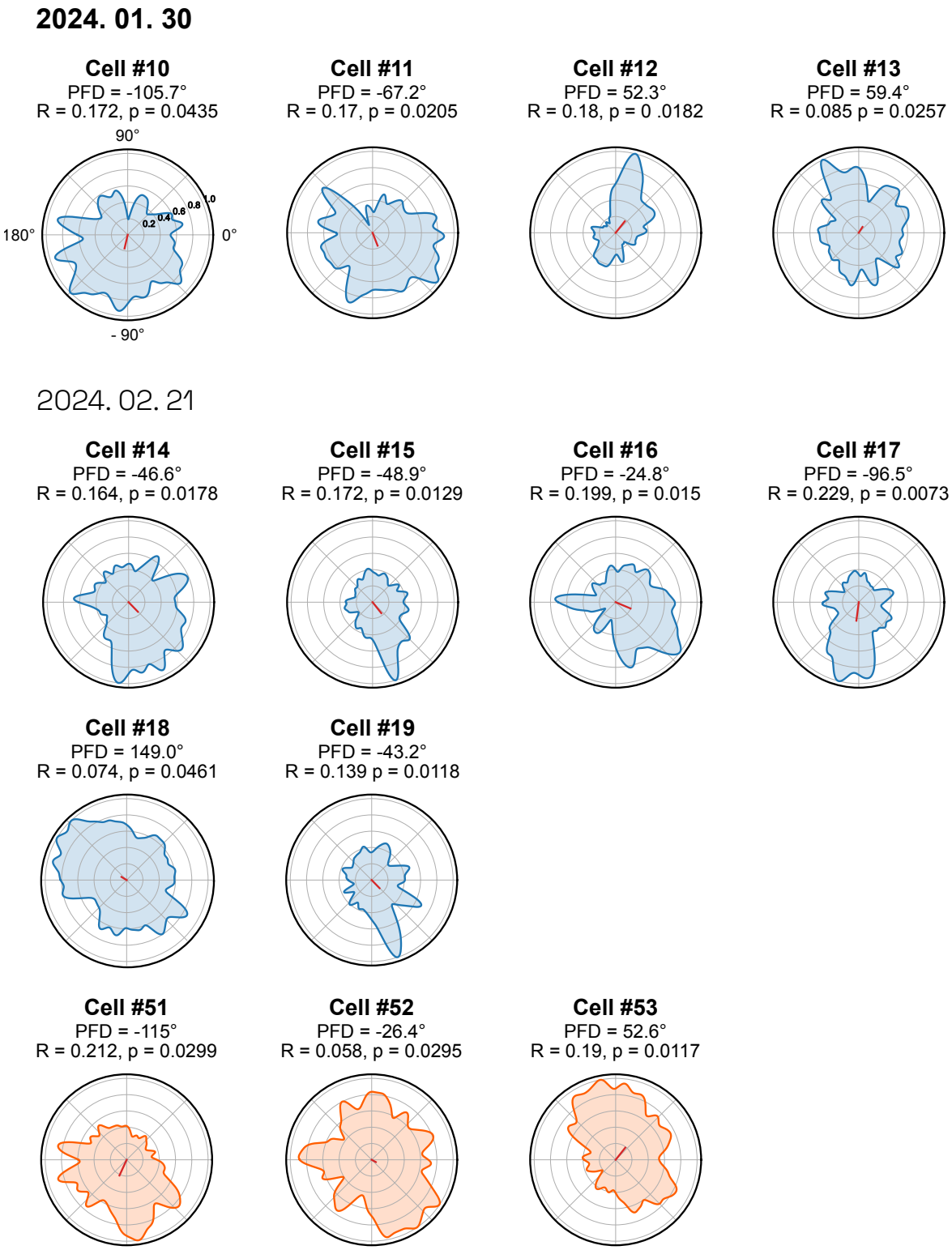

Figure 19 Polar plots of PrS-projecting AD and AV neurons observed on a single recording day.

Polar plots of AD neurons are presented in blue, and those of AV neurons are presented in orange.

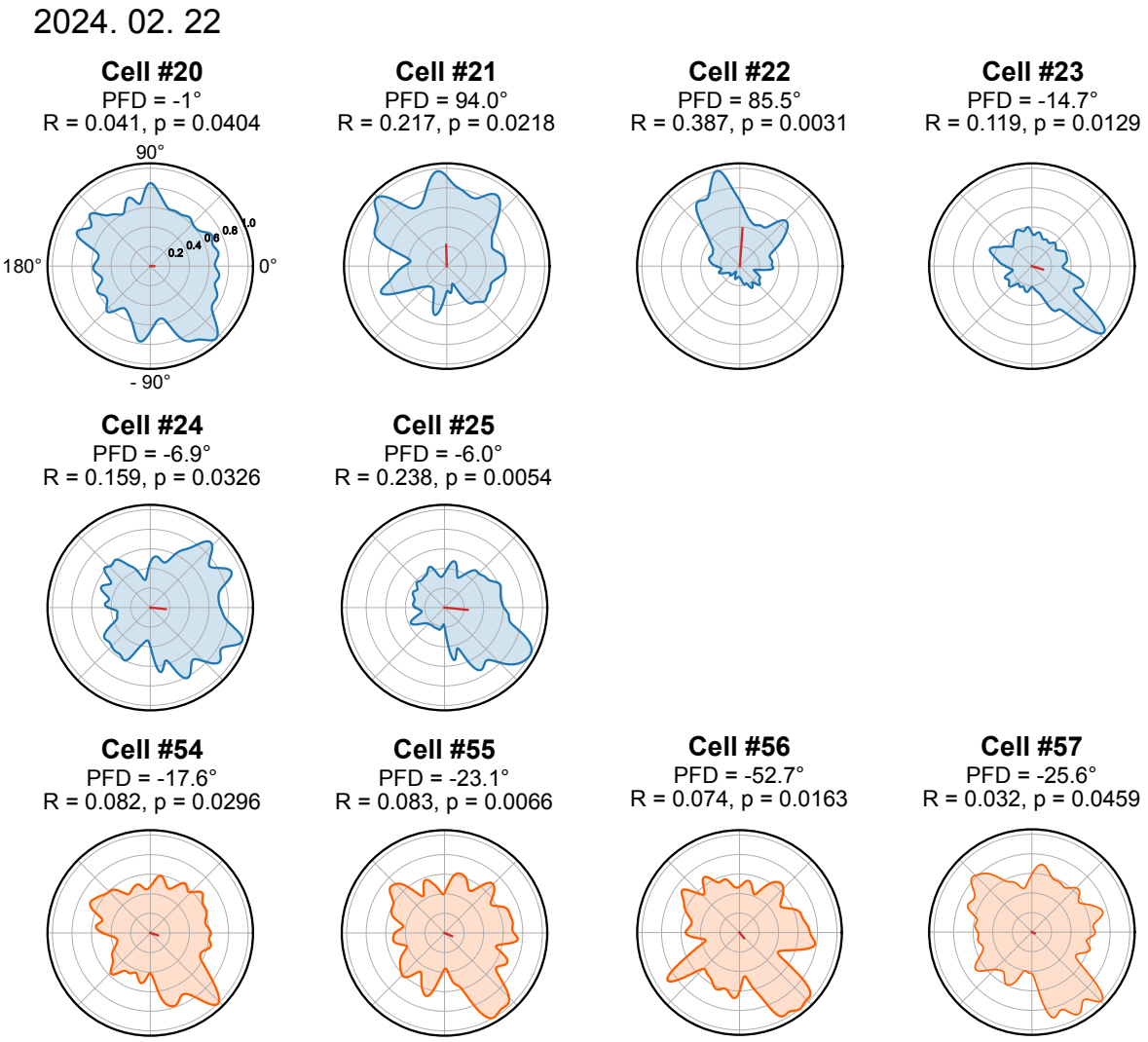

Figure 19(continued)

4 Co-authored publications

4.1 Projection-specific integration of convergent thalamic and retrosplenial signals in the presubicular head direction cortex

The PrS is a well-established region within the HD system. It contains HD cells that exhibit stable directional firing, supporting the brain's internal representation of spatial orientation. The PrS is anatomically positioned to receive input from the ATN, which conveys internally generated HD signals, and from the RSC, which transmits visual landmark-based directional information. Although the anatomical convergence of these afferents in the PrS is well documented, the functional integration of ATN and RSC inputs by PrS neurons has not been fully elucidated.

To address this gap, Louis Richevaux, formal PhD student in the lab, employed a combination of viral tracing, dual-wavelength optogenetics, and *ex-vivo* whole-cell electrophysiology to investigate how ATN and RSC inputs converge and are integrated in the PrS using mouse model. Functional inputs were tested using independent photostimulation of Chronos-expressing ATN and Chrimson-expressing RSC afferents, which enables to precisely isolate the contribution of each input source at the cellular level. I joined the project with the aim of learning patch clamp recording techniques and becoming familiar with electrophysiological data analysis in the initial stage of my PhD. In addition to my role as a trainee, I contributed by performing high-resolution imaging to visualise biocytin-labelled layer III and layer IV PrS neurons with the projections from the ATN and RSC. I also carried out the analysis of electrophysiological changes in layer IV neurons following carbachol application.

First, anterograde and retrograde labeling confirmed strong projections from both the ATN and RSC to superficial layers (I and III) of the PrS. High resolution imaging further demonstrated that both afferents form putative synaptic contacts with layer III pyramidal neurons. Electrophysiological recordings revealed that the layer III neurons receive monosynaptic excitatory inputs from both ATN and RSC axons. Simultaneous activation of the two pathways produced supralinear summation of EPSPs, leading to a significantly increased probability of action potential generation. This nonlinear integration was partly mediated by N-Methyl-D-aspartate (NMDA) receptor activation. Layer IV neurons in the PrS exhibited subtle functional responses to inputs from ATN and RSC stimulated by photostimulation. Also their postsynaptic response latencies were longer than those observed in layer III. In paired recordings of layer III and layer IV neurons during photostimulation of ATN and RSC afferents, EPSPs in layer IV neurons followed action potentials in layer III cells. These findings suggest that ATN and RSC inputs activate layer III neurons, which in turn relay the excitatory drive to layer IV neurons. Moreover, the excitability of layer IV neurons was enhanced by cholinergic agonists.

In summary, this research reveals a two-stage integrative process within the PrS. Layer III neurons receive strong inputs from ATN and RSC, while layer IV neurons serve as a threshold second stage broadcasting updated signals to the LMN.

eLife

RESEARCH ARTICLE

Projection-specific integration of convergent thalamic and retrosplenial signals in the presubicular head direction cortex

Louis Richevaux[1]*, Dongkyun Lim[1,2], Mérie Nassar[1], Léa Dias Rodrigues[1], Constanze Mauthe[1], Ivan Cohen[3], Nathalie Sol-Foulon[4], Desdemona Fricker[1,2]*

[1]Université Paris Cité, CNRS, Integrative Neuroscience and Cognition Center, Paris, France; [2]Université Paris Cité, CNRS, Saints-Pères Paris Institute of the Neurosciences, Paris, France; [3]Sorbonne Université, INSERM, CNRS, Neuroscience ParisSeine, Institut de Biologie Paris Seine, Paris, France; [4]Sorbonne Université, INSERM, CNRS, Paris Brain Institute, ICM, Pitié-Salpêtrière Hospital, Paris, France

***For correspondence:** louis.richevaux@parisdescartes.fr (LR); desdemona.fricker@parisdescartes.fr (DF)

Competing interest: The authors declare that no competing interests exist.

Funding: See page 21

Sent for Review 15 September 2023
Preprint posted 02 October 2023
Reviewed preprint posted 09 November 2023
Reviewed preprint revised 27 August 2025
Version of Record published 24 December 2025

Reviewing Editor: Lisa M Giocomo, Stanford School of Medicine, United States

© Copyright Richevaux *et al*. This article is distributed under the terms of the Creative Commons Attribution License, which permits unrestricted use and redistribution provided that the original author and source are credited.

eLife Assessment

This **valuable** study combines anatomical tracing and slice physiology to examine how anterior thalamic and retrosplenial inputs converge in the presubiculum, a key region in the navigation circuit. The authors show that near-simultaneous co-activation of retrosplenial and thalamic inputs drives supra-linear presubiculum responses, revealing a potential cellular mechanism for anchoring the brain's head direction system to external visual landmarks. Their thorough experimental approach and analyses provide **convincing** evidence for the cellular basis of how the brain's internal compass may be anchored to the external world, laying the groundwork for future experimental testing in vivo.

Abstract Head direction (HD) signals function as the brain's internal compass. They are organized as an attractor and anchor to the environment via visual landmarks. Here, we examine how thalamic HD signals and visual information from the retrosplenial cortex combine in the presubiculum. We find that monosynaptic excitatory connections from anterior thalamic nucleus and from retrosplenial cortex converge on single layer 3 pyramidal neurons in the dorsal portion of mouse presubiculum. Independent dual-wavelength photostimulation of these inputs in slices leads to action potential generation preferentially for near-coincident inputs, indicating that layer 3 neurons can transmit a visually matched HD signal to medial entorhinal cortex. Layer 4 neurons, which innervate the lateral mammillary nucleus, form a second step in the association of HD and landmark signals. They receive little direct input from thalamic and retrosplenial axons. We show that layer 4 cells are excited di-synaptically, transforming regular spiking activity into bursts of action potentials, and that their firing is enhanced by cholinergic agonists. Thus, a coherent sense of orientation involves projection-specific translaminar processing in the presubiculum, where neuromodulation facilitates landmark updating of HD signals in the lateral mammillary nucleus.

Introduction

The head direction (HD) system functions as the brain's compass system. It is distributed across several interconnected brain structures and hierarchically organized from the brainstem to the lateral mammillary nucleus (LMN; ***Stackman and Taube, 1998***), the anterior thalamic nuclei (ATN; ***Taube, 1995***), and the dorsal presubiculum (PrS; ***Ranck, 1984***; ***Taube et al., 1990a***). Modeling work suggests the HD system functions as a ring attractor, where the population of HD neurons is arranged in a one-dimensional manifold (***Blair and Sharp, 1995***; ***McNaughton et al., 2006***; ***Skaggs et al., 1995***). The activity of thalamic and PrS HD neurons is correlated across different brain states, even during sleep, independently of sensory cues (***Peyrache et al., 2015***). The bump-like activity dynamics of an attractor network can maintain HD signals based on excitatory-excitatory or excitatory-inhibitory interactions (***Knierim and Zhang, 2012***; ***Simonnet et al., 2017***). However, HD signals may drift in the dark (***Taube et al., 1990b***; ***Zugaro et al., 2003***). For precise navigation, internally generated information on head direction must be combined with awareness of location in an environment. Mechanisms underlying the combination of egocentric head direction signals with anchoring to allocentric landmarks remain to be clarified.

Head direction and visual landmark signals may be integrated in the presubiculum (***Jeffery et al., 2016***; ***Yoder et al., 2019***). Head direction cells are found in the superficial and deep layers of dorsal presubiculum, also termed postsubiculum (***Boccara et al., 2010***), and most layer 3 neurons in the dorsal presubiculum are head direction cells (***Tukker et al., 2015***; ***Preston-Ferrer et al., 2016***). These cells receive monosynaptic head direction inputs from the anterior thalamus (***Nassar et al., 2018***; ***Peyrache et al., 2015***; ***Balsamo et al., 2022***). Lesions of the PrS impair the visual landmark control of a cell's preferred direction in ATN and in LMN (***Goodridge and Taube, 1997***; ***Yoder et al., 2015***). Presubicular lesions also induce place field instability in the hippocampus (***Calton et al., 2003***), suggesting this region may be crucial to the anchoring of directionally modulated neurons to environmental landmarks.

Landmark-based navigation depends on reliable visual cues. The PrS appears to receive direct projections from the primary visual cortex and indirect visual input via the retrosplenial cortex (***Van Groen and Wyss, 2003***; ***Vogt and Miller, 1983***). The retrosplenial cortex encodes angular head velocity (***Alexander and Nitz, 2015***; ***Keshavarzi et al., 2022***) and visual landmark information (***Auger et al., 2012***; ***Clark et al., 2010***; ***Sit and Goard, 2023***), and supports an array of cognitive functions, including memory, spatial and non-spatial context, and navigation (***Vann et al., 2009***; ***Vedder et al., 2017***). In particular, some neurons in the dysgranular retrosplenial cortex encode landmark-dominated head direction signals (***Jacob et al., 2017***). Presubicular layer 3 cells receiving projections from both the anterior thalamus and the retrosplenial cortex (***Kononenko and Witter, 2012***) could update the compass and bind landmarks to head direction signals. Presubicular neurons could then broadcast integrated HD-landmark signals directly to the MEC, via deep layers to the ADN, and via layer 4 neurons to the LMN (***Huang et al., 2017***; ***Yoder et al., 2015***; ***Yoder and Taube, 2011***). The different target-specific presubicular projection neurons are well positioned to integrate anterior thalamic and retrosplenial inputs, but technical constraints have limited understanding of how known anatomical inputs are transformed into functional integrated output signals.

This work was therefore designed to examine the convergence of visual landmark information, that is possibly integrated in the RSC, and vestibular-based thalamic head direction signals, in the PrS. Retrograde tracing was used to confirm inputs to the PrS from the ATN and the RSC. The spatial distribution of ATN and RSC targets in the dorsal and ventral PrS was investigated by stereotaxic injection of viral vectors inducing anterograde expression of light-gated ion channels fused to fluorescent reporters. We found that superficial layers of the dorsal PrS are major targets of ATN and RSC projections. We analyzed functional convergence of these inputs in the PrS using dual-wavelength optogenetic stimulations in ex vivo brain slices, while recording from layer 3 and 4 pyramidal neurons. Both ATN and RSC projections made mono-synaptic excitatory connections with single layer 3 principal cells and mostly di-synaptic ones with layer 4 cells. We show that EPSPs induced with close to coincident timing by ATN and RSC fibers summed non-linearly in layer 3 neurons. Layer 4 cell firing is facilitated by cholinergic activation. These data provide insights into the integration of landmark and head direction inputs and their distribution to downstream targets by PrS pyramidal cells.

Results

ATN and RSC send strong axonal projections to the dorsal Presubiculum

The origins of the main afferents projecting to the presubiculum were explored by injecting retrogradely transported fluorescent beads into the PrS (***Figure 1A***). After 4 days, coronal slices were prepared to examine the injection site and transport of the beads. Some beads remained close to the PrS injection site, due in part to local projections. Strong bead signals were detected within two of the subnuclei that form the anterior thalamus, the anterodorsal (AD) and anteroventral (AV) part of ATN. Neurons in AD were labeled most strongly in the medial portion of the AD, while labeled neurons in AV were found in its lateral portion (***Figure 1B***). Many neurons in the RSC were labeled. Cells with somata in layers 2 and 5 of the dysgranular dRSC were labeled, while mostly layer 5 cells of granular gRSC contained beads (***Figure 1C***). Regions adjacent to the presubiculum, including the subiculum (Sub), parasubiculum (PaS), and the medial and lateral entorhinal cortices (MEC, LEC) were labeled as was the contralateral PrS. Beads were also detected in the laterodorsal thalamic nucleus (LD). ***Figure 1—figure supplement 1*** shows an example of a series of labeled coronal sections from one out of two mice, indicating some labeling also in the visual cortices, perirhinal cortex, the nucleus reuniens of the thalamus, the dorsolateral geniculate nucleus, and the claustrum. Some beads were observed in the CA1 region, which has not previously been reported. Potentially, though, this labeling could derive from a bead leak into the nearby PaS which is innervated by CA1 (***van Groen and Wyss, 1990a***). In summary, the ATN and RSC are the major sources of afferents projecting to the presubiculum with lesser inputs from other sites.

Projections from the ATN or RSC to the presubiculum were explored by injecting at these sites an anterogradely transported viral construct which expressed the modified Channelrhodopsin Chronos fused to GFP (***Figure 1D***). After 4 weeks, horizontal slices were prepared to verify the ATN injection site. Chronos-GFP labeling was mostly confined to the ATN, occasionally extending to medial thalamic and reticular nuclei nearby, possibly as bundles of projecting fibers (***Figure 1E***). After injection at the RSC site, coronal sections (***Figure 1F***) showed strong expression in layer 5, especially deeper zones, and layer 6 of both dysgranular and granular RSC, while labeled dendrites were evident in layer 1. Chronos-GFP expression extended throughout the RSC, from –1.7 to –3.7 posterior to Bregma on the antero-posterior axis.

Projections of the ATN to the presubiculum were examined in horizontal sections (***Figure 1G***). ATN axons expressing the Chronos-GFP construct targeted layers 1 and 3 of the presubiculum, mostly avoiding layer 2 (***Simonnet et al., 2017***; ***Nassar et al., 2018***). Labeling was precisely limited to the presubiculum with a sharp reduction of green fluorescence at the posterior border with the parasubiculum, the anterior border with the subiculum, and the lateral border with deep layers. Axon terminals in layer 3 were not homogeneously distributed. Patches of higher density were evident in deep layer 3 (***Figure 1G***, left panel) or in the upper layer 3 (***Figure 1G***, fourth panel, and ***Figure 1K***). Along the dorso-ventral axis, ATN axons projected from –2 to –4 mm ventral to Bregma. Fluorescence was not detected in adjacent regions, including the Sub, PaS, and DG. ATN axons avoided layer 2 of the PrS, including regions with patches of calbindin-positive neurons that project to contralateral PrS (***Preston-Ferrer et al., 2016***; ***Figure 1K***).

RSC projections to the presubiculum (***Figure 1H***), traced with the fluorescent Chronos-GFP construct, also projected to layers 1 and 3. Unlike ATN axons, they were restricted to dorsal regions of the presubiculum (from –2 to –3 mm ventrally to Bregma on the dorso-ventral axis; ***Figure 1H, I and J***). RSC axons also presented a patchy innervation pattern in L1-3, and tended to avoid microdomains of high-density ATN projections (***Figure 1G and K***; Figure 3). Overall, these data show ATN and RSC afferents innervate overlapping dorsal regions of the PrS, in layer 1 and parts of layer 3. Different spatial patterns of fiber terminations suggest distinct local connectivities.

Layer 3 neurons are directly excited by both ATN and RSC afferents

We next examined physiological effects of ATN and RSC afferents on PrS pyramidal cells (***Rees et al., 2017***). Responses to photo-stimulation of the Chronos-GFP construct injected either in the thalamus or in the retrosplenial cortex (***Figure 2A***) were recorded in layer 3 neurons (***Figure 2B***). These cells had robust regular firing patterns in response to depolarizing current injections (***Figure 2C***). Intrinsic

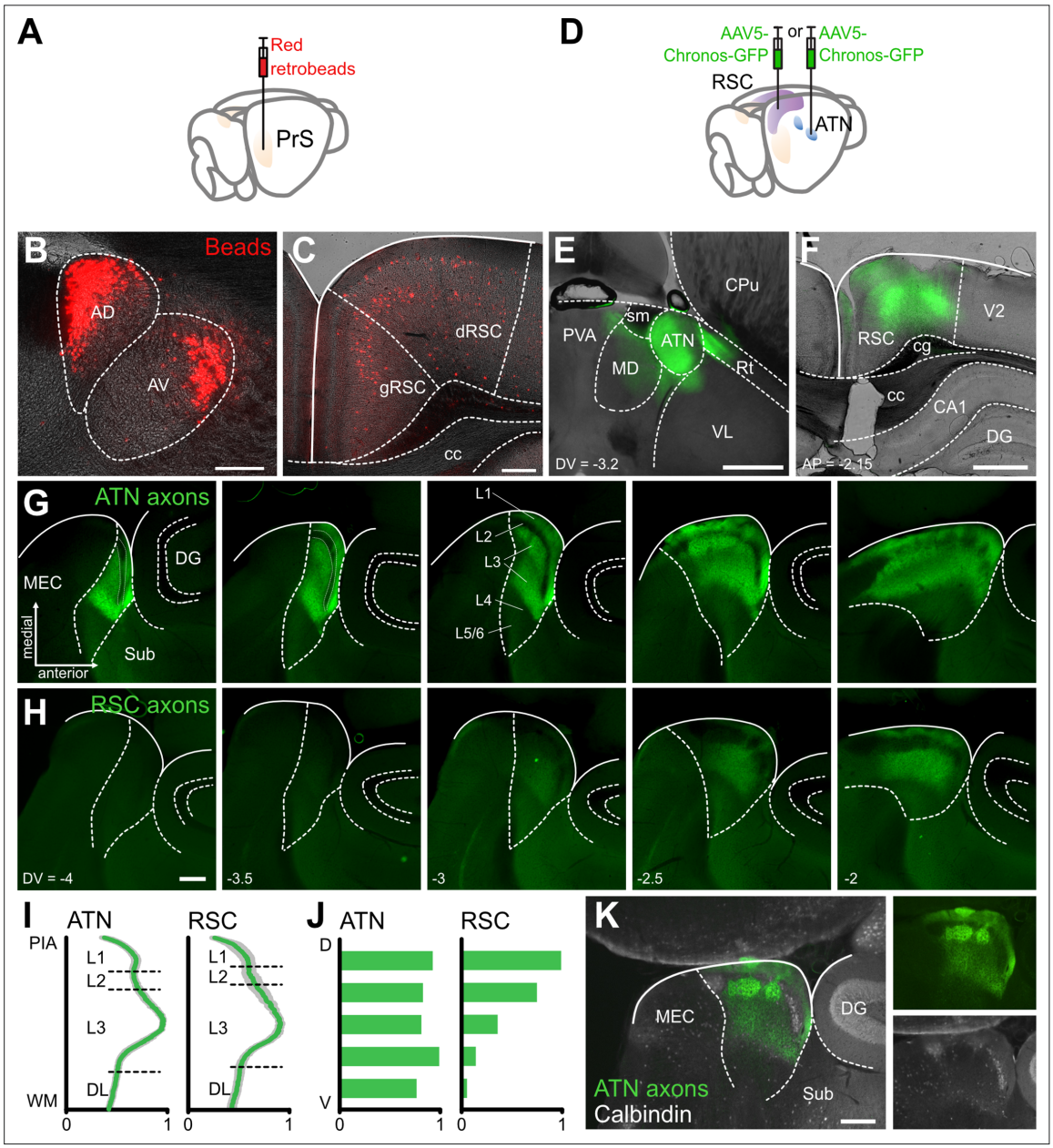

Figure 1. Anterior thalamic nuclei (ATN) and RSC send strong axonal projections to the superficial layers of dorsal presubiculum. (**A**) Retrograde labeling of cortical and subcortical regions projecting to the presubiculum (PrS) with retrobeads. (**B**) Ipsilateral anterodorsal and anteroventral thalamic nuclei are labeled with beads. (**C**) Ipsilateral granular (gRSC) and dysgranular (dRSC) retrosplenial cortex labeling. Scale bars (**B**, **C**), 200 µm. (**D**) Anterograde labeling of thalamic and retrosplenial projections to PrS with AAV-Chronos-GFP. (**E**, **F**) Injection sites in ATN (**E**) and RSC (**F**). AD: anterodorsal thalamic nucleus, AV: anteroventral thalamic nucleus, CA1: field of the hippocampus, cc: corpus callosum, cg: cingulum, CPu: caudate putamen, DG: dentate gyrus, MD: thalamic medial dorsal nucleus, MEC: medial entorhinal cortex, PaS: parasubiculum, PVA: paraventricular thalamic nucleus, anterior, Rt: thalamic reticular nucleus, sm: stria medullaris, Sub: subiculum, VL: thalamic ventrolateral nucleus. (**G, H**) Five sequential 100 µm horizontal slices of the parahippocampal region show ATN (**G**) and RSC (**H**) axons expressing Chronos-GFP (green). Dashed lines show limits of the parahippocampal region to the left and of the dentate gyrus to the right. Numbers show dorsoventral level with respect to bregma. Scale bars 100 µm. (**I**) Normalized profiles of fluorescent intensity for ATN and RSC projections to the presubiculum, from white matter (WM) to pia (PIA). Mean (green) ± SEM (gray), n=8 slices each. (**J**) Ventral (**V**) to dorsal (**D**) normalized distribution of ATN and RSC projections to the presubiculum, n=3 mice. (**K**) ATN axon labeling (green) is segregated from calbindin labeling (white) in the PrS. Scale bar, 100 µm. See also ***Figure 1—figure supplement 1***.

Figure 1 continued on next page

Figure 1 continued

The online version of this article includes the following figure supplement(s) for figure 1:

Figure supplement 1. Brain regions providing input to the presubiculum.

Figure supplement 2. Calbindin immunostaining and GFP-expressing anterior thalamic nuclei (ATN) axons in horizontal sections.

properties of layer 3 cells were rather uniform and an unsupervised cluster analysis suggested they formed a single population (***Figure 2D***).

Blue light activation of either ATN or RSC axons expressing Chronos-GFP reliably evoked synaptic responses in whole-cell patch-clamp records from layer 3 cells. High-intensity stimulation (1–3 mW) evoked EPSCs or EPSPs with a probability of 84% (70/83 neurons from 14 mice) for ATN fibers and 85% (104/123 neurons from 20 mice) for RSC fibers (***Figure 2E***). Excitatory postsynaptic currents or potentials evoked by optical stimulation of thalamic and retrosplenial inputs will be referred to as oEPSCs and oEPSPs. Mean oEPSC amplitudes (***Figure 2F***) were similar for ATN (–305.0±61.0 pA, n=24) and RSC fiber stimuli (–305.8±59.1 pA, n=27). Response latency (***Figure 2G***) to ATN axon stimulation was 2.45±0.19 ms (n=24) and that for RSC axon stimulation was 2.93±0.23 ms (n=27). The variability in latency of oEPSCs (***Figure 2—figure supplement 1A, B***) induced by RSC afferent stimuli was 0.35±0.09 ms (n=27) and that for oEPSCs induced by ATN stimuli was 0.19±0.06 ms (n=24). These short oEPSC latencies suggest monosynaptic transmission. We confirmed this point by showing that oEPSCs were maintained in the presence of TTX (1 μM) and 4AP (100 μM) (***Figure 2H***, n=2 and 12 for ATN and RSC, respectively). EPSCs induced by stimulation of ATN and RSC fibers were reduced in amplitude and decayed more quickly in the presence of the NMDA receptor antagonist APV (50 μM) and were completely abolished by further application of the AMPA receptor antagonist NBQX (1 mM) (***Figure 2I***). The shape of oEPSCs induced by light stimulation of ATN and RSC fibers was comparable. Rise times were 1.38±0.15 ms for ATN EPSCs (n=15) and 1.38±0.08 ms for RSC-mediated EPSCs (n=15) and mean half-widths were 4.00±1.02 ms for ATN-induced ESPCs (n=15) and 4.34±1.18 ms for RSC EPSCs (n=15). The mean time constant (tau decay) for ATN-mediated EPSCs was 3.01±0.21 (n=15) and for RSC-induced EPSCs 3.17±0.27 (n=15) (***Figure 2—figure supplement 1***).

Optical stimulation of ATN and RSC fibers at lower light intensities elicited sub-threshold synaptic events in layer 3 cells. oEPSP amplitude for ATN-mediated events was 4.09±1.18 mV (n=11) and for RSC events it was 4.80±0.84 mV (n=11). Maximal rising slopes were 2.93±0.82 mV/ms for ATN-mediated events (n=11) and 3.02±0.53 mV/ms for RSC EPSPs (n=11), and decay time constants were 81.4±11.6 ms for ATN EPSPs (n=11) and 86.9±11.2 ms for RSC EPSPs (n=11). Rise times were shorter for subthreshold EPSPs induced by ATN afferents at 3.00±0.24 ms (n=11) while those for RSC-initiated EPSPs were 3.59±0.34 (n=11, p=0.042, Wilcoxon test; ***Figure 2—figure supplement 1***). These data show that ATN and RSC axons make monosynaptic, glutamatergic excitatory contacts on layer 3 PrS cells.

The dynamics of responses to repetitive stimulation of layer 3 PrS cells were tested using 20 Hz trains of light stimuli to activate either ATN or RSC afferents. oEPSCs for both inputs followed depressing kinetics. Amplitude decreased for both inputs (***Figure 2J and K***), significantly after the fourth pulse (Friedman's test and Dunn's multiple comparison test). The *10/1* ratio was significantly lower than the paired-pulse ratio (PPR) in both cases (ATN *10/1* 0.56±0.05 vs PPR 0.86±0.05, n=15, p<0.0001, Wilcoxon test, RSC *10/1* 0.64±0.05 vs PPR 0.83±0.03, n=15, Wilcoxon test) (***Figure 2L***). ATN fiber stimulation induced PrS cell firing in current-clamp with a high probability for initial stimuli and lower stable probabilities for later stimuli in the train. Similarly, 20 Hz stimulation of RSC afferents evoked spikes with high probability for initial stimuli and decreasing probabilities for later stimuli (on fourth and 7th-10th pulses, Friedman's and Dunn's multiple comparison tests; ***Figure 2M and N***). Responses to repeated subthreshold stimuli had similar dynamics (***Figure 2O***). Stimulation with lower light intensities (<1 mW) to initiate sub-threshold oEPSPs elicited different dynamic responses. ATN afferent trains elicited responses with depressing dynamics: the amplitude of the fifth oEPSP was significantly less than the first one (3.18±0.88 vs 5.11±1.64 mV, p=0.0185, Friedman's and Dunn's tests). In contrast, subthreshold 20 Hz stimulation of RSC afferents evoked little or no oEPSP depression (***Figure 2—figure supplement 1***). These data reveal distinct patterns of integration of repetitive activity in glutamatergic ATN and RSC afferents terminating on PrS layer 3 pyramidal cells.

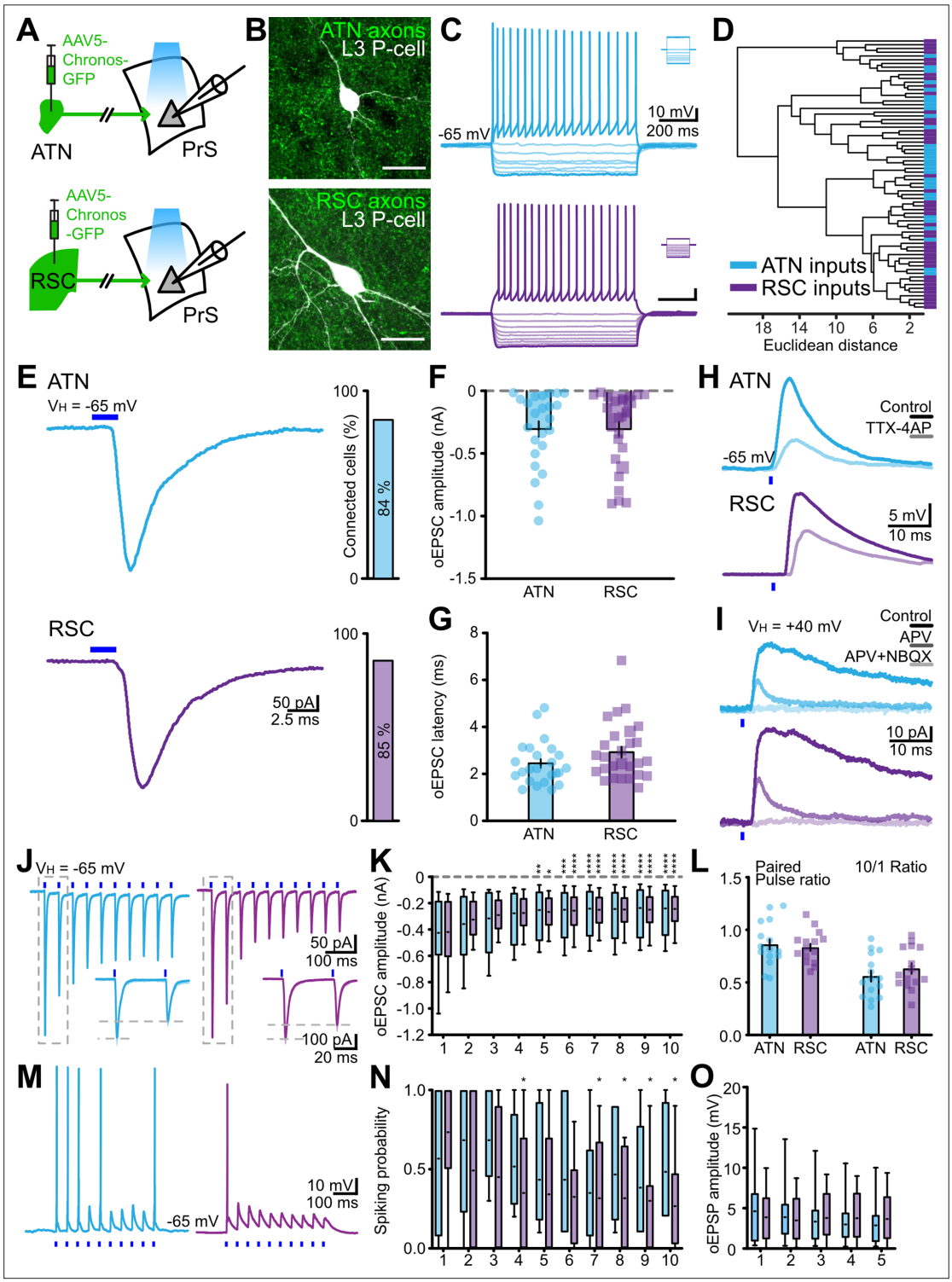

Figure 2. Responses of layer 3 presubicular cells to photoactivation of anterior thalamic nuclei (ATN) and RSC fibers. (**A**) Expression of AAV5-Chronos in ATN or RSC. (**B**) Biocytin-labeled layer 3 cells (white) and GFP-positive axons (green) from the ATN or RSC. Scale bar 10 µm. (**C**) Firing pattern of two layer 3 cells receiving inputs from the ATN (*cerulean*) and the RSC (*purple*). Insets show current commands. (**D**) Cluster analysis of physiological parameters for cells tested by stimulating ATN (n=29 cells /14 mice) or RSC (n=43 cells/20 mice) fibers. (**E**) Representative EPSCs evoked in layer 3 cells

Figure 2 continued on next page

Figure 2 continued

by light stimulation (blue bar) of ATN or RSC inputs. Right, the proportion of cells receiving ATN or RSC inputs. (**F**) Average amplitudes of ATN and RSC induced synaptic currents. Mann-Whitney U test revealed no significant difference (p=0.95). (**G**) Latency of EPSCs evoked by light stimulation of ATN (n=24 cells/12 mice) or RSC fibers (n=27 cells/14 mice). Mann-Whitney U test revealed no significant difference (p=0.13). (**H**) EPSPs induced in layer 3 cells (single traces) by stimulating ATN or RSC inputs in the absence and presence of 1 µM TTX and 100 µM 4-AP. (**I**) EPSCs induced by stimulating ATN or RSC fibers in the absence and presence of 100 µM APV and APV + 10 µM NBQX. Holding potential + 40 mV. (**J**) Voltage-clamp responses of layer 3 cells to 20 Hz train stimulations of ATN (*left*) and RSC (*right*) inputs. Insets show EPSCs in response to the first two stimuli. (**K**) oEPSC amplitudes for 10 ATN or RSC fiber stimuli at 20 Hz (ATN, n=15 cells/8 mice, RSC, n=15 cells/11 mice). Short middle line, mean; Min to max and quartiles. (**L**) Paired-pulse ratio (PPR) and 10/1 ratio (ratio between 10th and fist event amplitudes) for ATN or RSC inputs. Wilcoxon matched-pairs signed rank test: ATN PPR vs 10/1 **** p<0.0001, RSC PPR vs 10/1 *** p=0.0001. (**M**) Current clamp traces showing action potentials and EPSPs evoked by 10 stimuli at 20 Hz. (**N**) Spiking probability during trains of 10 stimuli. ATN, n=6 cells/4 mice, RSC, n=12 cells/9 mice. Full line, median; short line, mean; Min to max and quartiles. In (**K** and **N**), *p<0.05, **p<0.01, ***p<0.001, ****p<0.0001 from Friedman's test followed by Dunn's *post-hoc* test. (**O**) oEPSP amplitudes for trains of five stimuli at 20 Hz. See also .

The online version of this article includes the following source data and figure supplement(s) for figure 2:

Source data 1. Table showing the intrinsic electrophysiological physiological properties of layer 3 cells tested for responses to stimulating anterior thalamic nuclei (ATN) or RSC fibers.

Figure supplement 1. Comparison of evoked synaptic events in presubicular layer 3 neurons following photostimulations of anterior thalamic nuclei (ATN) or RSC axons.

Convergence of ATN and RSC inputs on single layer 3 neurons

Are single layer 3 pyramidal cells innervated by both ATN and RSC afferents? It seemed likely since the probability of connection to a given cell was 84% for ATN fibers and 85% for RSC afferents, and cluster analysis (***Figure 2D***) provided no evidence for subpopulations of layer 3 cells in terms of intrinsic electrophysiological properties (see also ***Balsamo et al., 2022***).

We tested the hypothesis using photostimulation at two different light frequencies to activate ATN and RSC afferents independently. However, this approach may be compromised since there is an overlap in the excitation spectra of blue-light activated Chronos (400–600 nm) and red-light activated Chrimson (450–700 nm ; ***Klapoetke et al., 2014***). Excitation of Chronos with high intensities of blue light might also excite Chrimson. Stimulating with red light at 630 nm should elicit neurotransmitter release in Chrimson-containing but not Chronos-expressing fibers, which we found was indeed the case. Blue light stimuli at 470 nm and intensities higher than 0.01 mW elicited oEPSPs in layer 3 cells of animals with Chronos-expressing fibers. In contrast, blue light intensities higher than 0.25 mW were needed to induce oEPSPs in different animals with Chrimson-expressing axons (***Figure 3—figure supplement 1A–D***). Moreover, the amplitude of these events was smaller in Chrimson-injected than in Chronos-injected mice. Thus, in our experimental conditions, blue light intensities up to 0.25 mW could be used to excite Chronos-positive axons with confidence that Chrimson-expressing fibers would not be stimulated.

We also tested the inverse, red light component of the dual stimulus strategy. Intensities were tested in mice injected either with AAV5-Chronos to label ATN fibers or AAV5-Chrimson to label RSC afferents. The strategy was validated by showing that red light induced oEPSPs in Chrimson-containing, but not Chronos-expressing fibers, while blue light evoked synaptic events in Chronos-, but not Chrimson-expressing fibers (***Figure 3—figure supplement 1E–K***).

Injection in the same animal of the Chronos construction to the thalamus and that for Chrimson to the retrosplenial cortex let us visualize ATN and RSC afferents to the presubiculum (***Figure 3A, B***). Axon terminal fields of ATN and RSC projections were evident in superficial layers of dorsal PrS (***Figure 1***). Layer specificities and labeling inhomogeneities were apparent, as were high-density ATN patches below layer 2 with no RSC axon innervation (***Figure 3B***). Layer 3 pyramidal cells could be innervated by ATN and RSC contacts both with apical dendrites in layer 1 and basilar dendrites of layer 3 (***Figure 3D***). We found optical stimulation of ATN and RSC axons evoked synaptic responses in 14 out of 17 layer 3 pyramidal cells tested (current-clamp and voltage-clamp; ***Figure 3E, F***).

In order to quantify substrates of these innervations, we counted the numbers of labeled ATN or RSC terminals located at less than 1 µm from dendrites of biocytin-filled layer 3 pyramidal cells (n=6; ***Figure 3G***). The distribution of these potential contact sites on dendritic trees of layer 3 neurons was diverse. Some neurons exhibited highly segregated domains receiving either ATN or RSC inputs. For instance, cell 1 had a high proportion of clustered RSC putative synapses on its apical tuft while

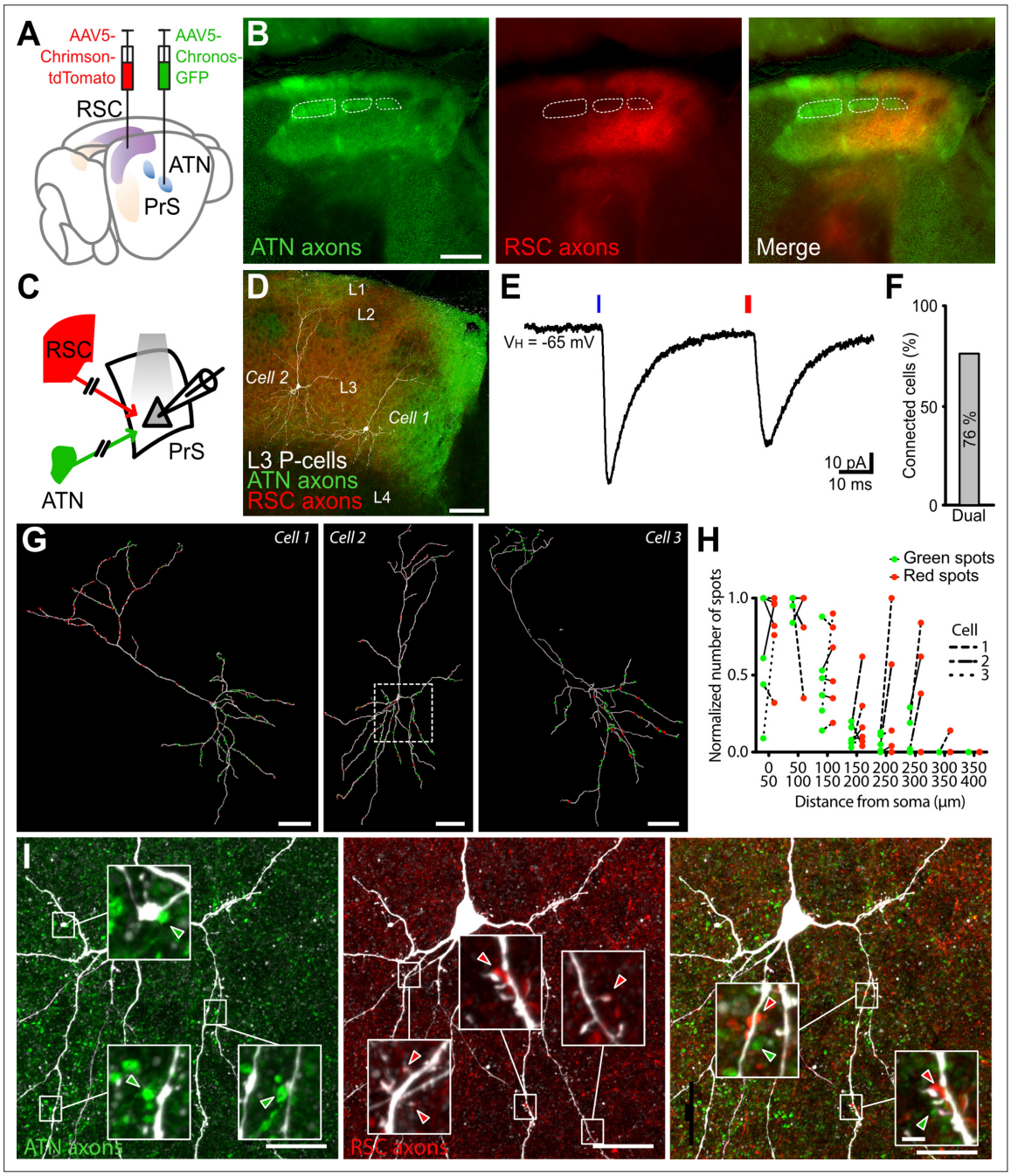

Figure 3. Anterior thalamic nuclei (ATN) and RSC axons converge in dorsal presubiculum and contact single layer 3 pyramidal neurons. (**A**) Expression of the blue light-sensitive opsin Chronos in ATN and the red light-sensitive opsin Chrimson in RSC. (**B**) Axons from ATN (GFP labeled, green) and RSC (tdTomato labeled, red) overlap in layer 1 and 3 of dorsal presubiculum. Layer 2 possesses patches of axon-dense and axon-poor zones. RSC fibers avoid axon-dense microstructures formed by ATN fibers in upper layer 3. Scale bar, 200 µm. (**C**) Independent dual-wavelength optogenetic stimulation of light-sensitive afferent fibers in presubicular slices. (**D**) Two biocytin-labeled PrS layer 3 pyramidal cells surrounded by ATN (green) and RSC (red) axons. (**E**) Patch clamp recording from a layer 3 neuron shows optical EPSCs following photostimulation of ATN axons (blue light) and RSC axons (red light). (**F**) 76% of layer 3 pyramidal neurons tested (n=17 cells/4 mice) received both ATN and RSC input. (**G**) Distributions of putative synaptic contacts from ATN (green) and RSC (red) on the dendrites of three layer 3 neurons. Scale bar 50 µm. The boxed area on Cell 2 is shown in panel **I**. (**H**) Normalized number of green and red spots for 6 neurons as a function of the distance from soma. Paired values are indicated by dotted lines for the 3 cells in **G**. (**I**)

Figure 3 continued on next page

Figure 3 continued

Examples of ATN-labeled (left), RSC-labeled (middle), and both (right) synapses closely apposed to dendrites of a biocytin-filled layer 3 pyramidal cell. Scale bar 20 µm. Insets show representative high-magnification images. Scale bar, 2 µm. See also ***Figure 3—figure supplement 1***.

The online version of this article includes the following figure supplement(s) for figure 3:

Figure supplement 1. Calibration of blue and red light stimulation of Chronos and Chrimson.

basilar dendrites were mostly surrounded by potential thalamic terminals. In cell 2, RSC terminals were clustered close to apical dendrites and also together with ATN terminals close to basilar dendrites. In contrast, many ATN terminals were located closer to apical dendrites of cell 3. Segregation of cortical RSC inputs to apical dendrites and thalamic ATN inputs to basal dendrites might favor supralinear EPSP summation. However, afferent terminal distributions differed, and we found no clear pattern of sub- or supralinear summation (cell 1, supralinear summation (Dual/summed EPSP, 1.39); cell 2, roughly linear (0.91); cell 3, sublinear (0.69), ***Figure 3G, H***). Furthermore, we noted certain potential contacts were located with separations less than 20 µm on the same dendrite (***Figure 3I***). Such proximity might underly local dendritic computations and supra-linearities, such as NMDA-mediated dendritic spikes which are suggested to contribute to non-linear summation of synaptic events (***Larkum et al., 1999***; ***Larkum et al., 2007***; ***Larkum et al., 2009***).

Supralinear integration and amplification of ATN and RSC excitatory postsynaptic potentials

We explored interactions between excitatory inputs to layer 3 neurons by stimulating ATN and RSC axons separately with blue or red light. Excitatory synaptic potentials evoked by ATN or RSC axon stimulation were compared to responses elicited when both sets of axons were activated at short time intervals (dual; ***Figure 4A***). The mean amplitude of dual oEPSPs (synchronous light onset, ***Figure 4A–C***) was significantly larger than calculated summed amplitudes of single oEPSPs (n=11 cells, dual/summed amplitude 2.06±0.55 mV, p=0.0068, Wilcoxon test). Charge transfer, quantified as the surface under the dual oEPSP, was greater than the summed values for single oEPSPs (Dual/summed surface 2.21±0.54 mV.s, n=11, p=0.0098, Wilcoxon test). These mean values cover variability between individual neurons. The summation of responses to ATN and RSC axon stimuli was supralinear in 7 out of 11 cells tested, linear for 3 cells and sublinear for 1 cell.

Dynamic responses to repetitive stimulations were also transformed by dual photostimulation. Amplitudes of 5 dual oEPSPs elicited at 20 Hz were higher than for a linear summation (Amplitudes in mV, Summed vs. Dual: Stim 1, 7.7±1.9 vs 11.1±1.9; Stim 2, 6.7±1.6 vs 9.5±1.5; Stim 3, 6.5±1.4 vs 9.5±1.5; Stim 4, 6.1±1.3 vs 9.2±1.5; Stim 5, 5.9±1.3 vs 8.6±1.4, p=0.0117, Two-way ANOVA; ***Figure 4E***) and charge transfer, quantified as the surface under the 5 oEPSPs, also typically summed supralinearly (20 Hz, Surface in mV.s, Summed vs. Dual: Stim 1, 136.9±30.6 vs 221.2±41.5; Stim 2, 143.3±25.7 vs 242±43.9; Stim 3, 147.3±22.5 vs 259.2±44; Stim 4, 145.1±22 vs 263.5±49.2; Stim 5, 145.6±23.2 vs 258.7±45.2, p=0.0128, two-way ANOVA; ***Figure 4F***). Trains of dual ATN and RSC fiber stimulations also showed increased oEPSP integrals, compared to the stimulation of either one set of fibers alone, indicating stronger excitation over time (***Figure 4E and F***). Taken together, these data show supralinear summation of ATN and RSC inputs in most single layer 3 pyramidal cells, and also a facilitation of dynamic responses to repetitive inputs at 20 Hz.

We next asked how efficiently action potentials were induced by combined ATN and RSC inputs. Firing probability of layer 3 cells was higher for dual than for single input stimulation at a membrane potential of –65 mV (ATN 0.008 vs Dual 0.268, n=5, p=0.0216, RSC 0.024 vs Dual 0.268, n=5, p=0.1195, Friedman's and Dunn's tests) and higher still at –55 mV (***Figure 4G and H***). Firing was induced over a narrow window of time delays between stimulation of the two inputs (***Figure 4I and J***). It occurred for delays of –2 to +5 ms (RSC preceding ATN stimulus) reaching a maximum at a delay of +1 ms.

Supralinear summed responses of excitatory synaptic events may be mediated via the activation of NMDA receptors or voltage-dependent intrinsic currents that amplify EPSPs (***Fricker and Miles, 2000***), especially if synaptic inhibition is reduced. We assessed these mechanisms in records made from layer 3 pyramidal neurons using a cesium-based internal solution to favor cationic amplifying currents, and also containing QX314 to suppress action potentials (***Figure 5***). In 3 cells (from 2 mice), photostimulation of ATN fibers evoked oEPSPs of amplitude 10.9±2.0 mV and RSC fiber stimulation

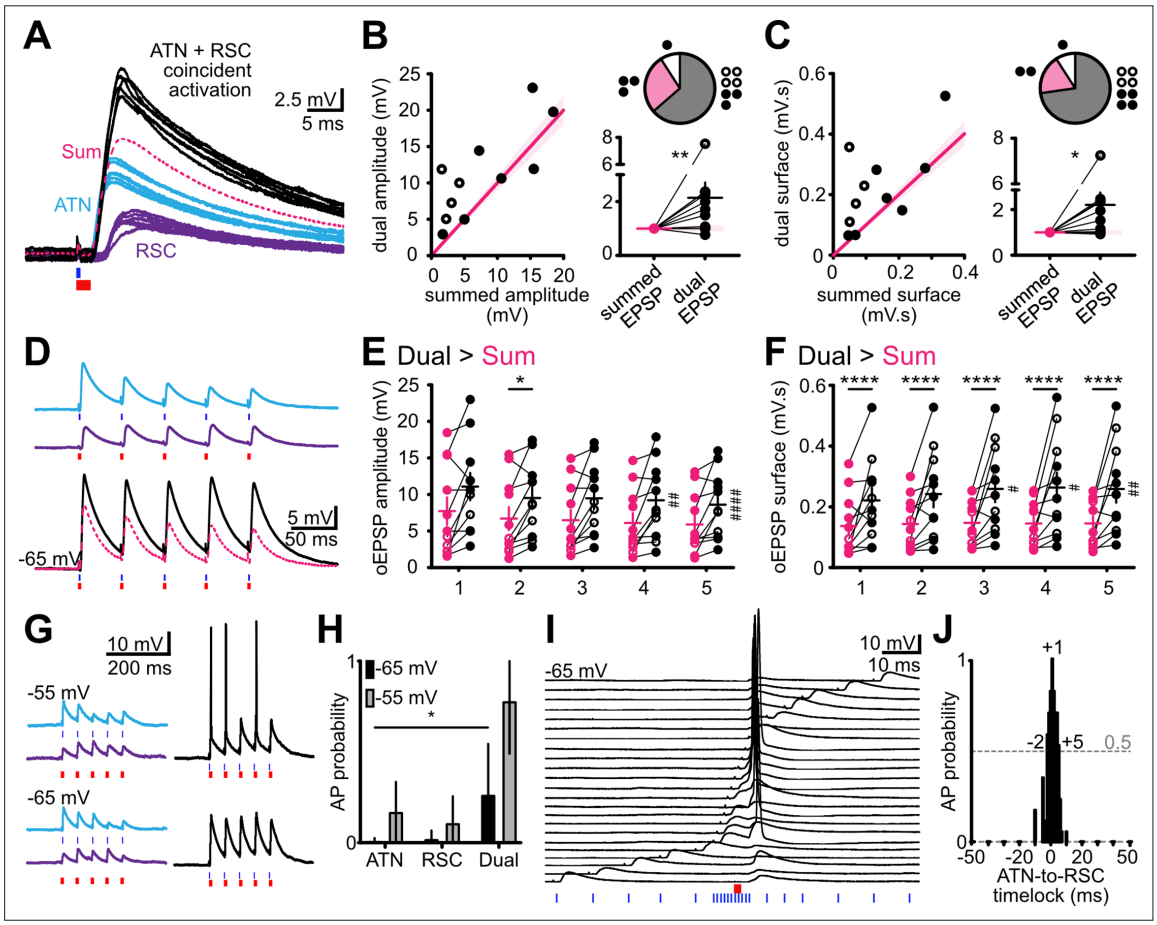

Figure 4. Supralinear summation of EPSPs and action potential firing following photostimulation of anterior thalamic nuclei (ATN) and RSC axons. (**A**) Optical EPSPs in layer 3 neurons in response to blue light activation of ATN axons (cerulean traces), red light activation of RSC axons (purple traces). Supralinear summation of EPSPs following coincident activation of both ATN and RSC axons (black traces). The pink broken line indicates the calculated linear sum of oEPSPs evoked by stimulation of either ATN or RSC axons. Records from cell 1, ***Figure 3D***. (**B**) Amplitudes of dual ATN and RSC oEPSPs plotted as a function of the sum of separate ATN and RSC stimulations (*left*). Each circle is a cell (n=11 cells/4 mice). Pink line (±10%) indicates linearity. Pie charts give the number of tested layer 3 neurons with supralinear (gray), linear (pink), or sublinear (white) summation. oEPSPs normalized to linear sum (*bottom right*). Solid circle, Chronos in ATN/Chrimson in RSC, empty circle, Chronos in RSC/Chrimson in ATN. *p<0.05, **p<0.01, from Wilcoxon test. (**C**) As in (**B**) for dual ATN and RSC oEPSP integrals. (**D**) oEPSPs induced by 20 Hz stimulation of ATN (cerulean), RSC (purple), or both (black). The pink broken line indicates the calculated linear sum of oEPSPs evoked by separate ATN and RSC photostimulation. (**E**) Amplitudes of dual oEPSPs compared to those of the sum of ATN and RSC oEPSPs show that supralinearity increases across five stimulations. Two-way ANOVA, p=0.0117. *p<0.05, ****p<0.0001, Šidák's multiple comparison test. # p<0.05, ## p<0.01, Friedman's and *post-hoc* Dunn's test. (**F**) As in **E**, for dual ATN and RSC oEPSP integrals. Two-way ANOVA, p=0.0128. (**G**) Excitatory postsynaptic responses to photostimulation of ATN (blue light, cerulean traces) or RSC axons (red light, purple traces), or both (blue and red light, black traces) at resting membrane potential (–65 mV) or at a depolarized holding potential (–55 mV). Synaptic excitation led to action potentials when dual ATN and RSC stimuli reached firing threshold. (**H**) Action potential (AP) probability for either or both stimuli at –65 and –55 mV. Data are presented as mean ± SEM. (**I**) Action potentials were induced in presubicular layer 3 neurons by near-coincident activation of ATN axons (red light) and RSC axons (blue light). Time delays varied from –50 to +50 ms. (**J**) Firing probability was maximal for short delays between –2 to +5 ms (RSC preceding ATN).

induced events of 13.7±2.5 mV. The response dynamics to 5 light pulses at 20 Hz were moderately facilitating (second vs first amplitude ratio: ATN 1.39, RSC 1.17; fifth vs first: ATN 1.18, RSC 1.20; n=3). Coincident activation of ATN and RSC afferents induced supralinear oEPSP summation. Furthermore, repetitive stimulation generated large all-or-none depolarizations on the second or third stimulus at 20 Hz (second vs first amplitude ratio: 1.52; fifth vs first: 2.90; n=3 cells, ***Figure 5A***). It may be mediated by VGCC or a QX-314-resistant Na + inward current (***Fricker et al., 2009***). This component appeared with higher probability and shorter latency in the presence of the $GABA_A$ receptor blocker gabazine

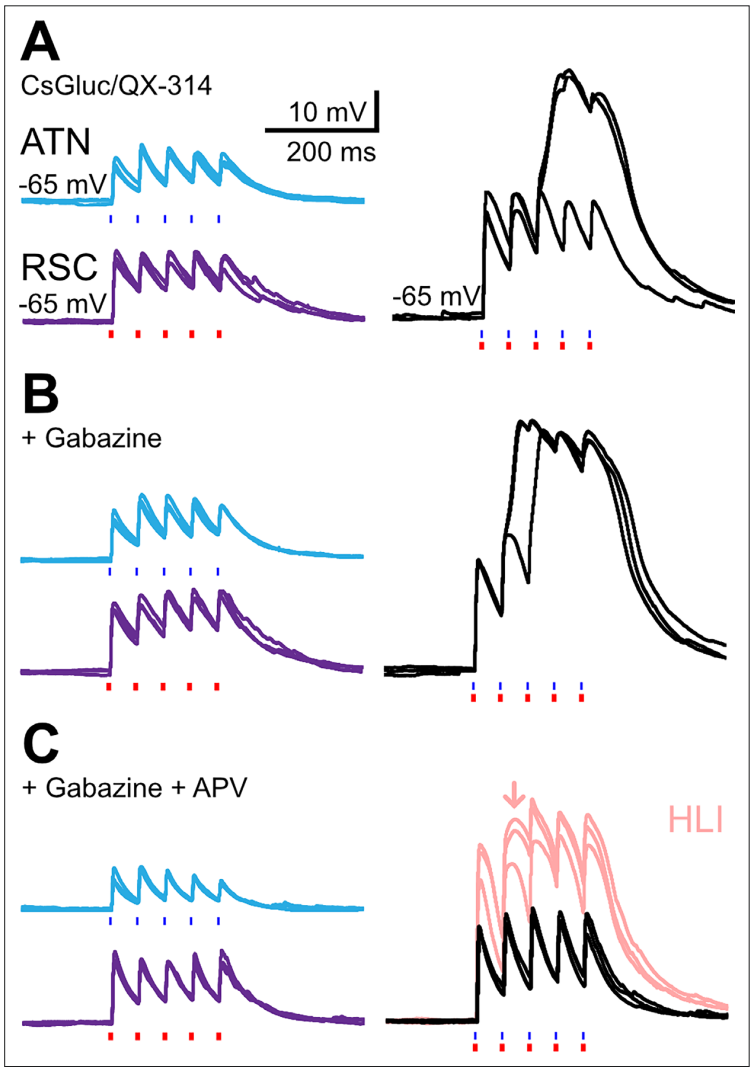

Figure 5. EPSP amplifications in layer 3 pyramidal neurons. (**A**) Optical EPSPs evoked in layer 3 pyramidal neurons following the stimulation of anterior thalamic nuclei (ATN) axons (blue light, cerulean traces), RSC axons (red light, purple traces), or both (blue and red light, black traces). The recording pipette contained a cesium gluconate-based internal solution and the Na^+ channel blocker QX-314. A large all–or-none EPSP amplification occurred for dual stimuli at 20 Hz, on some trials. (**B**) In the presence of the $GABA_A$ receptor antagonist gabazine (10 μM), dual EPSP amplification occurred earlier in the train. (**C**) The additional presence of the NMDA receptor antagonist APV (100 μM) abolished dual EPSP amplification (black trace). EPSP amplification was partially restored by increasing red light intensity 2x (pale pink traces).

(***Figure 5B***). The NMDA receptor antagonist APV largely abolished the dual EPSP amplification initially (***Figure 5C***, black trace; second vs first integral ratio: 1.22; fifth vs first: 1.32), although amplification was partially restored by increasing RSC stimulus intensity (pale pink trace; 'amplification' refers to the shape of the plateau-like prolongation of the peak, most pronounced on the second EPSP, indicated with an arrow). NMDA receptor activation thus assists depolarization towards the threshold of a voltage-dependent process contributing to supra-linear EPSP summation but is not the only charge carrier involved.

Cholinergic modulation and recruitment of presubicular layer 4 neurons by ATN and RSC afferents

Presubicular layer 4 neurons are intrinsic bursting pyramidal neurons that project to the lateral mammillary nucleus (***Huang et al., 2017***). This pathway is critical for the coordinated stable landmark control of HD cells in the thalamus and throughout the HD cell circuit (***Yoder et al., 2015***; ***Yoder et al., 2017***). To investigate the input connectivity of layer 4 principal cells, we recorded responses of these neurons to stimulation of ATN and RSC afferents.

Layer 4 neurons labeled by retrograde tracers injected in the lateral mammillary nucleus were located in the *lamina dissecans* of the presubiculum, below layer 3, where thalamic axons ramify (***Figure 6A–D***). At the proximal end of the presubiculum, and in its continuity (***Ishihara and Fukuda, 2016***), some subicular neurons projecting to the medial portion of the mammillary bodies are also labeled (***Figure 6B***). The apical dendrites of layer 4 presubicular neurons extended towards presubicular layer 1 as previously described (***Huang et al., 2017***), but tended to circumvent layer 3 and avoid thalamic afferent, by swerving towards the subiculum. Apical dendrites of some neurons crossed layer 3 obliquely, while others avoided thalamic afferents in layer 3 (***Figure 6Cand D***, ***Figure 6—figure supplement 1***).

Layer 4 neurons had a more depolarized resting membrane potential, lower input resistance, and time constant than layer 3 neurons (***Figure 6—figure supplement 2*** compares active and passive properties). A characteristic voltage sag in responses to hyperpolarizing steps indicated the presence of an I_h current. Layer 4 neurons discharged bursts of two or three action potentials at the onset of a depolarizing step current injection and also after the offset of hyperpolarizing steps (***Figure 6E***). These bursts were abolished by the T-type Ca^{2+} channel blocker TTA-P2 (***Figure 6F***).

We next recorded responses of layer 4 neurons to optical activation of ATN or RSC afferents together with effects of the same stimuli on layer 3 pyramidal cells (***Figure 6G***). Overall, latencies

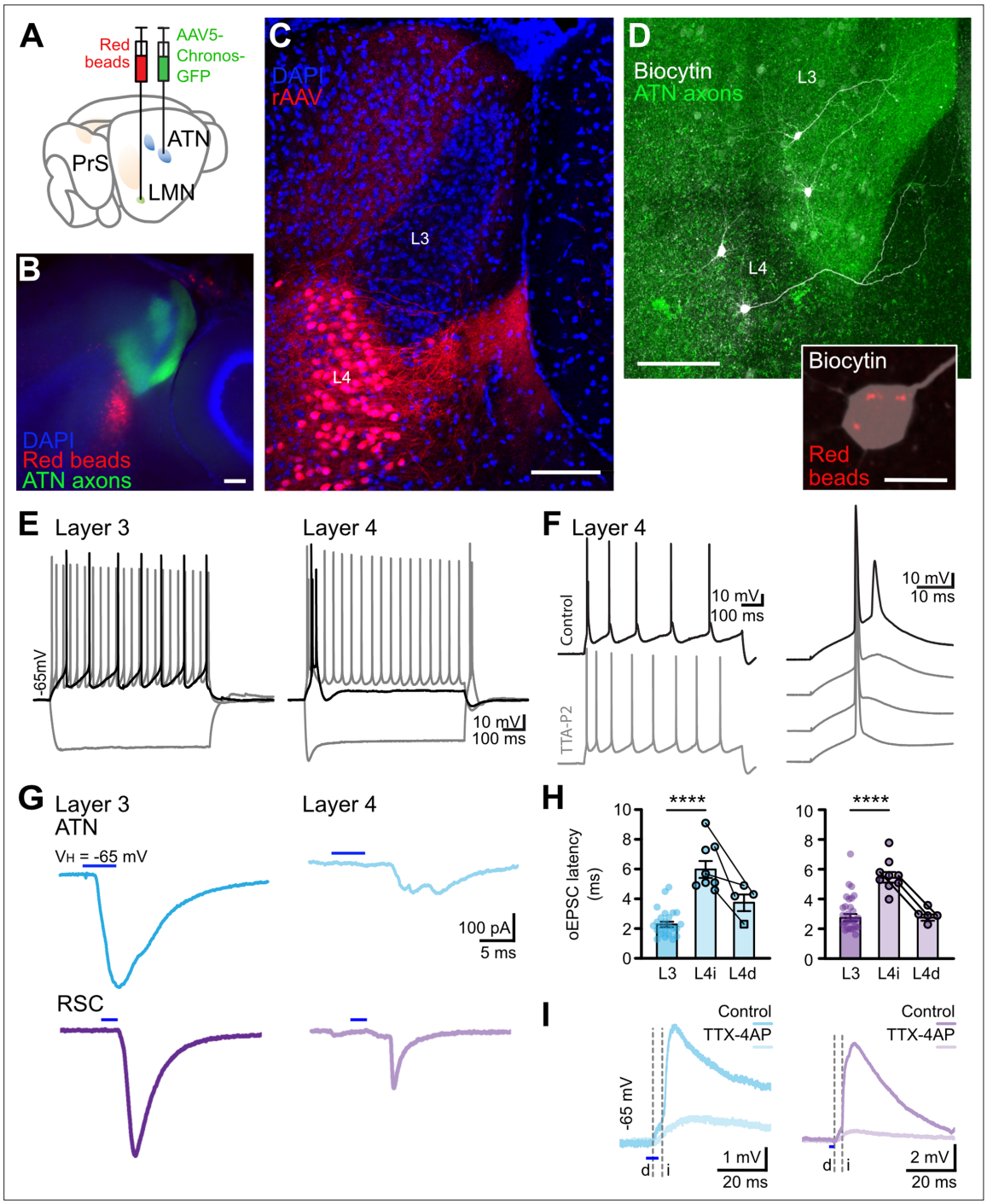

Figure 6. Presubicular lateral mammillary nucleus (LMN)-projecting layer 4 neurons avoid thalamo-recipient layer 3 and receive little direct input from anterior thalamic nuclei (ATN) and RSC. (**A**) Expression of Chronos-GFP in ATN and retrograde labeling of neurons that target LMN. (**B**) Thalamic axons (green) in superficial layers 1 and 3 of presubiculum. Retrobeads label cell bodies of presubicular layer 4 cells (red). (**C**) Retrograde rAAV2-tdTomato label cell bodies and dendrites of layer 4 LMN projecting neurons (red). Apical dendrites of layer 4 pyramidal neurons avoid layer 3 where thalamic axons ramify. (**D**) Presubicular slice containing two layer 3 and two layer 4 neurons filled with biocytin (white) and GFP-expressing thalamic axons (green). Scale bar 100 µm. Inset, retrobeads (red) in the soma of a biocytin-filled LMN-projecting layer 4 neuron. Scale bar, 10 µm. (**E**) Layer 3 neurons are regular spiking and layer 4 neurons are burst firing, initially and at rebound, in response to current injection. Black trace, rheobase. (**F**) T-type Ca^{2+} channel

Figure 6 continued on next page

Figure 6 continued

blocker TTA-P2 (1 μM) suppressed burst firing in presubicular layer 4 neurons, while single action potentials were preserved. (**G**) Representative oEPSCs in layer 3 (left) and layer 4 (right) pyramidal cells, in response to stimulation of ATN (cerulean) or RSC (purple) inputs. (**H**) oEPSC latencies in layer 3 and layer 4 cells, for ATN inputs (left, cerulean), or RSC inputs (right, purple). Each dot is a cell. Same layer 4 cells are indicated by connecting lines to show the difference in latency for direct and indirect synaptic responses. (**I**) oEPSPs in layer 4 neurons in response to stimulation of ATN (cerulean) or RSC (purple) inputs in control and in the presence of TTX (1 μM) and 4-AP (100 μM). Dashed lines indicate the timing of the large disynaptic component of the responses (i, indirect), and the small monosynaptic response (d, direct), isolated in TTX-4AP. See also ***Figure 6—figure supplement 1***.

The online version of this article includes the following figure supplement(s) for figure 6:

Figure supplement 1. Apical dendrites of presubicular layer 4 neurons avoid the thalamorecipient layer 3.

Figure supplement 2. Electrophysiological passive and active intrinsic properties of layer 3 vs. layer 4 neurons.

of oEPSCs in layer 4 neurons were longer than for layer 3 (ATN layer 4, 6.2±0.6 ms, n=8, vs. layer 3, 2.4±0.2 ms, n=24; RSC layer 4, 5.6±0.4 ms, n=9, vs. layer 3, 2.9±0.2 ms, n=27; ***Figure 6H***), indicating possible polysynaptic excitation of layer 4 neurons. Bath application of TTX-4AP did not abolish oEPSPs entirely, leaving a low amplitude component with short, potentially monosynaptic latencies (latency ATN 3.9±0.6 ms, RSC 2.9±0.2 ms, n=5; ***Figure 6I***).

Comparison of the timing of synaptic events and firing (***Figure 7A***) showed that oEPSP onset in layer 4 neurons occurred after firing in the layer 3 neuron, following ATN afferent stimuli, in 4 out of 5 cell pairs. We also observed this sequence when RSC input was activated, in one tested pair. Depolarization of the layer 3 cell via the patch pipette, initiated firing, but EPSPs were not elicited in any simultaneously recorded layer 4 neuron (0 out of six cell pairs tested). These data suggest that excitation of layer 3 cells by ATN and likely by RSC afferents is transmitted to layer 4 neurons, even in the absence of direct evidence for mono-synaptic coupling between cell pairs.

In records from pairs of layer 3 and 4 neurons (n=3; ***Figure 7D and E***) layer 3 cells responded with precisely timed action potentials to low intensity stimulation of ATN afferents, while only very small oEPSPs were initiated in layer 4 neurons. Increasing the excitatory drive by stimulating RSC afferents elicited larger oEPSPs more reliably in layer 4 neurons. Higher intensity stimulation of both ATN and RSC axons could evoke bursts of action potentials, with the activation of an underlying Ca^{2+} current in layer 4 cells (***Figure 7E***). We hypothesize that increasing the activity of layer 3 neurons by strong (and non-specific) stimulation of ATN and RSC afferents is needed to induce discharges in layer 4 cells. We should also note that strong photostimulation of a single set of afferent fibers could initiate discharges in layer 4 pyramidal cells, as was shown in records from mice where only one afferent brain area, ATN or RSC, expressed an opsin (***Figure 7—figure supplement 1***).

Overall, it seems probable that layer 3 neurons relay activity projected by ATN and RSC inputs onto layer 4 pyramidal neurons. However, evidence on this point could be improved. In n=9 paired recordings, we did not detect functional synapses between layer 3 and layer 4 neurons. Anatomically, putative synaptic contacts between filled axons of layer 3 and dendrites of layer 4 cells were not evident (n=5 filled layer 4 cells; see also ***Peng et al., 2017***). We did find a possible synaptic connection between two neighboring L4 neurons in one case (***Figure 6—figure supplement 1D***), with a close apposition between axon and dendrite. Recurrent excitation may promote bursting in a positive feedback loop in layer 4 neurons, and NMDA receptor-related EPSP amplification favors burst firing (***Figure 7F***).

Neuromodulatory factors may help drive layer 4 cells to fire action potentials. As the presubiculum is rich in acetylcholinesterase (***Slomianka and Geneser, 1991***), we examined excitability changes in the presence of a broad cholinergic agonist. The application of Carbachol (10 μM; ***Figure 7G***) led to a depolarization of the recorded layer 4 neurons' membrane potential by 13±4 mV, with increased action potential firing during a positive step current injection, and from the baseline (***Figure 7Gi,ii***).

Discussion

Understanding the anchoring of HD signals to environmental landmarks provides a useful framework to ask how external information is integrated to revise and improve brain representations. Here, we show that thalamic ATN afferents signaling HD data and cortical RSC projections that carry landmark information converge on layer 3 pyramidal cells of the dorsal presubiculum. Independent optogenetic stimulation of these two glutamatergic afferents in slices was used to define mechanisms of their

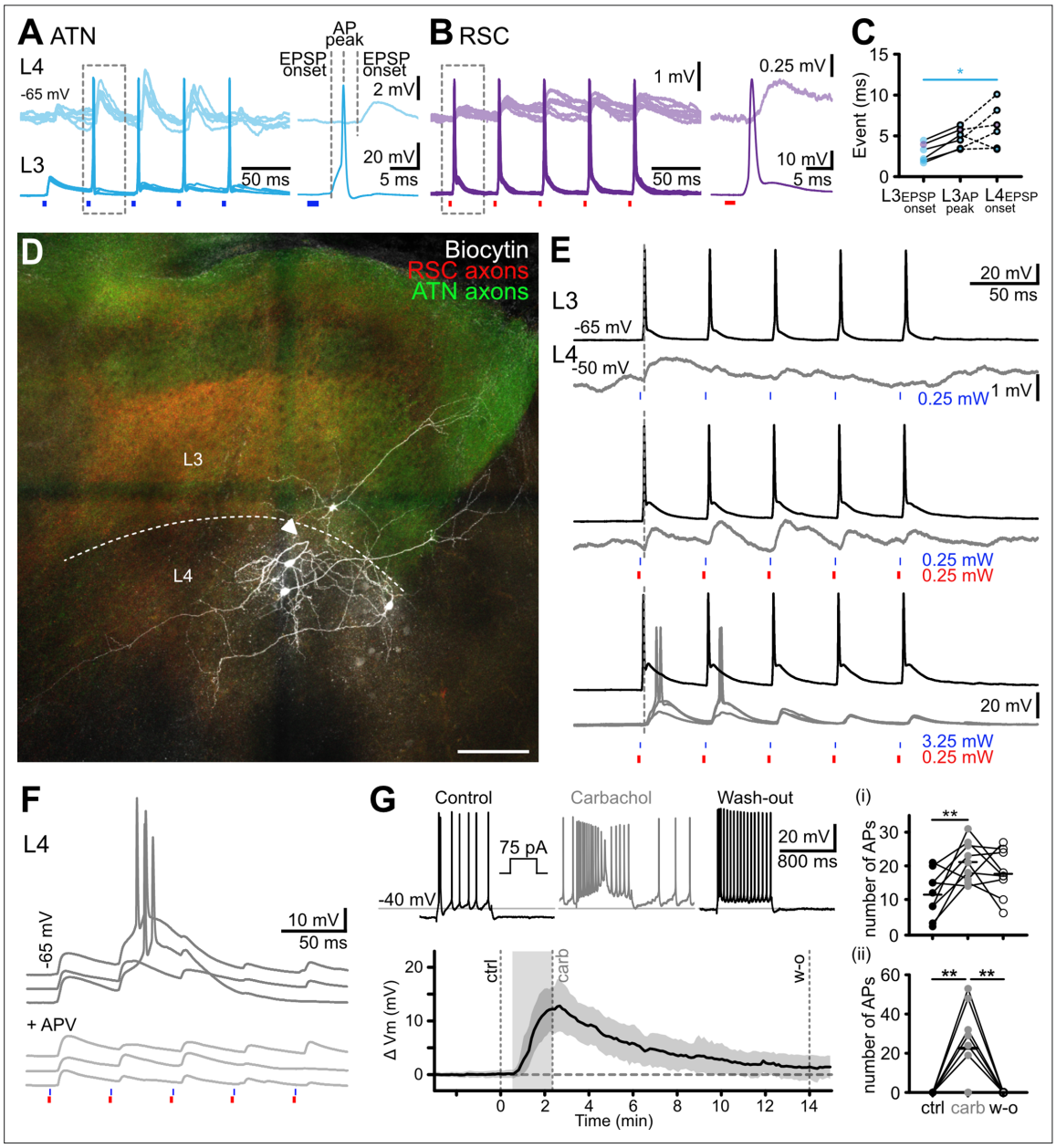

Figure 7. Cross-laminar activation of lateral mammillary nucleus (LMN)-projecting layer 4 bursting neurons. (**A**) Simultaneous records of a layer 4 and a layer 3 neuron during photostimulation of anterior thalamic nuclei (ATN) afferents. EPSP onset was delayed in the layer 4 neuron. Right panel, expanded view of the boxed area. (**B**) Simultaneous records of a layer 4 and a layer 3 neuron during photostimulation of RSC afferents. As in **A**, layer 4 neurons responded with a delay. Right panel, expanded view of the boxed area. (**C**) Latencies of synaptic activation indicated by the dotted lines in **A**, **B** (ATN stimulation, n=4 cells; RSC stimulation, n=1). EPSP onset and antero-posterior (AP) peak from layer 3 neurons (n=5). Dotted lines link to the EPSP onset in simultaneously recorded layer 4 neurons (n=5). $p<0.05$, Kruskal-Wallis multiple comparison test. (**D**) Biocytin-labeled layer 3 and layer 4 pyramidal neurons, in a presubicular slice containing thalamic (green) and retrosplenial (red) axons. The apical dendrite of one layer 4 neuron makes a U-turn (arrowhead), away from layer 3, where the thalamic axons ramify. The neighboring layer 4 neuron's apical dendrite crosses the thalamo-recipient layer 3 for a short distance before arborizing outside of ATN targeted area, towards the subiculum, on the right. Another biocytin-filled layer 4 neuron's dendrites extend toward the deep layers. Scale bar, 100 µm. (**E**) Simultaneous records from a layer 3 and a layer 4 cell to ATN input stimulation (top, 0.25 mW, blue light), ATN and RSC input stimulation (middle, 0.25 mW blue and 0.25 mW red light; light intensities compatible with independent photostimulation) or non-specific ATN and RSC input stimulation (bottom, 3.25 mW blue and 0.25 mW red light). ATN fibers expressed Chronos-GFP (green) and RSC fibers expressed Chrimson-tdTomato (red). (**F**) Top, oEPSPs and bursts of action potentials in a layer 4 neuron, evoked by dual

Figure 7 continued on next page

Figure 7 continued

wavelength stimulation of ATN and RSC afferents at 20 Hz. Amplifications of dual oEPSPs led to firing. Bottom, the NMDA receptor antagonist APV (100 µM) reduced EPSP amplification and prevented action potential firing. (**G**) Layer 4 bursting neurons are sensitive to the acetylcholine receptor agonist carbachol (10 µM). Action potential firing in response to step current injections in control (black), in the presence of carbachol (gray), and after wash-out (black). Bottom graph, membrane potential depolarization during a 2 min carbachol application. The number of action potentials increased during the depolarizing steps (i) and on the baseline (ii). See also ***Figure 7—figure supplement 1***.

The online version of this article includes the following figure supplement(s) for figure 7:

Figure supplement 1. Regular firing layer 3 vs. intrinsically bursting layer 4 neurons responded to high-intensity light stimulations of anterior thalamic nuclei (ATN) or RSC afferents.

Figure supplement 2. Schematic models for landmark anchoring of head direction (HD) signals.

integration in the presubiculum. Most layer 3 cells were innervated by both ATN and RSC fibers, sometimes close on the same dendritic branches, sometimes on different dendrites. Nearly coincident EPSPs (2–5 ms) induced independently by ATN and RSC afferents evoked non-linear membrane responses to trigger layer 3 cell firing, transmitted to the MEC. In a second processing step, layer 3 neurons also excite layer 4 pyramidal cells which receive little direct ATN and RSC innervation. These burst-firing neurons may project a distinct, di-synaptically mediated, visually updated HD signal to the LMN. Our data thus suggest that the dorsal presubiculum integrates HD and landmark signals producing two distinct output signals which are transmitted to different regions. Cholinergic modulation may facilitate responses to salient stimuli for flexible anchoring to landmarks.

Anatomical convergence of ATN and RSC projections in the dorsal presubiculum

Retrograde tracing in this study confirmed strong projections to the presubiculum from the ATN and the RSC to the presubiculum (***Figure 1***). Anterior thalamic fibers (***van Groen and Wyss, 1990c***; ***van Groen and Wyss, 1990a***; ***van Groen and Wyss, 1990b***; ***van Groen and Wyss, 1992***; ***Shibata and Honda, 2012***; ***Vogt and Miller, 1983***) ramify in and delimit the anatomical borders of the presubiculum (***Liu et al., 2021***; ***Simonnet et al., 2017***). HD signals from HD cells of the anterior thalamus project to the presubiculum (***Goodridge and Taube, 1997***) where they form synapses directly with layer 3 pyramidal cells (***Nassar et al., 2018***). The retrosplenial cortex was the most strongly labeled cortical region innervating the presubiculum. We detected retrogradely transported beads in cells of layers 2 and 5 of dysgranular RSC, and layer 5 of the granular RSC across its antero-posterior axis (***Sugar and Witter, 2016***).

We examined the anatomy and physiology of these two afferent systems to ask how visual landmark signals from the RSC are combined with HD signals relayed via the ATN. Anterograde fiber tracing, with an AAV5 construct expressing Chronos-GFP, confirmed that axons from both regions project to superficial layers of the dorsal presubiculum. No RSC projections were found in ventral PrS for injections in rostral RSC, as previously noted (***Jones and Witter, 2007***; ***Kononenko and Witter, 2012***). Both RSC and ATN innervated superficial presubicular layers 1 and 3, while sparing layer 2 containing somata of calbindin-positive neurons (***Figure 1K*** and ***Balsamo et al., 2022***). We detected microzones containing a high density of ATN-positive fibers, but no RSC fibers, in upper layer 3. It remains to be shown how these anatomical inhomogeneities may translate to functional modularity.

Pathway-specific functional connectivity onto PrS layer 3 neurons

Photostimulation of GFP-Chronos-expressing axons let us compare synaptic events initiated in layer 3 pyramidal cells by fibers from the ATN or the RSC in dorsal presubiculum slices (***Figure 2***). Both ATN and RSC afferents formed mono-synaptic glutamatergic connections with components mediated by NMDA and AMPA receptors. The amplitudes of synaptic currents varied between neurons, with an overall similar amplitude distribution for ATN and RSC stimulation. This may be due to variable expression levels (***Hooks et al., 2015***), or may imply variations in coupling weights across cells. ATN and RSC fiber-mediated EPSCs depressed during repetitive activation at 20 Hz. EPSPs induced firing early during repetitive stimulation. RSC inputs tended to produce more sustained EPSP dynamics and slower rise times than ATN afferents for low-intensity stimulation. ATN synapses with presubicular pyramidal cells resemble those made by thalamic afferents in the somatosensory cortex - high release

with depressing dynamics (***Gil et al., 1999***), possibly due to presynaptic expression of VGLut2 (***Liu et al., 2021***).

Dual-wavelength optogenetic stimulation was used for independent activation of intermingled afferents expressing blue-light-sensitive Chronos in ATN fibers and red-shifted Chrimson in RSC fibers (***Klapoetke et al., 2014***). Precautions were taken to avoid cross-stimulation since all channelrhodopsin variants are somewhat sensitive to blue light. With the fast, sensitive opsin Chronos expressed in ATN fibers, synaptic events were induced by very short (0.5 ms), low intensity, 0.25 mW, stimuli. For RSC fibers expressing Chrimson, using light stimuli of duration 2 ms, adjusting intensity up to 2 mW initiated synaptic events of comparable amplitude. Calibration experiments (***Figure 3—figure supplement 1***) provided strong evidence for the independence of responses. While Chrimson has slower dynamics than Chronos (***Klapoetke et al., 2014***), synaptic events induced by stimulating either opsin were similar, as we showed by swapping the two opsin variants injected in ATN and RSC fibers, respectively (***Figure 4***).

This dual opsin approach permitted independent stimulation with blue and red light pulses. Most (76%) recorded layer 3 neurons generated synaptic events in response to stimulation of both ATN and RSC fibers providing a substrate for integration of landmark information from the RSC with thalamic HD signals. Layer 3 cell firing was most effectively triggered by nearly coincident inputs (–2 to +5 ms separation, ***Figure 4I and J***). This is of interest since HD representations in the AD and RSC are highly coherent (***Fallahnezhad et al., 2023***), with short intervals between spikes in these two regions (<5 ms; ***van der Goes et al., 2024***). Converging inputs from thalamic and retrosplenial axons can, therefore, excite common postsynaptic presubicular layer 3 neurons with very short delays, such that coincidence detection by these cells will tend to enhance HD signals. Response dynamics to combined stimulation of both inputs at 20 Hz were maintained or facilitating, in contrast to the depressing dynamics of repetitive stimulation of one set of afferent fibers. Combined and temporally precise inputs from ATN and RSC may thus help maintain HD signaling during immobility. Our findings may well underlie the recent in vivo observation by ***Siegenthaler et al., 2025*** that visual objects refine HD coding, and that presubicular HD cells whose preferred firing direction corresponds to a visual landmark respond with higher firing rates.

Nonlinear signal integration in layer 3 thalamo-recipient neurons and physiological significance for HD-to-landmark anchoring

Convergence of ATN and RSC axons onto single layer 3 pyramidal cells provides the anatomical basis of synaptic integration. Putative synaptic contacts from both afferent fiber systems were found on the basal dendrites of pyramidal cells (***Figure 3***), sometimes on the same branch. Photostimulation centered on the soma of recorded neurons predominantly activated synapses on basal dendrites. Supralinear summation could result from local spike-generating mechanisms if the activated synapses were located on a same dendritic branch (***Makarov et al., 2023***; ***Poirazi and Papoutsi, 2020***; ***Polsky et al., 2004***). Clustered synapses could also guide the formation of new spines and synapses during integration of landmark information in the HD signal. Learning might bind new inputs into functional synaptic clusters (***Hedrick et al., 2022***). Our small sample of layer 3 pyramidal cells suggests that both ATN and RSC axons target basal dendrites, and more RSC than ATN axons contact apical dendrites (***Figure 3***). Tests on the effects of precise, near-coincident activation of basal and apical synapses could be revealing but were not technically possible in this study. Distinct dendritic inputs to layer 3 cells may improve spatial perception (***Takahashi et al., 2016***) enhancing HD signal quality by integration with landmark information.

Our data show that EPSPs elicited by nearly coincident ATN and RSC inputs which exceed a threshold are amplified by NMDA receptor activation and voltage-gated inward dendritic currents (***Figure 5***; ***Fricker et al., 2009***). From a small sample of cells, it appears that EPSP amplification may be facilitated by a reduction in synaptic inhibition (n=3; ***Figure 5***), indicating that disinhibition may be permissive for supralinearity and gate firing by dynamic modulation of the balance between inhibition and excitation (***Milstein et al., 2015***). VIP-expressing interneurons, which are excited by cholinergic modulation could provide such disinhibition of the presubicular microcircuit (***Porter et al., 1999***; ***Slomianka and Geneser, 1991***). The excitation-inhibition balance in pyramidal cells may become tipped towards excitation in the case of coincident, co-tuned thalamic and retrosplenial input. A 'when-to-learn' signal for HD updating in the presubiculum might function analogously to

the promotion by dopamine of associations between sensory cues and head direction cells in the fly (***Fisher et al., 2022***). It is, however, unclear whether LTP-type learning takes place in the mammalian head direction circuit. Presubicular layer 3 cells do not express the GluR1 subunit of AMPA receptors (***Martin et al., 1993***; ***Ishihara and Fukuda, 2016***) that is critical for LTP expression (***Boehm et al., 2006***). The absence of GluR1 might indicate that the thalamo-presubicular synapses in layer 3 function without classical long-term synaptic plasticity. Matching directional with visual landmark information based on temporal coincidence may be sufficient. Algorithms for dynamic control of cognitive maps without synaptic plasticity (***Whittington et al., 2025*** Neuron) propose that working memory is stored in neural attractor activity and updated by recurrent connections, which might generalize to the HD system.

Layer 3 pyramidal cells may be described as multi-compartmental computational devices (***Häusser and Mel, 2003***; ***Mel, 1993***; ***Poirazi et al., 2003***; ***Spruston, 2008***) which integrate HD and landmark information. ATN axons drive presubicular HD neurons (***Peyrache et al., 2015***) and RSC mixed selectivity neurons contribute visual landmark information and allocentric spatial references (***Jacob et al., 2017***; ***Mitchell et al., 2018***; ***Vann et al., 2009***). NMDA-mediated dendritic spikes enhance tuning selectivity in visual cortex (***Smith et al., 2013***; ***Wilson et al., 2016***) and barrel cortex (***Lavzin et al., 2012***). Dendritic events in Layer 3 PrS cells may enable binding of visual landmarks with HD tuning. It is tempting to speculate that nonlinear synaptic integration and inhibitory gating may be involved in flexibly updating the allocentric direction of HD cells based on the integration of visual landmark information to the current HD signal (***Siegenthaler et al., 2025***). In the primary sensory cortex, nonlinearities act to increase perceptual threshold of sensory information (***Takahashi et al., 2016***; ***Takahashi et al., 2020***). The attractor network in the PrS could thus be either stabilized or flexibly reset to external spatial cues.

Alternative models of HD-to-landmark anchoring have focused on the RSC, which also treats HD and landmark signals (***Page and Jeffery, 2018***; ***Yan et al., 2021***). Possibly, the RSC registers a direction to a landmark rather than comparing it with the current HD (***Sit and Goard, 2023***). The integrated information would then reach PrS, which, in contrast to RSC, is uniquely positioned to update the signal in the LMN (***Yoder and Taube, 2011***).

What is the neuronal and circuit mechanism for integrating the 'right' set of landmarks to anchor the HD signal? In our slice work, we are blind to the exact nature of the signal that is carried by ATN and RSC axons. Critical missing information to understand the logic of HD-to-landmark anchoring also includes the degree of divergence and convergence of connections from a single thalamic or retrosplenial neuron. Do HD-tuned inputs from the thalamus converge on similarly tuned HD neurons only? Is divergence greater for the retrosplenial inputs? If so, thalamic input might pre-select a range of HD neurons, and converging RSC input might narrow down the precise HD neurons that become active (***Figure 7—figure supplement 2***). In the future, activity-dependent labeling strategies might help to tie together information on the tuning of pre-synaptic neurons and their convergence or divergence onto functionally defined postsynaptic target cells.

Functional significance of two-layer processing preceding projection to LMN

Burst-firing layer 4 PrS cells project a distinct version of HD-landmark signals to the LMN. The dendrites of these LMN projecting neurons overlap little with direct ATN and RSC inputs granting partial isolation from direct excitation, and permitting a second level of integration of information from layer 3 neurons. Layer 3 axons may innervate layer 4 neurons basal dendrites, which may be driven to fire by sufficiently strong excitatory inputs from layer 3, especially if combined with cholinergic activation.

There are advantages to segregating the integration of converging input signals from the updating signal across layers. Segregation permits both a fast transmission of an integrated signal to the medial entorhinal cortex and the conditional transmission of an updating signal mediated by burst firing to upstream HD circuit elements. The synaptic threshold implicit in this two-stage system permits a gated updating. Functionally, layer 4 neurons are uniquely positioned to update the HD signal in the LMN with visual landmark information (***Yoder et al., 2015***). In this way, cell-type specific cholinergic facilitation may help idiothetic cue-based navigation (***Yoder et al., 2017***). These cellular and synaptic circuit data support and expand the findings of ***Yoder et al., 2015***; ***Yoder et al., 2017***. They clarify how the thalamic HD signal integrated with visual landmark

information is relayed to the grid cell system in the medial entorhinal cortex and to the lateral mammillary nuclei.

Limitations

Burst firing may play a role in learning in hierarchical circuits (***Friedenberger et al., 2023***; ***Payeur et al., 2021***). In the HD circuit, landmark information contained in bursts might reset or anchor the HD attractor in the LMN and beyond. The effects of burst firing signals transmitted to the LMN remain to be assessed. Potentially, HD signals may be updated with visual signals at several sites, including the PrS, but PrS uniquely provides a feedback projection to the lateral mammillary nucleus. Further work on layer 3 to layer 4 transmission is warranted, and the link to spatial perception and behavioral updating needs to be strengthened.

Methods

Key resources table

Reagent type (species) or resource	Designation	Source or reference	Identifiers	Additional information
Other	AAV5.Syn.Chronos-GFP.WPRE.bGH	Addgene	RRID:Addgene_59170	59,170P
Other	AAV5.Syn.ChrimsonR-tdTomato. WPRE.bGH	Addgene	RRID:Addgene_59171	59,171P
Other	pAAVretro-CAG-tdTomato	Addgene	RRID:Addgene_59462	59,462P
Chemical compound, drug	Retrobeads	Lumafluor	Red Retrobeads	
Peptide, recombinant protein	Streptavidin, Alexa Fluor 647 Conjugate	Thermo Fisher Scientific	S32357	
Chemical compound, drug	TTX, tetrodotoxin citrate	Tocris	PubChemID:16759596	1069
Chemical compound, drug	4-Aminopyridine	Sigma-Aldrich	PubChemID:24891285	A78403
Chemical compound, drug	D-APV	Tocris	PubChemID:135342	0106
Chemical compound, drug	NBQX	Abcam	PubChemID:3272523	Ab120046
Chemical compound, drug	Gabazine	Tocris	PubChemID:107895	SR 95531
Chemical compound, drug	Carbachol, carbamoylcholine chloride	Sigma	PubChemID:24277829	C4382
Strain, strain background	C57BL/6J	Janvier Labs	https://janvier-labs.com/en/fiche_produit/2_c57bl-6j_mouse/	
Strain, strain background	B6.Cg-*Gt(ROSA)26Sor*$^{tm14(CAG-tdTomato)Hze}$/J	Jackson	RRID:IMSR_JAX:007914	007914
Software, algorithm	MATLAB	MathWorks	RRID:SCR_001622	
Software, algorithm	pClamp	Molecular devices	RRID:SCR_011323	
Software, algorithm	AxoGraphX	Axograph	RRID:SCR_014284	
Other	Prolong Gold antifade mountant	Invitrogen	RRID:SCR_015961	P36930

Animals

Experiments were performed on male and female wild-type and transgenic (Ai14 reporter line - Jax n007914) C57BL/6 mice of age 35–70 days, housed on a 12 hr light/dark cycle with food and water available ad libitum. Animal care and use conformed to the European Community Council Directive (2010/63/EU) and French law (87/848). Our study was approved by the local ethics committee (CEEA - 34) and the French Ministry for Research 01025.02.

Viral vectors and beads

Projecting neurons were labeled with retrograde fluorescent tracers (Retrobeads, Lumafluor, and AAV2retro-CAG-tdTomato, Addgene 59,462P). Fluorescent beads were stored at 4°C before use. Channelrhodopsin expression was achieved by injecting adeno-associated viral constructs. AAV5.Syn.Chronos-GFP.WPRE.bGH (AAV5-Chronos, Penn Vector Core, Addgene 59,170P) was used to induce neuronal expression of the blue light-induced channelrhodopsin Chronos fused to the GFP marker and under the control of the Synapsin promoter. AAV5.Syn.ChrimsonR-tdTomato.WPRE.bGH (AAV5-Chrimson, Penn Vector Core, Addgene 59,171P) induced neuronal expression of the red light-gated channelrhodopsin Chrimson fused to the tdTomato marker, under the control of the Synapsin promoter. Viral vectors were stored at –80°C before use.

Stereotaxic surgery

Mice at ages of 4–5 weeks were anesthetized by intraperitoneal (i.p.) injection of a mixture of ketamine hydrochloride and xylazine (100 and 15 mg/kg, respectively, in NaCl 0.9%). They were placed in a stereotaxic frame for injections. Fluorescent beads for retrograde tracing were injected (300–500 nl) into the PrS at the coordinates: –4.06 antero-posterior (AP), 2.00 medio-lateral (ML) and –2.15 mm dorso-ventral (DV), and into the LMN (–2.8 AP, 0.75 ML, –5.35 DV) with respect to the bregma. Note, due to the small size of LMN, some overflow to the medial mammillary nucleus (MMN) may have occurred.

Viral injections were performed unilaterally (***Mathon et al., 2015***; ***Richevaux et al., 2019***) at the coordinates –0.82 AP, 0.75 ML, and –3.2 mm DV for the ADN, and at –2.1 to –2.15 AP, 0.65 ML, and –0.65 mm DV for the RSC. Volumes of 200–250 nl were injected with a 10 µL Hamilton syringe equipped with 33 ga needle over a time of 10 min. The needle was slowly removed after a delay of 10 min to avoid leakage from the injection site. The best expression of AAV5 serotypes was achieved after 3–4 weeks.

Tissue fixation and slicing for retrograde tracing

Brains were removed for anatomy at 4 days after retrobead injection. Mice were anesthetized by i.p. injection of the ketamine/xylazine mixture. An intracardiac perfusion with 0.1 M PBS was followed by perfusion with 4% paraformaldehyde. Brains were stored overnight in paraformaldehyde at 4°C and then washed in PBS. Coronal or horizontal sections were cut at 100 µm with a vibratome and stored in sucrose at 4°C.

Preparation of brain slices for physiology

Slices of the temporal lobe were prepared 3–4 weeks after injection of AAV5 viral constructions. Mice were anesthetized by i.p. injection of the ketamine/xylazine mixture. They were then perfused intracardially with a cutting solution containing (in mM): 125 NaCl, 25 sucrose, 2.5 KCl, 25 $NaHCO_3$, 1.25 NaH_2PO_4, 2.5 D-glucose, 0.1 $CaCl_2$, 7 $MgCl_2$, cooled to 4°C, and oxygenated with a 5% CO_2/95% O_2. The brain was removed and a vibratome was used to cut horizontal slices at 300 µm in the same solution. Slices were stored for 15 min at 34°C in an ACSF containing (in mM): 124 NaCl, 2.5 KCl, 26 $NaHCO_3$, 1 NaH_2PO_4, 2 $CaCl_2$, 2 $MgCl_2$, and 11 D-glucose, bubbled with 5% CO_2/95% O_2. They were then kept in the same solution at room temperature until recording.

Whole-cell patch-clamp recordings

Slices were transferred to a recording chamber perfused with oxygenated, warmed (~32°C) ACSF mounted on an epifluorescence microscope. Patch-clamp records were made from neurons with borosilicate glass pipettes of external diameter 1.5 mm (Clark Capillary Glass, Harvard Apparatus) pulled with a Brown-Flaming electrode puller (Sutter Instruments). Electrodes, filled with a potassium-gluconate-based solution containing (in mM): 135 K-gluconate, 1.2 KCl, 10 HEPES, 0.2 EGTA, 2 $MgCl_2$, 4 MgATP, 0.4 Tris-GTP, and 10 Na_2-phosphocreatine, had a resistance of 4–8 MΩ. An alternative, cesium-gluconate-based solution facilitated neuronal depolarization to examine synaptic inhibition, in ***Figure 5***. It contained (in mM): 125 Cs-gluconate, 10 HEPES, 0.2 EGTA, 2 $MgCl_2$, 4 MgATP, 0.4 Tris-GTP, and 10 Na_2-Phosphocreatine, together with 5 mM QX-314 to block Na^+ channels. Pipette solutions also contained 3 mM biocytin to reveal morphology after recording. They were adjusted to pH 7.3 and osmolarity 290 mOsm. Whole-cell, patch-clamp signals were filtered at 3 kHz, amplified

with a MultiClamp 700B amplifier and acquired with pCLAMP software (Molecular Devices). In a subset of experiments, the following drugs were used to modulate the responses to optogenetic stimulations; the presence of these drugs is indicated in the figure and figure legend, whenever applicable. Monosynaptic excitation induced by optical stimulation was tested in the presence of TTX (1 µM) and 4-AP (100 µM). NBQX (10 µM) and APV (100 µM) were used to block AMPA and NMDA receptors, respectively. Gabazine (10 µM) was used to block $GABA_A$ receptors. Carbachol (10 µM) was used to activate acetylcholine receptors. All drugs were bath applied.

Optical stimulation

LED illumination (Cairn Research, OptoLED) was used to visualize the fluorescent reporters GFP and tdTomato, and to stimulate opsin-expressing axons, using a 470 nm LED for Chronos and a 627 nm LED for Chrimson. Illuminated spots had a diameter of 200 µm with a 60x objective and were centered on the recorded cell soma. Photostimulation thus covered most of the basilar dendrites of layer 3 pyramidal neurons (typical distance from tip of apical to tip of basilar dendrite <400 µm). Stimuli consisted of light pulses of 0.5–5 ms duration, repeated 5–10 times at 20 Hz.

A multiband filter allowed simultaneous stimulation by blue and red LEDs of axons containing Chronos and Chrimson (***Simonnet et al., 2021***). Stimulus power intensity (set in mV) was calibrated as light intensity. The response probability of layer 3 cells was calibrated to blue or red illumination of ATN or RSC afferents expressing Chronos or Chrimson to avoid stimulus overlap (***Figure 3—figure supplement 1***). Chronos was targeted to the ATN and Chrimson to the RSC after testing the reverse configuration. Projections from the thalamus are larger and Chronos is more sensitive to blue light, so this configuration assured reliable activation of thalamic fibers at minimal blue-light intensities. For experiments investigating the integration of ATN and RSC inputs, we aimed to give similar weights to both inputs: Chrimson-expressing fibers were stimulated with light of intensity adjusted to initiate optically evoked excitatory postsynaptic potentials (oEPSPs) of amplitude similar to those induced by blue light Chronos-fiber stimuli.

Data analysis

ATN and RSC projections to the PrS were analyzed from Chronos and Chrimson expression, using the ImageJ Plot Profile plug-in to quantitate normalized plot profiles (2000 pixels) of horizontal presubicular sections. Dorso-ventral differences were derived by dividing differences in labeling intensity between the PrS and the dentate gyrus (DG) molecular layer by DG intensity in slices from five dorso-ventral PrS levels. Values from all animals were averaged and then normalized.

Cells were qualified as synaptically 'connected' when they responded to light stimulation of afferent axons with a delay <8 ms. Slices with very low or absent expression of the fluorescent reporter were excluded. Cells were qualified as 'non-connected' synaptically if they did not respond to light stimulation, but at least one neighboring cell in the same slice did.

Intrinsic neuronal properties were analyzed with custom MATLAB routines to derive 15 electrophysiological parameters (***Huang et al., 2017***). Parameters were standardized and unsupervised cluster analysis performed with MATLAB was used to compare different neurons (***Huang et al., 2017***; ***Simonnet et al., 2013***).

Axograph was used to analyze responses to optical stimulation of ATN and RSC fibers. Layer 3 neurons were recorded at potentials near –65 mV. Responses to light were averaged from 10 stimulus trains at 20 Hz. Amplitudes and latencies of initial light-evoked EPSCs, of latency shorter than 10 ms, were quantified from voltage-clamp records. Latency was measured from stimulus onset to 10% of the peak amplitude of the first optically induced EPSC. Amplitude was measured with respect to the pre-stimulus baseline. Paired-pulse ratio (PPR) was defined as the ratio of the amplitude of the second to the first EPSC and 10/1 ratio as that between the 10th and the first EPSC, in responses to 20 Hz stimulations. Spike probability was counted over 5–10 trials per cell and then averaged over all cells. EPSPs induced by dual-wavelength stimulation were analyzed using Axograph and a custom-made software. Events evoked by light stimuli were detected in a window of 1–10 ms after stimulation. EPSP amplitude and integrated area were calculated over 50 ms after stimulation. Baseline suppression was applied using an average of membrane potential during 50 ms before stimulation. The summation of ATN and RSC-evoked EPSCs in layer 3 neurons was determined from the amplitude and integral of

averaged events. Summation was considered to be supralinear if values were more than 10% higher than a linear addition, linear for values within ±10%, and sublinear for values more than 10% lower.

Biocytin revelation and morphology

Recorded neurons were filled with biocytin to visualize their morphology and location. Slices were fixed in 4% PFA in 0.1 M PBS at 4°C overnight, washed three times in 0.1 PBS and cryoprotected in 30% sucrose. Cell membranes were permeabilized by three freeze-thaw cycles over dry ice and rinsed in PBS. Slices were agitated in a saturation buffer (2% milk, 1% Triton X-100 in 0.1 M PBS) for 2 hr at room temperature. They were then incubated with Streptavidin-Cy5 conjugate (1:500) and DAPI (1:1000) overnight at 4°C. Sections were washed 3 times with PBS and mounted on coverslips with ProLong Gold antifade mountant. For anatomical study, they were mounted in Mowiol medium. Cell, bead, and virus expression were visualized with an epifluorescence microscope. Higher resolution of morphology was obtained with confocal microscopy. Cell morphologies were reconstructed using IMARIS.

Quantification and statistical analysis

Data was analyzed with AxoGraphX and custom-written software (MATLAB, The MathWorks). Results are given as mean ± SEM. Statistical analysis was performed with Prism (GraphPad Software). The Mann-Whitney unpaired t-test was used to compare two groups. The Wilcoxon or Kruskal-Wallis test was used to compare paired groups. Evolution of parameters evoked by optical stimulation (current or potential amplitudes, spike probability) was analyzed with Friedman's test followed by multiple comparison Dunn's test. Šidák's multiple comparison test was also used to compare linear and observed responses to ATN and RSC stimulations. Significance levels are given as p-values.

Acknowledgements

This work is supported by the Centre National de la Recherche Scientifique and the Université Paris Cité. DF received funding from the Agence Nationale de la Recherche (ANR-DFG Program, ANR-18-CE92-0051 BURST), from the ERA-NET NEURON Program (ANR-20-NEUR-0005 VELOSO), and the FLAG-ERA HBP Program (ANR-21-HBPR-0002 VIPattract). This work has benefited from support by the BioMedTech Facilities at Université Paris Cité (Institut National de la Santé et de la Recherche Médicale Unité S36/Unité Mixte de Service 2009). We thank Dr. Li-Wen Huang for help with analysis routines. We thank Dr. Kate Jeffery and the Royal Society COST-share program, technical assistance from Fabrice Licata and Dr. Abdelali Jalil from the UPC Microscopy platform, Claire Lovo from ICM Quant, Dr. Boris Lamotte d'Incamps, and Dr. Richard Miles for helpful comments on the manuscript.

Additional information

Funding

Funder	Grant reference number	Author
Agence Nationale de la Recherche	ANR-18-CE92-0051	Desdemona Fricker
ERA-Net NEURON	ANR-20-NEUR-0005	Desdemona Fricker
FLAG-ERA HBP	ANR-21-HBPR-0002	Desdemona Fricker
Ministère de l'Enseignement Supérieur et de la Recherche	PhD fellowship	Louis Richevaux

The funders had no role in study design, data collection and interpretation, or the decision to submit the work for publication.

Author contributions

Louis Richevaux, Conceptualization, Data curation, Formal analysis, Investigation, Visualization, Methodology, Writing – original draft, Writing – review and editing; Dongkyun Lim, Léa Dias Rodrigues,

Constanze Mauthe, Nathalie Sol-Foulon, Investigation, Methodology; Mérie Nassar, Formal analysis, Investigation, Methodology; Ivan Cohen, Software, Methodology; Desdemona Fricker, Conceptualization, Supervision, Funding acquisition, Validation, Investigation, Methodology, Writing – original draft, Project administration, Writing – review and editing

Author ORCIDs
Louis Richevaux https://orcid.org/0000-0001-7837-3489
Dongkyun Lim https://orcid.org/0009-0004-8756-6505
Desdemona Fricker https://orcid.org/0000-0001-7328-9480

Ethics
Animal care and use conformed to the European Community Council Directive (2010/63/EU) and French law (87/848). Our study was approved by the local ethics committee (CEEA - 34) and the French Ministry for Research 01025.02.

Peer review material
Reviewer #1 (Public review): https://doi.org/10.7554/eLife.92443.3.sa1
Reviewer #2 (Public review): https://doi.org/10.7554/eLife.92443.3.sa2
Reviewer #3 (Public review): https://doi.org/10.7554/eLife.92443.3.sa3
Author response https://doi.org/10.7554/eLife.92443.3.sa4

Additional files

Supplementary files
MDAR checklist

Data availability
Data are stored on local servers at the Université Paris Cité and available on https://doi.org/10.5061/dryad.9ghx3ffxd. The Matlab code for analysis of intrinsic properties is available at https://github.com/schoki0710/Intrinsic_Properties (copy archived at ***schoki0710, 2025***).

The following dataset was generated:

Author(s)	Year	Dataset title	Dataset URL	Database and Identifier
Richevaux L, Lim D, Nassar M, Dias Rodrigues L, Mauthe C, Cohen I, Sol-Foulon N, Fricker D	2025	Projection-specific integration of convergent thalamic and retrosplenial signals in the presubicular head direction cortex	https://doi.org/10.5061/dryad.9ghx3ffxd	Dryad Digital Repository, 10.5061/dryad.9ghx3ffxd

References

Alexander AS, Nitz DA. 2015. Retrosplenial cortex maps the conjunction of internal and external spaces. *Nature Neuroscience* **18**:1143–1151. DOI: https://doi.org/10.1038/nn.4058, PMID: 26147532

Auger SD, Mullally SL, Maguire EA. 2012. Retrosplenial cortex codes for permanent landmarks. *PLOS ONE* **7**:e43620. DOI: https://doi.org/10.1371/journal.pone.0043620, PMID: 22912894

Balsamo G, Blanco-Hernández E, Liang F, Naumann RK, Coletta S, Burgalossi A, Preston-Ferrer P. 2022. Modular microcircuit organization of the presubicular head-direction map. *Cell Reports* **39**:110684. DOI: https://doi.org/10.1016/j.celrep.2022.110684, PMID: 35417686

Blair HT, Sharp PE. 1995. Anticipatory head direction signals in anterior thalamus: evidence for a thalamocortical circuit that integrates angular head motion to compute head direction. *The Journal of Neuroscience* **15**:6260–6270. DOI: https://doi.org/10.1523/JNEUROSCI.15-09-06260.1995, PMID: 7666208

Boccara CN, Sargolini F, Thoresen VH, Solstad T, Witter MP, Moser EI, Moser MB. 2010. Grid cells in pre- and parasubiculum. *Nature Neuroscience* **13**:987–994. DOI: https://doi.org/10.1038/nn.2602, PMID: 20657591

Boehm J, Kang MG, Johnson RC, Esteban J, Huganir RL, Malinow R. 2006. Synaptic incorporation of AMPA receptors during LTP is controlled by a PKC phosphorylation site on GluR1. *Neuron* **51**:213–225. DOI: https://doi.org/10.1016/j.neuron.2006.06.013, PMID: 16846856

Calton JL, Stackman RW, Goodridge JP, Archey WB, Dudchenko PA, Taube JS. 2003. Hippocampal place cell instability after lesions of the head direction cell network. *The Journal of Neuroscience* **23**:9719–9731. DOI: https://doi.org/10.1523/JNEUROSCI.23-30-09719.2003, PMID: 14585999

4.2 Presubicular VIP expressing interneurons receive facilitating excitation from anterior thalamus

The PrS contains diverse types of interneurons that contribute to the temporal precision, sensitivity, and selectivity of HD signals. Previous work by Nassar et al. (2015) and Nassar et al. (2018) has elucidated the functional identity of PV and SST-expressing interneurons in the region. However, the properties of Vasoactive intestinal peptide (VIP)-expressing interneurons had remained unclear. In this study, presubicular VIP interneurons were studied to identify their intrinsic electrophysiological properties, morphology, and functional connectivity with anterior thalamic inputs. As part of this project, I contributed to the patch-clamp data acquisition and gained hands-on expertise through close collaboration with experienced members of the laboratory.

In the first part of this project, the specificity of the transgenic VIP-Cre::tdTomato mouse line was validated. The genetically labelled VIP-expressing cells were compared to VIP-positive cells revealed by post hoc immunostaining with an anti-VIP antibody. Quantitative analysis showed no significant difference between the two labelling methods, confirming the fidelity of the genetic labelling. Following this validation, the transgenic line was used with confidence for subsequent experiments throughout the study.

Next, the intrinsic electrophysiological properties of presubicular VIP interneurons were examined. Unsupervised cluster analysis based on these properties revealed three distinct subgroups. Cluster 1 VIP interneurons were highly excitable, showing high input resistance. Cluster 2 showed broader action potentials, reduced spike amplitudes, and lower maximum depolarisation rates. Cluster 3 exhibited relatively low input resistance and shared number of properties with layer III pyramidal neurons. Morphological reconstruction showed that the axons of VIP interneurons were predominantly confined to layer III, indicating that their primary targets are likely located in this layer.

Lastly, optogenetic activation of ATN fibers evoked postsynaptic currents in VIP interneurons. These were monosynaptic, confirmed by their short latency and pharmacological experiments. These responses displayed frequency-dependent facilitation, with increased success rates and spiking probabilities during repetitive stimulation, particularly at higher frequencies (30-70 Hz). Additionally, stimulation could evoke both excitatory and inhibitory postsynaptic potentials, suggesting VIP interneurons are embedded in both excitatory and disinhibitory motifs.

The results are interpreted in the context of presubicular microcircuits. The study proposes that VIP may become activated during the mismatch between the internal prediction of the HD signal and visual context-based input from the RSC. Also, by interacting with SST interneurons, VIP interneurons may support the fine-tuning of HD representation through a transient weakening of the attractor network. Furthermore, the heterogeneity observed in their firing properties and connectivity patterns suggests a capacity to modulate local circuit dynamics with precision. Overall, this study provides the first systematic analysis of presubicular PrS interneurons within the HD system.

Neuroscience 578 (2025) 91–104

Contents lists available at ScienceDirect

Neuroscience

journal homepage: www.elsevier.com/locate/nsc

Presubicular VIP expressing interneurons receive facilitating excitation from anterior thalamus

Mérie Nassar [1,*], Louis Richevaux [1], Dongkyun Lim, Dario Tayupo, Erwan Martin, Desdemona Fricker [*]

Université Paris Cité, CNRS UMR 8002, Integrative Neuroscience and Cognition Center, F-75006 Paris, France

ARTICLE INFO

Keywords:
Interneurons
Patch clamp
Electrophysiology
Presubiculum
Postsubiculum
Head direction

ABSTRACT

The presubiculum is part of the parahippocampal cortex and plays a fundamental role for orientation in space. Many principal neurons of the presubiculum signal head direction, and show persistent firing when the head of an animal is oriented in a specific preferred direction. GABAergic neurons of the presubiculum control the timing, sensitivity and selectivity of head directional signals from the anterior thalamic nuclei. However, the role of vasoactive intestinal peptide (VIP) expressing interneurons in the presubicular microcircuit has not yet been addressed. Here, we examined the intrinsic properties of VIP interneurons as well as their input connectivity following photostimulation of anterior thalamic axons. We show that presubicular VIP interneurons are more densely distributed in superficial than in deep layers. They are highly excitable. Three groups emerged from the unsupervised cluster analysis of their electrophysiological properties. We demonstrate a frequency dependent recruitment of VIP cells by thalamic afferences and facilitating synaptic input dynamics. Our data provide initial insight into the contribution of VIP interneurons for the integration of thalamic head direction information in the presubiculum.

Introduction

The presubicular cortex, located between the hippocampus and the medial entorhinal cortex, plays a crucial role in spatial navigation. Most presubicular neurons signal head direction (HD) (Taube et al., 1990; Boccara et al., 2010; Preston-Ferrer et al., 2016). They fire persistently when the head of an animal is oriented in a specific direction, and they transmit directional information to the medial entorhinal cortex (McNaughton et al., 2006; Langston et al., 2010, Winter et al., 2015, Tukker et al., 2015, Preston-Ferrer et al., 2016).

Recent work has revealed how thalamic HD signals converge with retrosplenial inputs in the presubicular cortex (Richevaux et al., 2023), and the properties of the local microcircuit (Duszkiewicz et al., 2024; Nassar et al., 2015; Peng et al., 2017; Simonnet et al., 2013). Thalamic inputs differentially affect presubicular neurons: layer 3 pyramidal neurons and fast-spiking parvalbumin-expressing interneurons are directly and monosynaptically activated, with strong initial responses, whereas somatostatin-expressing interneurons are indirectly excited, with activity dependent, facilitating dynamics. Feedforward inhibition is largely mediated by parvalbumin interneurons, and may enforce temporally precise head direction tuning during head turns (Nassar et al., 2018). In contrast, feedback and lateral inhibition mediated by Martinotti type somatostatin expressing interneurons onto principal neurons may help sustain firing in head direction cells (Simonnet et al., 2017; Simonnet and Fricker, 2018). In addition to interneurons expressing parvalbumin (PV), somatostatin (SST), another major subtype of GABAergic neurons expresses vasoactive intestinal peptide (VIP) (Kepecs and Fishell, 2016). The intrinsic properties and the functional role of presubicular VIP interneurons have not yet been investigated.

VIP interneurons form a population that is largely non-overlapping with PV and SST interneurons, representing 15 % of total interneurons (Hajos et al., 1996; Xu et al., 2010; Rudy et al., 2011; Tremblay et al., 2016). The cellular diversity even within the population of VIP expressing neurons is high, in the hippocampus and in the neocortex (Tyan et al., 2014; Topolnik and Tamboli, 2022). A recent large-scale study classified cortical VIP interneurons into 5 morpho-electric transcriptomic (MET) types (Gouwens et al., 2020). The connectivity motifs of VIP neurons encompass both inhibition of principal cells and

* Corresponding authors.
E-mail addresses: merie@naox-technologies.com (M. Nassar), desdemona.fricker@u-paris.fr (D. Fricker).
[1] Equally contributing.

https://doi.org/10.1016/j.neuroscience.2024.09.032
Received 8 February 2024; Accepted 16 September 2024
Available online 23 September 2024
0306-4522/© 2024 The Authors. Published by Elsevier Inc. on behalf of International Brain Research Organization (IBRO). This is an open access article under the CC BY license (http://creativecommons.org/licenses/by/4.0/).

inhibition of other interneurons (Acsády et al., 1996; Booker & Vida, 2019). The latter leads to VIP mediated disinhibition of principal glutamatergic neurons and has received much attention in various brain areas (Pi et al., 2013; Jackson et al., 2018; Krabbe et al., 2019; Williams and Holtmaat, 2019) including in the hippocampus (Turi et al., 2019; Wei et al., 2021). The disinhibitory influence of VIP interneurons on the circuit is largely thought to arise from their inhibition of SST interneurons and, to a lesser extent of PV interneurons (Pfeffer et al., 2013; Pi et al., 2013; Karnani et al., 2014; Karnani and Jackson, 2018; Apicella and Marchionni, 2022). Inhibitory-to-inhibitory synaptic interactions among VIP, SST and PV interneurons may help maintain a balance between inhibition and disinhibition, and help flexible computation (Millman et al., 2020; Sadeh and Clopath, 2021). The presubicular HD signaling may also be dependent on VIP interneuron activity. Specifically, VIP interneurons may be key for shaping the multisensory HD signal integration and HD signal updating. To investigate the role of VIP interneurons *in vitro* and in future *in vivo* studies, we need to be able to selectively target them for recording or manipulating.

Here we examined the VIP Cre mouse line (Taniguchi et al., 2011) for its specificity in labeling VIP interneurons in the presubiculum. We characterized the distribution and densities of VIP interneurons across presubicular layers, and characterized the phenotypic diversity of presubicular VIP interneurons in patch clamp recordings in slices. Unsupervised cluster analysis based on the intrinsic electrophysiological properties of VIP interneurons, compared to pyramidal neurons, let us separate three distinct groups. Photostimulation experiments indicate that at least a subset of VIP interneurons can be directly recruited by thalamic inputs, with strongly facilitating dynamics.

Methods

Animals

Experiments were performed on wild-type and transgenic C57Bl6 mice. VIP-Cre mice (Jax n010908, Taniguchi et al., 2011) were crossed with the Ai14 Cre reporter line (Jax n007914, Madisen et al., 2010). Cre mediated recombination resulted in the expression of red fluorescent tdTomato labeling in subsets of GABAergic neurons. VIPcre::tdTomato mice specifically express the red fluorescent protein tdTomato in VIPcre expressing neurons, enabling their visualization in brain slices. Previous studies showed a preferential paternal transmission of the Cre recombinase in the case of PVcre and SSTcre animals (Nassar et al., 2015). Here we bred male homozygous VIPcre mice with females homozygous for tdTomato, to study their offspring of both sexes. Animal care and use conformed to the European Community Council Directive of September 22, 2010 (2010/63/EU) and French law (87/848).

Viral vectors

Viral vectors were injected to induce expression of Chronos, a modified opsin with fast kinetics (Klapoetke et al., 2014). AAV5.Syn.Chronos-GFP.WPRE.bGH (AAV5-Chronos, Penn Vector Core, Addgene 59170P) was used to express this blue light sensitive opsin fused to GFP, under the control of the Synapsin promoter. Viral vectors were stored in aliquots at −80 °C until use.

Stereotaxic surgery

Mice, of age 30–45 days, were anesthetized intraperitoneally with ketamine hydrochloride and xylazine (100 and 15 mg/kg, respectively) and placed in a stereotaxic frame. Unilateral viral injections were performed as described previously (Mathon et al., 2015). AAV injections were targeted to ATN using coordinates from bregma of lateral, 0.75 mm; posterior, 0.82 mm; and depth, 3.2 mm. Injections were made with a Hamilton syringe using a syringe Pump Controller (Harvard Apparatus, Pump 11 elite) at 40 nl/min to deliver volumes of 220 nl AAV5.Syn.Chronos vectors. Leakage from an injection site to surrounding tissue was minimized by withdrawing the pipette slowly after a delay of 10 min. Maximal transgene expression occurred 4 weeks after injection.

Immunohistochemistry

Mice were anesthetized intraperitoneally with ketamine hydrochloride and xylazine (100 and 15 mg.kg^{-1}, respectively). They were then perfused transcardially with 0.9 % saline containing heparin (100–200 UI/ml) followed by 30–50 ml of a fixative solution containing 4 % paraformaldehyde in 0.1 M phosphate buffer (PB). Dissected brains were post-fixed 4 h in the same solution at 4 °C, rinsed three times for 3 min, and then placed in a 30 % sucrose solution at 4 °C for at least 24 h. Horizontal sections of thickness 40 µm were cut in 0.1 M PBS using a slicing vibratome (Camdem vibratom 7000smz-2). Membranes were permeabilized by three cycles of freeze-thawing slices on dry ice in a 30 % sucrose containing solution. Sections were washed three times (2 × 30 min, 1 × 60 min) with 0,3% Triton X100 in PBS 0.1 M (BupHTM Phosphate Buffered Saline Packs, Thermo Fisher Scientific), then transferred to a saturation buffer containing 5 % goat serum and 0.3 % Triton X-100 in PBS 0.1 M, and agitated for 2 h at room temperature. Sections were then transferred into the primary antibody solution of 5 % goat serum and 0.3 % Triton X-100 in PBS 0.1 M and gently agitated, overnight at 4 °C. Sections were rinsed three times (2 × 30 min, 1 × 60 min) with 0,3% Triton X100 in PBS 0.1 M, then incubated in dilutions of secondary antibody, conjugated to different fluorophores, overnight at 4 °C under gentle agitation.

4,6-diamidino-2-phenylindole (DAPI, Sigma) was always added to secondary antibodies containing solutions (1:5000) to stain cellular nuclei. For VIP immunostaining, we increased the incubation time with the primary antibody to 48 h and with the secondary antibody to 24 h, both at 4 °C.

The following primary antibody was used: Rabbit Anti-VIP (Immunostar, #20077, 1:500). Secondary antibodies were: Donkey Anti-Rabbit (A647, Jackson ImmunoResearch, 1:500) or Goat Anti-Rabbit (Fisher Scientific, A488, 1:500). Stained sections were mounted on glass slides, coverslipped with anti-fade Prolong Gold (Life technologies).

Image acquisition and analysis

Stained slices were visualized with a confocal microscope (Zeiss LSM710). Presubicular layers and borders were defined using specific cytoarchitectonic features identified by DAPI staining. Images were adjusted for contrast and brightness. For each brain slice, fluorescent tdTomato+ cells from all layers of the presubiculum were identified visually by complete scans of optical sections.

To determine the density of the VIP-INs expressing the tdTomato reporter, we first took Z-stack pictures of the 40 µm thick presubicular sections under the 20x objective of a confocal microscope (Zeiss LSM710). The Cell counter plugin of the ImageJ software was used to count the cells. According to the cell density, the PrS layers were manually and individually selected and their volume was measured (area × range). The density of cells in number/mm3 was determined on n = 53 sections from 6 animals.

Antibody fluorescence was examined for each tdTomato+ cell. A cell was regarded as positive for a given antibody when somatic fluorescence was clearly higher than background levels. Colocalization of antibody labeling was confirmed from observations at all levels of a stack of optical sections for the soma of a neuron. Percentages of single and dual-immuno labeled fluorescent neurons were obtained by dividing the number of immuno-labeled fluorescent neurons by the total number of tdTomato+ neurons. Data are given as mean ± SEM.

Slice preparation and whole cell patch-clamp recordings

Acute slices containing the hippocampus, subicular complex and entorhinal cortex were prepared 4 weeks after AAV5 injections. Animals were anesthetized with ketamine hydrochloride and xylazine mix, treated with 0.1 mL heparin injected intraperitoneally, and perfused intracardially by a cutting solution containing (in mM): 125 NaCl, 25 sucrose, 2.5 KCl, 25 $NaHCO_3$, 1.25 NaH_2PO_4, 2.5 D-glucose, 0.1 $CaCl_2$, 7 $MgCl_2$, cooled to 4 °C, and equilibrated with 5 % CO_2 in O_2. The brain was removed and cut in 300 μm horizontal slices in the same cutting solution with a vibratome (Leica VT1200S). These slices were stored for 15 min in warm (34 °C) ACSF, containing (in mM): 124 NaCl, 2.5 KCl, 26 $NaHCO_3$, 1 NaH_2PO_4, 2 $CaCl_2$, 2 $MgCl_2$, and 11 D-glucose, bubbled with 5 % CO_2 in O_2. Slices were then transferred to a recording chamber (volume 2–3 ml, temperature 33 °C–35 °C) mounted on a BX51WI microscope (Olympus). Experiments were discontinued if transfection at the injection site was weak or if leakage had occurred. The dorsoventral level of horizontal slices that were used for recordings ranged from dorsoventral 2.6 to 3.6 mm with respect to bregma corresponding to the mid to dorsal portion of presubiculum (Paxinos and Franklin, 2013).

Recordings were made with glass pipettes pulled using a Brown-Flaming electrode puller (Sutter Instruments) from borosilicate glass of external diameter 1.5 mm (Clark Capillary Glass, Harvard Apparatus). Electrodes were filled with a solution containing the following (in mM): 135 K-gluconate, 1.2 KCl, 10 HEPES, 0.2 EGTA, 2 $MgCl_2$, 4 MgATP, 0.4 Tris-GTP, 10 Na_2- phosphocreatine, and 2.7–7.1 biocytin. The pH of the pipette solution was adjusted to 7.3 with KOH, and the osmolarity was 290 mOsm. Electrode resistance in the bath, filled with the internal solution, was typically 5–8 MΩ. We used small tip sizes for recording the small GABAergic VIP interneurons (diameter of soma, 10–15 μm). Fluorescent VIP cells were identified using LED illumination with appropriate emission/excitation filters (OptoLED, Cairn Research) using a Luca CCD Camera (Andor). Whole-cell current-clamp recordings were made using a MultiClamp 700B amplifier and pCLAMP software (Molecular Devices). Membrane potential signals were filtered at 6 kHz and digitized at 20–50 kHz. VIP-expressing interneurons were red fluorescent cells in slices from VIPcre::tdTomato mice. Pyramidal neurons of layer III were unlabeled principal neurons, identified as cells with a triangular or ovoid shaped soma. We included them as an external reference population (data from Richevaux et al., 2023). Successful recordings were defined by a high seal resistance above 2 GΩ in cell attached mode. Quality criteria for proceeding with whole cell recordings included a stable access resistance (Ra) < 40 MΩ. Ra was estimated in whole cell voltage clamp mode using the instantaneous current change in response to a −10 mV pulse. The seal test mode in pClamp software was used to estimate the access resistance on-line, before switching to current clamp mode. Bridge balance was set automatically (MultiClamp Commander Software Interface) and monitored throughout the recording. For changes >20 % the recording was discarded. Action potentials needed to be overshooting above 0 mV.

Electrophysiological analysis

Cells intrinsic properties were analyzed as described previously (Huang et al., 2017). Cellular parameters were measured at least 3–5 min after whole-cell records were established. RMP was measured at the beginning of the recording over at least 10 s. Then the membrane potential was kept at −65 mV, for all cells, using a constant current injection as necessary. Electrophysiological parameters were measured from responses to step current injections of 800 ms duration, in VIP interneurons and in principal cells, in a standardized manner. Injected currents increased from negative to positive values, with a range of amplitudes that resulted in hyperpolarization to about −100 mV during the first step and depolarizations close to the maximum sustained firing frequency (evident as noticeably reduced spike amplitudes at the end of the step). Depending on the resistance of the recorded neuron, the first hyperpolarizing step was in the range of −50 pA to −200 pA with an incremental step change of 1/10th of the initial value. Neuronal input resistance R_{in} was determined as the slope of the current–voltage (I-V) relationship between −75 and −55 mV. Membrane time constants (τ) were estimated from a double exponential fit to the negative deflection of membrane voltage (Levenberg–Marquardt algorithm; Golowasch et al., 2009) in response to a 800 ms hyperpolarizing current injection inducing a voltage change of up to 10 mV. A "sag ratio," indicative of Ih expression, was calculated for steps in which the voltage deflection reached values between −105 and −90 mV, as the ratio of the maximal negative potential, typically from 0 to 200 ms, divided by the mean steady state voltage deflection, between 400 and 800 ms.

Action potentials of amplitude at least 20 mV were detected from continuous periods of rising membrane potential. Rheobase (or threshold current for firing) was defined as the smallest positive current step of 800 ms that elicited at least one AP. Firing frequency (Hz) was deduced by dividing the number of APs over time (APs/sec). Input–output (I–O) curves were constructed by plotting firing frequency (APs/sec) as a function of injected current. The I–O gain was measured from a linear fit to frequencies measured from the 4 current steps after rheobase. First AP latency was calculated from the first AP elicited, at latency less than 100 ms. Action potential waveform features were obtained by averaging the measures from the first AP elicited, on the rheobase current step, at latency less than 100 ms. AP threshold (threshold) was defined as the membrane potential when $dV/dt > 35$ mV/ms. AP peak was its maximum potential. The AP rising amplitude (amplitude) was the difference between the threshold and the peak AP voltage. AP width (width) was measured from the half-height of the AP rising phase. Max depolarization rate and max repolarization rate were defined as the maximum and minimum dV/dt, during rising and falling phases of APs, respectively. The AHP was the voltage minimum after the AP peak and its amplitude (AHP) was defined as the difference from the threshold.

Optical stimulations

Chronos-expressing ATN axons were stimulated optically with a single-wavelength LED system (470 nm; Cairn Research OptoLED) connected to the microscope via a custom-made triple port (Cairn Research). Synaptic responses of presubicular VIP interneurons were recorded in whole-cell current- or voltage-clamp modes. LED illumination gave a 200 μm diameter spot with a 60 1.0 NA plan-Apochromat objective. Flashes of 0.5 ms were delivered close to recorded somata. We typically used low-intensity stimulation of 0.1– 0.5 mW, set to induce near threshold responses, reducing network activation after ATN axon stimulation. Excitatory and inhibitory postsynaptic responses were evoked by 10 Hz, 30 Hz and 70 Hz stimulus trains. We tested for monosynaptic excitation by stimulating in the presence of TTX (1 μM; Tocris Bioscience) to block polysynaptic excitation and 100 μM 4-AP (Sigma-Aldrich) to enhance axonal depolarization (Cruikshank et al., 2010; Mao et al., 2011).

Biocytin staining and morphological 3D reconstructions across presubicular layers

VIP interneurons were filled with 0.3–0.4 % biocytin (3–4 mg/ml) during recordings to reveal their morphology post hoc (Nassar et al., 2015; Simonnet et al., 2013). After recording, slices were fixed in 4 % PFA in 0.1 M phosphate buffer at 4 °C for 24 h. Slices were then rinsed in PBS and cryoprotected in 30 % sucrose mixture at 4 °C overnight. Membranes were permeabilized by three cycles of freeze-thawing over dry ice and then washed with PBS. Slices were agitated in a saturation buffer containing 2 % milk powder and 1 % Triton X-100 in PBS 0.1 M for 3 h at room temperature. Then, sections were gently agitated with Streptavidin-Cy5 conjugate (1:500, Molecular Probes) and DAPI in the blocking solution overnight at 4 °C. After washing with PBS, slices were

mounted on coverslips using ProLong Gold Antifade Mountant (Invitrogen). Filled cells were visualized with a confocal microscope (Zeiss LSM710). Neuronal anatomy was derived from z stacks of acquired images (Neurolucida, RRID:SCR_001775; MBF Bioscience).

The presubiculum has a curved trapezoid shape in horizontal sections, and its radial axis is defined by the pyramidal cell apical dendrites. Blood vessels follow the same main orientation. Six presubicular layers were identified based on the following cytoarchitectonic features: Layer I stands out as an almost cell free layer. Layer II possesses a high density of DAPI labeled cell bodies. The beginning of layer II was used to define the proximal border to the subiculum, and the distal end of layer II corresponds to the transition to the parasubiculum. Layer III has a medium cell body density. Anterior thalamic axons ramify across the superficial layers I and III (Fig. 5A; see also Nassar et al., 2018). Layer IV is sparsely populated, it is part of the deep layers, and lies below the thalamo-recipient superficial layers (Richevaux et al., 2023). The deep layers V/VI appear as the continuation of the subiculum.

Statistical analysis

Signals were analyzed with AxoGraphX and custom-written software (Labview, National Instruments; MATLAB, The MathWorks). Algorithms to detect APs and measure active and passive neuronal properties are as described previously (Simonnet et al., 2013; Huang et al., 2017). Results are given as mean ± SEM (number of cells, slices, or animals as indicated). Statistical analysis was performed with Prism (GraphPad Software). The Wilcoxon signed rank test for matched pairs was used to compare nonparametric data in matched samples. A Kruskal–Wallis one-way ANOVA test was followed by Dunn's post hoc test to compare more than two groups. Mann-Whitney non parametric tests were also performed to compare differences between two independent groups. Two-way ANOVA was also used to study the effect of two independent

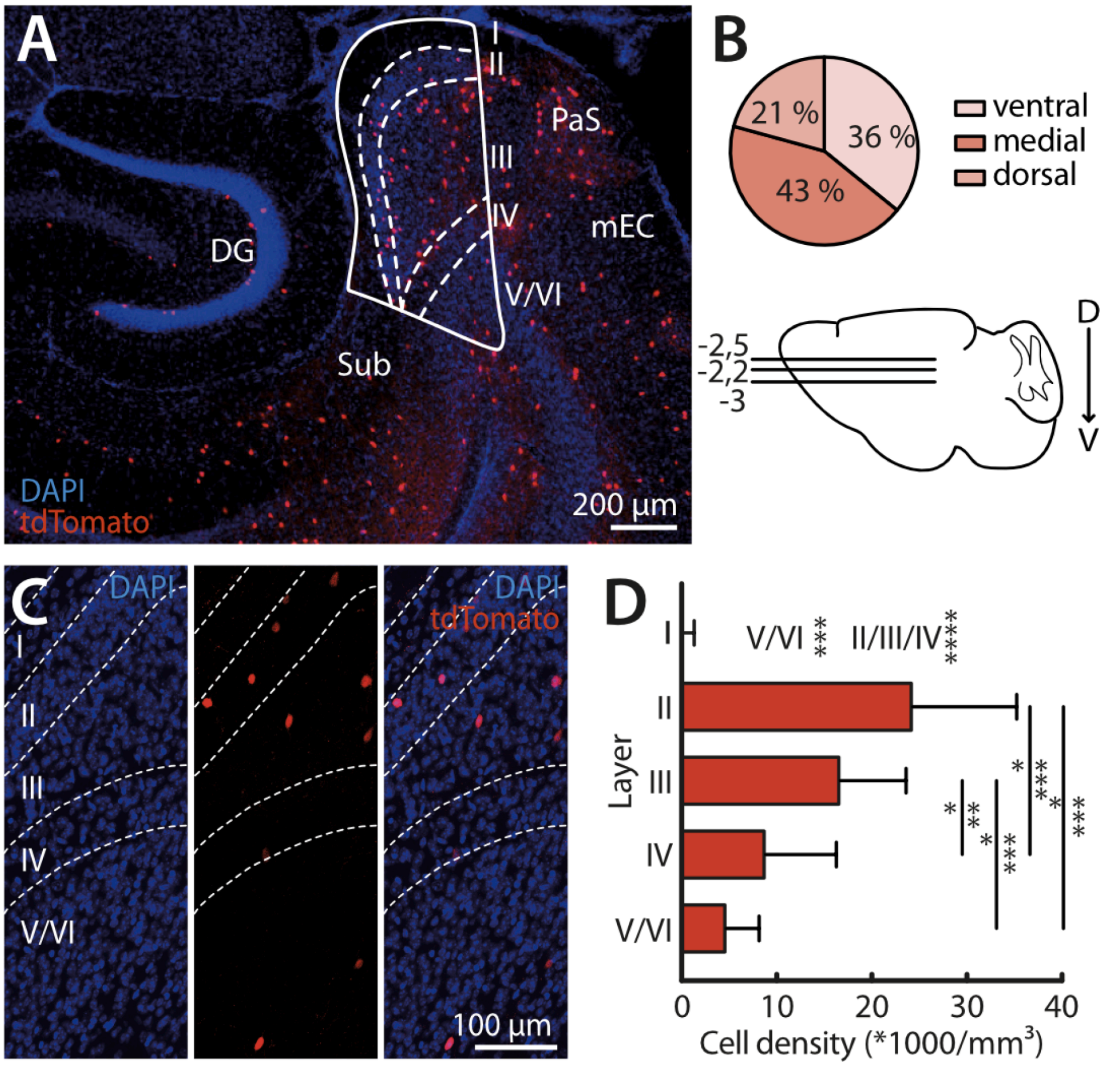

Fig. 1. Layer-specific distribution of VIP interneurons in the presubicular HD cortex A) Horizontal section of the presubiculum with red tdTomato labeled neurons from a VIPcre::tdTomato mouse. The presubiculum continues from the subiculum (Sub), faces the dentate gyrus (DG), and lies adjacent to parasubiculum (PaS) and medial entorhinal cortex (mEC). DAPI staining in blue. B) Slices obtained from different dorso-ventral levels, ranging from −2,2 mm (most dorsal) to −3 mm (most ventral). C) DAPI staining (left, blue), tdTomato labeled VIP interneurons (middle, red), and an overlay (right) of presubicular layers I to V/VI. D) Densities (mean ± SEM) of labeled VIP interneurons in different layers of presubiculum. Data from 10 slices of 3 animals (Kruskal-Wallis test, *** $P < 0.001$, **** $P < 0.0001$). (For interpretation of the references to color in this figure legend, the reader is referred to the web version of this article.)

variables at the same time.

Results

Mouse model validation and layer distribution of VIP interneurons in the presubiculum

We first aimed to confirm the specificity of the VIPcre mouse line (Taniguchi et al., 2011) as a genetic tool for accessing VIP interneurons in presubiculum. To do this, VIPcre mice were crossed with a reporter line expressing a red fluorescent protein, tdTomato (Ai14, Madisen et al., 2010), that let us visualize VIP interneurons in slices. We then examined the distribution of VIP expressing interneurons across the different layers of the presubiculum in these transgenic mice. Fig. 1A shows the presubiculum in the context of the mouse hippocampal formation. Six cytoarchitectonic layers can be recognized. The distribution of fluorescently labeled VIP interneurons was quantified in 19 ventral, 23 medial and 11 dorsal presubicular slices from three animals. (Fig. 1B). VIP interneurons were sparse in layer I (286 ± 143.5). Their density was higher in layer II (24324 ± 1499 cells/mm3) than in layer III (16712 ± 946 cells/mm3). It further decreased in layer IV and even more in layers V/VI. Overall, VIP interneuron density was significantly higher in the superficial layer II and III than in the deep layers, IV and V/VI (Fig. 1C,D).

We then used antibodies against VIP to examine the specificity of labeling in the VIPcre::tdTomato mice (Fig. 2) in superficial layers I-III and in deep layers IV and V/VI of the presubiculum. The tdTomato+ fluorescent presubicular cells that were also immunopositive for VIP were quantified in 8 non-adjacent slices from three animals (Fig. 2A,B). As expected, the great majority of tdTomato+ neurons in the VIPcre line were immunopositive for VIP (393/413). VIP labeling of TdTomato+ cells was even higher in superficial layers (95 ± 1 %) than in deep layers (87 ± 6 %) with no significant difference.

Cluster analysis of electrophysiological parameters reveals groups of presubicular VIP interneurons

We measured passive membrane properties, AP waveforms and firing patterns of 85 presubicular VIP interneurons and compared them to 71 layer III pyramidal neurons. The classification is based on electrophysiological criteria, where pyramidal neurons were used as an external reference for the interneuron containing clusters, in order to define a significant cut-off value for clusters. All recordings were made from neurons in slices from the mid-to-dorsal portion of the presubiculum. Dorso-ventral depths ranged from −3 to −2.2 mm, with most interneurons recorded from a level close to −2.5 mm (cf. Fig. 1B). Fluorescently labeled neurons in VIPcre::tdTomato mice and unlabeled pyramidal neurons in layer III were recorded from male and female mice, and mostly from superficial layers of presubiculum. Unsupervised cluster analysis using Ward's method (Ward, 1963) was based on 13 electrophysiological variables as listed in Table 1. Supplementary Fig. 1 shows these parameters in the space defined by the three first principal components. The hierarchical tree diagram (Fig. 3A) points to the existence of two VIP interneuron containing clusters (Cluster 1 and 2) that were segregated from a cluster containing pyramidal neurons, and a third group of VIP interneurons (Cluster 3). Within-cluster Euclidean distances for clusters 1, 2 and 3 were similar (10, 11 and 15, respectively). We explore VIP interneurons in the three clusters in detail below. All datapoints are plotted for each cell, represented by a dot, for each cluster (Fig. 3F).

Cluster 1: Highly excitable VIP interneurons

Cluster 1 comprised 39 VIP interneurons and one unlabelled neuron. A representative firing pattern of a VIP interneuron with irregular or quasi fast-spiking firing pattern and fast AP is shown (Fig. 3B-D, blue traces). Cluster 1 interneurons typically fired spontaneously both in the whole-cell mode and in cell-attached records made before rupturing the membrane. Their mean RMP was relatively depolarized, similar to VIP interneurons in Cluster 2 and 3 (−53.7 ± 1.7 mV; n = 39; mean ± SEM). Input resistance was particularly high, 1287 ± 108 MΩ, similar to Cluster 2 and significantly higher than for cluster 3 VIP interneurons (Fig. 3E, F). Membrane time constant, tau, was 28 ± 2 ms. Hyperpolarizing current injections induced a moderate voltage sag (Fig. 3B; sag ratio 1.11 ± 0.01). Cluster 1 cells could fire in quasi fast patterns. They were very excitable, and APs were elicited at a very low rheobase current of 10.5 ± 1.0 pA. The maximum firing rate, determined from a subset of n = 7 cells, was 100.2 ± 14.6 Hz. Firing rate gain was 1564 ±

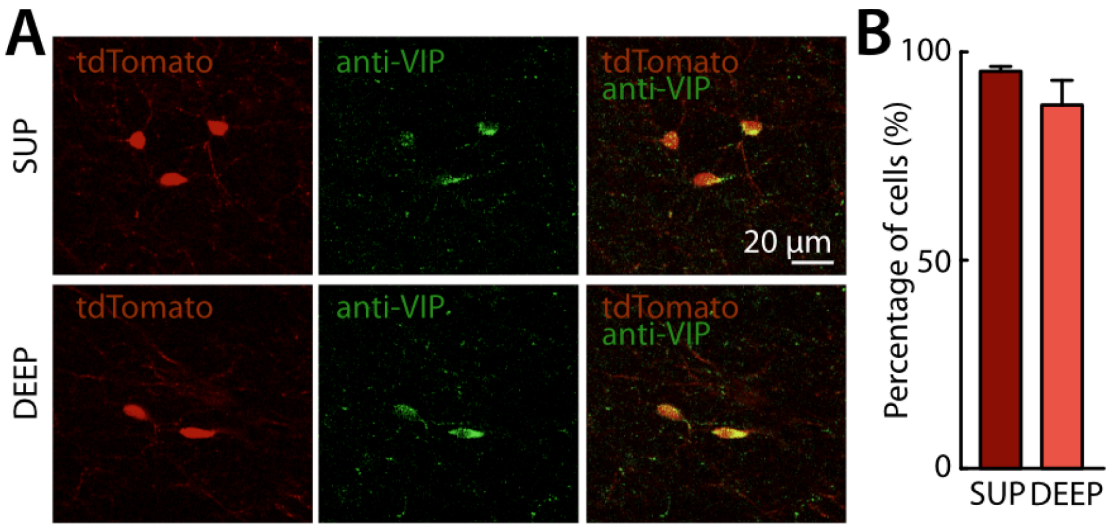

Fig. 2. Immunostaining confirms the specificity of the VIPcre::tdTomato labeling. A) Presubicular sections from VIPcre::tdTomato mice stained with anti-VIP antibody in superficial (SUP, top panels) and deep (DEEP, bottom panels) layers. For each row, tdTomato labeled neurons (red) are on the right, immunostaining against VIP in the middle (green) and merge on the right. B) Bar graphs indicate percentages of antibody labeling of tdTomato+ VIP interneurons (mean ± SEM). Data obtained from 8 slices of 3 animals. (For interpretation of the references to color in this figure legend, the reader is referred to the web version of this article.)

Table 1
Electrophysiological intrinsic properties of 85 presubicular VIP interneurons recorded from the VIPcre::tdTomato mouse line and 71 presubicular layer 3 pyramidal neurons recorded from transgenic or wild-type animals. Using these 13 parameters for Ward's unsupervised cluster analysis let us separate the population of VIP interneurons in two main clusters and a third cluster, composed of both VIP interneurons and pyramidal neurons. Values (mean ± SEM) for each parameter are given for each cluster. p-values indicate statistical differences between clusters and between VIP and pyramidal neurons within cluster 3 and between VIP neurons across the three clusters, calculated using a Mann-Whitney test. Values in green are inferior to 0.05.

	Cluster 1			Cluster 2			Cluster 3									Mann-Whitney test			Mann-Whitney test		
	VIP			VIP			All			VIP			MW	PYR					Cluster 3 VIP only		
	Mean	SEM	N	Mean	SEM	N	Mean	SEM	N	Mean	SEM	N	*p-value*	Mean	SEM	N	Cluster 1-2	Cluster 1-3	Cluster 2-3	Cluster 1-2	Cluster 1-3	Cluster 2-3
Resting membrane potential (mV)	-53.67	1.70	39	-56.34	2.13	29	-69.00	1.19	88	-57.00	1.59	17	3.24E-06	-71.87	1.20	71	2.69E-01	1.35E-09	4.24E-06	2.69E-01	2.53E-01	9.09E-01
Input resistance (MΩ)	1286.63	107.82	39	1163.84	120.71	29	467.19	26.97	88	762.42	77.70	17	1.86E-05	396.50	20.51	71	4.35E-01	3.16E-14	7.93E-12	4.35E-01	3.28E-03	1.49E-02
Tau (ms)	27.95	1.73	39	39.09	2.88	29	25.20	1.01	88	30.03	1.80	17	9.32E-03	24.04	1.14	71	2.38E-03	1.90E-01	8.83E-06	2.38E-03	4.17E-01	7.04E-02
Sag ratio	1.11	0.01	39	1.08	0.01	29	1.09	0.01	88	1.14	0.03	17	7.60E-02	1.08	0.01	71	2.18E-01	6.85E-02	1.90E-01	2.18E-01	7.14E-01	4.22E-01
Rheobase current (pA)	10.50	1.04	39	14.96	1.17	29	47.95	2.93	88	37.09	5.47	17	2.06E-02	50.55	3.33	71	2.97E-03	2.05E-17	6.16E-13	2.97E-03	2.83E-07	4.83E-05
Input-output slope (Hz/nA)	1564.28	138.18	39	836.34	115.38	29	422.30	22.37	88	553.48	84.42	17	1.86E-01	390.89	17.54	71	3.90E-04	1.15E-12	5.38E-02	3.90E-04	1.90E-05	2.75E-01
AP threshold (mV)	-38.82	1.03	39	-33.90	1.02	29	-32.32	0.65	88	-27.25	1.71	17	1.96E-03	-33.54	0.62	71	1.44E-03	8.74E-07	5.16E-01	1.44E-03	6.81E-06	5.50E-03
AP width (ms)	0.45	0.02	39	0.71	0.03	29	0.69	0.03	88	0.61	0.02	17	2.67E-01	0.70	0.03	71	3.63E-10	2.33E-12	5.77E-02	3.63E-10	4.84E-06	3.00E-02
AP AHP (mV)	-20.36	0.69	39	-15.01	0.76	29	-19.19	0.36	88	-18.41	0.94	17	4.37E-01	-19.38	0.39	71	8.50E-06	2.51E-01	5.33E-06	8.50E-06	2.47E-01	1.23E-02
AP amplitude (mV)	74.25	1.13	39	54.22	2.23	29	77.19	0.93	88	69.53	1.55	17	3.76E-06	79.02	0.97	71	1.17E-08	1.37E-02	1.10E-11	1.17E-08	2.20E-02	1.20E-04
AP maximum depolarization rate (V/s)	423.08	14.25	39	220.89	13.34	29	340.36	6.42	88	338.30	16.61	17	4.59E-01	340.85	6.95	71	2.54E-10	7.54E-07	9.35E-10	2.54E-10	8.89E-04	1.25E-05
AP maximum repolarization rate (V/s)	-180.06	7.10	39	-82.00	4.99	29	-117.13	3.37	88	-117.18	4.66	17	9.83E-01	-117.12	4.04	71	9.91E-12	6.91E-13	5.65E-07	9.91E-12	2.15E-07	3.80E-05
Onset latency (ms)	113.04	13.97	39	205.36	28.82	29	148.27	11.64	88	128.43	19.88	17	6.19E-01	153.03	13.62	71	4.88E-03	3.11E-02	1.79E-01	4.88E-03	2.93E-01	2.32E-01

138 Hz/nA. The latency to fire, at rheobase, was 113 ± 14 ms. AP threshold was significantly more negative than in cluster 2 and 3 VIP interneurons, at −38.8 ± 1.0 mV. AP width was significantly shorter than in the other two clusters, 0.45 ± 0.02 ms, and AP amplitude was very high, 74 ± 1 mV. The maximum AP depolarization and repolarization rates were 423 ± 14 V/s and −180 ± 7 V/s, respectively, significantly greater than in other VIP interneurons. Spike AHPs were biphasic (Fig. 3B, C), with mean maximal amplitude of −20.4 ± 0.7 mV.

Cluster 2: VIP interneurons with broad AP waveforms

Cluster 2 comprised 29 VIP interneurons. A representative firing pattern of a VIP interneuron with regular firing pattern and a broad AP waveform is shown (Fig. 3B-D, green traces). Cluster 2 neurons also fired spontaneously with mean RMP −56.3 ± 2.1 mV. Input resistance was also very high, 1164 ± 121 MΩ (Fig. 3E, F). Membrane time constant was significantly higher than in cluster 1 cells (39 ± 3 ms). Hyperpolarizing current injections also induced a moderate voltage sag (Fig. 3B; sag ratio 1.08 ± 0.01). Cluster 2 cells could fire in regular patterns. APs were elicited at a rheobase current of 15.0 ± 1.2 pA, higher than for cluster 1. The maximum firing frequency for a subset of n = 5 neurons was relatively low, 48.3 ± 10.4 Hz. Firing rate gain was 836 ± 115 Hz/nA, about twice lower than for cluster 1. Neurons from cluster 2 had significantly longer onset latencies to fire at rheobase (205 ± 29 ms for cluster 2, Fig. 3F). AP threshold was higher (−33.9 ± 1.0 mV), and AP width was broader than for cluster 1 (0.71 ± 0.03 ms). AP amplitude was 56 ± 2 mV, significantly lower compared to cluster 1 and to cluster 3 VIP interneurons (Fig. 3C-D). The maximum AP depolarization and repolarization rates were significantly slower than for cluster 1 and 3 (221 ± 13 V/s, −82 ± 5 V/s respectively). Spike AHPs were simple (Fig. 3C) and with lower amplitude compared to cluster 1 and 3 neurons (−15.0 ± 0.8 mV, Fig. 3C, D).

Cluster 3: A third group of VIP interneurons with lower input resistance

Cluster 3 was composed mostly of pyramidal neurons (black, n = 71) and also of a third group of VIP interneurons. Representative recordings with firing pattern and AP waveform of a pyramidal neuron and an irregular spiking VIP interneuron are shown (Fig. 3B-D). In the following we focus on this third group of VIP interneurons in cluster 3 (red, n = 17). These interneurons had a mean membrane potential of −57.0 ± 1.6 mV. Most remarkably, their input resistance was 467 ± 27 MΩ, significantly lower than that in cluster 1 and 2 VIP interneurons, but still significantly higher than the pyramidal cells in cluster 3 (Fig. 3E,F). The time constant was 30 ± 2 ms. The voltage sag was similar to the other clusters (1.09 ± 0.00). Rheobase was significantly higher than in the two other clusters, at 37.1 ± 5.5 pA. Firing was often irregular, and the maximum firing frequency for one example neuron of this group was 66 Hz. The input–output slope quantifying the firing rate gain of this VIP interneuron group was 553 ± 84 Hz/nA, lower than in the other two VIP interneuron clusters 1 and 2. Action potential threshold was on average more depolarized than in the other VIP interneuron clusters, at −27.3 ± 1.7 mV. The AP width was 0.61 ± 0.0 ms, more similar to pyramidal neurons and also to cluster 2 VIP interneurons. AP AHPs were −18.4 ± 0.9 mV, intermediate compared to values in cluster 1 and 2. Also the AP amplitudes (69.5 ± 1.6 mV), depolarization rates (338 ± 17 V/s), repolarization rates (−117 ± 5 V/s) and spiking onset latencies (128 ± 20 ms) for cluster 3 VIP interneurons were intermediate compared to the other clusters (cf. Table 1).

Morphology

All recorded VIP interneurons were filled with biocytin to reveal their soma position. Axonal and dendritic morphologies of a sample of 7 well-filled cells were completely reconstructed with Neurolucida. We characterized the morphologies of neurons from the electrophysiologically defined VIP interneuron groups. Fig. 4A shows the axonal and dendritic arborizations of three VIP interneurons from cluster 1, two VIP interneurons from cluster 2 and two from the group of VIP interneurons in cluster 3. The somata of these VIP expressing cells were ovoid, and located in superficial layers II or III. The complexity of neuronal morphologies for the example neurons was overall similar. Dendritic trees were rather short, typically multipolar, ramifying in all directions from the soma. Axons emerged from the soma or from an ascending dendritic trunk. They were dense and possessed extensive arborizations. Their main orientation was perpendicular to the layer organization, innervating both superficial and deep layers, and generally following the radial axis of presubiculum. For one VIP interneuron in cluster 1, axons were oriented toward deep layers only.

Sholl analysis let us quantify the spatial distribution of neurites for each cell (Fig. B-E). Axonal Sholl plots showed a heterogenous distribution of axon intersections, with a peak at a distance of 100 µm from the soma (Fig. 4B). Dendrites occupied a radius of 100–150 µm around the soma and were oriented in all directions (Fig. 4C). The axonal length analysis indicated that most of the axons from the reconstructed VIP interneurons were located in layer III and IV (Fig. 4D), indicating that these neurons target mostly other neurons in layer III. Dendrites were rather short and mostly located in layer III (Fig. 4E).

Anterior thalamic axons terminals directly contact VIP interneurons

We asked whether ATN axons innervate presubicular VIP interneurons using the viral expression of Chronos in the anterior thalamic nuclei. Injection of AAV5-Chronos in the ATN led to the expression of

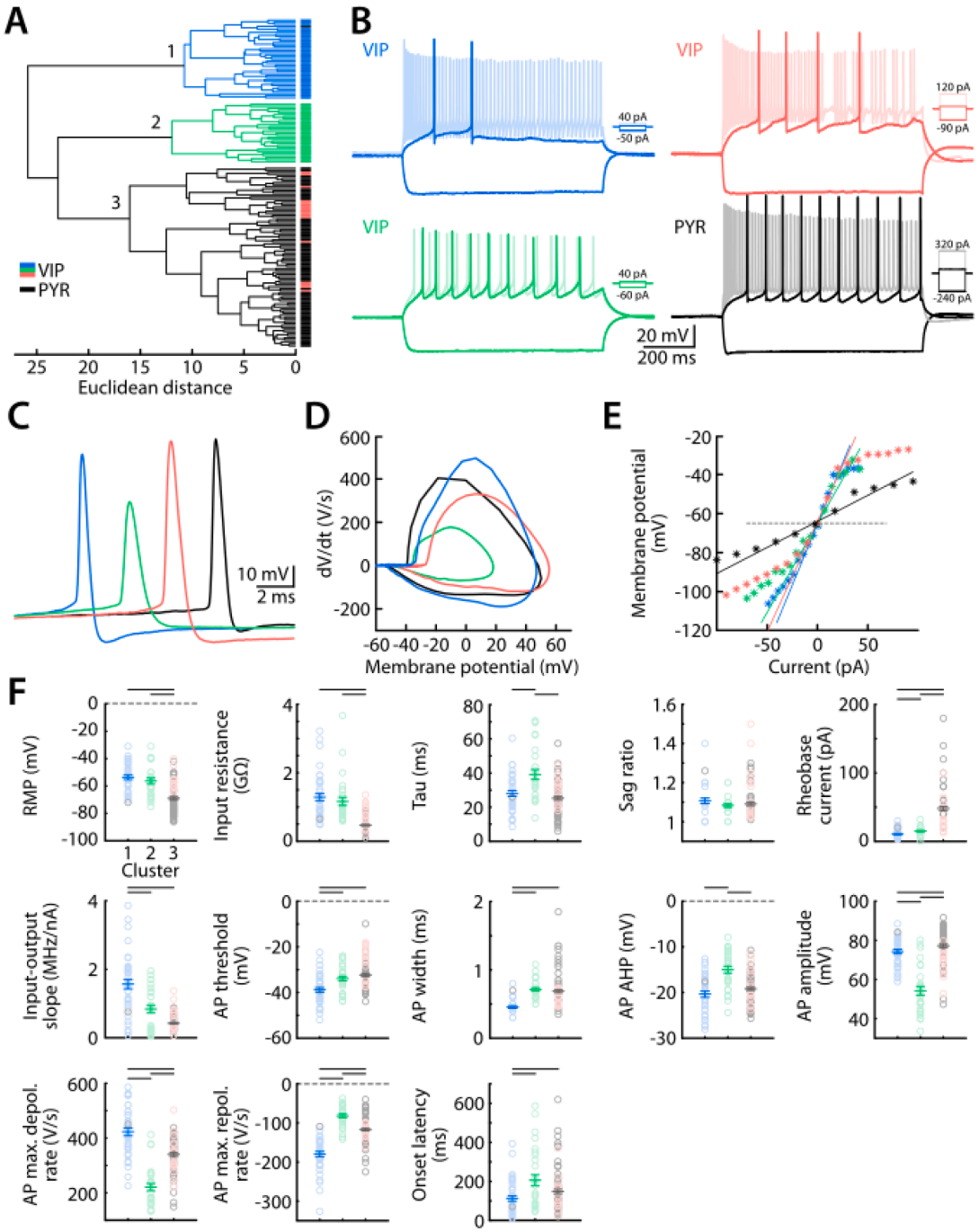

Fig. 3. Cluster analysis classification of presubicular VIP interneurons. A) Unsupervised cluster analysis of 13 parameters, detailed in Table 1, revealed two main subpopulations of VIP interneurons. A cut-off at a Euclidean distance of 16 separated VIP interneurons in Cluster 1 in blue, and Cluster 2 in green, from the Cluster 3 that contains mainly pyramidal cells, in black. A group of VIP interneurons, in red, clustered together with the pyramidal neurons in Cluster 3. B) Representative examples of firing patterns for each cluster and cell type. Neurons were maintained at −65 mV and injected with hyperpolarizing and depolarizing current steps. Voltage responses to hyperpolarizing and rheobase current injections are indicated in full color. C) First action potential waveforms at rheobase and D) the corresponding phase plots. E) Current–voltage relations at subthreshold potentials are plotted for neurons from each cluster. F) The values for active and passive electrophysiological properties are plotted for each neuron (mean ± SEM), as a function of the cluster. Each dot is a neuron. Lines represent significant differences measured by a Mann-Whitney test, complete p-values are detailed in Table 1. (For interpretation of the references to color in this figure legend, the reader is referred to the web version of this article.)

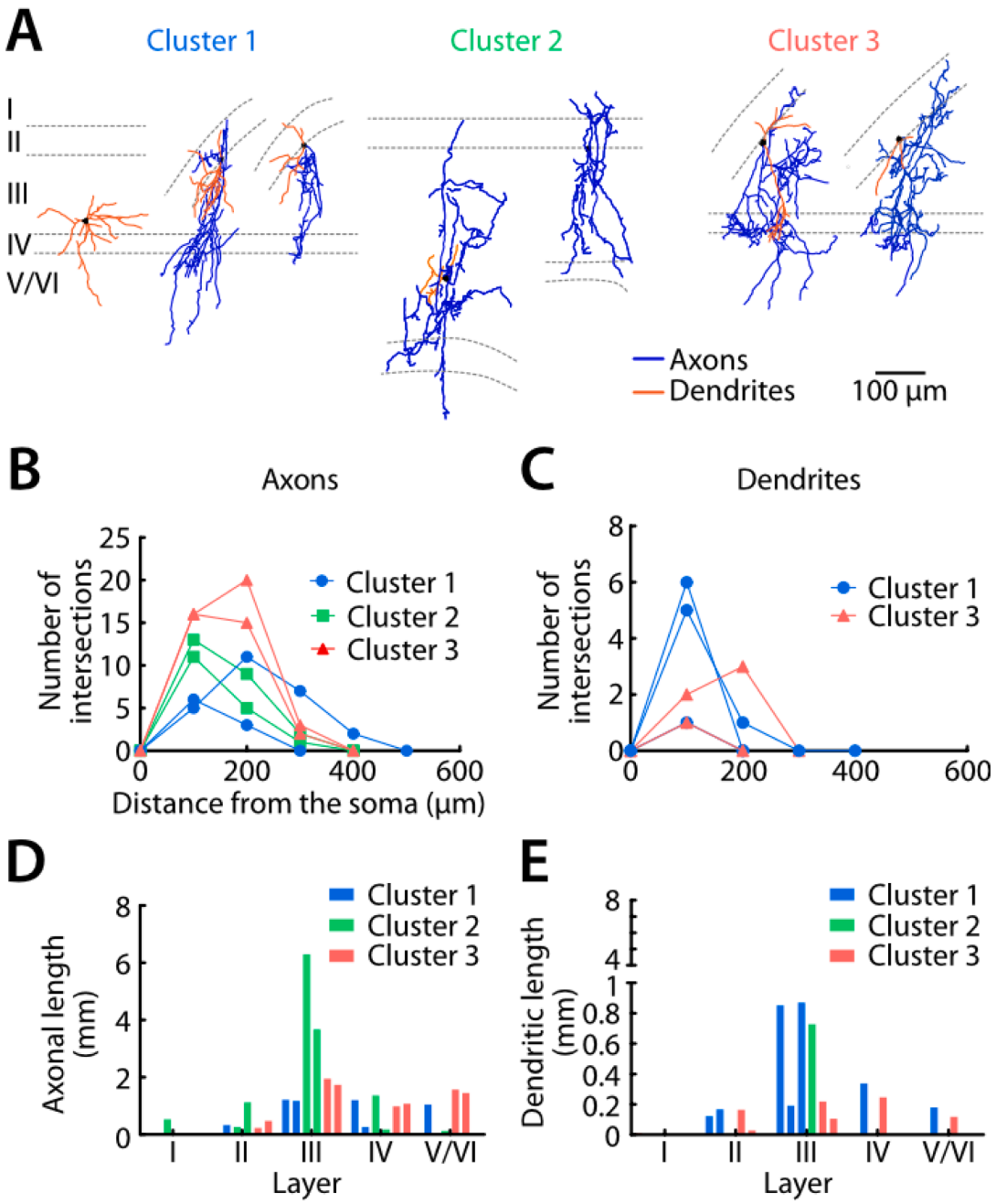

Fig. 4. Axo-dendritic morphology of presubicular VIP interneurons. A) Axo-dendritic arbors of seven biocytin-filled and reconstructed VIP interneurons. They were part of cluster 1 (blue), 2 (green), or the cluster 3 VIP-cell group (red). Axons in blue, dendrites in red, and cell bodies in black. B, C) Sholl plots of the number of axon (left panel) and dendrite (right panel) crossings for concentric circles against distance from the soma for each reconstructed neuron from each cluster. D, E) Axonal (left) and dendritic (right) length per layer for each cluster of neurons. (For interpretation of the references to color in this figure legend, the reader is referred to the web version of this article.)

this modified opsin (Klapoetke et al., 2014), in their axons that form the main afferents to the presubiculum (Simonnet et al., 2017, Nassar et al., 2018, Richevaux et al., 2023). As expected, ATN axons ramified in the superficial layers I and III of the presubiculum, while they were largely absent from layer II and from deep layers. Thus, the main dendritic domain of VIP interneurons overlapped with thalamic axons (Fig. 5A, B).

In *ex vivo* slice recordings, Chronos expressing ATN axons were stimulated by whole field illumination of the presubiculum with a 470 nm blue LED. We found that photostimulation induced excitatory postsynaptic currents (EPSCs) in all recorded superficial layer VIP interneurons. The mean amplitude and delay to EPSC onset was 17.86 ± 3.86 pA and 3.48 ± 0.27 ms respectively (Fig. 5D, n = 11). Responses persisted in the presence of TTX-AP, indicating the excitatory ATN-PrS

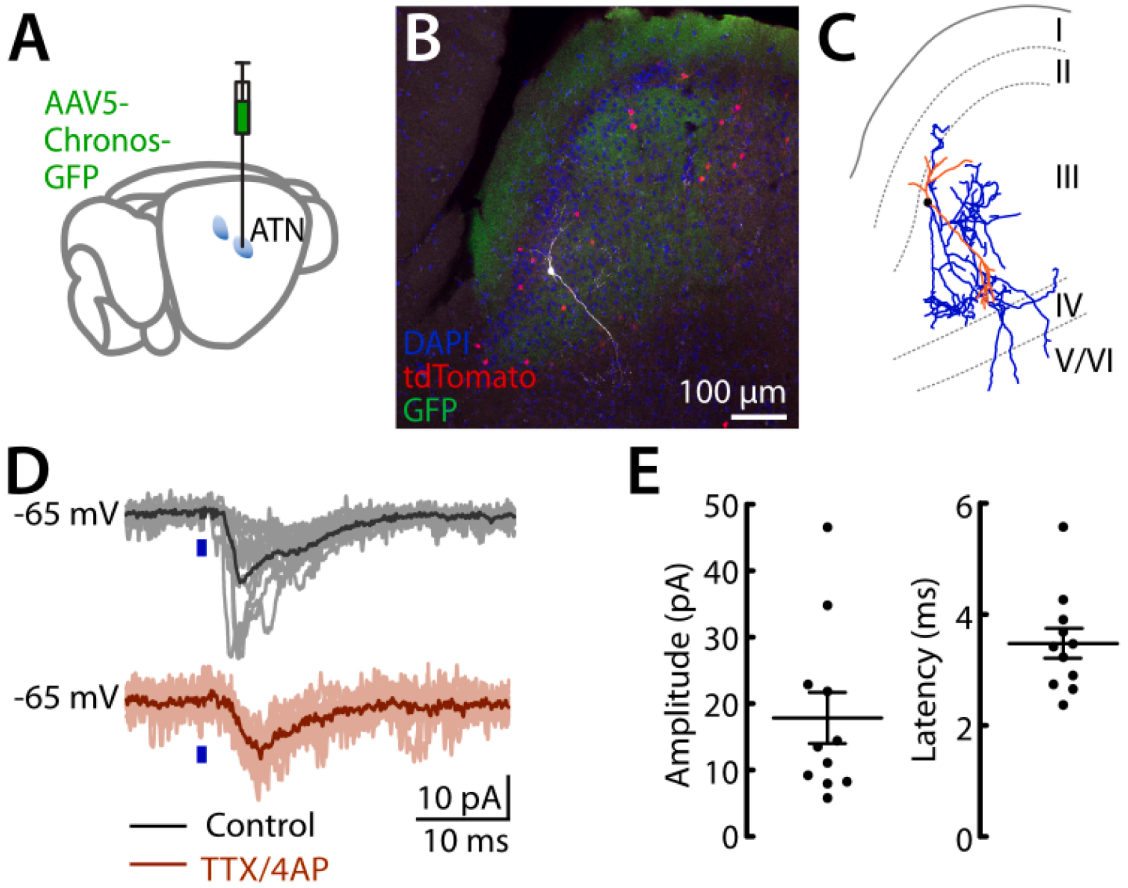

Fig. 5. Anterior thalamic fibers excite VIP interneurons in superficial layers. A) AAV5 viral vector was injected in ATN to express the channelrhodopsin Chronos fused with GFP in thalamic afferents to the presubiculum. B) Presubicular horizontal slice with a biocytin-filled VIP interneuron (white) in layer 3. DAPI in blue. tdTomato+ neurons in red. ATN axons in superficial layers in green. C) Neurolucida reconstruction of axons (blue) and dendrites (red) of this VIP interneuron of Cluster 3. D) Light-evoked EPSCs at holding potential of −65 mV in control conditions (black, top) and in the presence of TTX (1 µM) and 4-AP (100 µM) in the bath solution (red, bottom). Blue bars indicate photostimulation. E) EPSC amplitudes (left) and latencies (right) from n = 11 VIP interneurons (mean ± SEM). (For interpretation of the references to color in this figure legend, the reader is referred to the web version of this article.)

connection is monosynaptic (Fig. 5C, n = 11).

We next compared the dynamics of firing during repetitive ATN fiber stimulation with low light intensities (0.1–0.5 mW; Fig. 6A-C). The tested frequencies ranged from 10 to 70 Hz. The first light pulse in a train very often failed to evoke EPSPs, or, the EPSPs were too small to induce spiking responses. The following simulations led to more reliable EPSP generation that could reach firing threshold and thus initiate action potentials. We quantified the failure rate for EPSP initiation for the first and second pulse of stimulation. Failures occurred with a 49 % probability for the first pulse (success rate, 0.51 ± 0.06) and 22 % probability for the second pulse (success rate, 0.78 ± 0.05; Fig. 6D). Across all frequencies, failures were significantly reduced at the second pulse of stimulation. The probability to initiate firing in VIP interneurons increased for later pulses in a train, and in particular for higher stimulation frequencies that favored EPSP summation. Spiking probabilities were highest for the sixth pulse at 30 Hz and the seventh pulse at 10 Hz and at 70 Hz (n = 11 neurons from 3 animals, Fig. 6E). High spiking probability was maintained during the last 5 pulses. Strongly facilitating dynamics were apparent for 30 Hz and 70 Hz stimulations: a significant facilitation was observed for the sixth and seventh pulse at 30 Hz and 70 Hz stimulation (Kruskal–Wallis and Dunn's multiple comparison post hoc test, *<p 0.05 test; Fig. 6E) compared to the first pulse. These data indicate that ATN inputs directly connect VIP interneurons that integrate these inputs with facilitating dynamics.

Recording VIP interneurons at a slightly depolarized holding potential while stimulating afferent thalamic fibers let us distinguish direct excitatory and indirect inhibitory subthreshold components of the synaptic responses. A single stimulation could induce either an EPSP only, an IPSP only, or a sequence of both (Fig. 6F, G). For low-intensity light stimulation, 69 % of trials were successful to initiate a detectable postsynaptic response, while the remaining 31 % of trials failed to do so (single stimulation or first stimulation in a train; n = 11 cells, Fig. 6G). The majority of all trials resulted either in postsynaptic excitation (55 ± 11 %) or inhibition (52 ± 16 %). Occasionally a sequence of excitatory followed by inhibitory postsynaptic potentials (6 ± 0 %) was induced.

The typical excitatory postsynaptic responses occurred with a very short latency, as measured either from EPSCs (Fig. 5D) or EPSPs (Fig. 6), as expected for a direct monosynaptic connection. The latencies for inhibitory postsynaptic events were more variable. We distinguish early inhibition with short onset latencies (early I, 4.9 ± 0.6 ms, light green histogram), and inhibition with somewhat longer onset latencies (late I, 6.6 ± 0.7 ms, dark blue histogram; Fig. 6H,I). Inhibition could be preceded by an excitatory event in the case of excitatory-inhibitory

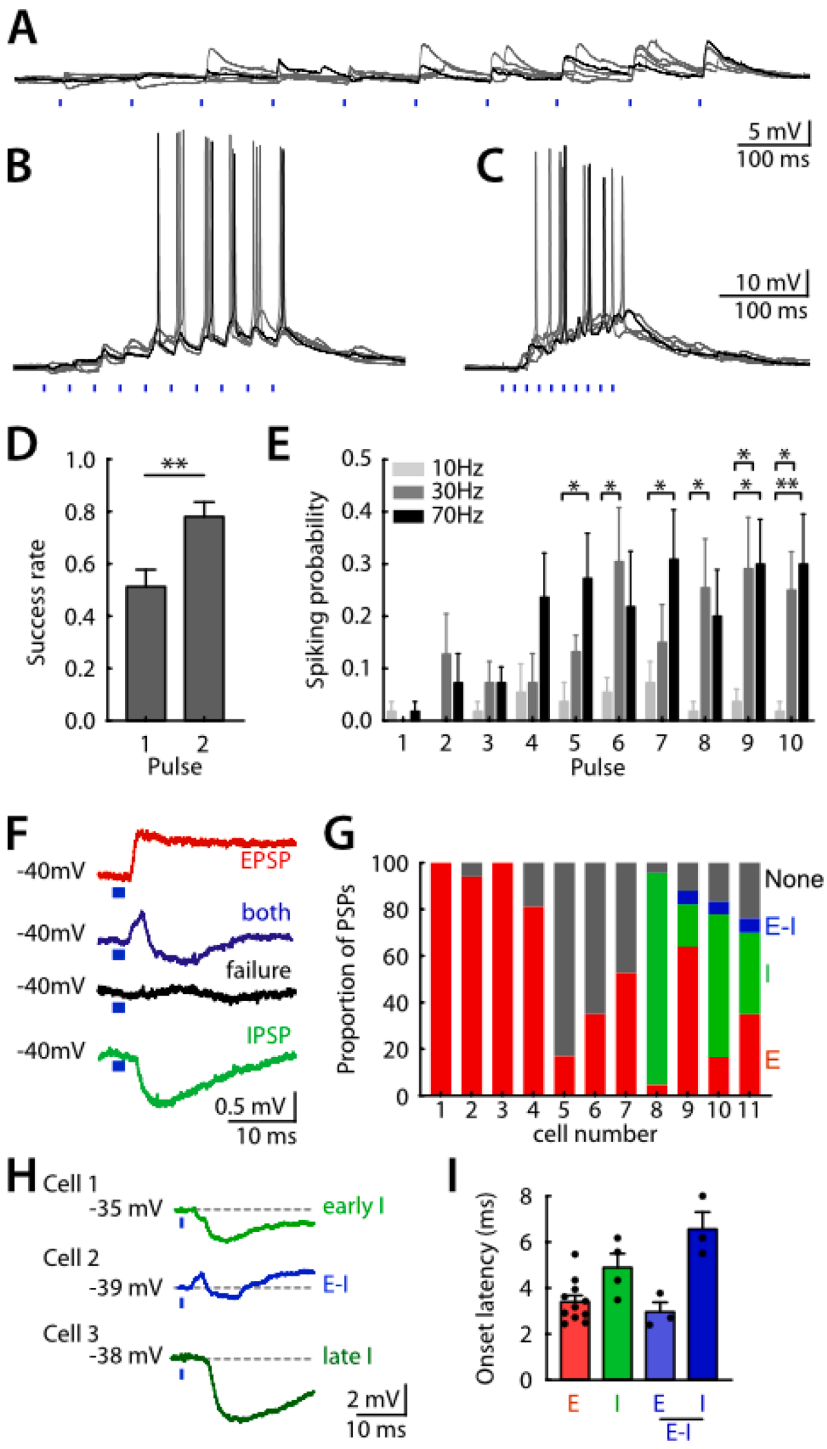

(caption on next page)

Fig. 6. VIP interneuron recruitment following optical stimulation of Chronos-expressing ATN fibers. A, B, C) Membrane potential responses of a VIP interneuron to photostimulation of ATN axons at different frequencies. D) The first and second light pulses in a train often do not lead to detectable EPSPs (success rates calculated from 5 trials in n = 11 VIP interneurons. Wilcoxon matched-pairs signed rank test, **p < 0.01. E) AP spiking probabilities following 10 repetitive stimulations at 10 Hz (light grey), 30 Hz (dark grey) and 70 Hz (black). Data are shown as mean ± SEM. Kruskal–Wallis and Dunn's multiple comparison post hoc test, *p 0.05; Two-way ANOVA, *p < 0.05. F) Individual unitary PSPs recorded from a VIP interneuron (holding potential, −40 mV). Low intensity photostimulation of ATN fibers evoked postsynaptic responses that were either EPSP-only (red), IPSP-only (green), biphasic (blue) PSPs or failures (grey) in this VIP interneuron. G) Summary of postsynaptic responses to single pulses of low intensity photostimulation grouped as EPSP-only (red), IPSP-only (green), biphasic (blue) or failures (grey) for each of the recorded VIP interneurons. Neurons #1, #4 and #5 and #10 are cluster 2 interneurons. Neurons #2, #3, #6, #7, #8, #9 and #11 are from cluster 3. H) Inhibitory postsynaptic potentials occurred either as early IPSPs (early I, light green), as sequence of excitation-inhibition (E-I, blue) or, as late IPSPs (late I, darker green). I) Onset latencies of EPSPs from 11 neurons, and of IPSPs from a subset of n = 4 VIP interneurons. (For interpretation of the references to color in this figure legend, the reader is referred to the web version of this article.)

postsynaptic responses (E-I). Excitatory events had very short latencies when occurring alone (excitation only, 3.4 ± 0.3 ms) and when followed by an inhibitory response (excitatory-inhibitory response, E-I, 2.9 ± 0.4 ms; Fig. 6H, I).

Discussion

Here we report for the first time the layer distribution, morphologies, and electrophysiological properties of VIP interneurons in the presubiculum. We find a high specificity of the VIPcre driver mouse line, validated by VIP immunoreactivity of tdTomato labeled neurons. Presubicular VIP interneurons are highly excitable. They can be divided into groups based on their electrophysiological properties. At least a subset of VIP interneurons receives anterior thalamic input, which may shape HD signal integration and updating via disinhibition.

VIPcre mice have been used previously for studies on other hippocampal regions. Our result on the overlap between tdTomato-positive cells and VIP immunoreactivity was similar to that reported for hippocampal area CA1 and dentate gyrus (Wei et al., 2021), suggesting that this mouse line is well-suited for studying VIP interneurons in the hippocampus and in the presubicular HD cortex. The quantification of the layer distribution and density of VIP interneurons in the PrS shows an absence of VIP interneurons in layer I, which is a largely cell free layer (Simonnet et al., 2013). Layer II has an overall high cell density, and the highest density of VIP interneurons per volume in the PrS. In layer III, the density of VIP interneurons decreased, and further so in deep layers IV and V/VI. Presubicular VIP cell density is similar to that of VIP cells in the barrel cortex showing a clear peak in superficial layer II/III (Prönneke et al., 2015). This layer distribution of VIP cells contrasts with that of SST interneurons, that are more densely distributed in the deep layers. It is more similar to that of PV interneurons with a high density in layer III (Nassar et al., 2015). The layer distribution of VIP interneuron somata may not predict their connectivity. Indeed, we show in Fig. 1 that the axons of VIP cells mostly ramify in layer III and to a lesser extent in the deep layers.

VIP interneurons co-express other neurochemical markers. Previous work from our group found a substantial portion of all GABAergic neurons (9 %) co-expressing VIP and calretinin (CR) in the presubiculum (Lofredi, 2017). The majority of VIP+ cells (78 %) were also positive for CR, and most numerous in layers II and III. VIP+/CR+ co-expressing neurons also exist in other cortical areas and in the hippocampus (termed type 3 interneuron-specific interneurons (IS3), Guet-McCreight et al., 2020; Francavilla et al., 2015; see also Kawaguchi and Kubota, 1997; Gonchar et al., 2008; Xu et al., 2010; Somogyi and Klausberger, 2005). VIP+/CR+ interneurons in the hippocampus are vertical mono- or bipolar cells, mediating disinhibition, while VIP+/CCK+ basket cells are multipolar and target the perisomatic region of CA1 pyramidal neurons (Acsády et al., 1996, Tyan et al., 2014). VIP interneuron co-expression of either CR or CCK appears to be exclusive (Kawaguchi and Kubota, 1997; Xu et al, 2010; Somogyi and Klausberger 2005; Huang and Paul, 2019). Sparsely distributed throughout the cortex are VIP interneurons (0.5 %) that co-express choline acetyl-transferase (ChAT; von Engelhardt et al., 2007; Dudai et al., 2020). We speculate that the groups of VIP interneurons in the presubiculum described here might correspond to distinct molecular profiles of VIP interneurons.

The classification of interneurons relies on multiple criteria, including electrophysiological properties, and also morphology, molecular markers and their transcriptome (Parra et al., 1998; Markram et al., 2004; Petilla Interneuron Nomenclature Group, 2008; Huang and Paul, 2019; Gouwens et al., 2020). Several electrophysiological parameters may be obtained from the voltage responses of neurons to hyperpolarizing and depolarizing current steps (Nassar et al., 2015; Simonnet et al., 2013). Here, we used an unsupervised cluster analysis (Ward, 1963) based only on electrophysiological parameters to search for potential subpopulations of VIP interneurons. Our analysis revealed two groups of VIP interneurons that segregated from a cluster containing the reference group of presubicular pyramidal cells, with distinct firing patterns and action potential shapes. A third group of VIP interneurons clustered together with the pyramidal cells (Fig. 3). The input resistance values were very high in all groups of presubicular VIP interneurons (in particular in Clusters 1 and 2). Indeed, input resistance may vary depending on the holding membrane potential it is measured at. Here it was calculated around −65 mV (in a voltage range between −55 mV and −75 mV), which is the region of the highest resistance (cf Fig. 3E). Therefore, the presubicular VIP interneurons in Cluster 1 and 2 may be similar to VIP+/CR+ neocortical and hippocampal IS3 interneurons, that are identified by a high input resistance, excitability and irregularly spiking firing pattern (Porter et al., 1998; Tyan et al., 2014; Miyoshi et al., 2010; Badrinarayanan et al., 2021). Presubicular VIP interneurons may also possess these combined features. They differ from VIP+/CCK+ basket cells in the hippocampus and from long range projecting hippocampal VIP interneurons, as those have a lower input resistance (Chamberland et al., 2010; Tyan et al., 2014; Francavilla et al., 2018). Those might be comparable to the group of VIP interneurons in cluster 3. Many presubicular VIP interneurons did not sustain firing over the 800 ms depolarization, with irregular firing patterns similar to the morpho-electric transcriptomic Vip-MET type 2 to 5 of visual cortex (Gouwens et al., 2020). The membrane potential in presubicular VIP interneurons (overall average, −55 ± 1 mV) was relatively depolarized, similar to cortical irregular spiking VIP interneurons (Miyoshi et al., 2010) and to VIP interneurons in the medial entorhinal cortex (Badrinarayanan et al., 2021). Comparable RMP values were also found in Martinotti type SST interneurons (Simonnet et al., 2017, Nassar et al., 2018). We note that the variance of electrical properties within our VIP interneuron groups is relatively high, pointing to possible additional subdivisions and heterogeneity within the subtypes. The low number of reconstructed VIP interneurons does not allow correlating the electrophysiological features of each group with particular morphological traits. More reconstructions are needed to determine if VIP interneuron heterogeneity of electrophysiological properties correlates with morphological features.

Across the cortex and the hippocampus, GABAergic interneurons with various intrinsic properties, connectivities and synaptic dynamics are known to shape circuit operations (Rudy et al., 2011; Pfeffer et al., 2013; Tremblay et al., 2016). Inhibitory-to-inhibitory synaptic interactions among VIP, SST, and PV interneurons maintain a balance between inhibition and disinhibition, and participate in stabilizing cortical circuit functions (Ozeki et al., 2009; Litwin-Kumar et al., 2016;

Millman et al., 2020; Sadeh and Clopath, 2021). The activity of VIP interneurons can be regulated through cholinergic inputs, according to context. They become activated in relation to locomotion, arousal, surprise and the expectation of reward (Lee et al., 2013; Fu et al., 2014; Pakan et al., 2016; Dipoppa et al., 2018; Ramamurthy et al., 2023). VIP interneurons mediate gain control of cortical activity via disinhibition, as a function of behavioral states (Fu et al., 2014). In visual cortex, VIP interneurons inhibit SST interneurons in particular, altering state-dependent modulation of cortical activity and visual perception (Ferguson et al., 2023). In barrel cortex, VIP interneurons mediate disinhibition and gate plasticity of intracortical synapses, following their activation by high-order thalamic input (Williams and Holtmaat, 2019). In the hippocampus, VIP interneuron mediated disinhibition supports spatial reward learning (Turi et al., 2019).

In the presubicular HD cortex, the excitatory-inhibitory interactions between pyramidal neurons and Martinotti type SST interneurons stabilize the HD attractor network locally (Simonnet et al., 2017). What could be the functional role of VIP interneurons? Our data show that at least two groups of presubicular VIP interneurons receive direct thalamic input, and the facilitating recruitment of VIP interneurons matches that of Martinotti type interneurons (which are indirectly recruited, Simonnet et al., 2017). We speculate that VIP interneurons may become active when the internal prediction of the HD signal does not match the current landmark context signaled by retrosplenial input (Van Groen and Wyss, 1990; Vann et al., 2009; Vogt and Miller, 1983). VIP interneuron inhibition of SST interneurons would then destabilize the bump state, and weaken the attractor, which may be a necessary condition for HD updating. And because SST interneurons synapse on the dendrites of pyramidal neurons, VIP disinhibition may also gate dendritic integration of thalamic and retrosplenial synaptic excitation in pyramidal neurons (Miles et al., 1996; Richevaux et al., 2023). More knowledge on the microcircuit connectivity and input–output characteristics of VIP interneurons will be necessary to infer how they govern circuit computation. Different subpopulations of VIP interneurons might differentially target principal cells or other interneurons, mediating inhibitory or disinhibitory operations. Simultaneous double recording of VIP interneurons together with pyramidal cells, or PV or SST interneurons could address this point. Deciphering the role of VIP interneurons for the presubicular HD circuit function will require the manipulation or the direct recording of identified VIP interneurons *in vivo*. In the future, experimental access to genetically defined VIP interneuron subtypes will be helpful. Enhancer-driven viral vectors (Nair et al., 2020) promise to enable subtype and circuit specific functional studies.

Author contributions

Conception and design of the work: MN, LR, DF. Acquisition, analysis or interpretation of data: MN, LR, DL, DT, EM, DF. Drafting the work or revising it critically: MN, LR, DF. Final approval of the version to be published: MN, LR, DL, DT, EM, DF.

CRediT authorship contribution statement

Mérie Nassar: Conceptualization, Data curation, Formal analysis, Investigation, Methodology, Supervision, Validation, Visualization, Writing – original draft, Writing – review & editing. **Louis Richevaux:** Conceptualization, Data curation, Formal analysis, Investigation, Methodology, Supervision, Validation, Visualization, Writing – original draft, Writing – review & editing. **Dongkyun Lim:** Investigation. **Dario Tayupo:** Investigation. **Erwan Martin:** Investigation. **Desdemona Fricker:** Conceptualization, Data curation, Funding acquisition, Methodology, Project administration, Supervision, Validation, Writing – original draft, Writing – review & editing.

Declaration of Competing Interest

The authors declare that they have no known competing financial interests or personal relationships that could have appeared to influence the work reported in this paper.

Acknowledgements

We benefited from support by the BioMedTech Facilities at Université Paris Cité (Institut National de la Santé et de la Recherche Médicale Unité S36/Unité Mixte de Service 2009). We acknowledge technical assistance from Fabrice Licata from the UPC Microscopy platform. This work was financially supported by the Centre National de la Recherche Scientifique and the Université Paris Cité. DF received funding from the Agence Nationale de la Recherche from the ERA-NET NEURON Program (ANR-20-NEUR-0005 VELOSO) and the FLAG-ERA HBP Program (ANR-21-HBPR-0002 VIPattract).

Appendix A. Supplementary data

Supplementary data to this article can be found online at https://doi.org/10.1016/j.neuroscience.2024.09.032.

References

Acsády, L., Görcs, T.J., Freund, T.F., 1996. Different populations of vasoactive intestinal polypeptide-immunoreactive interneurons are specialized to control pyramidal cells or interneurons in the hippocampus. Neuroscience 73 (2), 317–334.
Apicella, A.J., Marchionni, I., 2022. VIP-expressing GABAergic neurons: disinhibitory vs. inhibitory motif and its role in communication across neocortical areas. Front. Cell. Neurosci. 16, 811484.
Badrinarayanan, S., Manseau, F., Williams, S., Brandon, M.P., 2021. A characterization of the electrophysiological and morphological properties of vasoactive intestinal peptide (VIP) interneurons in the medial entorhinal cortex (MEC). Front. Neural Circuits 15, 653116.
Boccara, C.N., Sargolini, F., Thoresen, V.H., Solstad, T., Witter, M.P., Moser, E.I., Moser, M.-B., 2010. Grid cells in pre- and parasubiculum. Nat. Neurosci. 13, 987–994.
Booker, S.A., Vida, I., 2019. Morphological diversity and connectivity of hippocampal interneurons. Cell Tissue Res. 373 (3), 619–641.
Chamberland, S., Salesse, C., Topolnik, D., Topolnik, L., 2010. Synapse-specific inhibitory control of hippocampal feedback inhibitory circuit. Front. Cell. Neurosci. 15 (4), 130.
Cruikshank, S.J., Urabe, H., Nurmikko, A.V., Connors, B.W., 2010. Pathway-specific feedforward circuits between thalamus and neocortex revealed by selective optical stimulation of axons. Neuron 65 (2), 230–245.
Dipoppa, M., Ranson, A., Krumin, M., Pachitariu, M., Carandini, M., Harris, K.D., 2018. Vision and locomotion shape the interactions between neuron types in mouse visual cortex. Neuron 98 (3), 602–615.e8.
Dudai, A., Yayon, N., Lerner, V., Tasaka, G.I., Deitcher, Y., Gorfine, K., Niederhoffer, N., Mizrahi, A., Soreq, H., London, M., 2020. Barrel cortex VIP/ChAT interneurons suppress sensory responses in vivo. PLoS Biol. 18 (2), e3000613.
Duszkiewicz, A.J., Orhan, P., Skromne Carrasco, S., Brown, E.H., Owczarek, E., Vite, G. R., Wood, E.R., Peyrache, A., 2024. Local origin of excitatory-inhibitory tuning equivalence in a cortical network. Nat. Neurosci. 27 (4), 782–792.
Ferguson, K.A., Salameh, J., Alba, C., Selwyn, H., Barnes, C., Lohani, S., Cardin, J.A., 2023. VIP interneurons regulate cortical size tuning and visual perception. Cell Rep. 03.14.532664.
Francavilla, R., Luo, X., Magnin, E., Tyan, L., Topolnik, L., 2015. Coordination of dendritic inhibition through local disinhibitory circuits. Front. Synaptic Neurosci. 7, 5. https://doi.org/10.3389/fnsyn.2015.00005.
Francavilla, R., Villette, V., Luo, X., Chamberland, S., Muñoz-Pino, E., Camiré, O., Wagner, K., Kis, V., Somogyi, P., Topolnik, L., 2018. Connectivity and network state dependent recruitment of long-range VIP-GABAergic neurons in the mouse hippocampus. Nat. Commun. 9 (1), 5043.
Fu, Y., Tucciarone, J.M., Espinosa, J.S., Sheng, N., Darcy, D.P., Nicoll, R.A., Huang, Z.J., Stryker, M.P., 2014. A cortical circuit for gain control by behavioral state. Cell 156 (6), 1139–1152.
Golowasch, J., Thomas, G., Taylor, A.L., Patel, A., Pineda, A., Khalil, C., Nadim, F., 2009. Membrane capacitance measurements revisited: dependence of capacitance value on measurement method in nonisopotential neurons. J. Neurophysiol. 102 (4), 2161–2175.
Gonchar, Y., Wang, Q., Burkhalter, A., 2008. Multiple distinct subtypes of GABAergic neurons in mouse visual cortex identified by triple immunostaining. Front. Neuroanat. 1, 3.
Gouwens, N.W., Sorensen, S.A., Baftizadeh, F., Budzillo, A., Lee, B.R., Jarsky, T., Alfiler, L., Baker, K., Barkan, E., Berry, K., Bertagnolli, D., Bickley, K., Bomben, J., Braun, T., Brouner, K., Casper, T., Crichton, K., Daigle, T.L., Dalley, R., de Frates, R.

Discussion

My PhD thesis characterised the anatomical and electrophysiological properties of thalamic neurons within the HD network. I identified topographically organised neurons projecting to cortical areas, with bifurcating neurons located at the overlap of the subpopulations in the AD and AV. I demonstrated that AD and AV neurons are electrophysiologically and morphologically distinct, although not in a projection-specific manner. Furthermore, I revealed ipsilaterally weighted input efficiency in the parallel mammillothalamic pathways, LMN-AD and MMN-AV. In addition, I found a cholinergic modulatory effect on thalamic neurons and suggest how to further examine this point *in vivo*. I also contributed to related research led by previous lab members. The first study examined the functional integration of ATN and RSC inputs in layer III of PrS, and the second characterised the electrophysiological and morphological properties of presubicular VIP interneurons.

In the following, I will discuss my findings in the AD and AV, interpreting the results in relation to the literature. The discussion is divided into five parts: 1) re-visiting the mammillo-thalamo-cortical pathway by comparing the conventional view with my result, 2) the distinct electrophysiological properties of AD and AV neurons, together with their genetic profiles regarding ion channels, 3) linking the functionally distinct roles of AD and AV in the HD system with their electrophysiological properties, 4) potential cholinergic modulation in the AD and AV, and 5) anatomical convergence of AD and AV inputs in the HD cortices. Technical and conceptual limitations, as well as direction of future studies, will also be addressed within each part.

1 The mammillo-thalamo-cortical pathway revisited

The limbic system forms a critical axis linking the MBO with the ATN and, in turn, the cortex. Within this framework, the mammillo-thalamo-cortical pathway represents a major route where subcortical structures influence higher-order cortical functions. This pathway not only preserves the historical significance of Papez's circuit but has also become central to modern models of spatial system and memory.

The mammillothalamic pathways have been described as consisting of two parallel and separate circuits: the LMN-AD pathway and the MMN-AV pathway (Cruce, 1975; Dillingham et al., 2015; Guison et al., 1995; Jankowski et al., 2013; Seki & Zyo, 1984; H. Shibata, 1992; Veazey et al., 1982). Anatomical tracing studies have established that LMN projects bilaterally to AD, and that bilateral lesion of LMN is required to abolish HD activity in AD (H. T. Blair et al., 1999). In contrast, the laterality of MMN-AV connectivity has remained less clear. The prevailing view is that MMN projects to the ipsilateral but not the contralateral AV (Dillingham et al., 2015; H. Shibata, 1992; Vann & Aggleton, 2004; Wiener & Taube, 2005). However, as noted in the introduction, although recent reviews described MMN-AD connectivity as strictly ipsilateral (Cruce, 1975; Dillingham et al., 2015; Seki & Zyo, 1984; H. Shibata, 1992; J. S. Taube, 2007; Vann & Aggleton, 2004; Veazey et al., 1982; Wiener & Taube, 2005), some of the anatomical tracing results did show a small contralateral contribution (See Introduction 6 and Figure 6.3). Beyond this point, it has not been shown whether mammillary inputs establish synaptic connections onto specific thalamocortical projection neurons. Thus, current evidence leaves important gaps in our anatomical and functional understanding of the mamillo-thalamo-cortical pathway. My monosynaptic retrograde tracing experiments and optogenetic experiments provide several advances. First, I demonstrated that mammillary inputs form excitatory monosynaptic connections onto thalamic projection neurons. Second, I observed a small population of contralaterally labelled MMN neurons from retrograde monosynaptic tracing, suggesting bilateral MMN-AV connectivity. Some previous studies had also found retrogradely labelled contralateral MMN neurons, using unilateral fast blue injections into ATN, but the authors chose to neglect the - admittedly sparse - labelling of cells in the contralateral side (Mathiasen et al., 2021). The bilateral projection resulting from unilateral Chronos expression in the MBO provides additional support for contralateral connectivity. Third, my optogenetics data confirm that mammillary input is functionally stronger from the ipsilateral pathways. In AD, contralateral input connectivity was frequently observed (85% of recordings showed oEPSPs). These inputs were rather weak, with low spike probability (18%) and smaller EPSC amplitude compared to the ipsilateral inputs. In AV, the contralateral input connectivity rate was lower (39%), but when present, the inputs were functionally efficient, supporting high spiking probability (57%). Finally, in the case of Chronos expression restricted to LMN, postsynaptic responses were observed exclusively in AD but not in AV, corroborating the parallel nature of the lateral (to AD) and medial (to AV) mammillothalamic pathways. Therefore, my results provide evidence that the mammillo-thalamo-cortical pathway is monosynaptic and bilateral for both MMN-AV and LMN-AD, with stronger input efficiency on the ipsilateral side.

Several methodological strengths and limitations should be discussed. First, in the optogenetic experiments, Chronos was expressed unilaterally in the MBO, and only cases with

confirmed unilateral expression were selected for analysis. Even so, we cannot fully exclude the possibility of minimal viral overflow which could not be detected by imaging. Second, although monosynaptic tracing revealed clearly labelled contralateral neurons in the MMN, technical constraints limited the specificity of this approach. In particular, we were not able to separately label MMN-AV and LMN-AD pathways because the subnucleus-specific injection was difficult to achieve. Therefore, TVA-virus was delivered to both AD and AV and we had to rely on previous evidence for the existence of parallel mammillothalamic pathways. Also, the viral set we employed showed higher efficiency of TVA infection in AV, resulting in fewer AD neurons. Thus, an optimised viral strategy with improved targeting selectivity will provide a more definitive picture of mammillothalamic connectivity.

2 The distinct electrophysiological properties of AD and AV neurons

Based on the analysis of the intrinsic electrophysiological characteristics of AD and AV neurons, I sought to understand how these properties arise from their genetic profiles. Phillips et al. (2019) presented genetic profiles of thalamic nuclei using the 500 most differently expressed genes. Within these thalamic nuclei, AD formed its own category, indicating that it is genetically distinct from AV. Since my result also showed clear electrophysiological differences between AD and AV neurons, I interpreted how these contrasting properties may be explained by their divergent genetic profiles (Figure 20).

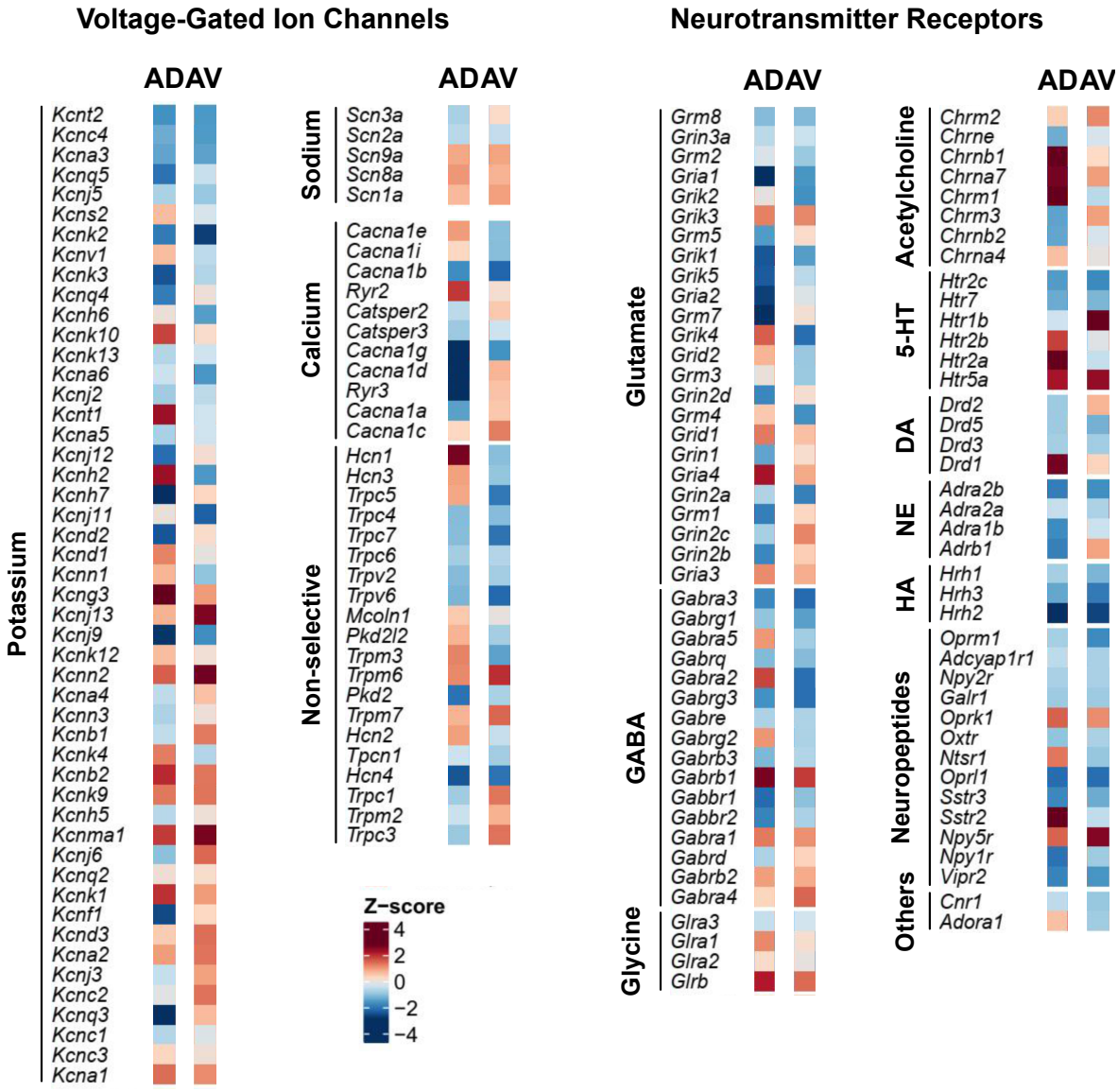

Figure 20 Expression profiles of AD and AV.

Expression profiles of voltage-gated ion channels and neurotransmitter receptors in AD and AV are shown. Expression levels are expressed as Z-scores, where positive values indicate above-average expression relative to the dataset mean (including whole thalamic regions), and negative values indicate below-average expression. The figure shows only AD and AV profiles adapted from Phillips et al. (2019)

The resting membrane potential was significantly more depolarised in AD neurons (approximately -60 mV) compared to AV neurons (approximately -71 mV). To investigate the underlying mechanisms of this difference, I first examined the expression of leak K^+ channels belonging to the KCNK family. These leaky K^+channels typically contribute to membrane hyperpolarisation by facilitating a persistent outward K^+ current, thereby stabilising the resting potential close to the K^+ equilibrium. However, the overall expression pattern of KCNK family genes was similar between AD and AV neurons. Kcnk1, Kcnk4, and Kcnk10 were rather expressed at relevantly higher levels in AD neurons, despite these neurons exhibiting more depolarised resting membrane potential. This suggests additional factors are involved in setting the resting potential. Next, I checked the expression of Kv7 potassium channels (encoded by the Voltage-gated potassium channel (Kv7) (KCNQ) family), which generate the neuronal M-current. These channels promote K^+ efflux at subthreshold, playing a critical role in maintaining hyperpolarised resting membrane potential (Borgini et al., 2021). In AD neurons, Kv7 channel expression was significantly lower than AV neurons, potentially diminishing this hyperpolarising influence. Furthermore, HCN channel expression was markedly higher in AD neurons. HCN channels produce the I_h current, which is permeable to both Na^+ and K^+ ions. At resting membrane potentials, HCN channels generate a net inward current dominated by Na^+ influx, thereby depolarising the membrane (Kase & Imoto, 2012). Experimental evidence further demonstrates that blockade of HCN channels results in membrane hyperpolarisation (Combe & Gasparini, 2021; Endo et al., 2008). Many AD and AV neurons in my experiments also became more hyperpolarised following the ZD7288 application, although the effect did not reach statistical significance (Figure 4A-C in my manuscript). Taken together, the combination of reduced Kv7 channel expression and increased HCN channel expression likely contribute to the depolarised resting membrane potential observed in AD neurons compared to AV neurons.

The differential HCN expression also explains the larger sag ratio observed in AD neurons. HCN channels generate a mixed Na^+/K^+ current that becomes prominent when the membrane is hyperpolarised, resulting in a characteristic depolarising sag response. Thus, high HCN expression in AD neurons produces significant sag, whereas AV neurons, with reduced HCN expression, show little sag. This interpretation is further supported by my ZD7288 experiments: pharmacological blockade of HCN channels abolished the sag in AD neurons.

Compared with AV neurons, AD neurons show a faster membrane time constant, lower input resistance, and a steeper input-output curve. These intrinsic properties are determined by membrane conductances, which arise from the composite activity of several ion channels including leak K^+ channels, and voltage-gated Na^+/K^+ channels. However, it is difficult to directly link the differences in these electrophysiological properties as expression levels of individual isoforms within the same channel families varied, with some higher in AD and other higher in AV. One possible exception is KCNK which was more strongly expressed in AD and may contribute to the lower input resistance by enhancing resting K^+conductance. Nevertheless, the overall expression profiles of these channels were broadly similar between the two thalamic regions, and the inconsistency across isoforms makes it difficult to draw a firm relationship. Another possible explanation lies in the higher expression of HCN channels in AD. HCN channels are open near resting potential and carry an inward depolarising. This conductance depolarises the membrane, lowers the input res-

istance, and shortens the time constant, thus promoting rapid and robust responses to injected current. In addition, the pharmacological evidence from my results (Figure 4 in my manuscript) supports this interpretation: blockade of HCN channels selectively increased input resistance in AD neurons, while AV neurons were largely unaffected. The decreased rebound spike probability after HCN channel blockade indicates that the higher rebound activity observed in AD neurons arises from their stronger HCN channel expression. In summary, while other factors may also contribute to the neuronal excitability, enhanced HCN channel activity explains some differences in membrane properties between AD and AV neurons.

The distinct genetic channel profiles of AD and AV neurons provide possible mechanistic explanations for their typical firing characteristics. In AD, Cacna1i gene, encoding CaV3.3 that mediatesLow voltage activated (LVA) T-type voltage gated calcium currents, is expressed at higher levels than in AV and this might contribute to its rebound activity and sustained firing. CaV3.3 is known for its slow activation and inactivation (He et al., 2022; Monteil et al., 2000; Perez-Reyes, 2003). Hyperpolarisation de-inactivates T-type channels such that they can generate low-threshold calcium currents triggering rebound spikes. Indeed, deletion of CaV3.3 abolished the rebound spiking activity in the TRN (Astori et al., 2011). Following suprathreshold current injection, AD neurons display adaptive and sustained spiking activity. The slowly inactivating CaV3.3 and persistent HCN currents maintain membrane depolarisation, supporting ongoing excitability. Adaptation could be achieved through cumulative inactivation of Na^+ and Ca^{2+} channels, resulting in slowing firing rate. Furthermore, the high expression of Kcnt1, which encodes a Na^+-activated K^+ channel, may contribute to adaptive firing, as deletion of this gene has shown to impair spike-frequency adaptation (Martinez-Espinosa et al., 2015). In contrast, AV neurons exhibit relatively higher expression of Cacna1g encoding CaV3.1, a fast-inactivating T-type channel, and Cacna1a (CaV2.1, P/Qtype), which together promote classic thalamocortical burst firing, a mechanism experimentally demonstrated in ventrobasal thalamic relay neurons (Y. Chen et al., 2014; D. Kim et al., 2001). Upon depolarising current injection, the rapid recruitment and inactivation of CaV3.1 trigger a brief, high-frequency burst. These bursts could be quickly curtailed as T-type and P/Q type channel inactivation and repolarising potassium current activation inhibit subsequent firing. The low probability of rebound spiking in AV is likely due to lower T-type and HCN channel expression.

Regarding AP dynamics, AV neurons showed delayed onset of the rheobase action potential. AV express relatively higher A-type potassium channels Kv4.2 and Kv4.3 encoded by Kcnd2 and Kcnd3 which are known to transiently oppose depolarisation and delay spike onset. Indeed, the deletion of Kv4.2 and Kv4.3 can change the intrinsic electrophysiological properties of cortical pyramidal neurons, resulting in earlier onset of action potential and wider action potentials (Cai et al., 2004; Carrasquillo et al., 2012).

Post-train AHP was identified as a brief sag-like hyperpolarisation immediately following the cessation of positive current injection in AD neurons. This feature is likely related to HCN channel activity, as these channels are rapidly recruited when the membrane potential is transiently driven below the typical resting potential. Although AD neurons rest at approximately -60 mV, recordings were performed at -70 mV to enable comparison with AV neurons. This additional hyperpolarisation may have contributed to the appearance

of the post-train AHP. Supporting this interpretation, when recordings were made at -60 mV the post-train AHP was attenuated, and it was completely abolished by the application of HCN channel blocker ZD7288 (Figure 4C in my manuscript). In the PCA, post-train AHP and sag ratio showed a relatively strong covariance (+0.71), consistent with a shared mechanism.

Taken together, the functional divergence between AD and AV neurons can be partially explained by their distinct ion channel expression profiles. Their molecular signatures provide plausible mechanisms for the differences in intrinsic properties observed between the two populations. Of course, this interpretation is limited by its reliance on a single large-scale transcriptomic dataset of thalamic nuclei. Also, mRNA expression level may not directly reflect functional channel abundance at the membrane. Electrophysiological signals also arise from the coordinated activity of many conductances, rather than the action of individual channels alone. A precise mapping between ion channel identity and electrophysiological properties will require more work, including targeted pharmacological blockade and genetic manipulation, to fully define the molecular determinants of AD and AV neuronal physiology.

3 Parallel mammillothalamic pathways in the HD system: linking functional and electrophysiological characteristics in AD and AV

How might the electrophysiological properties that characterise AD and AV neurons contribute to enhance HD activity? As summarised in the introduction, the functional contributions of AD and AV thalamic nuclei to HD processing are distinct: AD exhibits classical HD activity, whereas AV shows theta-modulated HD activity with phase precession. Linking my results with previous reports, a broader hypothesis can be suggested. LMN HD cells not only encode HD but also anticipate future orientation by shifting their PFD depending on the direction of the head turn. During clockwise movements, HD tuning curves shift leftward, and during counterclockwise movements, they shift rightward (Stackman & Taube, 1998; Wiener & Taube, 2005). Importantly, this shift interacts with hemispheric bias in angular velocity signals. LMN HD cells show subtle asymmetries in their tuning depending on the direction of head turns, which differs between left and right hemisphere: LMN neurons in the right hemisphere sharpen during clockwise turns, whereas LMN neurons in the left hemisphere sharpen during counterclockwise turn. My results raise the possibility that AD functions as an integrative hub for asymmetric LMN inputs across hemispheres, with stronger contributions from the ipsilateral side. AD HD cells inherit lateralised anticipatory signals, as they continue to displace clockwise versus counterclockwise shifts. However, the magnitude of these shifts is reduced and the tuning curves are narrower than in LMN. AD receives strong ipsilateral input that preserves hemispheric preference, while contralateral input may balance these asymmetries to stabilise directional coding. This could ensure that the HD representation in AD remains predictive yet less shifted by turn-specific asymmetries, supporting its role in refining HD signals. This refinement may further take place along the thalamocortical pathway, as angular velocity effects are observed in AD as well as in presubicular principal neurons and fast-spiking interneurons (H. Blair & Sharp, 1995; Preston-Ferrer et al., 2016; Spalla et al., 2022). Moreover, the shift of the PFD depending on turning direction and the tuning width are reduced in the thalamic and cortical HD regions (Figure 5.3).

In the case of vestibular deficits, the contralateral LMN contribution may also have a compensatory function. A study from El Mahmoudi et al. (2025) reported that unilateral lesion of the vestibular nuclei disrupted HD activity in the ipsilateral thalamus, but this was recovered over time. One possible interpretation is that contralateral LMN-AD connectivity may undergo plastic changes to strengthen their functional connectivity under conditions of vestibular imbalance. The presence of dendritic spines on thalamic projecting neurons supports the possibility that these cells possess the structural basis for synaptic plasticity (Figure 5D-(iii) in my manuscript). In this view, contralateral projection could provide a reserve capacity that stabilises the HD signal when ipsilateral inputs are compromised.

The intrinsic properties of AD neurons may directly support their role as HD neurons. Their relatively depolarised resting membrane potential and their excitability may make these neurons well suited to rapidly update ongoing directional signals in response to incoming inputs. While the electrophysiological differences between AD and AV were

compared at -70 mV (Table 1 in the manuscript), it is important to consider the properties of AD neurons at their physiological resting potential, -60 mV. At this potential, the AP threshold was slightly depolarised (-29.1 ± 0.9 mV at -60 mV and -30.8 ± 1.0 mV at -70 mV, Figure 3 - figure supplement 3 and table supplement 1 in my manuscript), and relatively small positive currents could drive AD neurons to fire action potentials (48 ± 4 pA at -60 mV and 77 ± 4 pA at -70 mV). AD neuron resting excitability showed a steep input-output slope (283 ± 47 Hz/nA at -60 mV and 127 ± 21 Hz/nA at -70 mV) and relatively high firing rates at 200 pA (78 ± 4 Hz at -60 mV and 47 ± 4 Hz at -70 mV). However, their input resistance was rather lower, at -60 mV (151 ± 10 MΩ at -60 mV and 170 ± 13 MΩ at -70 mV). This suggests that AD neurons may act as a 'selective integrative amplifier' within the HD system. At the subthreshold level, their relatively less excitable state may filter out noise, while coherent, convergent inputs can summate to reach threshold and reliably trigger spiking activity. Their excitability can be robust once reaching the threshold. This interpretation is consistent with my optogenetic experiments showing high connectivity rate between mammillary input and AD neurons, but relatively low oEPSC amplitudes at subthreshold light intensities, that were not strong enough to directly initiate action potentials. Photostimulation with increasing intensities led to a gradual increase in spiking probability. Such properties align well with attractor network models, where stable signals emerge from the collective activity of many inputs. Thus, the intrinsic electrophysiological mechanisms of AD neurons may be well suited to generate reliable and stable HD signals, supporting their role in classical HD coding.

In addition, their adaptive yet sustained firing pattern may support stable HD coding. The presence of a pronounced sag and strong rebound activity may further contribute to this function by enabling AD neurons to integrate fluctuating synaptic inputs while maintaining responsiveness after hyperpolarisation. Together, these features provide a cellular basis for the ability of AD to sustain a predictive and continuously updated HD signal, integrating and stabilising the input it receives from LMN.

The MMN projection likely provides the principal source of theta rhythmic drive to the AV. MMN contains theta-rhythmic neurons and receives inputs from the VTN and the MS, both essential for hippocampal theta modulation (Dillingham et al., 2015; Gonzalo-Ruiz et al., 1992; King et al., 1998; Kirk et al., 1996; Kocsis & Vertes, 1994; Kocsis et al., 2001; R. P. Vertes et al., 2004). Consistent with this organisation, a large proportion of AV neurons discharge rhythmically in synchrony with LFPs and hippocampal CA1 theta, a pattern far less common in neighbouring AD (Albo, 2003; R. Vertes et al., 2001). Many AV neurons are theta-bursting, with burst segments usually comprising 2-5 spikes (Tsanov, Chah, Vann et al., 2011; Welday et al., 2011). Simultaneous recordings revealed strong coherence between AV and hippocampal CA3 in the 7-10 Hz range, with AV activity leading hippocampal theta by approximately 7-10 ms, suggesting a potential pacing influence rather than a passive relay (Tsanov, Chah, Vann et al., 2011). Other studies indicate frequency-specific contributions of MMN and AV to hippocampal theta power, further supporting their role in organising theta dynamics (Żakowski et al., 2017). Within AV, HD, theta-modulated, and theta-by-HD cells have been reported (Lomi et al., 2023; Tsanov, Chah, Vann et al., 2011; Yoganarasimha et al., 2006). Also, recent studies (Ji, Chu et al., 2025; Ji, Lomi et al., 2025) have demonstrated a distinct relationship between theta skipping and phase precession in AV HD cells. Theta-skipping HD cells fire on alternate theta cycles. As the animal turns

its head, these cells fire as HD sweeps over their PFD. The degree of phase precession is strongly correlated with the extent of theta skipping. Those cells exhibiting robust theta skipping also show a higher probability and greater magnitude of phase precession. Therefore, HD activity in AV is distinguished by these temporal coding properties.

My anatomical tracing and optogenetic results show contralateral MMN inputs to AV can reliably evoke postsynaptic events. Considering the proportion of labelled cells and input efficiency, contralateral AV is not a primary target. Potentially, this contralateral projection could contribute as a reserve system or maintenance of bilateral theta synchrony across the limbic network. However, further studies are required to examine the functional significance of this bilateral projection.

An intriguing possibility is that theta-modulated HD signals from AV contribute to downstream computation in the PaS, which in turn provides major inputs to entorhinal grid cells (Winter et al., 2015). Theta skipping HD activity in AV (Ji, Lomi et al., 2025) may represent the source of the alternating 'sweeping' activity observed in PaS neurons (Vollan et al., 2025). Theta-skipping HD cells may coordinate rhythmic left-right alternation in internal directional signals on successive theta cycles. Importantly, these alternating population sweeps are temporally aligned with sweep dynamics in entorhinal grid cells. In this framework, AV could provide a temporarily organised HD signal that interacts with entorhinal circuitry to shape grid cell dynamics in the extended navigation system, through PaS. An unresolved question is the origin of HD signals in AV. As MMN neurons have not been reported to code for HD, the other source for HD information in AV could be the RSC and PrS, through corticothalamic feedback projections. Within this hypothesis, AV potentially acts as a site where theta rhythmic inputs from MMN converge with HD inputs from cortical sources, allowing it to deliver a temporally structured and directionally specific signal to the PaS and ultimately to the hippocampal and entorhinal navigation system.

The intrinsic electrophysiological properties of AV neurons align well with their theta rhythmic functional profile. AV neurons typically display a hyperpolarised resting membrane potential and a strong initial burst of 1-5 spikes from my results. This burst profile matches the bursts of 2-5 action potentials reported *in vivo* (Tsanov, Chah, Wright et al., 2011). In whole-cell recordings with sustained depolarisation, AV neurons generated an initial burst followed by single spikes with interspike intervals of approximately 100-200 ms during strong current injections (Figure 3 - figure supplement 2 in my manuscript). These features suggest that AV neurons intrinsically constrain their firing into periodic segments, potentially providing temporally precise output aligned with the ongoing theta cycle. The absence of sag and rebound responses further support this feature, as it limits prolonged depolarisations and enhances phasic bursting signalling. While these interpretations remain speculative, they point to a cellular mechanism by which AV preserves and provides temporally structured activity. Theta-rhythmic stimulation or resonance experiments could provide further insights.

4 Cholinergic modulation in the AD and AV and its potential effect on the HD system

I next consider cholinergic modulation in the AD and AV and its potential role for thalamic HD activity. Anatomical studies report strong ChAT staining in the AV (M. Parent & Descarries, 2008; Paxinos & Franklin, 2013; Sofroniew et al., 1985). Some reports indicate that cholinergic afferents are absent from AD (Gonzalo-Ruiz et al., 1995; Hallanger et al., 1987), yet systemic muscarinic antagonism disrupts HD activity recorded in the AD (Yoder et al., 2017). Moreover, ChAT immunostaining in Gonzalo-Ruiz et al. (1995) and M. Parent and Descarries (2008) show subtle but detectable ChAT labelling in the AD.

To investigate cholinergic neuromodulation, I applied carbachol in slices containing AD and AV neurons. My results showed that carbachol abolished action potential firing in response to small depolarising current injections, which under baseline conditions typically evoked 1-5 spikes (Figure 9). The spiking activity recovered after washout in most of the recordings. One of the possible interpretations is that cholinergic input hinders the membrane potential to reach firing threshold. Relevant reports exist that the activation of muscarinic receptors in LDT cholinergic neurons showed a direct hyperpolarisation in their membrane potential through opening G protein-coupled inward rectifying potassium (GIRK) channels (Kohlmeier & Leonard, 2006; Kohlmeier et al., 2012; Leonard & Llinás, 1994; Luebke et al., 1993). This putative mechanism is not easily reconciled with the genetic profiles of anterior thalamic neurons, where AD shows high expression of Chrnb1(nicotinic), Chrna7(nicotinic) and Chrm1(muscarinic), and AV shows high expression of Chrna7(nicotinic) and Chrm3(muscarinic), which are rather associated with membrane depolarisation and increased excitability (Figure 20) (Phillips et al., 2019). Further investigation is required to understand the molecular mechanism underlying the spike-suppressing effect of carbachol in AD and AV neurons.

I asked, which brain area provides the endogenous cholinergic input? The most probable regions are brainstem nuclei. Prior work implicates the LDT, PPN, and PAG (Gonzalo-Ruiz et al., 1995; Hallanger et al., 1987; Satoh & Fibiger, 1986). The CnF appears to be another potential source based on its high proportion of overlap between ChAT neurons and retrogradely labelled neurons projecting to AD and AV (Figure 12). Another interesting point was that ChAT positive, retrogradely labelled neurons were observed in both hemispheres of the four nuclei, suggesting bilateral projections. More experiments are needed to identify whether the cholinergic influence in the AD and AV indeed arises from these cholinergic sources.

One key question is the correlation of neuronal activity with behaviour in freely behaving animals. In a collaboration with Dr. Michael Graupner, I began to use calcium imaging for analysing HD activity in thalamic projection neurons in AD and AV. I approached it in four ways: 1) expressing GCaMP8f selectively in PrS or gRSC-projecting thalamic neurons using retro-cre and Flip-excision switch (FLEX)-GCaMP8f, 2) expressing GCaMP8f in PrS-projecting neurons and Genetically encoded red fluorescent calcium indicator (jRGECO) in gRSC-projecting neurons via retrograde viral system, then recording each population by changing Miniscopes with different optical filters, 3) expressing non-conditional GCaMP8f

in the thalamus and retrogradely labelling the thalamic neurons with retrobeads in the PrS and gRSC for *post hoc* identification, and 4) using a prism GRIN lens to have clear delineation of AD and AV during the recording using viral strategy from 2). The most successful approach in my hands was to record PrS-projecting thalamic neurons using the strategy 1) with a cylindrical GRIN lens. Preliminary data from one animal demonstrate the feasibility of analysing HD activity from AD and AV. Some practical refinements have been implemented and GRIN lens targeting needs to be optimal in each case. A 1 mm lens can span across both AD and AV, but in my current dataset the lens insertion only partially recovered the two nuclei. I attempted to align the *in vivo* imaging field with the distribution of GCaMP8f-expressing cells in *ex vivo* brain slices to assign AD or AV identity. The recorded cells were most likely thalamic projection neurons, given the conditional expression of GCaMP and taking into account the tissue distortion from the lens insertion. Overall, this result shows technical feasibility. In addition, a subset of HD-modulated cells (Cell #1 and #2 on the first and third recording day, and Cell #6, #8 and #9 on the second and third day) showed shifts in their PFD across days that were aligned in both direction and angle, a possible reflection of coherent population activity. My work has provided a foundation to pursue the study of thalamic HD activity specifically in AD and AV. Although the limited number of detected ROIs and experiments makes it difficult to draw firm conclusions, putative HD cells in the AV region generally exhibited broader tuning curves than those in the AD region (Figure 17-19). This difference may reflect characteristic HD activity, with classical HD cells predominating in the AD and theta-skipping precession HD activity in the AV. In the future, the strategies outlined above are worth considering. For example, using a Prism GRIN lens combined with differential labelling of PrS- and gRSC-projecting neurons with distinct calcium indicators is expected to be technically feasible and could provide valuable insights into how the thalamic nuclei process the HD signals to different cortical targets. This will also allow a clearer delineation of AD and AV. The effects of cholinergic modulation might be investigated by inhibiting candidate brainstem nuclei with DREADDs in cholinergic neurons while imaging thalamic HD signals. Based on the spiking removal effect of carbachol in both AD and AV, it would be interesting to explore the functional contribution of cholinergic inputs in fine-tuning of HD signals or shift in HD dynamics within attractor network frameworks.

5 Anatomical convergence of AD and AV axonal projections in the PrS and gRSC

Retrograde labelling experiments showed that PrS- and gRSC-projecting subpopulations are topographically organised within both AD and AV. Then, what proportion of neurons in AD and AV are projection neurons? Since the quantification was based on DAPI-labelled cells, the suggested proportion includes glial cells. Although no study has reported the neuron-glia ratio in the ATN, the LGN is known to contain neurons and glia in a ratio of 1 : 0.7 (Heumann & Rabinowicz, 1980). Applying this to the ATN, we estimate that at least 93% of AD neurons are projection neurons. Specifically, 47% projected exclusively to the PrS, 20% to the gRSC, and 26% to both cortical regions. In AV, 75% of neurons were projection neurons while roughly one-third of the ventral portion of AV remained unlabelled in our hands. We note that this point is likely determined by our injection strategy, and the exact portion of PrS and gRSC that had been covered. 27% of AV neurons projected exclusively to the PrS, 40% only to the gRSC, and 9% were bifurcating. This projection profile may differ if other subregions of the gRSC were targeted, or if the Sub was targeted. However, the overall labelling pattern in AD and AV was robust and reproducible, even if injections were placed at slightly different anterior-posterior levels (Figure 2 - supplemental figure 1 in my manuscript).

The tracing results also indicate that the axonal projections from AD and AV subpopulations converge within both gRSC and PrS. Roy et al. (2021) provided partial evidence that AD and AV inputs converge in subsets of RSC neurons. While the functional significance of convergence of AD and AV signals in the cortical HD areas remains elusive, it is tempting to speculate. First, the hierarchical organisation of the HD system suggests distinct roles for the AD and AV thalamic nuclei. AD is essential for transmitting precise HD activity to both PrS and gRSC, whereas AV has probably a broader role, being strongly associated with theta-modulated activity but containing fewer classical HD cells. A recent study suggests that the AVDM-gRSC circuit may relay theta and HD signals, while the AVVL-dRSC circuit may integrate theta and other spatial signals ((Lomi et al., 2021, 2023). However, classical HD cells in RSC do not generally show theta modulation (Lozano et al., 2017). Instead, theta modulation appears in direction-dependent place cells, with 7% in dRSC and 12.5% in gRSC showing such properties (Cho & Sharp, 2001). The AD-RSC connection also is important for memory encoding, while AV-RSC connections are linked to memory specification (Roy et al., 2021). These authors showed that AD primarily excites RSC neurons to drive output to the EC, while AV preferentially activates VIP interneurons in RSC, thereby regulating RSC-EC interactions. Their findings suggest that direct functional convergence of the AD and AV thalamic axons in the RSC is limited. Potentially, the classical HD signalling convergence in the RSC may occur through the small proportion of HD cells in AV, but classical HD input from AD and theta-related input from AV may not be directly integrated. Further electrophysiological studies of AD and AV afferents in RSC neurons are needed to clarify the impact of their convergence, at the level of single neurons or at the level of the local microcircuit. In the PrS, similarly, most HD cells do not exhibit strong theta modulation (Boccara et al., 2010; Cho & Sharp, 2001; Lozano et al., 2017). Cellular-level convergence of AD and AV afferents has not been studied yet. While the key contribution of neurons in AD to HD coding in PrS is well established, the role of neurons in AV remains unclear. AV has

often been studied together with AD as part of ATN, which has limited the identification of its distinct function (Nassar et al., 2018; Richevaux et al., 2025). Regarding theta modulation, PrS generally shows some theta modulation including the modulation in grid cells (Boccara et al., 2010), and its functional significance is still poorly understood (Tukker et al., 2015)(Tukker et al., 2015). Theta rhythmic activity may suggest modulatory input from the septum, or from the AV. Direct evidence for the functional significance of converging AD and AV afferents in PrS is still lacking.

General Conclusion

This thesis advances our understanding of the mammillo-thalamo-cortical circuitry underlying the HD system by characterising both the distinct properties of AD and AV neurons and their integration within broader cortical/parahippocampal circuits. My main work demonstrates distinct anatomical and electrophysiological characteristics of anterior thalamic subnuclei, AD and AV. Anatomical tracing work revealed bilateral mammillothalamic projections, as well as topographically organised subpopulations of thalamic projection neurons in the AD and AV. These thalamic neurons receive monosynaptic inputs from the MBO in both hemispheres, with stronger inputs observed ipsilaterally. Whether the anatomical convergence of thalamic projection neurons within the cortical HD areas is accompanied by functional convergence remains to be investigated. The distinct electrophysiological and morphological properties of AD and AV neurons were studied. By relating these properties to their genetic profiles and to previously reported HD characteristics of the two thalamic subnuclei, the discussion proposes a potential link whereby each thalamic nucleus is specialised to support its characteristic HD activity. As preliminary findings, the cholinergic influence on the thalamic spiking activity, the identification of potential cholinergic source regions, and trial experiments analysing HD activity in the AD and AV point to future research direction for expanding our understanding of thalamic HD activity.

In parallel with this main work, I contributed to associated projects that expand the scope of this thesis to presubicular circuit integration. In the first study, the integration of ATN-derived signal and RSC-derived signal in the PrS was investigated. The functional and anatomical experiments in this project revealed supralinear summation of the two inputs in presubicular layer III pyramidal neurons, which in turn relay information to layer IV. In the second study, presubicular VIP interneurons were systematically characterised, revealing subtypes with distinct electrophysiological and morphological profiles. These cells receive facilitating excitation from ATN and participate in disinhibitory motifs. Such properties suggest a potential role in transiently reshaping the attractor dynamics of HD networks. These studies extend the thesis beyond thalamic mechanisms to highlight how ATN afferents are integrated within the PrS.

To conclude, my PhD research offers a broadened perspective on the fundamental roles of AD and AV within the HD system. It extends the current understanding of thalamic contributions to the HD network by integrating new anatomical, electrophysiological, and functional insights with previous findings and my preliminary findings point to new avenues for future research.

Bibliography

Adelman, W. J., & Palti, Y. (1969). The Effects of External Potassium and Long Duration Voltage Gonditioning on the Amplitude of Sodium Gurrents in the Giant Axon of the Squid, Loligo pealei.

Aggleton, J. P., & Brown, M. W. (1999). Episodic memory, amnesia, and the hippocampal–anterior thalamic axis. *Behavioral and Brain Sciences*, *22*(3), 425–444. https://doi.org/10.1017/S0140525X99002034

Ajabi, Z., Keinath, A. T., Wei, X.-X., & Brandon, M. P. (2023). Population dynamics of head-direction neurons during drift and reorientation. *Nature*, *615*(7954), 892–899. https://doi.org/10.1038/s41586-023-05813-2

Albo, Z. (2003). Anterior thalamic unit discharge profiles and coherence with hippocampal theta rhythm. *Thalamus & Related Systems*, *2*(2), 133–144. https://doi.org/10.1016/S1472-9288(03)00006-2

Alexander, A. S., Robinson, J. C., Stern, C. E., & Hasselmo, M. E. (2023). Gated transformations from egocentric to allocentric reference frames involving retrosplenial cortex, entorhinal cortex, and hippocampus. *Hippocampus*, *33*(5), 465–487. https://doi.org/10.1002/hipo.23513

Alitto, H. J., Rathbun, D. L., Fisher, T. G., Alexander, P. C., & Usrey, W. M. (2019). Contrast gain control and retinogeniculate communication. *European Journal of Neuroscience*, *49*(8), 1061–1068. https://doi.org/10.1111/ejn.13904

Allen, G. V., & Hopkins, D. A. (1989). Mamillary body in the rat: Topography and synaptology of projections from the subicular complex, prefrontal cortex, and midbrain tegmentum. *Journal of Comparative Neurology*, *286*(3), 311–336. https://doi.org/10.1002/cne.902860303

Amaral, D. G., & Cowan, W. M. (1980). Subcortical afferents to the hippocampal formation in the monkey. *Journal of Comparative Neurology*, *189*(4), 573–591. https://doi.org/10.1002/cne.901890402

Angelaki, D. E., & Laurens, J. (2020). The head direction cell network: Attractor dynamics, integration within the navigation system, and three-dimensional properties. *Current Opinion in Neurobiology*, *60*, 136–144. https://doi.org/10.1016/j.conb.2019.12.002

Aronov, D., Nevers, R., & Tank, D. W. (2017). Mapping of a non-spatial dimension by the hippocampal–entorhinal circuit. *Nature*, *543*(7647), 719–722. https://doi.org/10.1038/nature21692

Astori, S., Wimmer, R. D., Prosser, H. M., Corti, C., Corsi, M., Liaudet, N., Volterra, A., Franken, P., Adelman, J. P., & Lüthi, A. (2011). The CaV 3.3 calcium channel is the major sleep spindle pacemaker in thalamus. *Proceedings of the National Academy of Sciences*, *108*(33), 13823–13828. https://doi.org/10.1073/pnas.1105115108

Asumbisa, K., Peyrache, A., & Trenholm, S. (2022). Flexible cue anchoring strategies enable stable head direction coding in both sighted and blind animals. *Nature Communications*, *13*(1), 5483. https://doi.org/10.1038/s41467-022-33204-0

Auger, S. D., & Maguire, E. A. (2013). Assessing the mechanism of response in the retrosplenial cortex of good and poor navigators. *Cortex*, *49*(10), 2904–2913. https://doi.org/10.1016/j.cortex.2013.08.002

Auger, S. D., Mullally, S. L., & Maguire, E. A. (2012). Retrosplenial Cortex Codes for Permanent Landmarks (C. I. Baker, Ed.). *PLoS ONE*, *7*(8), e43620. https://doi.org/10.1371/journal.pone.0043620

Azouz, R., Jensen, M. S., & Yaari, Y. (1996). Ionic basis of spike after-depolarization and burst generation in adult rat hippocampal CA1 pyramidal cells. *The Journal of Physiology*, *492*(1), 211–223. https://doi.org/10.1113/jphysiol.1996.sp021302

Bankhead, P., Loughrey, M. B., Fernández, J. A., Dombrowski, Y., McArt, D. G., Dunne, P. D., McQuaid, S., Gray, R. T., Murray, L. J., Coleman, H. G., James, J. A., Salto-Tellez, M., & Hamilton, P. W. (2017). QuPath: Open source software for digital pathology image analysis. *Scientific Reports*, *7*(1), 16878. https://doi.org/10.1038/s41598-017-17204-5

Barnett, S., Parr-Brownlie, L., Perry, B., Young, C., Wicky, H., Hughes, S., McNaughton, N., & Dalrymple-Alford, J. (2021). Anterior thalamic nuclei neurons sustain memory. *Current Research in Neurobiology*, *2*, 100022. https://doi.org/10.1016/j.crneur.2021.100022

Barry, C., Lever, C., Hayman, R., Hartley, T., Burton, S., O'Keefe, J., Jeffery, K., & Burgess, N. (2006). The Boundary Vector Cell Model of Place Cell Firing and Spatial Memory. *Reviews in the Neurosciences*, *17*(1–2). https://doi.org/10.1515/REVNEURO.2006.17.1-2.71

Barry, C., Hayman, R., Burgess, N., & Jeffery, K. J. (2007). Experience-dependent rescaling of entorhinal grids. *Nature Neuroscience*, *10*(6), 682–684. https://doi.org/10.1038/nn1905

Bassant, M.-H., & Poindessous-Jazat, F. (2001). Ventral tegmental nucleus of Gudden: A pontine hippocampal theta generator? *Hippocampus*, *11*(6), 809–813. https://doi.org/10.1002/hipo.1096

Bassett, J. P., & Taube, J. S. (2001). Neural Correlates for Angular Head Velocity in the Rat Dorsal Tegmental Nucleus. *The Journal of Neuroscience*, *21*(15), 5740–5751. https://doi.org/10.1523/JNEUROSCI.21-15-05740.2001

Bassett, J. P., Tullman, M. L., & Taube, J. S. (2007). Lesions of the Tegmentomammillary Circuit in the Head Direction System Disrupt the Head Direction Signal in the Anterior Thalamus. *The Journal of Neuroscience*, *27*(28), 7564–7577. https://doi.org/10.1523/JNEUROSCI.0268-07.2007

Bassett, J. P., Zugaro, M. B., Muir, G. M., Golob, E. J., Muller, R. U., & Taube, J. S. (2005). Passive Movements of the Head Do Not Abolish Anticipatory Firing Properties of Head Direction Cells. *Journal of Neurophysiology*, *93*(3), 1304–1316. https://doi.org/10.1152/jn.00490.2004

Bean, B. P. (2007). The action potential in mammalian central neurons. *Nature Reviews Neuroscience*, *8*(6), 451–465. https://doi.org/10.1038/nrn2148

Berkefeld, H., Sailer, C. A., Bildl, W., Rohde, V., Thumfart, J.-O., Eble, S., Klugbauer, N., Reisinger, E., Bischofberger, J., Oliver, D., Knaus, H.-G., Schulte, U., & Fakler, B. (2006). BKCa-Cav Channel Complexes Mediate Rapid and Localized Ca2+-Activated K+ Signaling. *Science*, *314*(5799), 615–620. https://doi.org/10.1126/science.1132915

Bernáth, B., Blahó, M., Egri, Á., Barta, A., Kriska, G., & Horváth, G. (2013). Orientation with a Viking sun-compass, a shadow-stick, and two calcite sunstones under various weather conditions. *Applied Optics*, *52*(25), 6185. https://doi.org/10.1364/AO.52.006185

Bernáth, B., Farkas, A., Száz, D., Blahó, M., Egri, Á., Barta, A., Åkesson, S., & Horváth, G. (2014). How could the Viking Sun compass be used with sunstones before and after sunset? Twilight board as a new interpretation of the Uunartoq artefact fragment. *Proceedings of the Royal Society A: Mathematical, Physical and Engineering Sciences*, *470*(2166), 20130787. https://doi.org/10.1098/rspa.2013.0787

Bevan, M. D., & Wilson, C. J. (1999). Mechanisms Underlying Spontaneous Oscillation and Rhythmic Firing in Rat Subthalamic Neurons. *The Journal of Neuroscience*, *19*(17), 7617–7628. https://doi.org/10.1523/JNEUROSCI.19-17-07617.1999

Bicanski, A., & Burgess, N. (2020). Neuronal vector coding in spatial cognition. *Nature Reviews Neuroscience*, *21*(9), 453–470. https://doi.org/10.1038/s41583-020-0336-9

Blair, H., & Sharp, P. (1995). Anticipatory head direction signals in anterior thalamus: Evidence for a thalamocortical circuit that integrates angular head motion to compute head direction. *The Journal of Neuroscience*, *15*(9), 6260–6270. https://doi.org/10.1523/JNEUROSCI.15-09-06260.1995

Blair, H. T., Cho, J., & Sharp, P. E. (1998). Role of the Lateral Mammillary Nucleus in the Rat Head Direction Circuit. *Neuron*, *21*(6), 1387–1397. https://doi.org/10.1016/S0896-6273(00)80657-1

Blair, H. T., Cho, J., & Sharp, P. E. (1999). The Anterior Thalamic Head-Direction Signal Is Abolished by Bilateral But Not Unilateral Lesions of the Lateral Mammillary Nucleus. *The Journal of Neuroscience*, *19*(15), 6673–6683. https://doi.org/10.1523/JNEUROSCI.19-15-06673.1999

Blair, H. T., Lipscomb, B. W., & Sharp, P. E. (1997). Anticipatory Time Intervals of Head-Direction Cells in the Anterior Thalamus of the Rat: Implications for Path Integration in the Head-Direction Circuit. *Journal of Neurophysiology*, *78*(1), 145–159. https://doi.org/10.1152/jn.1997.78.1.145

Blair, H. T., & Sharp, P. E. (1996). Visual and vestibular influences on head-direction cells in the anterior thalamus of the rat. *Behavioral Neuroscience*, *110*(4), 643–660. https://doi.org/10.1037/0735-7044.110.4.643

Blanco-Hernández, E., Balsamo, G., Preston-Ferrer, P., & Burgalossi, A. (2024). Sensory and behavioral modulation of thalamic head-direction cells. *Nature Neuroscience*, *27*(1), 28–33. https://doi.org/10.1038/s41593-023-01506-1

Bland, B. H., Konopacki, J., Kirk, I. J., Oddie, S. D., & Dickson, C. T. (1995). Discharge patterns of hippocampal theta-related cells in the caudal diencephalon of the urethan-anesthetized rat. *Journal of Neurophysiology*, *74*(1), 322–333. https://doi.org/10.1152/jn.1995.74.1.322

Boccara, C. N., Sargolini, F., Thoresen, V. H., Solstad, T., Witter, M. P., Moser, E. I., & Moser, M.-B. (2010). Grid cells in pre- and parasubiculum. *Nature Neuroscience*, *13*(8), 987–994. https://doi.org/10.1038/nn.2602

Bonnevie, T., Dunn, B., Fyhn, M., Hafting, T., Derdikman, D., Kubie, J. L., Roudi, Y., Moser, E. I., & Moser, M.-B. (2013). Grid cells require excitatory drive from the hippocampus. *Nature Neuroscience*, *16*(3), 309–317. https://doi.org/10.1038/nn.3311

Borgini, M., Mondal, P., Liu, R., & Wipf, P. (2021). Chemical modulation of Kv7 potassium channels. *RSC Medicinal Chemistry*, *12*(4), 483–537. https://doi.org/10.1039/D0MD00328J

Brandon, M. P., Bogaard, A. R., Schultheiss, N. W., & Hasselmo, M. E. (2013). Segregation of cortical head direction cell assemblies on alternating theta cycles. *Nature Neuroscience*, *16*(6), 739–748. https://doi.org/10.1038/nn.3383

Brandon, M. P., Koenig, J., Leutgeb, J. K., & Leutgeb, S. (2014). New and Distinct Hippocampal Place Codes Are Generated in a New Environment during Septal Inactivation. *Neuron*, *82*(4), 789–796. https://doi.org/10.1016/j.neuron.2014.04.013

Brown, J. E., Card, J. P., & Yates, B. J. (2005). Polysynaptic pathways from the vestibular nuclei to the lateral mammillary nucleus of the rat: Substrates for vestibular input to head direction cells. *Experimental Brain Research*, *161*(1), 47–61. https://doi.org/10.1007/s00221-004-2045-4

Bubb, E. J., Kinnavane, L., & Aggleton, J. P. (2017). Hippocampal–diencephalic–cingulate networks for memory and emotion: An anatomical guide. *Brain and Neuroscience Advances*, *1*, 2398212817723443. https://doi.org/10.1177/2398212817723443

Burak, Y., & Fiete, I. R. (2009). Accurate path integration in continuous attractor network models of grid cells. *PLoS Computational Biology*, *5*(2), e1000291. https://doi.org/10.1371/journal.pcbi.1000291

Burgess, N., & O'Keefe, J. (2011). Models of place and grid cell firing and theta rhythmicity. *Current Opinion in Neurobiology*, *21*(5), 734–744. https://doi.org/10.1016/j.conb.2011.07.002

Butler, W. N., Smith, K. S., Van Der Meer, M. A., & Taube, J. S. (2017). The Head-Direction Signal Plays a Functional Role as a Neural Compass during Navigation. *Current Biology*, *27*(9), 1259–1267. https://doi.org/10.1016/j.cub.2017.03.033

Buzsáki, G. (2002). Theta Oscillations in the Hippocampus. *Neuron*, *33*(3), 325–340. https://doi.org/10.1016/S0896-6273(02)00586-X

Buzsáki, G. (2005). Theta rhythm of navigation: Link between path integration and landmark navigation, episodic and semantic memory. *Hippocampus*, *15*(7), 827–840. https://doi.org/10.1002/hipo.20113

Byock, J. L. (2012). *The Saga of the Volsungs: The Norse epic of Sigurd the Dragon Slayer* (3rd ed). University of California Press.

Cacucci, F., Lever, C., Wills, T. J., Burgess, N., & O'Keefe, J. (2004). Theta-Modulated Place-by-Direction Cells in the Hippocampal Formation in the Rat. *The Journal of Neuroscience*, *24*(38), 8265–8277. https://doi.org/10.1523/JNEUROSCI.2635-04.2004

Cai, X., Liang, C. W., Muralidharan, S., Kao, J. P., Tang, C.-M., & Thompson, S. M. (2004). Unique Roles of SK and Kv4.2 Potassium Channels in Dendritic Integration. *Neuron*, *44*(2), 351–364. https://doi.org/10.1016/j.neuron.2004.09.026

Calton, J. L., Stackman, R. W., Goodridge, J. P., Archey, W. B., Dudchenko, P. A., & Taube, J. S. (2003). Hippocampal Place Cell Instability after Lesions of the Head Direction Cell Network. *The Journal of Neuroscience*, *23*(30), 9719–9731. https://doi.org/10.1523/JNEUROSCI.23-30-09719.2003

Calton, J. L., Turner, C. S., Cyrenne, D.-L. M., Lee, B. R., & Taube, J. S. (2008). Landmark control and updating of self-movement cues are largely maintained in head direction cells after lesions of the posterior parietal cortex. *Behavioral Neuroscience*, *122*(4), 827–840. https://doi.org/10.1037/0735-7044.122.4.827

Campagner, D., Vale, R., Tan, Y. L., Iordanidou, P., Pavón Arocas, O., Claudi, F., Stempel, A. V., Keshavarzi, S., Petersen, R. S., Margrie, T. W., & Branco, T. (2023). A cortico-collicular circuit for orienting to shelter during escape. *Nature*, *613*(7942), 111–119. https://doi.org/10.1038/s41586-022-05553-9

Carrasquillo, Y., Burkhalter, A., & Nerbonne, J. M. (2012). A-type K+ channels encoded by Kv4.2, Kv4.3 and Kv1.4 differentially regulate intrinsic excitability of cortical pyramidal neurons. *The Journal of Physiology*, *590*(16), 3877–3890. https://doi.org/10.1113/jphysiol.2012.229013

Catterall, W. A. (1986a). Molecular Properties of Voltage-Sensitive Sodium Channels. *Annual Review of Biochemistry*, *55*(1), 953–985. https://doi.org/10.1146/annurev.bi.55.070186.004513

Catterall, W. A. (1986b). Voltage-dependent gating of sodium channels: Correlating structure and function. *Trends in Neurosciences*, *9*, 7–10. https://doi.org/10.1016/0166-2236(86)90004-4

Catterall, W. A. (2010). Ion Channel Voltage Sensors: Structure, Function, and Pathophysiology. *Neuron*, *67*(6), 915–928. https://doi.org/10.1016/j.neuron.2010.08.021

Catterall, W. A. (2023). Voltage gated sodium and calcium channels: Discovery, structure, function, and Pharmacology. *Channels*, *17*(1), 2281714. https://doi.org/10.1080/19336950.2023.2281714

Chen, W., Zhang, J.-J., Hu, G.-Y., & Wu, C.-P. (1996). Different mechanisms underlying the repolarization of narrow and wide action potentials in pyramidal cells and interneurons of cat motor cortex. *Neuroscience*, *73*(1), 57–68. https://doi.org/10.1016/0306-4522(96)00010-3

Chen, Y., Parker, W. D., & Wang, K. (2014). The Role of T-Type Calcium Channel Genes in Absence Seizures. *Frontiers in Neurology*, *5*. https://doi.org/10.3389/fneur.2014.00045

Chiaruttini, N., Castoldi, C., Requie, L. M., Camarena-Delgado, C., Dal Bianco, B., Gräff, J., Seitz, A., & Silva, B. A. (2025). ABBA+BraiAn, an integrated suite for whole-brain mapping, reveals brain-wide differences in immediate-early genes induction upon learning. *Cell Reports*, *44*(7), 115876. https://doi.org/10.1016/j.celrep.2025.115876

Cho, J., & Sharp, P. E. (2001). Head direction, place, and movement correlates for cells in the rat retrosplenial cortex. *Behavioral Neuroscience*, *115*(1), 3–25. https://doi.org/10.1037/0735-7044.115.1.3

Clark, B. J., Bassett, J. P., Wang, S. S., & Taube, J. S. (2010). Impaired Head Direction Cell Representation in the Anterodorsal Thalamus after Lesions of the Retrosplenial Cortex. *The Journal of Neuroscience*, *30*(15), 5289–5302. https://doi.org/10.1523/JNEUROSCI.3380-09.2010

Clark, B. J., Rice, J. P., Akers, K. G., Candelaria-Cook, F. T., Taube, J. S., & Hamilton, D. A. (2013). Lesions of the dorsal tegmental nuclei disrupt control of navigation by distal landmarks in cued, directional, and place variants of the Morris water task. *Behavioral Neuroscience*, *127*(4), 566–581. https://doi.org/10.1037/a0033087

Clark, B. J., & Taube, J. S. (2011). Intact landmark control and angular path integration by head direction cells in the anterodorsal thalamus after lesions of the medial entorhinal cortex. *Hippocampus*, *21*(7), 767–782. https://doi.org/10.1002/hipo.20874

Clark, B. J., & Taube, J. S. (2012). Vestibular and attractor network basis of the head direction cell signal in subcortical circuits. *Frontiers in Neural Circuits*, *6*. https://doi.org/10.3389/fncir.2012.00007

Claudi, F., Tyson, A. L., Petrucco, L., Margrie, T. W., Portugues, R., & Branco, T. (2021). Visualizing anatomically registered data with brainrender. *eLife*, *10*, e65751. https://doi.org/10.7554/eLife.65751

Coetzee, W. A., Amarillo, Y., Chiu, J., Chow, A., Lau, D., McCORMACK, T., Morena, H., Nadal, M. S., Ozaita, A., Pountney, D., Saganich, M., De Miera, E. V.-S., & Rudy, B. (1999). Molecular Diversity of K+ Channels. *Annals of the New York Academy of Sciences*, *868*(1), 233–255. https://doi.org/10.1111/j.1749-6632.1999.tb11293.x

Coletta, S., Frey, M., Nasr, K., Preston-Ferrer, P., & Burgalossi, A. (2018). Testing the Efficacy of Single-Cell Stimulation in Biasing Presubicular Head Direction Activity. *The Journal of Neuroscience*, *38*(13), 3287–3302. https://doi.org/10.1523/JNEUROSCI.1814-17.2018

Combe, C. L., & Gasparini, S. (2021). Ih from synapses to networks: HCN channel functions and modulation in neurons. *Progress in Biophysics and Molecular Biology*, *166*, 119–132. https://doi.org/10.1016/j.pbiomolbio.2021.06.002

Connor, J. A., & Stevens, C. F. (1971a). Prediction of repetitive firing behaviour from voltage clamp data on an isolated neurone soma. *The Journal of Physiology*, *213*(1), 31–53. https://doi.org/10.1113/jphysiol.1971.sp009366

Connor, J. A., & Stevens, C. F. (1971b). Voltage clamp studies of a transient outward membrane current in gastropod neural somata. *The Journal of Physiology*, *213*(1), 21–30. https://doi.org/10.1113/jphysiol.1971.sp009365

Connors, B. W., Gutnick, M. J., & Prince, D. A. (1982). Electrophysiological properties of neocortical neurons in vitro. *Journal of Neurophysiology*, *48*(6), 1302–1320. https://doi.org/10.1152/jn.1982.48.6.1302

Connors, B. W., & Gutnick, M. J. (1990). Intrinsic firing patterns of diverse neocortical neurons. *Trends in Neurosciences*, *13*(3), 99–104. https://doi.org/10.1016/0166-2236(90)90185-D

Cruce, J. A. (1975). An autoradiographic study of the projections of the mammillothalamic tract in the rat. *Brain Research*, *85*(2), 211–219. https://doi.org/10.1016/0006-8993(75)90072-4

Desai, N. V., & Varela, C. (2021). Distinct burst properties contribute to the functional diversity of thalamic nuclei. *Journal of Comparative Neurology*, *529*(17), 3726–3750. https://doi.org/10.1002/cne.25141

Didier, M. E. P., Tarun, O. B., Jourdain, P., Magistretti, P., & Roke, S. (2018). Membrane water for probing neuronal membrane potentials and ionic fluxes at the single cell level. *Nature Communications*, *9*(1), 5287. https://doi.org/10.1038/s41467-018-07713-w

Dillingham, C. M., Frizzati, A., Nelson, A. J., & Vann, S. D. (2015). How do mammillary body inputs contribute to anterior thalamic function? *Neuroscience & Biobehavioral Reviews*, *54*, 108–119. https://doi.org/10.1016/j.neubiorev.2014.07.025

Dillingham, C. M., & Vann, S. D. (2019). Why Isn't the Head Direction System Necessary for Direction? Lessons From the Lateral Mammillary Nuclei. *Frontiers in Neural Circuits*, *13*, 60. https://doi.org/10.3389/fncir.2019.00060

Do, M. T. H., & Bean, B. P. (2003). Subthreshold Sodium Currents and Pacemaking of Subthalamic Neurons. *Neuron*, *39*(1), 109–120. https://doi.org/10.1016/S0896-6273(03)00360-X

Du, J., Zhang, L., Weiser, M., Rudy, B., & McBain, C. (1996). Developmental expression and functional characterization of the potassium-channel subunit Kv3.1b in parvalbumin-containing interneurons of the rat hippocampus. *The Journal of Neuroscience*, *16*(2), 506–518. https://doi.org/10.1523/JNEUROSCI.16-02-00506.1996

Dupret, D., O'Neill, J., Pleydell-Bouverie, B., & Csicsvari, J. (2010). The reorganization and reactivation of hippocampal maps predict spatial memory performance. *Nature Neuroscience*, *13*(8), 995–1002. https://doi.org/10.1038/nn.2599

Duszkiewicz, A. J., Orhan, P., Skromne Carrasco, S., Brown, E. H., Owczarek, E., Vite, G. R., Wood, E. R., & Peyrache, A. (2024). Local origin of excitatory–inhibitory tuning equivalence in a cortical network. *Nature Neuroscience*, *27*(4), 782–792. https://doi.org/10.1038/s41593-024-01588-5

El Mahmoudi, N., Huret, A., Laurent, C., Laurens, J., Jacob, P.-Y., & Sargolini, F. (2025, April 3). *Dynamics of thalamic directional coding under vestibular imbalance*. https://doi.org/10.1101/2025.03.31.646416

Endo, T., Tarusawa, E., Notomi, T., Kaneda, K., Hirabayashi, M., Shigemoto, R., & Isa, T. (2008). Dendritic Ih Ensures High-Fidelity Dendritic Spike Responses of Motion-Sensitive Neurons in Rat Superior Colliculus. *Journal of Neurophysiology*, *99*(5), 2066–2076. https://doi.org/10.1152/jn.00556.2007

Erisir, A., Lau, D., Rudy, B., & Leonard, C. S. (1999). Function of Specific K^+ Channels in Sustained High-Frequency Firing of Fast-Spiking Neocortical Interneurons. *Journal of Neurophysiology*, *82*(5), 2476–2489. https://doi.org/10.1152/jn.1999.82.5.2476

Etienne, A. S., & Jeffery, K. J. (2004). Path integration in mammals. *Hippocampus*, *14*(2), 180–192. https://doi.org/10.1002/hipo.10173

Faber, E. S. L. (2003). Ca2+-activated K+ (BK) channel inactivation contributes to spike broadening during repetitive firing in the rat lateral amygdala. *The Journal of Physiology*, *552*(2), 483–497. https://doi.org/10.1113/jphysiol.2003.050120

Finkelstein, A., Derdikman, D., Rubin, A., Foerster, J. N., Las, L., & Ulanovsky, N. (2015). Three-dimensional head-direction coding in the bat brain. *Nature*, *517*(7533), 159–164. https://doi.org/10.1038/nature14031

Fischer, L. F., Mojica Soto-Albors, R., Buck, F., & Harnett, M. T. (2020). Representation of visual landmarks in retrosplenial cortex. *eLife*, *9*, e51458. https://doi.org/10.7554/eLife.51458

Frost, B. E., Martin, S. K., Cafalchio, M., Islam, M. N., Aggleton, J. P., & O'Mara, S. M. (2021). Anterior Thalamic Inputs Are Required for Subiculum Spatial Coding, with Associated Consequences for Hippocampal Spatial Memory. *The Journal of Neuroscience*, *41*(30), 6511–6525. https://doi.org/10.1523/JNEUROSCI.2868-20.2021

Fujita, H., Imura, K., Takiguchi, M., & Funakoshi, K. (2022). Postnatal development of thalamic reticular nucleus projections to the anterior thalamic nuclei in rats. *European Journal of Histochemistry*, *66*(2). https://doi.org/10.4081/ejh.2022.3370

Fyhn, M., Hafting, T., Treves, A., Moser, M.-B., & Moser, E. I. (2007). Hippocampal remapping and grid realignment in entorhinal cortex. *Nature*, *446*(7132), 190–194. https://doi.org/10.1038/nature05601

Galen. (1997). The Usefulness of Parts of the Body: *Clinical Orthopaedics and Related Research*, *337*, 3–12. https://doi.org/10.1097/00003086-199704000-00002

Gallistel, C. R. (1990). *The organization of learning*. the MIT press.

García-Cabezas, M. Á., Pérez-Santos, I., & Cavada, C. (2021). The Epic of the Thalamus in Anatomical Language. *Frontiers in Neuroanatomy*, *15*. https://doi.org/10.3389/fnana.2021.744095

Gardner, R. J., Hermansen, E., Pachitariu, M., Burak, Y., Baas, N. A., Dunn, B. A., Moser, M.-B., & Moser, E. I. (2022). Toroidal topology of population activity in grid cells. *Nature*, *602*(7895), 123–128. https://doi.org/10.1038/s41586-021-04268-7

Gener, T., Perez-Mendez, L., & Sanchez-Vives, M. V. (2013). Tactile modulation of hippocampal place fields: Tactile Modulation of Hippocampal Place Fields. *Hippocampus*, *23*(12), 1453–1462. https://doi.org/10.1002/hipo.22198

Giese, K. P., Storm, J. F., Reuter, D., Fedorov, N. B., Shao, L. R., Leicher, T., Pongs, O., & Silva, A. J. (1998). Reduced K+ channel inactivation, spike broadening, and after-

hyperpolarization in Kvbeta1.1-deficient mice with impaired learning. *Learning & Memory (Cold Spring Harbor, N.Y.)*, *5*(4–5), 257–273.

Giocomo, L. M., Stensola, T., Bonnevie, T., Van Cauter, T., Moser, M.-B., & Moser, E. I. (2014). Topography of Head Direction Cells in Medial Entorhinal Cortex. *Current Biology*, *24*(3), 252–262. https://doi.org/10.1016/j.cub.2013.12.002

Givon, S., Samina, M., Ben-Shahar, O., & Segev, R. (2022). From fish out of water to new insights on navigation mechanisms in animals. *Behavioural Brain Research*, *419*, 113711. https://doi.org/10.1016/j.bbr.2021.113711

Goldberg, J. A., & Wilson, C. J. (2005). Control of Spontaneous Firing Patterns by the Selective Coupling of Calcium Currents to Calcium-Activated Potassium Currents in Striatal Cholinergic Interneurons. *The Journal of Neuroscience*, *25*(44), 10230–10238. https://doi.org/10.1523/JNEUROSCI.2734-05.2005

Golob, E. J., Wolk, D. A., & Taube, J. S. (1998). Recordings of postsubiculum head direction cells following lesions of the laterodorsal thalamic nucleus. *Brain Research*, *780*(1), 9–19. https://doi.org/10.1016/S0006-8993(97)01076-7

Gonzalo-Ruiz, A., Alonso, A., Sanz, J. M., & Llinás, R. R. (1992). Afferent projections to the mammillary complex of the rat, with special reference to those from surrounding hypothalamic regions. *Journal of Comparative Neurology*, *321*(2), 277–299. https://doi.org/10.1002/cne.903210208

Gonzalo-Ruiz, A., & Lieberman, A. (1995). GABAergic projections from the thalamic reticular nucleus to the anteroventral and anterodorsal thalamic nuclei of the rat. *Journal of Chemical Neuroanatomy*, *9*(3), 165–174. https://doi.org/10.1016/0891-0618(95)00078-X

Gonzalo-Ruiz, A., Sanz-Anquela, M. J., & Lieberman, A. R. (1995). Cholinergic projections to the anterior thalamic nuclei in the rat: A combined retrograde tracing and choline acetyl transferase immunohistochemical study. *Anatomy and Embryology*, *192*(4), 335–349. https://doi.org/10.1007/BF00710103

Goodridge, J. P., Dudchenko, P. A., Worboys, K. A., Golob, E. J., & Taube, J. S. (1998). Cue control and head direction cells. *Behavioral Neuroscience*, *112*(4), 749–761. https://doi.org/10.1037/0735-7044.112.4.749

Goodridge, J. P., & Taube, J. S. (1995). Preferential use of the landmark navigational system by head direction cells in rats. *Behavioral Neuroscience*, *109*(1), 49–61. https://doi.org/10.1037/0735-7044.109.1.49

Goodridge, J. P., & Taube, J. S. (1997). Interaction between the Postsubiculum and Anterior Thalamus in the Generation of Head Direction Cell Activity. *The Journal of Neuroscience*, *17*(23), 9315–9330. https://doi.org/10.1523/JNEUROSCI.17-23-09315.1997

Green, J., Adachi, A., Shah, K. K., Hirokawa, J. D., Magani, P. S., & Maimon, G. (2017). A neural circuit architecture for angular integration in Drosophila. *Nature*, *546*(7656), 101–106. https://doi.org/10.1038/nature22343

Grenier, F., Timofeev, I., & Steriade, M. (1998). Leading role of thalamic over cortical neurons during postinhibitory rebound excitation. *Proceedings of the National Academy of Sciences*, *95*(23), 13929–13934. https://doi.org/10.1073/pnas.95.23.13929

Gu, N., Vervaeke, K., Hu, H., & Storm, J. F. (2005). Kv7/KCNQ/M and HCN/h, but not K Ca2/SK channels, contribute to the somatic medium after-hyperpolarization and excitability control in CA1 hippocampal pyramidal cells. *The Journal of Physiology*, *566*(3), 689–715. https://doi.org/10.1113/jphysiol.2005.086835

Guison, N. G., Ahmed, A. K., Dong, K., & Yamadori, T. (1995). Projections from the lateral mammillary nucleus to the anterodorsal thalamic nucleus in the rat. *The Kobe Journal of Medical Sciences*, *41*(6), 213–220.

Hafting, T., Fyhn, M., Bonnevie, T., Moser, M.-B., & Moser, E. I. (2008). Hippocampus-independent phase precession in entorhinal grid cells. *Nature*, *453*(7199), 1248–1252. https://doi.org/10.1038/nature06957

Hafting, T., Fyhn, M., Molden, S., Moser, M.-B., & Moser, E. I. (2005). Microstructure of a spatial map in the entorhinal cortex. *Nature*, *436*(7052), 801–806. https://doi.org/10.1038/nature03721

Haj-Dahmane, S., & Andrade, R. (1997). Calcium-Activated Cation Nonselective Current Contributes to the Fast Afterdepolarization in Rat Prefrontal Cortex Neurons. *Journal of Neurophysiology*, *78*(4), 1983–1989. https://doi.org/10.1152/jn.1997.78.4.1983

Halassa, M. M., & Sherman, S. M. (2019). Thalamocortical Circuit Motifs: A General Framework. *Neuron*, *103*(5), 762–770. https://doi.org/10.1016/j.neuron.2019.06.005

Hallanger, A. E., Levey, A. I., Lee, H. J., Rye, D. B., & Wainer, B. H. (1987). The origins of cholinergic and other subcortical afferents to the thalamus in the rat. *Journal of Comparative Neurology*, *262*(1), 105–124. https://doi.org/10.1002/cne.902620109

Hallanger, A. E., Price, S. D., Lee, H. J., Steininger, T. L., & Wainer, B. H. (1990). Ultrastructure of cholinergic synaptic terminals in the thalamic anteroventral, ventroposterior, and dorsal lateral geniculate nuclei of the rat. *Journal of Comparative Neurology*, *299*(4), 482–492. https://doi.org/10.1002/cne.902990408

Hallworth, N. E., Wilson, C. J., & Bevan, M. D. (2003). Apamin-Sensitive Small Conductance Calcium-Activated Potassium Channels, through their Selective Coupling to Voltage-Gated Calcium Channels, Are Critical Determinants of the Precision, Pace, and Pattern of Action Potential Generation in Rat Subthalamic Nucleus Neurons *In Vitro*. *The Journal of Neuroscience*, *23*(20), 7525–7542. https://doi.org/10.1523/JNEUROSCI.23-20-07525.2003

Harden, S. W. (2022). Analysis of electrophysiological recordings was performed with custom software written for this project using Python 3.10 and the pyABF package. https://pypi.org/project/pyabf

Harris, C. R., Millman, K. J., Van Der Walt, S. J., Gommers, R., Virtanen, P., Cournapeau, D., Wieser, E., Taylor, J., Berg, S., Smith, N. J., Kern, R., Picus, M., Hoyer, S., Van Kerkwijk, M. H., Brett, M., Haldane, A., Del Río, J. F., Wiebe, M., Peterson, P., … Oliphant, T. E. (2020). Array programming with NumPy. *Nature*, *585*(7825), 357–362. https://doi.org/10.1038/s41586-020-2649-2

He, L., Yu, Z., Geng, Z., Huang, Z., Zhang, C., Dong, Y., Gao, Y., Wang, Y., Chen, Q., Sun, L., Ma, X., Huang, B., Wang, X., & Zhao, Y. (2022). Structure, gating, and pharmacology

of human CaV3.3 channel. *Nature Communications*, *13*(1), 2084. https://doi.org/10.1038/s41467-022-29728-0

Heumann, D., & Rabinowicz, Th. (1980). Postnatal development of the dorsal lateral geniculate nucleus in the normal and enucleated albino mouse. *Experimental Brain Research*, *38*(1). https://doi.org/10.1007/bf00237933

Hindley, E., Nelson, A., Aggleton, J., & Vann, S. (2014). The rat retrosplenial cortex is required when visual cues are used flexibly to determine location. *Behavioural Brain Research*, *263*, 98–107. https://doi.org/10.1016/j.bbr.2014.01.028

Hodgkin, A. L., & Huxley, A. F. (1952). A quantitative description of membrane current and its application to conduction and excitation in nerve. *The Journal of Physiology*, *117*(4), 500–544. https://doi.org/10.1113/jphysiol.1952.sp004764

Hodgkin, A. L., Huxley, A. F., & Katz, B. (1952). Measurement of current-voltage relations in the membrane of the giant axon of *Loligo*. *The Journal of Physiology*, *116*(4), 424–448. https://doi.org/10.1113/jphysiol.1952.sp004716

Hok, V., Lenck-Santini, P.-P., Roux, S., Save, E., Muller, R. U., & Poucet, B. (2007). Goal-Related Activity in Hippocampal Place Cells. *The Journal of Neuroscience*, *27*(3), 472–482. https://doi.org/10.1523/JNEUROSCI.2864-06.2007

Huang, L.-W., Simonnet, J., Nassar, M., Richevaux, L., Lofredi, R., & Fricker, D. (2017). Laminar Localization and Projection-Specific Properties of Presubicular Neurons Targeting the Lateral Mammillary Nucleus, Thalamus, or Medial Entorhinal Cortex. *eneuro*, *4*(2), ENEURO.0370–16.2017. https://doi.org/10.1523/ENEURO.0370-16.2017

J. Delay & Brion, S. (1969). Le syndrome de Korsakoff.

Jacob, P.-Y., Casali, G., Spieser, L., Page, H., Overington, D., & Jeffery, K. (2017). An independent, landmark-dominated head-direction signal in dysgranular retrosplenial cortex. *Nature Neuroscience*, *20*(2), 173–175. https://doi.org/10.1038/nn.4465

Jacob, P.-Y., Van Cauter, T., Poucet, B., Sargolini, F., & Save, E. (2020). Medial entorhinal cortex lesions induce degradation of CA1 place cell firing stability when self-motion information is used. *Brain and Neuroscience Advances*, *4*, 239821282095300. https://doi.org/10.1177/2398212820953004

Jahnsen, H., & Llinás, R. (1984). Ionic basis for the electro-responsiveness and oscillatory properties of guinea-pig thalamic neurones in vitro. *The Journal of Physiology*, *349*(1), 227–247. https://doi.org/10.1113/jphysiol.1984.sp015154

Jain, D., Jakhalekar, I. R., & Deshmukh, S. S. (2017). Navigational Strategies and Their Neural Correlates. *Journal of the Indian Institute of Science*, *97*(4), 511–525. https://doi.org/10.1007/s41745-017-0053-1

Jankowski, M. M., Islam, M. N., Wright, N. F., Vann, S. D., Erichsen, J. T., Aggleton, J. P., & O'Mara, S. M. (2014). Nucleus reuniens of the thalamus contains head direction cells. *eLife*, *3*, e03075. https://doi.org/10.7554/eLife.03075

Jankowski, M. M., & O'Mara, S. M. (2015). Dynamics of place, boundary and object encoding in rat anterior claustrum. *Frontiers in Behavioral Neuroscience*, *9*. https://doi.org/10.3389/fnbeh.2015.00250

Jankowski, M. M., Passecker, J., Islam, M. N., Vann, S., Erichsen, J. T., Aggleton, J. P., & O'Mara, S. M. (2015). Evidence for spatially-responsive neurons in the rostral thalamus. *Frontiers in Behavioral Neuroscience*, *9*. https://doi.org/10.3389/fnbeh.2015.00256

Jankowski, M. M., Ronnqvist, K. C., Tsanov, M., Vann, S. D., Wright, N. F., Erichsen, J. T., Aggleton, J. P., & O'Mara, S. M. (2013). The anterior thalamus provides a subcortical circuit supporting memory and spatial navigation. *Frontiers in Systems Neuroscience*, *7*. https://doi.org/10.3389/fnsys.2013.00045

Jeffery, K. J., Page, H. J. I., & Stringer, S. M. (2016). Optimal cue combination and landmark-stability learning in the head direction system. *The Journal of Physiology*, *594*(22), 6527–6534. https://doi.org/10.1113/JP272945

Jeffery, K. J., Jovalekic, A., Verriotis, M., & Hayman, R. (2013). Navigating in a three-dimensional world. *Behavioral and Brain Sciences*, *36*(5), 523–543. https://doi.org/10.1017/S0140525X12002476

Ji, Z., Chu, T., Wu, S., & Burgess, N. (2025). A systems model of alternating theta sweeps via firing rate adaptation. *Current Biology*, *35*(4), 709–722.e5. https://doi.org/10.1016/j.cub.2024.08.059

Ji, Z., Lomi, E., Jeffery, K., Mitchell, A. S., & Burgess, N. (2025). Phase Precession Relative to Turning Angle in Theta-Modulated Head Direction Cells. *Hippocampus*, *35*(2), e70008. https://doi.org/10.1002/hipo.70008

Jiang, Y.-Q., Lee, D. K., Guo, W., Li, M., & Sun, Q. (2024). Hypothalamic regulation of hippocampal CA1 interneurons by the supramammillary nucleus. *Cell Reports*, *43*(11), 114898. https://doi.org/10.1016/j.celrep.2024.114898

Jones, E. G. (2007). *Thalamus* (Second edition). Cambridge University Press.

Kase, D., & Imoto, K. (2012). The Role of HCN Channels on Membrane Excitability in the Nervous System. *Journal of Signal Transduction*, *2012*, 1–11. https://doi.org/10.1155/2012/619747

Kelley, C., Dura-Bernal, S., Neymotin, S. A., Antic, S. D., Carnevale, N. T., Migliore, M., & Lytton, W. W. (2021). Effects of Ih and TASK-like shunting current on dendritic impedance in layer 5 pyramidal-tract neurons. *Journal of Neurophysiology*, *125*(4), 1501–1516. https://doi.org/10.1152/jn.00015.2021

Kim, D., Song, I., Keum, S., Lee, T., Jeong, M.-J., Kim, S.-S., McEnery, M. W., & Shin, H.-S. (2001). Lack of the Burst Firing of Thalamocortical Relay Neurons and Resistance to Absence Seizures in Mice Lacking α1G T-Type Ca2+ Channels. *Neuron*, *31*(1), 35–45. https://doi.org/10.1016/S0896-6273(01)00343-9

Kim, H. R., Hong, S. Z., & Fiorillo, C. D. (2015). T-type calcium channels cause bursts of spikes in motor but not sensory thalamic neurons during mimicry of natural patterns of synaptic input. *Frontiers in Cellular Neuroscience*, *9*. https://doi.org/10.3389/fncel.2015.00428

Kim, J., Wei, D.-S., & Hoffman, D. A. (2005). Kv4 potassium channel subunits control action potential repolarization and frequency-dependent broadening in rat hippocampal

CA1 pyramidal neurones. *The Journal of Physiology*, *569*(1), 41–57. https://doi.org/10.1113/jphysiol.2005.095042

Kim, S. S., Rouault, H., Druckmann, S., & Jayaraman, V. (2017). Ring attractor dynamics in the *Drosophila* central brain. *Science*, *356*(6340), 849–853. https://doi.org/10.1126/science.aal4835

King, C., Recce, M., & O'Keefe, J. (1998). The rhythmicity of cells of the medial septum/diagonal band of Broca in the awake freely moving rat: Relationships with behaviour and hippocampal theta. *European Journal of Neuroscience*, *10*(2), 464–477. https://doi.org/10.1046/j.1460-9568.1998.00026.x

Kirk, I. J., Oddie, S. D., Konopacki, J., & Bland, B. H. (1996). Evidence for Differential Control of Posterior Hypothalamic, Supramammillary, and Medial Mammillary Theta-Related Cellular Discharge by Ascending and Descending Pathways. *The Journal of Neuroscience*, *16*(17), 5547–5554. https://doi.org/10.1523/JNEUROSCI.16-17-05547.1996

Kjelstrup, K. B., Solstad, T., Brun, V. H., Hafting, T., Leutgeb, S., Witter, M. P., Moser, E. I., & Moser, M.-B. (2008). Finite Scale of Spatial Representation in the Hippocampus. *Science*, *321*(5885), 140–143. https://doi.org/10.1126/science.1157086

Knierim, J. J., Kudrimoti, H. S., & McNaughton, B. L. (1998). Interactions Between Idiothetic Cues and External Landmarks in the Control of Place Cells and Head Direction Cells. *Journal of Neurophysiology*, *80*(1), 425–446. https://doi.org/10.1152/jn.1998.80.1.425

Kocsis, B., & Vertes, R. (1994). Characterization of neurons of the supramammillary nucleus and mammillary body that discharge rhythmically with the hippocampal theta rhythm in the rat. *The Journal of Neuroscience*, *14*(11), 7040–7052. https://doi.org/10.1523/JNEUROSCI.14-11-07040.1994

Kocsis, B., Viana Di Prisco, G., & Vertes, R. (2001). Theta synchronization in the limbic system: The role of Gudden's tegmental nuclei. *European Journal of Neuroscience*, *13*(2), 381–388. https://doi.org/10.1111/j.1460-9568.2001.01392.x

Kohlmeier, K. A., Ishibashi, M., Wess, J., Bickford, M. E., & Leonard, C. S. (2012). Knockouts reveal overlapping functions of M_2 and M_4 muscarinic receptors and evidence for a local glutamatergic circuit within the laterodorsal tegmental nucleus. *Journal of Neurophysiology*, *108*(10), 2751–2766. https://doi.org/10.1152/jn.01120.2011

Kohlmeier, K. A., & Leonard, C. S. (2006). Transmitter modulation of spike-evoked calcium transients in arousal related neurons: Muscarinic inhibition of SNX-482-sensitive calcium influx. *European Journal of Neuroscience*, *23*(5), 1151–1162. https://doi.org/10.1111/j.1460-9568.2006.04640.x

Kornienko, O., Latuske, P., Bassler, M., Kohler, L., & Allen, K. (2018). Non-rhythmic head-direction cells in the parahippocampal region are not constrained by attractor network dynamics. *eLife*, *7*, e35949. https://doi.org/10.7554/eLife.35949

Laurens, J., & Angelaki, D. E. (2019). A model-based reassessment of the three-dimensional tuning of head direction cells in rats. *Journal of Neurophysiology*, *122*(3), 1274–1287. https://doi.org/10.1152/jn.00136.2019

Lawrence, J. J., Saraga, F., Churchill, J. F., Statland, J. M., Travis, K. E., Skinner, F. K., & McBain, C. J. (2006). Somatodendritic Kv7/KCNQ/M Channels Control Interspike Interval in Hippocampal Interneurons. *The Journal of Neuroscience*, *26*(47), 12325–12338. https://doi.org/10.1523/JNEUROSCI.3521-06.2006

Le Floch, A., Ropars, G., Lucas, J., Wright, S., Davenport, T., Corfield, M., & Harrisson, M. (2013). The sixteenth century Alderney crystal: A calcite as an efficient reference optical compass? *Proceedings of the Royal Society A: Mathematical, Physical and Engineering Sciences*, *469*(2153), 20120651. https://doi.org/10.1098/rspa.2012.0651

Lee, C. C., & Sherman, S. M. (2008). Synaptic Properties of Thalamic and Intracortical Inputs to Layer 4 of the First- and Higher-Order Cortical Areas in the Auditory and Somatosensory Systems. *Journal of Neurophysiology*, *100*(1), 317–326. https://doi.org/10.1152/jn.90391.2008

Lee, S.-C., Patrick, S. L., Richardson, K. A., & Connors, B. W. (2014). Two Functionally Distinct Networks of Gap Junction-Coupled Inhibitory Neurons in the Thalamic Reticular Nucleus. *The Journal of Neuroscience*, *34*(39), 13170–13182. https://doi.org/10.1523/jneurosci.0562-14.2014

Leonard, C., & Llinás, R. (1994). Serotonergic and cholinergic inhibition of mesopontine cholinergic neurons controlling rem sleep: An in vitro electrophysiological study. *Neuroscience*, *59*(2), 309–330. https://doi.org/10.1016/0306-4522(94)90599-1

Leutgeb, S., Leutgeb, J. K., Barnes, C. A., Moser, E. I., McNaughton, B. L., & Moser, M.-B. (2005). Independent Codes for Spatial and Episodic Memory in Hippocampal Neuronal Ensembles. *Science*, *309*(5734), 619–623. https://doi.org/10.1126/science.1114037

Lever, C., Burton, S., Jeewajee, A., O'Keefe, J., & Burgess, N. (2009). Boundary Vector Cells in the Subiculum of the Hippocampal Formation. *The Journal of Neuroscience*, *29*(31), 9771–9777. https://doi.org/10.1523/JNEUROSCI.1319-09.2009

Lever, C., Wills, T., Cacucci, F., Burgess, N., & O'Keefe, J. (2002). Long-term plasticity in hippocampal place-cell representation of environmental geometry. *Nature*, *416*(6876), 90–94. https://doi.org/10.1038/416090a

Lian, Y., Williams, S., Alexander, A. S., Hasselmo, M. E., & Burkitt, A. N. (2023). Learning the Vector Coding of Egocentric Boundary Cells from Visual Data. *The Journal of Neuroscience*, *43*(28), 5180–5190. https://doi.org/10.1523/JNEUROSCI.1071-22.2023

Liddell, H. G., Scott, R., Jones, H. S., McKenzie, R., & Glare, P. G. W. (1996). *A Greek-English lexicon* (Rev. and augm. throughout). Clarendon press.

Lien, C.-C., & Jonas, P. (2003). Kv3 Potassium Conductance is Necessary and Kinetically Optimized for High-Frequency Action Potential Generation in Hippocampal Interneurons. *The Journal of Neuroscience*, *23*(6), 2058–2068. https://doi.org/10.1523/JNEUROSCI.23-06-02058.2003

Lin, X., Ghafuri, A., Chen, X., Kazmi, M., Nitz, D. A., & Xu, X. (2024). Projection-specific circuits of retrosplenial cortex with differential contributions to spatial cognition. *Molecular Psychiatry*. https://doi.org/10.1038/s41380-024-02819-8

Livingston, K. E. (1971). Anatomical Bias of the Limbic System Concept: A Proposed Reorientation. *Archives of Neurology*, *24*(1), 17. https://doi.org/10.1001/archneur.1971.00480310045003

Llinás, R., & Yarom, Y. (1981). Electrophysiology of mammalian inferior olivary neurones in vitro. Different types of voltage-dependent ionic conductances. *The Journal of Physiology*, *315*(1), 549–567. https://doi.org/10.1113/jphysiol.1981.sp013763

Lomi, E., Jeffery, K. J., & Mitchell, A. S. (2023). Convergence of location, direction, and theta in the rat anteroventral thalamic nucleus. *iScience*, *26*(7), 106993. https://doi.org/10.1016/j.isci.2023.106993

Lomi, E., Mathiasen, M. L., Cheng, H. Y., Zhang, N., Aggleton, J. P., Mitchell, A. S., & Jeffery, K. J. (2021). Evidence for two distinct thalamocortical circuits in retrosplenial cortex. *Neurobiology of Learning and Memory*, *185*, 107525. https://doi.org/10.1016/j.nlm.2021.107525

Long, X., & Zhang, S.-J. (2021). A novel somatosensory spatial navigation system outside the hippocampal formation. *Cell Research*, *31*(6), 649–663. https://doi.org/10.1038/s41422-020-00448-8

Lozano, Y. R., Page, H., Jacob, P.-Y., Lomi, E., Street, J., & Jeffery, K. (2017). Retrosplenial and postsubicular head direction cells compared during visual landmark discrimination. *Brain and Neuroscience Advances*, *1*, 2398212817721859. https://doi.org/10.1177/2398212817721859

Luebke, J. I., McCarley, R. W., & Greene, R. W. (1993). Inhibitory action of muscarinic agonists on neurons in the rat laterodorsal tegmental nucleus in vitro. *Journal of Neurophysiology*, *70*(5), 2128–2135. https://doi.org/10.1152/jn.1993.70.5.2128

Ma, M., & Koester, J. (1995). Consequences and mechanisms of spike broadening of R20 cells in Aplysia californica. *The Journal of Neuroscience*, *15*(10), 6720–6734. https://doi.org/10.1523/JNEUROSCI.15-10-06720.1995

MacLean, P. D. (1952). Some psychiatric implications of physiological studies on frontotemporal portion of limbic system (Visceral brain). *Electroencephalography and Clinical Neurophysiology*, *4*(4), 407–418. https://doi.org/10.1016/0013-4694(52)90073-4

Maclean, P. D. (1949). Psychosomatic Disease and the "Visceral Brain": Recent Developments Bearing on the Papez Theory of Emotion. *Psychosomatic Medicine*, *11*(6), 338–353. https://doi.org/10.1097/00006842-194911000-00003

Maguire, E. A. (2001). The retrosplenial contribution to human navigation: A review of lesion and neuroimaging findings.

Marcuse, L. V., Langan, M., Hof, P. R., Panov, F., Saez, I., Jimenez-Shahed, J., Figee, M., Mayberg, H., Yoo, J. Y., Ghatan, S., Balchandani, P., & Fields, M. C. (2025). The thalamus: Structure, function, and neurotherapeutics. *Neurotherapeutics*, *22*(2), e00550. https://doi.org/10.1016/j.neurot.2025.e00550

Marozzi, E., Ginzberg, L. L., Alenda, A., & Jeffery, K. J. (2015). Purely Translational Realignment in Grid Cell Firing Patterns Following Nonmetric Context Change. *Cerebral Cortex*, *25*(11), 4619–4627. https://doi.org/10.1093/cercor/bhv120

Martina, M., Schultz, J. H., Ehmke, H., Monyer, H., & Jonas, P. (1998). Functional and Molecular Differences between Voltage-Gated K^+ Channels of Fast-Spiking Interneurons and Pyramidal Neurons of Rat Hippocampus. *The Journal of Neuroscience*, *18*(20), 8111–8125. https://doi.org/10.1523/JNEUROSCI.18-20-08111.1998

Martina, M., Yao, G. L., & Bean, B. P. (2003). Properties and Functional Role of Voltage-Dependent Potassium Channels in Dendrites of Rat Cerebellar Purkinje Neurons. *The Journal of Neuroscience*, *23*(13), 5698–5707. https://doi.org/10.1523/JNEUROSCI.23-13-05698.2003

Martinez-Espinosa, P. L., Wu, J., Yang, C., Gonzalez-Perez, V., Zhou, H., Liang, H., Xia, X.-M., & Lingle, C. J. (2015). Knockout of Slo2.2 enhances itch, abolishes KNa current, and increases action potential firing frequency in DRG neurons. *eLife*, *4*, e10013. https://doi.org/10.7554/eLife.10013

Massengill, J. L., Smith, M. A., Son, D. I., & O'Dowd, D. K. (1997). Differential Expression of K4-AP Currents and Kv3.1 Potassium Channel Transcripts in Cortical Neurons that Develop Distinct Firing Phenotypes. *The Journal of Neuroscience*, *17*(9), 3136–3147. https://doi.org/10.1523/JNEUROSCI.17-09-03136.1997

Mathiasen, M. L., Nelson, A. J. D., Amin, E., O'Mara, S. M., & Aggleton, J. P. (2021). A Direct Comparison of Afferents to the Rat Anterior Thalamic Nuclei and Nucleus Reuniens: Overlapping But Different. *eneuro*, *8*(5), ENEURO.0103–20.2021. https://doi.org/10.1523/ENEURO.0103-20.2021

McCormick, D. A., Connors, B. W., Lighthall, J. W., & Prince, D. A. (1985). Comparative electrophysiology of pyramidal and sparsely spiny stellate neurons of the neocortex. *Journal of Neurophysiology*, *54*(4), 782–806. https://doi.org/10.1152/jn.1985.54.4.782

McCormick, D. A., & Prince, D. A. (1988). Noradrenergic modulation of firing pattern in guinea pig and cat thalamic neurons, in vitro. *Journal of Neurophysiology*, *59*(3), 978–996. https://doi.org/10.1152/jn.1988.59.3.978

McGovern, T. H. (1990). The Archeology of the Norse North Atlantic. *Annual Review of Anthropology*, *19*(1), 331–351. https://doi.org/10.1146/annurev.an.19.100190.001555

McKay, B. E., & Turner, R. W. (2004). Kv3 K+ channels enable burst output in rat cerebellar Purkinje cells. *European Journal of Neuroscience*, *20*(3), 729–739. https://doi.org/10.1111/j.1460-9568.2004.03539.x

McNAUGHTON, B. L., Barnes, C. A., Gerrard, J. L., Gothard, K., Jung, M. W., Knierim, J. J., Kudrimoti, H., Qin, Y., Skaggs, W. E., Suster, M., & Weaver, K. L. (1996). Deciphering The Hippocampal Polyglot: The Hippocampus as a Path Integration System. *Journal of Experimental Biology*, *199*(1), 173–185. https://doi.org/10.1242/jeb.199.1.173

McNaughton, B., Barnes, C., & O'Keefe, J. (1983). The contributions of position, direction, and velocity to single unit activity in the hippocampus of freely-moving rats. *Experimental Brain Research*, *52*(1). https://doi.org/10.1007/BF00237147

McNaughton, B. L., Battaglia, F. P., Jensen, O., Moser, E. I., & Moser, M.-B. (2006). Path integration and the neural basis of the 'cognitive map'. *Nature Reviews Neuroscience*, *7*(8), 663–678. https://doi.org/10.1038/nrn1932

Metz, A. E. (2005). R-Type Calcium Channels Contribute to Afterdepolarization and Bursting in Hippocampal CA1 Pyramidal Neurons. *Journal of Neuroscience*, *25*(24), 5763–5773. https://doi.org/10.1523/JNEUROSCI.0624-05.2005

Mitchell, A. S., & Dalrymple-Alford, J. C. (2006). Lateral and anterior thalamic lesions impair independent memory systems. *Learning & Memory*, *13*(3), 388–396. https://doi.org/10.1101/lm.122206

Mitterdorfer, J., & Bean, B. P. (2002). Potassium Currents during the Action Potential of Hippocampal CA3 Neurons. *The Journal of Neuroscience*, *22*(23), 10106–10115. https://doi.org/10.1523/JNEUROSCI.22-23-10106.2002

Mizumori, S., & Williams, J. (1993). Directionally selective mnemonic properties of neurons in the lateral dorsal nucleus of the thalamus of rats. *The Journal of Neuroscience*, *13*(9), 4015–4028. https://doi.org/10.1523/JNEUROSCI.13-09-04015.1993

Mizuseki, K., Sirota, A., Pastalkova, E., & Buzsáki, G. (2009). Theta Oscillations Provide Temporal Windows for Local Circuit Computation in the Entorhinal-Hippocampal Loop. *Neuron*, *64*(2), 267–280. https://doi.org/10.1016/j.neuron.2009.08.037

Monteil, A., Chemin, J., Leuranguer, V., Altier, C., Mennessier, G., Bourinet, E., Lory, P., & Nargeot, J. (2000). Specific Properties of T-type Calcium Channels Generated by the Human α1I Subunit. *Journal of Biological Chemistry*, *275*(22), 16530–16535. https://doi.org/10.1074/jbc.C000090200

Morel, A., Magnin, M., & Jeanmonod, D. (1997). Multiarchitectonic and stereotactic atlas of the human thalamus. *The Journal of Comparative Neurology*, *387*(4), 588–630. https://doi.org/10.1002/(SICI)1096-9861(19971103)387:4<588::AID-CNE8>3.0.CO;2-Z

Morris, R. G. M., Schenk, F., Tweedie, F., & Jarrard, L. E. (1990). Ibotenate Lesions of Hippocampus and/or Subiculum: Dissociating Components of Allocentric Spatial Learning. *European Journal of Neuroscience*, *2*(12), 1016–1028. https://doi.org/10.1111/j.1460-9568.1990.tb00014.x

Morris, R. G. (1981). Spatial localization does not require the presence of local cues. *Learning and Motivation*, *12*(2), 239–260. https://doi.org/10.1016/0023-9690(81)90020-5

Moser, E. I., & Moser, M.-B. (2008). A metric for space. *Hippocampus*, *18*(12), 1142–1156. https://doi.org/10.1002/hipo.20483

Moser, M.-B., Rowland, D. C., & Moser, E. I. (2015). Place Cells, Grid Cells, and Memory. *Cold Spring Harbor Perspectives in Biology*, *7*(2), a021808. https://doi.org/10.1101/cshperspect.a021808

Muir, G. M., Brown, J. E., Carey, J. P., Hirvonen, T. P., Della Santina, C. C., Minor, L. B., & Taube, J. S. (2009). Disruption of the Head Direction Cell Signal after Occlusion of the Semicircular Canals in the Freely Moving Chinchilla. *The Journal of Neuroscience*, *29*(46), 14521–14533. https://doi.org/10.1523/JNEUROSCI.3450-09.2009

Muller, R., Bostock, E., Taube, J., & Kubie, J. (1994). On the directional firing properties of hippocampal place cells. *The Journal of Neuroscience*, *14*(12), 7235–7251. https://doi.org/10.1523/JNEUROSCI.14-12-07235.1994

Muller, R., & Kubie, J. (1987). The effects of changes in the environment on the spatial firing of hippocampal complex-spike cells. *The Journal of Neuroscience*, *7*(7), 1951–1968. https://doi.org/10.1523/JNEUROSCI.07-07-01951.1987

Nassar, M., Simonnet, J., Lofredi, R., Cohen, I., Savary, E., Yanagawa, Y., Miles, R., & Fricker, D. (2015). Diversity and overlap of parvalbumin and somatostatin expressing interneurons in mouse presubiculum. *Frontiers in Neural Circuits*, *9*. https://doi.org/10.3389/fncir.2015.00020

Nassar, M., Richevaux, L., Lim, D., Tayupo, D., Martin, E., & Fricker, D. (2025). Presubicular VIP expressing interneurons receive facilitating excitation from anterior thalamus. *Neuroscience*, *578*, 91–104. https://doi.org/10.1016/j.neuroscience.2024.09.032

Nassar, M., Simonnet, J., Huang, L.-W., Mathon, B., Cohen, I., Bendels, M. H., Beraneck, M., Miles, R., & Fricker, D. (2018). Anterior Thalamic Excitation and Feedforward Inhibition of Presubicular Neurons Projecting to Medial Entorhinal Cortex. *The Journal of Neuroscience*, *38*(28), 6411–6425. https://doi.org/10.1523/JNEUROSCI.0014-18.2018

Nelson, A. J. D., & Vann, S. D. (2014). Mammilliothalamic tract lesions disrupt tests of visuospatial memory. *Behavioral Neuroscience*, *128*(4), 494–503. https://doi.org/10.1037/bne0000001

Nelson, A. J. (2021). The anterior thalamic nuclei and cognition: A role beyond space? *Neuroscience & Biobehavioral Reviews*, *126*, 1–11. https://doi.org/10.1016/j.neubiorev.2021.02.047

Nelson, A. J., Kinnavane, L., Amin, E., O'Mara, S. M., & Aggleton, J. P. (2020). Deconstructing the Direct Reciprocal Hippocampal-Anterior Thalamic Pathways for Spatial Learning. *The Journal of Neuroscience*, *40*(36), 6978–6990. https://doi.org/10.1523/JNEUROSCI.0874-20.2020

Newman, E. L., & Hasselmo, M. E. (2014). Grid cell firing properties vary as a function of theta phase locking preferences in the rat medial entorhinal cortex. *Frontiers in Systems Neuroscience*, *8*. https://doi.org/10.3389/fnsys.2014.00193

Nowak, L. G., Azouz, R., Sanchez-Vives, M. V., Gray, C. M., & McCormick, D. A. (2003). Electrophysiological Classes of Cat Primary Visual Cortical Neurons In Vivo as Revealed by Quantitative Analyses. *Journal of Neurophysiology*, *89*(3), 1541–1566. https://doi.org/10.1152/jn.00580.2002

Nyberg, N., & Gahnstrom, C. (2022). Uncovering the Hippocampal Mechanisms Underpinning Spatial Learning and Flexible Navigation. *The Journal of Neuroscience*, *42*(48), 8915–8917. https://doi.org/10.1523/JNEUROSCI.1400-22.2022

O'Keefe, J., & Conway, D. (1978). Hippocampal place units in the freely moving rat: Why they fire where they fire. *Experimental Brain Research*, *31*(4). https://doi.org/10.1007/BF00239813

O'Keefe, J., & Dostrovsky, J. (1971). The hippocampus as a spatial map. Preliminary evidence from unit activity in the freely-moving rat. *Brain Research*, *34*(1), 171–175. https://doi.org/10.1016/0006-8993(71)90358-1

O'Keefe, J., & Speakman, A. (1987). Single unit activity in the rat hippocampus during a spatial memory task. *Experimental Brain Research*, *68*(1). https://doi.org/10.1007/BF00255230

O'Keefe, J., & Nadel, L. (1978). *The hippocampus as a cognitive map*. Clarendon Press ; Oxford University Press.

O'Keefe, J., & Recce, M. L. (1993). Phase relationship between hippocampal place units and the EEG theta rhythm. *Hippocampus*, *3*(3), 317–330. https://doi.org/10.1002/hipo.450030307

Ouhaz, Z., Fleming, H., & Mitchell, A. S. (2018). Cognitive Functions and Neurodevelopmental Disorders Involving the Prefrontal Cortex and Mediodorsal Thalamus. *Frontiers in Neuroscience*, *12*. https://doi.org/10.3389/fnins.2018.00033

Pachitariu, M., Stringer, C., Dipoppa, M., Schröder, S., Rossi, L. F., Dalgleish, H., Carandini, M., & Harris, K. D. (2016, June 30). *Suite2p: Beyond 10,000 neurons with standard two-photon microscopy*. https://doi.org/10.1101/061507

Page, H. J. I., Wilson, J. J., & Jeffery, K. J. (2018). A dual-axis rotation rule for updating the head direction cell reference frame during movement in three dimensions. *Journal of Neurophysiology*, *119*(1), 192–208. https://doi.org/10.1152/jn.00501.2017

Pape, H.-C. (1996). Queer Current and Pacemaker: The Hyperpolarization-Activated Cation Current in Neurons. *Annual Review of Physiology*, *58*(1), 299–327. https://doi.org/10.1146/annurev.ph.58.030196.001503

Papez, J. W. (1937). A PROPOSED MECHANISM OF EMOTION. *Archives of Neurology And Psychiatry*, *38*(4), 725. https://doi.org/10.1001/archneurpsyc.1937.02260220069003

Parent, A., Paré, D., Smith, Y., & Steriade, M. (1988). Basal forebrain cholinergic and noncholinergic projections to the thalamus and brainstem in cats and monkeys. *Journal of Comparative Neurology*, *277*(2), 281–301. https://doi.org/10.1002/cne.902770209

Parent, M., & Descarries, L. (2008). Acetylcholine innervation of the adult rat thalamus: Distribution and ultrastructural features in dorsolateral geniculate, parafascicular, and reticular thalamic nuclei. *Journal of Comparative Neurology*, *511*(5), 678–691. https://doi.org/10.1002/cne.21868

Park, E. H., Keeley, S., Savin, C., Ranck, J. B., & Fenton, A. A. (2019). How the Internally Organized Direction Sense Is Used to Navigate. *Neuron*, *101*(2), 285–293.e5. https://doi.org/10.1016/j.neuron.2018.11.019

Paxinos, G., & Franklin, K. B. J. (2013). *Paxinos and Franklin's the mouse brain in stereotaxic coordinates* (Fourth edition). Elsevier, Academic Press.

Pedregosa, F. (2011). Scikit-learn: Machine Learning in Python. *Journal of Machine Learning Research*.

Perez-Reyes, E. (2003). Molecular Physiology of Low-Voltage-Activated T-type Calcium Channels. *Physiological Reviews*, *83*(1), 117–161. https://doi.org/10.1152/physrev.00018.2002

Perry, V., Oehler, R., & Cowey, A. (1984). Retinal ganglion cells that project to the dorsal lateral geniculate nucleus in the macaque monkey. *Neuroscience*, *12*(4), 1101–1123. https://doi.org/10.1016/0306-4522(84)90006-X

Petrucco, L., Lavian, H., Wu, Y. K., Svara, F., Štih, V., & Portugues, R. (2023). Neural dynamics and architecture of the heading direction circuit in zebrafish. *Nature Neuroscience*, *26*(5), 765–773. https://doi.org/10.1038/s41593-023-01308-5

Peyrache, A., Lacroix, M. M., Petersen, P. C., & Buzsáki, G. (2015). Internally organized mechanisms of the head direction sense. *Nature Neuroscience*, *18*(4), 569–575. https://doi.org/10.1038/nn.3968

Peyrache, A., Schieferstein, N., & Buzsáki, G. (2017). Transformation of the head-direction signal into a spatial code. *Nature Communications*, *8*(1), 1752. https://doi.org/10.1038/s41467-017-01908-3

Phillips, J. W., Schulmann, A., Hara, E., Winnubst, J., Liu, C., Valakh, V., Wang, L., Shields, B. C., Korff, W., Chandrashekar, J., Lemire, A. L., Mensh, B., Dudman, J. T., Nelson, S. B., & Hantman, A. W. (2019). A repeated molecular architecture across thalamic pathways. *Nature Neuroscience*, *22*(11), 1925–1935. https://doi.org/10.1038/s41593-019-0483-3

Pothuizen, H. H., Davies, M., Aggleton, J. P., & Vann, S. D. (2010). Effects of selective granular retrosplenial cortex lesions on spatial working memory in rats. *Behavioural Brain Research*, *208*(2), 566–575. https://doi.org/10.1016/j.bbr.2010.01.001

Powell, T. P., Guillery, R. W., & Cowan, W. M. (1957). A quantitative study of the fornixmamillo-thalamic system. *Journal of Anatomy*, *91*(4), 419–437.

Preston-Ferrer, P., Coletta, S., Frey, M., & Burgalossi, A. (2016). Anatomical organization of presubicular head-direction circuits. *eLife*, *5*, e14592. https://doi.org/10.7554/eLife.14592

Ragan, T., Kadiri, L. R., Venkataraju, K. U., Bahlmann, K., Sutin, J., Taranda, J., Arganda-Carreras, I., Kim, Y., Seung, H. S., & Osten, P. (2012). Serial two-photon tomography for automated ex vivo mouse brain imaging. *Nature Methods*, *9*(3), 255–258. https://doi.org/10.1038/nmeth.1854

Raman, I. M., & Bean, B. P. (1997). Resurgent Sodium Current and Action Potential Formation in Dissociated Cerebellar Purkinje Neurons. *The Journal of Neuroscience*, *17*(12), 4517–4526. https://doi.org/10.1523/JNEUROSCI.17-12-04517.1997

Ranck, J. B. (1984). Head direction cells in the deep cell layer of dorsolateral pre-subiculum in freely moving rats. *Soc Neurosci Abstr.*

Redish, A. D., Elga, A. N., & Touretzky, D. S. (1996). A coupled attractor model of the rodent head direction system. *Network: Computation in Neural Systems*, *7*(4), 671–685. https://doi.org/10.1088/0954-898X_7_4_004

Richevaux, L., Lim, D., Nassar, M., Rodrigues, L. D., Mauthe, C., Cohen, I., Sol-Foulon, N., & Fricker, D. (2025, August 27). *Projection-specific integration of convergent thalamic and retrosplenial signals in the presubicular head direction cortex*. https://doi.org/10.7554/eLife.92443.2

Riolan, J. (1610). *Anatome.*

Robinson, R. B., & Siegelbaum, S. A. (2003). Hyperpolarization-Activated Cation Currents: From Molecules to Physiological Function. *Annual Review of Physiology*, *65*(1), 453–480. https://doi.org/10.1146/annurev.physiol.65.092101.142734

Ropars, G., Gorre, G., Le Floch, A., Enoch, J., & Lakshminarayanan, V. (2012). A depolarizer as a possible precise sunstone for Viking navigation by polarized skylight. *Proceedings of the Royal Society A: Mathematical, Physical and Engineering Sciences*, *468*(2139), 671–684. https://doi.org/10.1098/rspa.2011.0369

Ropars, G., Lakshminarayanan, V., & Le Floch, A. (2014). The sunstone and polarised skylight: Ancient Viking navigational tools? *Contemporary Physics*, *55*(4), 302–317. https://doi.org/10.1080/00107514.2014.929797

Roslund, C., & Beckman, C. (1994). Disputing Viking navigation by polarized skylight. *Applied Optics*, *33*(21), 4754. https://doi.org/10.1364/AO.33.004754

Roy, D. S., Zhang, Y., Aida, T., Choi, S., Chen, Q., Hou, Y., Lea, N. E., Skaggs, K. M., Quay, J. C., Liew, M., Maisano, H., Le, V., Jones, C., Xu, J., Kong, D., Sullivan, H. A., Saunders, A., McCarroll, S. A., Wickersham, I. R., & Feng, G. (2021). Anterior thalamic dysfunction underlies cognitive deficits in a subset of neuropsychiatric disease models. *Neuron*, *109*(16), 2590–2603.e13. https://doi.org/10.1016/j.neuron.2021.06.005

Roy, D. S., Zhang, Y., Aida, T., Shen, C., Skaggs, K. M., Hou, Y., Fleishman, M., Mosto, O., Weninger, A., & Feng, G. (2022). Anterior thalamic circuits crucial for working memory. *Proceedings of the National Academy of Sciences*, *119*(20), e2118712119. https://doi.org/10.1073/pnas.2118712119

Roy, D. S., Zhang, Y., Halassa, M. M., & Feng, G. (2022). Thalamic subnetworks as units of function. *Nature Neuroscience*, *25*(2), 140–153. https://doi.org/10.1038/s41593-021-00996-1

Royer, S., Sirota, A., Patel, J., & Buzsáki, G. (2010). Distinct Representations and Theta Dynamics in Dorsal and Ventral Hippocampus. *The Journal of Neuroscience*, *30*(5), 1777–1787. https://doi.org/10.1523/JNEUROSCI.4681-09.2010

Rudy, B. (1978). Slow inactivation of the sodium conductance in squid giant axons. Pronase resistance. *The Journal of Physiology*, *283*(1), 1–21. https://doi.org/10.1113/jphysiol.1978.sp012485

Rudy, B., & McBain, C. J. (2001). Kv3 channels: Voltage-gated K+ channels designed for high-frequency repetitive firing. *Trends in Neurosciences*, *24*(9), 517–526. https://doi.org/10.1016/S0166-2236(00)01892-0

Saalmann, Y. B. (2014). Intralaminar and medial thalamic influence on cortical synchrony, information transmission and cognition. *Frontiers in Systems Neuroscience*, *8*. https://doi.org/10.3389/fnsys.2014.00083

Sargolini, F., Fyhn, M., Hafting, T., McNaughton, B. L., Witter, M. P., Moser, M.-B., & Moser, E. I. (2006). Conjunctive Representation of Position, Direction, and Velocity in Entorhinal Cortex. *Science*, *312*(5774), 758–762. https://doi.org/10.1126/science.1125572

Sárkány, B., Dávid, C., Hortobágyi, T., Gombás, P., Somogyi, P., Acsády, L., & Viney, T. J. (2024). Early and selective localization of tau filaments to glutamatergic subcellular domains within the human anterodorsal thalamus. *Acta Neuropathologica*, *147*(1), 98. https://doi.org/10.1007/s00401-024-02749-3

Satoh, K., & Fibiger, H. C. (1986). Cholinergic neurons of the laterodorsal tegmental nucleus: Efferent and afferent connections. *Journal of Comparative Neurology*, *253*(3), 277–302. https://doi.org/10.1002/cne.902530302

Save, E., Nerad, L., & Poucet, B. (2000). Contribution of multiple sensory information to place field stability in hippocampal place cells. *Hippocampus*, *10*(1), 64–76. https://doi.org/10.1002/(SICI)1098-1063(2000)10:1<64::AID-HIPO7>3.0.CO;2-Y

Savelli, F., Yoganarasimha, D., & Knierim, J. J. (2008). Influence of boundary removal on the spatial representations of the medial entorhinal cortex. *Hippocampus*, *18*(12), 1270–1282. https://doi.org/10.1002/hipo.20511

Schiff, N. D., Shah, S. A., Hudson, A. E., Nauvel, T., Kalik, S. F., & Purpura, K. P. (2013). Gating of attentional effort through the central thalamus. *Journal of Neurophysiology*, *109*(4), 1152–1163. https://doi.org/10.1152/jn.00317.2011

Seelig, J. D., & Jayaraman, V. (2015). Neural dynamics for landmark orientation and angular path integration. *Nature*, *521*(7551), 186–191. https://doi.org/10.1038/nature14446

Seki, M., & Zyo, K. (1984). Anterior thalamic afferents from the mamillary body and the limbic cortex in the rat. *Journal of Comparative Neurology*, *229*(2), 242–256. https://doi.org/10.1002/cne.902290209

Shao, L.-R., Halvorsrud, R., Borg-Graham, L., & Storm, J. F. (1999). The role of BK-type Ca^{2+}-dependent K^+ channels in spike broadening during repetitive firing in rat hippocampal pyramidal cells. *The Journal of Physiology*, *521*(1), 135–146. https://doi.org/10.1111/j.1469-7793.1999.00135.x

Sharp, P. E., Tinkelman, A., & Cho, J. (2001). Angular velocity and head direction signals recorded from the dorsal tegmental nucleus of gudden in the rat: Implications for path integration in the head direction cell circuit. *Behavioral Neuroscience*, *115*(3), 571–588.

Sharp, P. E. (1999). Complimentary roles for hippocampal versus subicular/entorhinal place cells in coding place, context, and events. *Hippocampus*, *9*(4), 432–443. https://doi.org/10.1002/(SICI)1098-1063(1999)9:4<432::AID-HIPO9>3.0.CO;2-P

Sharp, P. E., Blair, H. T., & Cho, J. (2001). The anatomical and computational basis of the rat head-direction cell signal. *Trends in Neurosciences*, *24*(5), 289–294. https://doi.org/10.1016/S0166-2236(00)01797-5

Sharp, P. E., & Koester, K. (2008). Lesions of the mammillary body region alter hippocampal movement signals and theta frequency: Implications for path integration models. *Hippocampus*, *18*(9), 862–878. https://doi.org/10.1002/hipo.20474

Sharp, P. E., Turner-Williams, S., & Tuttle, S. (2006). Movement-related correlates of single cell activity in the interpeduncular nucleus and habenula of the rat during a pellet-chasing task. *Behavioural Brain Research*, *166*(1), 55–70. https://doi.org/10.1016/j.bbr.2005.07.004

Sherman, S. M. (2016). Thalamus plays a central role in ongoing cortical functioning. *Nature Neuroscience*, *19*(4), 533–541. https://doi.org/10.1038/nn.4269

Sherman, S. M., & Guillery, R. W. (1998). On the actions that one nerve cell can have on another: Distinguishing "drivers" from "modulators". *Proceedings of the National Academy of Sciences*, *95*(12), 7121–7126. https://doi.org/10.1073/pnas.95.12.7121

Sherman, S. M., & Guillery, R. W. (2011). Distinct functions for direct and transthalamic corticocortical connections. *Journal of Neurophysiology*, *106*(3), 1068–1077. https://doi.org/10.1152/jn.00429.2011

Shibata, H. (1992). Topographic organization of subcortical projections to the anterior thalamic nuclei in the rat. *Journal of Comparative Neurology*, *323*(1), 117–127. https://doi.org/10.1002/cne.903230110

Shibata, H. (1993a). Direct projections from the anterior thalamic nuclei to the retrohippocampal region in the rat. *Journal of Comparative Neurology*, *337*(3), 431–445. https://doi.org/10.1002/cne.903370307

Shibata, H. (1993b). Efferent projections from the anterior thalamic nuclei to the cingulate cortex in the rat. *Journal of Comparative Neurology*, *330*(4), 533–542. https://doi.org/10.1002/cne.903300409

Shibata, H., & Naito, J. (2005). Organization of anterior cingulate and frontal cortical projections to the anterior and laterodorsal thalamic nuclei in the rat. *Brain Research*, *1059*(1), 93–103. https://doi.org/10.1016/j.brainres.2005.08.025

Shibata, R., Nakahira, K., Shibasaki, K., Wakazono, Y., Imoto, K., & Ikenaka, K. (2000). A-Type K+ Current Mediated by the Kv4 Channel Regulates the Generation of Action Potential in Developing Cerebellar Granule Cells. *The Journal of Neuroscience*, *20*(11), 4145–4155. https://doi.org/10.1523/JNEUROSCI.20-11-04145.2000

Shinder, M. E., & Taube, J. S. (2011). Active and passive movement are encoded equally by head direction cells in the anterodorsal thalamus. *Journal of Neurophysiology*, *106*(2), 788–800. https://doi.org/10.1152/jn.01098.2010

Simonnet, J., Nassar, M., Stella, F., Cohen, I., Mathon, B., Boccara, C. N., Miles, R., & Fricker, D. (2017). Activity dependent feedback inhibition may maintain head direction signals in mouse presubiculum. *Nature Communications*, *8*(1), 16032. https://doi.org/10.1038/ncomms16032

Skaggs, W. E., Knierim, J. J., Kudrimoti, H. S., & McNaughton, B. L. (1995). A model of the neural basis of the rat's sense of direction. *Advances in Neural Information Processing Systems*, *7*, 173–180.

Skaggs, W. E., McNaughton, B. L., Wilson, M. A., & Barnes, C. A. (1996). Theta phase precession in hippocampal neuronal populations and the compression of temporal sequences. *Hippocampus*, *6*(2), 149–172. https://doi.org/10.1002/(SICI)1098-1063(1996)6:2<149::AID-HIPO6>3.0.CO;2-K

Small, S. A., Schobel, S. A., Buxton, R. B., Witter, M. P., & Barnes, C. A. (2011). A pathophysiological framework of hippocampal dysfunction in ageing and disease. *Nature Reviews Neuroscience*, *12*(10), 585–601. https://doi.org/10.1038/nrn3085

Sofroniew, M., Priestley, J., Consolazione, A., Eckenstein, F., & Cuello, A. (1985). Cholinergic projections from the midbrain and pons to the thalamus in the rat, identified by

combined retrograde tracing and choline acetyltransferase immunohistochemistry. *Brain Research*, *329*(1–2), 213–223. https://doi.org/10.1016/0006-8993(85)90527-X

Solstad, T., Boccara, C. N., Kropff, E., Moser, M.-B., & Moser, E. I. (2008). Representation of Geometric Borders in the Entorhinal Cortex. *Science*, *322*(5909), 1865–1868. https://doi.org/10.1126/science.1166466

Song, P., & Wang, X.-J. (2005). Angular Path Integration by Moving "Hill of Activity": A Spiking Neuron Model without Recurrent Excitation of the Head-Direction System. *The Journal of Neuroscience*, *25*(4), 1002–1014. https://doi.org/10.1523/JNEUROSCI.4172-04.2005

Southan, A. P., & Robertson, B. (2000). Electrophysiological Characterization of Voltage-Gated K^+ Currents in Cerebellar Basket and Purkinje Cells: Kv1 and Kv3 Channel Subfamilies Are Present in Basket Cell Nerve Terminals. *The Journal of Neuroscience*, *20*(1), 114–122. https://doi.org/10.1523/JNEUROSCI.20-01-00114.2000

Spalla, D., Treves, A., & Boccara, C. N. (2022). Angular and linear speed cells in the parahippocampal circuits. *Nature Communications*, *13*(1), 1907. https://doi.org/10.1038/s41467-022-29583-z

Stackman, R. W., & Taube, J. S. (1997). Firing properties of head direction cells in the rat anterior thalamic nucleus: Dependence on vestibular input. *The Journal of Neuroscience: The Official Journal of the Society for Neuroscience*, *17*(11), 4349–4358. https://doi.org/10.1523/JNEUROSCI.17-11-04349.1997

Stackman, R. W., Golob, E. J., Bassett, J. P., & Taube, J. S. (2003). Passive Transport Disrupts Directional Path Integration by Rat Head Direction Cells. *Journal of Neurophysiology*, *90*(5), 2862–2874. https://doi.org/10.1152/jn.00346.2003

Stackman, R. W., & Taube, J. S. (1998). Firing Properties of Rat Lateral Mammillary Single Units: Head Direction, Head Pitch, and Angular Head Velocity. *The Journal of Neuroscience*, *18*(21), 9020–9037. https://doi.org/10.1523/JNEUROSCI.18-21-09020.1998

Staff, N. P., Jung, H.-Y., Thiagarajan, T., Yao, M., & Spruston, N. (2000). Resting and Active Properties of Pyramidal Neurons in Subiculum and CA1 of Rat Hippocampus. *Journal of Neurophysiology*, *84*(5), 2398–2408. https://doi.org/10.1152/jn.2000.84.5.2398

Stock, J. T., & Orna, M. V. (Eds.). (1989, January). *Electrochemistry, Past and Present* (Vol. 390). American Chemical Society. https://doi.org/10.1021/bk-1989-0390

Stocker, M. (2004). Ca2+-activated K+ channels: Molecular determinants and function of the SK family. *Nature Reviews Neuroscience*, *5*(10), 758–770. https://doi.org/10.1038/nrn1516

Storm, J. F. (1987). Action potential repolarization and a fast after-hyperpolarization in rat hippocampal pyramidal cells. *The Journal of Physiology*, *385*(1), 733–759. https://doi.org/10.1113/jphysiol.1987.sp016517

Storm, J. F. (1988). Temporal integration by a slowly inactivating K+ current in hippocampal neurons. *Nature*, *336*(6197), 379–381. https://doi.org/10.1038/336379a0

Storm, J. F. (1990). Chapter 12 Potassium currents in hippocampal pyramidal cells. In *Progress in Brain Research* (pp. 161–187, Vol. 83). Elsevier. https://doi.org/10.1016/S0079-6123(08)61248-0

Suzuki, S., & Rogawski, M. A. (1989). T-type calcium channels mediate the transition between tonic and phasic firing in thalamic neurons. *Proceedings of the National Academy of Sciences*, *86*(18), 7228–7232. https://doi.org/10.1073/pnas.86.18.7228

Swensen, A. M., & Bean, B. P. (2003). Ionic Mechanisms of Burst Firing in Dissociated Purkinje Neurons. *The Journal of Neuroscience*, *23*(29), 9650–9663. https://doi.org/10.1523/JNEUROSCI.23-29-09650.2003

Száz, D., Farkas, A., Blahó, M., Barta, A., Egri, Á., Kretzer, B., Hegedüs, T., Jäger, Z., & Horváth, G. (2016). Adjustment errors of sunstones in the first step of sky-polarimetric Viking navigation: Studies with dichroic cordierite/ tourmaline and birefringent calcite crystals. *Royal Society Open Science*, *3*(1), 150406. https://doi.org/10.1098/rsos.150406

Talley, E. M., Solórzano, G., Lei, Q., Kim, D., & Bayliss, D. A. (2001). CNS Distribution of Members of the Two-Pore-Domain (KCNK) Potassium Channel Family. *The Journal of Neuroscience*, *21*(19), 7491–7505. https://doi.org/10.1523/JNEUROSCI.21-19-07491.2001

Tan, H. M., Bassett, J. P., O'Keefe, J., Cacucci, F., & Wills, T. J. (2015). The Development of the Head Direction System before Eye Opening in the Rat. *Current Biology*, *25*(4), 479–483. https://doi.org/10.1016/j.cub.2014.12.030

Taube, J. S. (2007). The Head Direction Signal: Origins and Sensory-Motor Integration. *Annual Review of Neuroscience*, *30*(1), 181–207. https://doi.org/10.1146/annurev.neuro.29.051605.112854

Taube, J. S., Butler, W. N., Dumont, J. R., Graham, J. A., Marcroft, J. L., Shinder, M. E., Stackman, R. W., & Yoder, R. M. (2025, April 18). *Generating the head direction signal: Two types of head direction cells in the lateral mammillary nuclei and dorsal tegmental nuclei*. https://doi.org/10.1101/2025.04.11.648409

Taube, J. S., & Muller, R. U. (1998). Comparisons of head direction cell activity in the postsubiculum and anterior thalamus of freely moving rats. *Hippocampus*, *8*(2), 87–108. https://doi.org/10.1002/(SICI)1098-1063(1998)8:2<87::AID-HIPO1>3.0.CO;2-4

Taube, J. (1995). Head direction cells recorded in the anterior thalamic nuclei of freely moving rats. *The Journal of Neuroscience*, *15*(1), 70–86. https://doi.org/10.1523/JNEUROSCI.15-01-00070.1995

Taube, J., Muller, R., & Ranck, J. (1990a). Head-direction cells recorded from the postsubiculum in freely moving rats. I. Description and quantitative analysis. *The Journal of Neuroscience*, *10*(2), 420–435. https://doi.org/10.1523/JNEUROSCI.10-02-00420.1990

Taube, J., Muller, R., & Ranck, J. (1990b). Head-direction cells recorded from the postsubiculum in freely moving rats. II. Effects of environmental manipulations. *The Journal of Neuroscience*, *10*(2), 436–447. https://doi.org/10.1523/JNEUROSCI.10-02-00436.1990

Taverna, S., Tkatch, T., Metz, A. E., & Martina, M. (2005). Differential Expression of TASK Channels between Horizontal Interneurons and Pyramidal Cells of Rat Hippocam-

pus. *The Journal of Neuroscience*, *25*(40), 9162–9170. https://doi.org/10.1523/JNEUROSCI.2454-05.2005

Thinschmidt, J., Kinney, G., & Kocsis, B. (1995). The supramammillary nucleus: Is it necessary for the mediation of hippocampal theta rhythm? *Neuroscience*, *67*(2), 301–312. https://doi.org/10.1016/0306-4522(95)00045-K

Tolman, E. C. (1948). Cognitive maps in rats and men. *Psychological Review*, *55*(4), 189–208. https://doi.org/10.1037/h0061626

Tsanov, M., Chah, E., Vann, S. D., Reilly, R. B., Erichsen, J. T., Aggleton, J. P., & O'Mara, S. M. (2011). Theta-Modulated Head Direction Cells in the Rat Anterior Thalamus. *Journal of Neuroscience*, *31*(26), 9489–9502. https://doi.org/10.1523/JNEUROSCI.0353-11.2011

Tsanov, M., Chah, E., Wright, N., Vann, S. D., Reilly, R., Erichsen, J. T., Aggleton, J. P., & O'Mara, S. M. (2011). Oscillatory Entrainment of Thalamic Neurons by Theta Rhythm in Freely Moving Rats. *Journal of Neurophysiology*, *105*(1), 4–17. https://doi.org/10.1152/jn.00771.2010

Tukker, J. J., Tang, Q., Burgalossi, A., & Brecht, M. (2015). Head-Directional Tuning and Theta Modulation of Anatomically Identified Neurons in the Presubiculum. *The Journal of Neuroscience*, *35*(46), 15391–15395. https://doi.org/10.1523/JNEUROSCI.0685-15.2015

Turner-Evans, D., Wegener, S., Rouault, H., Franconville, R., Wolff, T., Seelig, J. D., Druckmann, S., & Jayaraman, V. (2017). Angular velocity integration in a fly heading circuit. *eLife*, *6*, e23496. https://doi.org/10.7554/eLife.23496

Umaba, R., Kitanishi, T., & Mizuseki, K. (2021). Monosynaptic connection from the subiculum to medial mammillary nucleus neurons projecting to the anterior thalamus and Gudden's ventral tegmental nucleus. *Neuroscience Research*, *171*, 1–8. https://doi.org/10.1016/j.neures.2021.01.006

Valerio, S., Clark, B. J., Chan, J. H., Frost, C. P., Harris, M. J., & Taube, J. S. (2010). Directional learning, but no spatial mapping by rats performing a navigational task in an inverted orientation. *Neurobiology of Learning and Memory*, *93*(4), 495–505. https://doi.org/10.1016/j.nlm.2010.01.007

Van Der Goes, M.-S. H., Voigts, J., Newman, J. P., Toloza, E. H., Brown, N. J., Murugan, P., & Harnett, M. T. (2024). Coordinated head direction representations in mouse anterodorsal thalamic nucleus and retrosplenial cortex. *eLife*, *13*, e82952. https://doi.org/10.7554/eLife.82952

Van Groen, T., & Michael Wyss, J. (1990). Connections of the retrosplenial granular a cortex in the rat. *Journal of Comparative Neurology*, *300*(4), 593–606. https://doi.org/10.1002/cne.903000412

Van Groen, T., & Wyss, J. M. (1990a). The connections of presubiculum and parasubiculum in the rat. *Brain Research*, *518*(1–2), 227–243. https://doi.org/10.1016/0006-8993(90)90976-I

Van Groen, T., & Wyss, J. M. (1990b). The postsubicular cortex in the rat: Characterization of the fourth region of the subicular cortex and its connections. *Brain Research*, *529*(1–2), 165–177. https://doi.org/10.1016/0006-8993(90)90824-U

Van Groen, T., & Wyss, J. M. (1995). Projections from the anterodorsal and anteroveniral nucleus of the thalamus to the limbic cortex in the rat. *Journal of Comparative Neurology*, *358*(4), 584–604. https://doi.org/10.1002/cne.903580411

Van Groen, T., & Wyss, J. M. (2003). Connections of the retrosplenial granular b cortex in the rat. *Journal of Comparative Neurology*, *463*(3), 249–263. https://doi.org/10.1002/cne.10757

Van Wijngaarden, J. B., Babl, S. S., & Ito, H. T. (2020). Entorhinal-retrosplenial circuits for allocentric-egocentric transformation of boundary coding. *eLife*, *9*, e59816. https://doi.org/10.7554/eLife.59816

Vann, S. D., & Aggleton, J. P. (2004). The mammillary bodies: Two memory systems in one? *Nature Reviews Neuroscience*, *5*(1), 35–44. https://doi.org/10.1038/nrn1299

Vann, S. D., & Aggleton, J. P. (2005). Selective dysgranular retrosplenial cortex lesions in rats disrupt allocentric performance of the radial-arm maze task. *Behavioral Neuroscience*, *119*(6), 1682–1686. https://doi.org/10.1037/0735-7044.119.6.1682

Vann, S. D., Saunders, R. C., & Aggleton, J. P. (2007). Distinct, parallel pathways link the medial mammillary bodies to the anterior thalamus in macaque monkeys. *European Journal of Neuroscience*, *26*(6), 1575–1586. https://doi.org/10.1111/j.1460-9568.2007.05773.x

Vantomme, G., Rovó, Z., Cardis, R., Béard, E., Katsioudi, G., Guadagno, A., Perrenoud, V., Fernandez, L. M., & Lüthi, A. (2020). A Thalamic Reticular Circuit for Head Direction Cell Tuning and Spatial Navigation. *Cell Reports*, *31*(10), 107747. https://doi.org/10.1016/j.celrep.2020.107747

Vassilev, P., Scheuer, T., & Catterall, W. A. (1989). Inhibition of inactivation of single sodium channels by a site-directed antibody. *Proceedings of the National Academy of Sciences*, *86*(20), 8147–8151. https://doi.org/10.1073/pnas.86.20.8147

Vassilev, P., Scheuer, T., & Catterall, W. (1988). Identification of an intracellular peptide segment involved in sodium channel inactivation. *Science*, *241*(4873), 1658–1661. https://doi.org/10.1126/science.241.4873.1658

Veazey, R. B., Amaral, D. G., & Cowan, W. M. (1982). The morphology and connections of the posterior hypothalamus in the cynomolgus monkey (*Macaca fascicularis*). II. Efferent connections. *Journal of Comparative Neurology*, *207*(2), 135–156. https://doi.org/10.1002/cne.902070204

Vertes, R. P., Hoover, W. B., & Di Prisco, G. V. (2004). Theta Rhythm of the Hippocampus: Subcortical Control and Functional Significance. *Behavioral and Cognitive Neuroscience Reviews*, *3*(3), 173–200. https://doi.org/10.1177/1534582304273594

Vertes, R., Albo, Z., & Viana Di Prisco, G. (2001). Theta-rhythmically firing neurons in the anterior thalamus: Implications for mnemonic functions of Papez's circuit. *Neuroscience*, *104*(3), 619–625. https://doi.org/10.1016/S0306-4522(01)00131-2

Vetere, G., Xia, F., Ramsaran, A. I., Tran, L. M., Josselyn, S. A., & Frankland, P. W. (2021). An inhibitory hippocampal–thalamic pathway modulates remote memory retrieval. *Nature Neuroscience*, *24*(5), 685–693. https://doi.org/10.1038/s41593-021-00819-3

Viejo, G., & Peyrache, A. (2020). Precise coupling of the thalamic head-direction system to hippocampal ripples. *Nature Communications*, *11*(1), 2524. https://doi.org/10.1038/s41467-020-15842-4

Vilin, Y. Y., & Ruben, P. C. (2001). Slow Inactivation in Voltage-Gated Sodium Channels: Molecular Substrates and Contributions to Channelopathies. *Cell Biochemistry and Biophysics*, *35*(2), 171–190. https://doi.org/10.1385/CBB:35:2:171

Virtanen, P., Gommers, R., Oliphant, T. E., Haberland, M., Reddy, T., Cournapeau, D., Burovski, E., Peterson, P., Weckesser, W., Bright, J., Van Der Walt, S. J., Brett, M., Wilson, J., Millman, K. J., Mayorov, N., Nelson, A. R. J., Jones, E., Kern, R., Larson, E., … Vázquez-Baeza, Y. (2020). SciPy 1.0: Fundamental algorithms for scientific computing in Python. *Nature Methods*, *17*(3), 261–272. https://doi.org/10.1038/s41592-019-0686-2

Vollan, A. Z., Gardner, R. J., Moser, M.-B., & Moser, E. I. (2025). Left–right-alternating theta sweeps in entorhinal–hippocampal maps of space. *Nature*, *639*(8056), 995–1005. https://doi.org/10.1038/s41586-024-08527-1

Wang, Q., Ding, S.-L., Li, Y., Royall, J., Feng, D., Lesnar, P., Graddis, N., Naeemi, M., Facer, B., Ho, A., Dolbeare, T., Blanchard, B., Dee, N., Wakeman, W., Hirokawa, K. E., Szafer, A., Sunkin, S. M., Oh, S. W., Bernard, A., … Ng, L. (2020). The Allen Mouse Brain Common Coordinate Framework: A 3D Reference Atlas. *Cell*, *181*(4), 936–953.e20. https://doi.org/10.1016/j.cell.2020.04.007

Wang, W., Schuette, P. J., Nagai, J., Tobias, B. C., Cuccovia V. Reis, F. M., Ji, S., De Lima, M. A., La-Vu, M. Q., Maesta-Pereira, S., Chakerian, M., Leonard, S. J., Lin, L., Severino, A. L., Cahill, C. M., Canteras, N. S., Khakh, B. S., Kao, J. C., & Adhikari, A. (2021). Coordination of escape and spatial navigation circuits orchestrates versatile flight from threats. *Neuron*, *109*(11), 1848–1860.e8. https://doi.org/10.1016/j.neuron.2021.03.033

Warburton, E., & Aggleton, J. P. (1998). Differential deficits in the Morris water maze following cytotoxic lesions of the anterior thalamus and fornix transection. *Behavioural Brain Research*, *98*(1), 27–38. https://doi.org/10.1016/S0166-4328(98)00047-3

Watanabe, K., & Kawana, E. (1980). A horseradish peroxidase study on the mammillothalamic tract in the rat. *Cells Tissues Organs*, *108*(3), 394–401. https://doi.org/10.1159/000145322

Welday, A. C., Shlifer, I. G., Bloom, M. L., Zhang, K., & Blair, H. T. (2011). Cosine Directional Tuning of Theta Cell Burst Frequencies: Evidence for Spatial Coding by Oscillatory Interference. *The Journal of Neuroscience*, *31*(45), 16157–16176. https://doi.org/10.1523/JNEUROSCI.0712-11.2011

West, J. W., Patton, D. E., Scheuer, T., Wang, Y., Goldin, A. L., & Catterall, W. A. (1992). A cluster of hydrophobic amino acid residues required for fast Na(+)-channel inactiv-

ation. *Proceedings of the National Academy of Sciences*, *89*(22), 10910–10914. https://doi.org/10.1073/pnas.89.22.10910

Wiener, S. I., & Taube, J. S. (2005). *Head direction cells and the neural mechanisms of spatial orientation*. MIT Press.

Wigmore, M. A., & Lacey, M. G. (2000). A Kv3-like persistent, outwardly rectifying, Cs+ -permeable, K+ current in rat subthalamic nucleus neurones. *The Journal of Physiology*, *527*(3), 493–506. https://doi.org/10.1111/j.1469-7793.2000.t01-1-00493.x

Williams, S. R., Tóth, T. I., Turner, J. P., Hughes, S. W., & Crunelli, V. (1997). The 'window' component of the low threshold Ca^{2+} current produces input signal amplification and bistability in cat and rat thalamocortical neurones. *The Journal of Physiology*, *505*(3), 689–705. https://doi.org/10.1111/j.1469-7793.1997.689ba.x

Williams, S., Serafin, M., Mühlethaler, M., & Bernheim, L. (1997). Distinct Contributions of High- and Low-Voltage-Activated Calcium Currents to Afterhyperpolarizations in Cholinergic Nucleus Basalis Neurons of the Guinea Pig. *The Journal of Neuroscience*, *17*(19), 7307–7315. https://doi.org/10.1523/JNEUROSCI.17-19-07307.1997

Willis, T. (1664). *Cerebri Anatome, nervorumque descriptio et usus.*

Wilson, M. A., & McNaughton, B. L. (1993). Dynamics of the Hippocampal Ensemble Code for Space. *Science*, *261*(5124), 1055–1058. https://doi.org/10.1126/science.8351520

Winter, S. S., Clark, B. J., & Taube, J. S. (2015). Disruption of the head direction cell network impairs the parahippocampal grid cell signal. *Science*, *347*(6224), 870–874. https://doi.org/10.1126/science.1259591

Wirtshafter, D., & Stratford, T. R. (1993). Evidence for GABAergic projections from the tegmental nuclei of Gudden to the mammillary body in the rat. *Brain Research*, *630*(1–2), 188–194. https://doi.org/10.1016/0006-8993(93)90656-8

Wolfart, J., Neuhoff, H., Franz, O., & Roeper, J. (2001). Differential Expression of the Small-Conductance, Calcium-Activated Potassium Channel SK3 Is Critical for Pacemaker Control in Dopaminergic Midbrain Neurons. *The Journal of Neuroscience*, *21*(10), 3443–3456. https://doi.org/10.1523/JNEUROSCI.21-10-03443.2001

Wolfart, J., & Roeper, J. (2002). Selective Coupling of T-Type Calcium Channels to SK Potassium Channels Prevents Intrinsic Bursting in Dopaminergic Midbrain Neurons. *The Journal of Neuroscience*, *22*(9), 3404–3413. https://doi.org/10.1523/JNEUROSCI.22-09-03404.2002

Womack, M. D., Chevez, C., & Khodakhah, K. (2004). Calcium-Activated Potassium Channels Are Selectively Coupled to P/Q-Type Calcium Channels in Cerebellar Purkinje Neurons. *The Journal of Neuroscience*, *24*(40), 8818–8822. https://doi.org/10.1523/JNEUROSCI.2915-04.2004

Womack, M. D., & Khodakhah, K. (2002). Characterization of large conductance Ca2+ -activated K+ channels in cerebellar Purkinje neurons. *European Journal of Neuroscience*, *16*(7), 1214–1222. https://doi.org/10.1046/j.1460-9568.2002.02171.x

Wood, E. R., Dudchenko, P. A., & Eichenbaum, H. (1999). The global record of memory in hippocampal neuronal activity. *Nature*, *397*(6720), 613–616. https://doi.org/10.1038/17605

Wright, N. F., Erichsen, J. T., Vann, S. D., O'Mara, S. M., & Aggleton, J. P. (2010). Parallel but separate inputs from limbic cortices to the mammillary bodies and anterior thalamic nuclei in the rat. *Journal of Comparative Neurology*, *518*(12), 2334–2354. https://doi.org/10.1002/cne.22336

Wright, N. F., Vann, S. D., Erichsen, J. T., O'Mara, S. M., & Aggleton, J. P. (2013). Segregation of parallel inputs to the anteromedial and anteroventral thalamic nuclei of the rat. *Journal of Comparative Neurology*, *521*(13), 2966–2986. https://doi.org/10.1002/cne.23325

Wyss, J., Swanson, L., & Cowan, W. (1979). A study of subcortical afferents to the hippocampal formation in the rat. *Neuroscience*, *4*(4), 463–476. https://doi.org/10.1016/0306-4522(79)90124-6

Xiong, W., Farukhi, Y. Z., Tian, Y., DiSilvestre, D., Li, R. A., & Tomaselli, G. F. (2006). A conserved ring of charge in mammalian Na^+ channels: A molecular regulator of the outer pore conformation during slow inactivation. *The Journal of Physiology*, *576*(3), 739–754. https://doi.org/10.1113/jphysiol.2006.115105

Yamawaki, N., Li, X., Lambot, L., Ren, L. Y., Radulovic, J., & Shepherd, G. M. G. (2019). Long-range inhibitory intersection of a retrosplenial thalamocortical circuit by apical tuft-targeting CA1 neurons. *Nature Neuroscience*, *22*(4), 618–626. https://doi.org/10.1038/s41593-019-0355-x

Yan, Y., Burgess, N., & Bicanski, A. (2021). A model of head direction and landmark coding in complex environments (B. Webb, Ed.). *PLOS Computational Biology*, *17*(9), e1009434. https://doi.org/10.1371/journal.pcbi.1009434

Yartsev, M. M., & Ulanovsky, N. (2013). Representation of Three-Dimensional Space in the Hippocampus of Flying Bats. *Science*, *340*(6130), 367–372. https://doi.org/10.1126/science.1235338

Yoder, R. M., Chan, J. H. M., & Taube, J. S. (2017). Acetylcholine contributes to the integration of self-movement cues in head direction cells. *Behavioral Neuroscience*, *131*(4), 312–324. https://doi.org/10.1037/bne0000205

Yoder, R. M., Clark, B. J., Brown, J. E., Lamia, M. V., Valerio, S., Shinder, M. E., & Taube, J. S. (2011). Both visual and idiothetic cues contribute to head direction cell stability during navigation along complex routes. *Journal of Neurophysiology*, *105*(6), 2989–3001. https://doi.org/10.1152/jn.01041.2010

Yoder, R. M., Clark, B. J., & Taube, J. S. (2011). Origins of landmark encoding in the brain. *Trends in Neurosciences*, *34*(11), 561–571. https://doi.org/10.1016/j.tins.2011.08.004

Yoder, R. M., Peck, J. R., & Taube, J. S. (2015). Visual Landmark Information Gains Control of the Head Direction Signal at the Lateral Mammillary Nuclei. *The Journal of Neuroscience*, *35*(4), 1354–1367. https://doi.org/10.1523/JNEUROSCI.1418-14.2015

Yoder, R. M., & Taube, J. S. (2009). Head Direction Cell Activity in Mice: Robust Directional Signal Depends on Intact Otolith Organs. *The Journal of Neuroscience*, *29*(4), 1061–1076. https://doi.org/10.1523/JNEUROSCI.1679-08.2009

Yoder, R. M., & Taube, J. S. (2014). The vestibular contribution to the head direction signal and navigation. *Frontiers in Integrative Neuroscience*, *8*. https://doi.org/10.3389/fnint.2014.00032

Yoganarasimha, D., Yu, X., & Knierim, J. J. (2006). Head Direction Cell Representations Maintain Internal Coherence during Conflicting Proximal and Distal Cue Rotations: Comparison with Hippocampal Place Cells. *The Journal of Neuroscience*, *26*(2), 622–631. https://doi.org/10.1523/JNEUROSCI.3885-05.2006

Yuan, W., Burkhalter, A., & Nerbonne, J. M. (2005). Functional Role of the Fast Transient Outward K+ Current IA in Pyramidal Neurons in (Rat) Primary Visual Cortex. *The Journal of Neuroscience*, *25*(40), 9185–9194. https://doi.org/10.1523/JNEUROSCI.2858-05.2005

Żakowski, W. (2017). Neurochemistry of the Anterior Thalamic Nuclei. *Molecular Neurobiology*, *54*(7), 5248–5263. https://doi.org/10.1007/s12035-016-0077-y

Żakowski, W., Zawistowski, P., Braszka, Ł., & Jurkowlaniec, E. (2017). The effect of pharmacological inactivation of the mammillary body and anterior thalamic nuclei on hippocampal theta rhythm in urethane-anesthetized rats. *Neuroscience*, *362*, 196–205. https://doi.org/10.1016/j.neuroscience.2017.08.043

Zhang, K. (1996). Representation of spatial orientation by the intrinsic dynamics of the head-direction cell ensemble: A theory. *The Journal of Neuroscience*, *16*(6), 2112–2126. https://doi.org/10.1523/JNEUROSCI.16-06-02112.1996

Zhang, N., Grieves, R. M., & Jeffery, K. J. (2022). Environment Symmetry Drives a Multidirectional Code in Rat Retrosplenial Cortex. *The Journal of Neuroscience*, *42*(49), 9227–9241. https://doi.org/10.1523/JNEUROSCI.0619-22.2022

Zhang, S., SchÃ¶nfeld, F., Wiskott, L., & Manahan-Vaughan, D. (2014). Spatial representations of place cells in darkness are supported by path integration and border information. *Frontiers in Behavioral Neuroscience*, *8*. https://doi.org/10.3389/fnbeh.2014.00222

Zhou, F. M., & Hablitz, J. J. (1996). Layer I neurons of rat neocortex. I. Action potential and repetitive firing properties. *Journal of Neurophysiology*, *76*(2), 651–667. https://doi.org/10.1152/jn.1996.76.2.651

Zugaro, M. B., Tabuchi, E., Fouquier, C., Berthoz, A., & Wiener, S. I. (2001). Active Locomotion Increases Peak Firing Rates of Anterodorsal Thalamic Head Direction Cells. *Journal of Neurophysiology*, *86*(2), 692–702. https://doi.org/10.1152/jn.2001.86.2.692